A Theoretical Study of Rabi Oscillations in Dirac-Weyl Fermionic System

Upendra Kumar

A thesis
submitted for the degree of
Doctor of Philosophy

Department of Physics
Indian Institute of Technology Guwahati
Guwahati 781039, India

A Theoretical Study of Rabi Oscillations in Dirac-Weyl Fermionic System

Upendra Kumar

A thesis
submitted for the degree of
Doctor of Philosophy

Supervisor:
Prof. Girish. S. Setlur

Department of Physics
Indian Institute of Technology Guwahati
Guwahati 781039, India

Declaration

The work in this thesis is based on research carried out at the Department of Physics, Indian Institute of Technology Guwahati, India under the supervision of Dr. Girish S. Setlur. No part of this thesis has been submitted elsewhere for award of any other degree or qualification. Works presented in the thesis are entirely my own unless referenced to the contrary in the text.

Signed: _____

Date: _____

Certificate

Dr. Girish S. Setlur
Professor
Department of Physics, IIT Guwahati
Email: gsetlur@iitg.ernet.in

It is certified that the work contained in the thesis entitled " **A Theoretical Study of Rabi Oscillations in Dirac-Weyl Fermionic System** " by Mr. Upendra Kumar, a PhD student of the Department of Physics, IIT Guwahati was carried out under my supervision and has not been submitted elsewhere for award of any degree.

Dr. Girish S. Setlur

Dedicate to My Teachers

K.K. Pandey, Om Praksh Ji and Anand Kumar Chakraborty

Acknowledgements

I am highly grateful to my Ph.D. supervisor Dr. Girish S. Setlur. I am obliged to him for his excellent guidance, valuable suggestions, inspiration towards research and support throughout my research work.

I am also thankful to my doctoral committee members Dr. M. K. Nandy, Dr. Alika Khare and Dr. Siddhartha P. Chakrabarty for reviewing my progress and for giving me their frank comments and suggestions. I express my gratitude to the other teachers of department Dr. Subhradip Ghosh, Dr. Saurabh Basu, Dr. T. N. Dey and others, who helped to learn many things in physics during my course work. I am grateful head of the department of physics, Dr. P. Poulose for supplying the full support and facilities at their best. I am thankful to IIT Guwahati for providing me the financial assistantship during my research period. I am thankful to the technical staff Mr. B. B. Purakayasthya and Mr. Hemanta Medhi for their assistance in various ways during my research period.

I am also highly grateful to Dr. Uma Dutta of Cotton University for her moral support and words of encouragement. I am also thankful to my senior Dr. Enamullah, Dr. Vipin Kumar and juniors Mr. Joy Prakash Das, Rahul Keshrwani for their supportive and helping nature. I learned from Dr. Vipin, how you work hard without making noise. I would like to extend my sincere thanks to my lab senior Dr. Satendra Kumar, Dr. Mukesh Singh, Dr. Indrajeet Kumar and my class-mates Dr. Ramesh Ghosh, Dr. Maulana Obaidullah, Biswajit Karmakar, Partha Dey and Bhagwan Kisan for the great funny moments of Ph.D. life shared with one another.

I want to give special thanks to my beloved friend Dr. Gyanendra Patel (IIT Kanpur), who always motivate me in pursuing career in Ph.D., Dr. Ramesh Ghosh (Guruji) without him I never pass this IIT course work examination and Shashank Shekhar Mishra (BHU), who solved my many physics problem during preparation of GATE examination.

I am highly obliged with Prof. Leonas Valkunas and Prof. Darius Abramavicius for introducing me with 2D spectroscopy, a new branch of physics during my ERASMUS fellowship period. I am also thankful to Vytautas Butkus, Vytautas Balevičius, Jevgenij Chmeliov, Vladimir Chorošajev and other colleagues of Vilnius University. Special thanks to Emilis Pileckis with whom I learned many things such as MATLAB software, making the timetable for every single minute of the day.

Finally, I am extremely indebted to my primary teacher K. K. Pandey and Om Prakash Ji, they helped and motivated me so much that I can not explain in my word. I would like to extend my sincere thanks to Shakun Prashad Pandey, who cleared my doubt with extreme patience at the level of Matriculation. I am highly thankful to my beloved best teachers, got in my life, Mr. Anand Kumar Chakraborty, who helped in fulfilling my dream to reach IIT. His passion towards teaching us, cannot be explained in the word.

My final and foremost thank go to the land of Assam, Brahmputra river and Kamakhya temple for giving me everything which I deserve and not giving many things from which I learned so many lessons.

Abstract

Conventional Rabi oscillations are studied using the rotating wave approximation (RWA). It is an approximation used for the approximate analytic solution of time-dependent Schrödinger eqn. of a two-level system coupled to a weak electric field in resonant with the transition. In this approximation, we remove rapidly oscillating terms of the effective Hamiltonian, but its validity is limited to only when the internal frequency of the two-level system is close to the external frequency of field, i.e. in case of resonance. Far from conventional resonance, only relativistic fermionic systems exhibit a new type of Rabi oscillation, which is absent in conventional semiconductors and two-level systems. Our aim is to study nonlinear optics of these systems at the Weyl (Dirac) node, since all interesting physics at low energy occurs in the vicinity of the Weyl(Dirac) node - particularly the phenomenon of anomalous Rabi oscillation (ARO), which has been predicted theoretically in single layer graphene by our group (and also by others where these ideas go under the name of "Floquet theory"). In order to study this, we employ an approximation known as asymptotic rotating wave approximation (ARWA). We have studied this phenomenon as well as its conventional counterpart that occurs close to resonance (ordinary Rabi oscillations) and verified the claims numerically.

Graphene is a prototype of a two-dimensional massless Dirac-fermion system. The three-dimensional (3D) analog of graphene is called a Weyl semimetal. 3D topological insulators (TI) have surface states that consist of massless 2D Dirac fermions. These three systems have some features in common - in addition to being composed of massless fermions, they possess spin-like internal degrees of freedom. Such relativistic fermion systems are best characterized using the phenomenon of anomalous Rabi oscillation (ARO) that occurs far from conventional resonance and is unique to these systems. These oscillations are absent in two-level atoms and conventional semiconductors. The main difference in the non-linear optical response between graphene-like materials and Weyl semimetal (or surface state states of TI) is the latter's pronounced anisotropy in the wave vector dependence of both the conventional and anomalous Rabi frequencies. A detailed analysis of this anisotropy shows that in Weyl metals (or on TI surface), the Rabi frequency has a form that resembles massless Dirac particles at certain points in the reciprocal space. Hence, in these systems, both the quasiparticles and the collective modes that exist in them in response to time-varying fields are ultra-relativistic in nature whereas in graphene only the original quasiparticles are massless, but the Rabi modes are massive. On surface states of TI, this anisotropy may be attributed to

the Zeeman term. It is shown that the Zeeman term has no qualitative effect on the conventional Rabi frequency, but its absence makes the anomalous Rabi modes massless. A fully numerical solution of the Floquet-Bloch equations unequivocally establishes the presence of not only anomalous Rabi oscillations in these systems but also their massless character.

In two-level systems, it is recognized that conventional Rabi oscillations undergo a shift in the resonant frequency which is the Bloch-Siegert shift. This shift is quite small in such systems and hence largely of academic interest. The present work shows that in graphene, such shifts can be substantial - especially upon the inclusion of band curvature effects and Rashbha coupling. Both conventional and anomalous Rabi oscillations are resonance phenomena, in other words, the amplitude of these oscillations peak when the condition for resonance is obeyed. The purpose of study the shift in the conditions for resonance brought about by **(a)** the presence of strong fields upon the inclusion of frequency doubling effects or **(b)** band anisotropy due to next nearest neighbor hopping or Rashba effect. We refer to both these shifts as Bloch-Siegert shifts, although only **(a)** was envisaged by Bloch and Siegert.

In science, verification of a theory is usually accomplished by performing a suitable experiment. We have described pump-probe spectroscopy, which is used to experimentally probe the phenomenon of anomalous Rabi oscillations - a central idea in this thesis. In this experiment, two successive laser pulses are used, one for exciting the system in a certain way, called pump pulse and other to test it after a variable time delay, called probe pulse. This simply involves looking for periodic oscillations in the differential transmission coefficient versus pump pulse duration (alternatively, the area of the pump pulse). When all else remains fixed (including pump-probe delay), these plots exhibits oscillations with a frequency corresponding to the anomalous Rabi frequency. Furthermore, the amplitude of these oscillations decay as a power law in the pump duration with a characteristic exponent that is indicative of the particular system under consideration.

Furthermore, it is shown that ARO exists even if the EM field is treated quantum mechanically. This establishes that the AROs are not due to approximations or assumptions we have made. By using probability amplitude equation, we have studied anomalous Rabi oscillations in the presence of a quantum field. Finally, we described limiting case, how these quantum result will convert in the classical result. New phenomena such as zero-point or vacuum anomalous Rabi oscillations are seen. Therefore, it is no exaggeration to say that the anomalous Rabi

oscillation is a phenomenon that is uniquely suited to study condensed matter realizations of relativistic systems.

Contents

List of Figures

List of Tables

Chapter 1

Introduction

Topological states of matter has become one of the most important research areas in the field of condensed matter physics and materials science [1–4]. A new class of semimetals, known as topological semimetals, has generated interest due to experimental observation of Weyl and Dirac semimetals [5–7]. Dirac and Weyl semimetals are two specific types of topological semimetals, where low energy bulk excitations are described by Dirac and Weyl equations, respectively. In case of the Weyl semimetal, either time-reversal (TR) or inversion symmetry is broken [8]. The low energy physics is described near the Weyl point by three-dimensional (3D) two-component Weyl fermions, $H = \pm v\boldsymbol{\sigma} \cdot \mathbf{p}$, where $\boldsymbol{\sigma}$ is the Pauli matrix and $\mathbf{p}$ is the momentum as measured from band touching (Weyl) points [9, 10]. In presence of both the TR and inversion symmetries, a 3D Dirac semimetal state is a four-component Dirac fermion composed of two Weyl fermions of opposite chirality. There is an additional symmetry viz. crystal rotational symmetry, which protects this Dirac semimetal [11–13]. The Weyl points can be separated in momentum and energy by breaking TR and inversion symmetry, respectively [14]. In both situations, the Fermi surface of surface states also splits into open segments, which are Fermi arcs discussed in Weyl semimetals [11–13]. So there should be qualitative and quantitative differences in the properties of Dirac and Weyl semimetals. Topological semimetal is a gapless metal characterized by topological invariants. This development leads to a broadening of the classification of topological phases of matter beyond insulators. In case of topological insulators, only surface states are interesting [2]. On the other hand, a topological semimetal has an unusual band structure in their bulk and on the surface. In the bulk, conduction and valence bands of a topological semimetal touch linearly at the Weyl points, through which the bands disperse linearly along all the three momentum directions. There

are many interesting phenomena in topological semimetals such as topological surface states, chiral anomalies, quantum anomalous Hall effects and unusual optical conductivity [15, 16]. The article of Mehrdad Dadsetani and Ali Ebarhimian [17] has been the resource for much of the above description.

The era of Dirac-Weyl fermionic systems has started in the condensed matter physics. These systems work as a bridge between condensed matter and relativistic electrodynamics [18]. In presence of a strong oscillatory driving field, the typical dynamics for the coherent interaction of two-level atoms with light is dominated by a phenomenon known as Rabi oscillation [19]. This is an important effect in various branches of physics such as quantum optics, magnetic resonance and quantum computing. In this thesis, we study the phenomenon of Rabi oscillation in systems such as graphene, topological insulator and Weyl semimetal and try to make a connection between them.

1.1 Graphene

Graphene is a type of Dirac semimetal related to the family of carbon allotropes. Carbon is one of the most important and abundant element found on the earth after hydrogen, helium and oxygen. Diamond and graphite are two completely different allotropes of carbon. Both possess different physical properties, due to the different arrangement of carbon atoms in their structure. Diamond is insulating and very hard, while graphite is conducting and lubricative. Fullerene was the first artificial pure carbon material discovered in 1985 [20]. After that, an intense research effort began for finding other allotropic forms of carbon. The one-dimensional carbon nanotube was discovered in 1991 [21]. Graphene is a new addition in the family of carbon allotropes. Due to its extraordinary 2D nature, it became a Nobel prize winning discovery [22, 23]. Graphene is a 2D structure of carbon atoms arranged in a honeycomb pattern. It was first synthesized in 2004, by the group of physicists Andre Geim and Konstantin Novoselov at Manchester. However, ultrathin graphite (not one atom thick) was described in the early 1960's [24–27]. By wrapping graphene, it can be made effectively zero dimensional (0D), known as a fullerene, one dimensional (1D) known as carbon nanotube, it can be stacked into three dimensions known as graphite. Graphene [22, 23] becomes a bridge between condensed matter and relativistic electrodynamics [18]. It has linear low-energy dispersion (energy vs momentum relation) near some specific points called Dirac points [23]. Near these points, charge carriers behaves like

massless Dirac fermions due to linear low-energy dispersion [28–33]. The conduc-

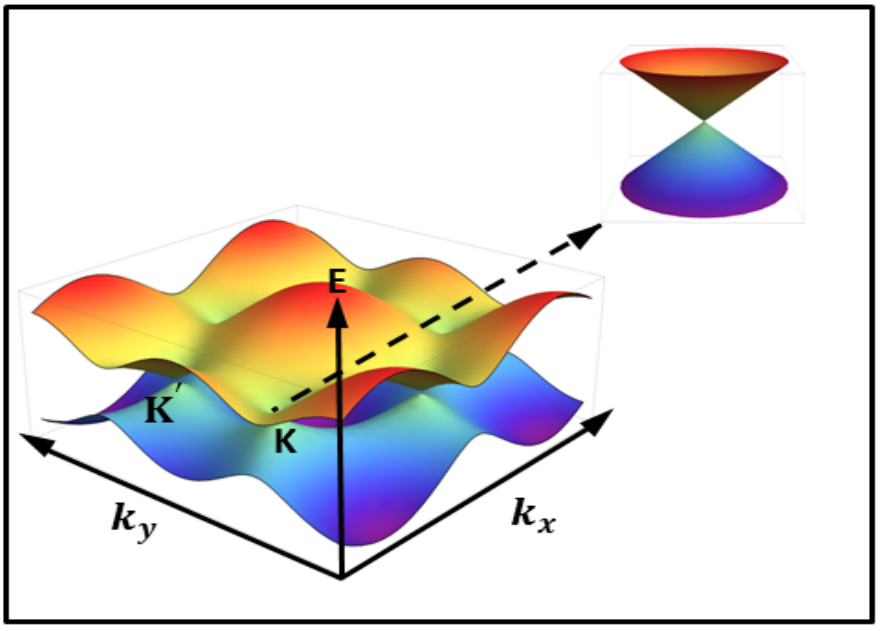

FIGURE 1.1: Band structure of graphene is shown where the conduction band and valence band touch at certain locations in the reciprocal space known as Dirac points. The linear energy momentum relation described in inset.

tion band and the valence band touch each other at the Dirac points, so it is also called zero band gap semiconductor. The crucial difference between conventional semiconductor and graphene is that graphene possesses charge carriers that obey the relativistic Dirac equation near the Dirac point and have a pseudo spin degree of freedom [23], while conventional semiconductors have charge carriers that obey a parabolic dispersion relation and do not possess pseudo spin. Graphene is a one atom thick, single layer of graphite material fully comprises carbon atoms arranged in a honeycomb crystal lattice [22, 23]. There are two triangular sub-lattices which are labeled by 'A' and 'B' by splitting of honeycomb crystal lattice of graphene in fig.(1.2). In graphene, there is no energy gap between the conduction band and valence band, also no overlap between these bands as shown in fig.(1.1), so it is also called 'gapless' semiconductor or semimetal. The two inequivalent points where conduction and valence bands intersect each other, called Dirac points **K** and $\mathbf{K}^{'}$ in first Brillouin zone. The charge carriers in graphene near these Dirac points obeys Dirac equation, having speed $\frac{1}{300}^{th}$ of the speed of light in vacuum. So these quasi-particles are generally known as massless Dirac fermions [34–36].

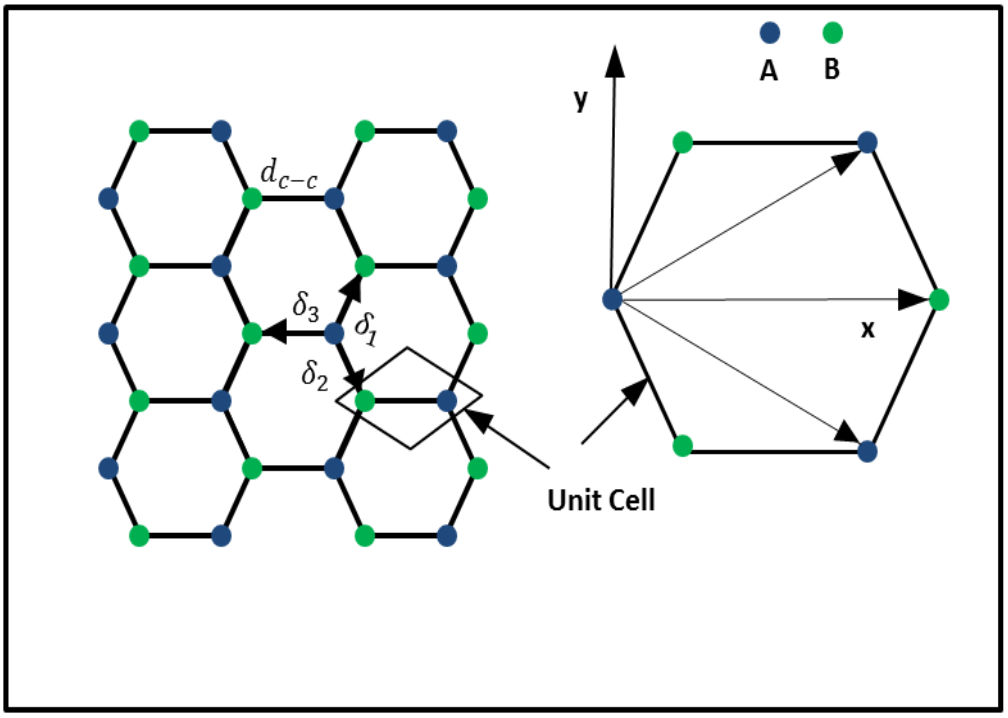

FIGURE 1.2: In this figure, we can see the ideal 2D graphene honeycomb lattice which is the interpenetration of two triangular sublattices labeled 'A' and 'B' type of atoms. There are two atoms per unit cell of graphene lattice (shown in the figure). The right figure shows the unit cell since it effectively contains two atoms.

1.1.1 Geometry of Graphene

As we have described earlier, graphene is a allotrope of carbon with a honeycomb crystal lattice. Each carbon atom contains four electrons in its outer shell called valence electrons. Each carbon atom shares three electrons with its neighboring carbon atoms. There are two types of carbon-carbon bonds known as sigma (σ) and pi (π) bonds. The valance orbital configuration of carbon atom is $2s^2, 2p^2$. There is a much smaller energy difference between valance orbital and the binding energy of neighboring carbon atoms, which enables the wavefunction of electrons to combine by the process known as hybridization [37]. Due to hybridization, carbon atom has sp^2 hybridized orbital (orbital formed from one s and two p orbitals).The σ bonds are formed when $2s$, $2p_x$ and $2p_y$ orbitals are mixed together. They lie in the x-y plane with 120^0 angle between two neighboring chemical bonds. An electron which resides in $2p_z$ orbital forms a π bond aligned in the z direction. The electrons of the p orbitals are free and responsible for the conduction and transport processes in graphene. The trigonal planar structure in graphene is formed by sp^2

hybridized orbitals. By interpenetration of two trigonal planar structures, referred to as A and B sublattices, graphene can be formed. The graphene lattice contains two atoms per unit cell. The atoms at A sublattices connected with B type of atoms with time reversal symmetry. The distance between carbon atom is 1.42 Å. The ideal monolayer graphene is depicted in fig.(1.2). Graphene has two direct lattice vectors $\mathbf{R}_1$ and $\mathbf{R}_2$ and the nearest neighbor vector $\boldsymbol{\delta}_i$ (i= 1,2 and 3) in real space. The direct lattice vectors can be expressed as

$$\mathbf{R}_1 = \frac{3}{2}d_{c-c}\,\hat{x} + \frac{\sqrt{3}}{2}d_{c-c}\,\hat{y}, \qquad \mathbf{R}_2 = \frac{3}{2}d_{c-c}\,\hat{x} - \frac{\sqrt{3}}{2}d_{c-c}\,\hat{y}. \tag{1.1}$$

d_{c-c} represents the carbon-carbon distance (≈ 1.42Å), $|\mathbf{R}_1| = |\mathbf{R}_2| = \sqrt{3}\ d_{c-c}$ is the lattice constant and $\hat{x}$ and $\hat{y}$ are the unit vectors. The vector form of nearest neighbor distances are given by

$$\boldsymbol{\delta}_1 = \frac{1}{2}d_{c-c}\,\hat{x} + \frac{\sqrt{3}}{2}d_{c-c}\,\hat{y}, \quad \boldsymbol{\delta}_2 = \frac{1}{2}d_{c-c}\,\hat{x} - \frac{\sqrt{3}}{2}d_{c-c}\,\hat{y}, \quad \boldsymbol{\delta}_3 = -d_{c-c}\,\hat{x}. \tag{1.2}$$

By using this basis we denote the reciprocal lattice as points $\mathbf{G}$. The volume of reciprocal lattice space is called first Brillouin zone (fig.(1.3)) which is the interior formed by planes that bisect the nearest neighbors in reciprocal space. The angle between reciprocal lattice and direct lattice is always 90^0 shown in the fig.(1.3). Γ denotes the center of the first Brillouin zone, corner points denoted by $\mathbf{K}$ and $\mathbf{K}'$ are known as Dirac points. The conduction and valence band touch each other at these points, so they become important for defining the nature of graphene. The reciprocal lattice vectors $\mathbf{G}_1$ and $\mathbf{G}_2$ can be expressed by following relation

$$\mathbf{R}_i \cdot \mathbf{G}_j = 2\pi\delta_{ij}, \tag{1.3}$$

The reciprocal lattice vectors are

$$\mathbf{G}_1 = \frac{2\pi}{3d_{c-c}}\hat{x} + \frac{2\pi}{\sqrt{3}d_{c-c}}\hat{y}, \quad \mathbf{G}_2 = \frac{2\pi}{3d_{c-c}}\hat{x} - \frac{2\pi}{\sqrt{3}d_{c-c}}\hat{y}. \tag{1.4}$$

There are two sets of inequivalent Dirac points $\mathbf{K}$ and $\mathbf{K}'$ in the first Brillouin zone. Each set contains three equivalent Dirac points. In momentum space, these points can be expressed

$$\mathbf{K} = \frac{2\pi}{3d_{c-c}}\hat{x} + \frac{2\pi}{\sqrt{3}d_{c-c}}\hat{y}, \quad \mathbf{K}' = \frac{2\pi}{3d_{c-c}}\hat{x} - \frac{2\pi}{\sqrt{3}d_{c-c}}\hat{y}. \tag{1.5}$$

[0] https://asbury.com/technical-presentations-papers/introduction-to-graphite/structural-description/

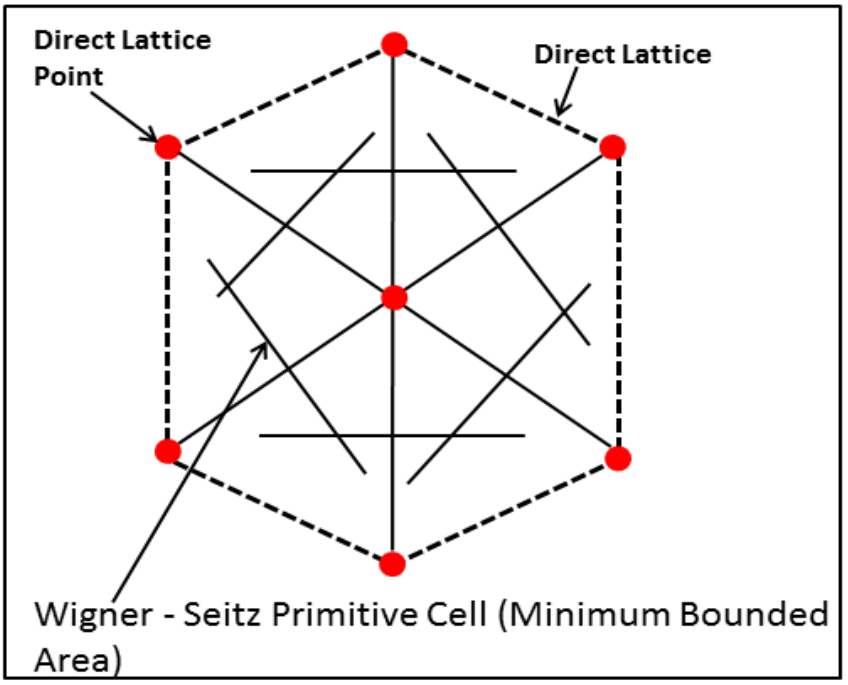

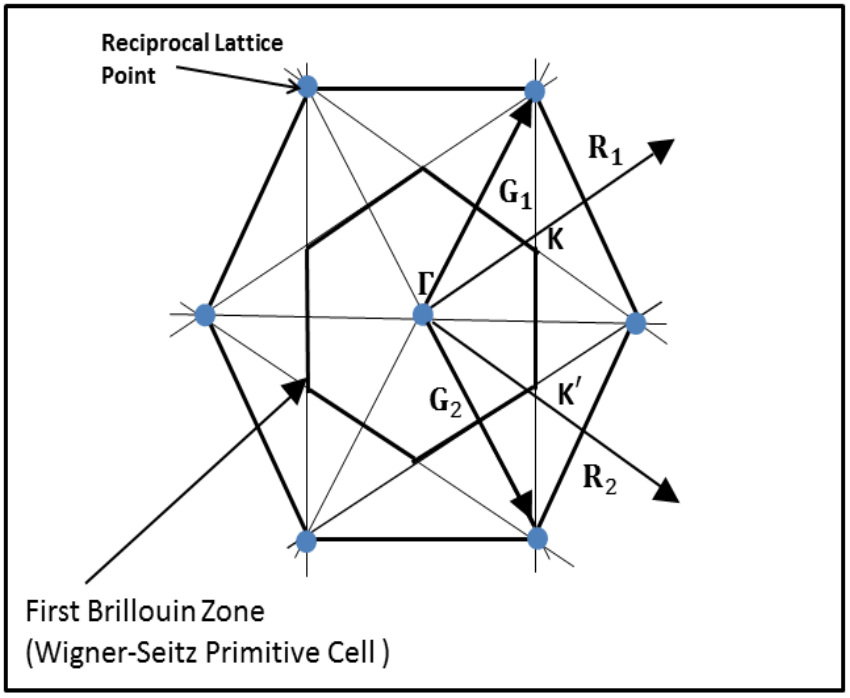

FIGURE 1.3: The first figure shows the Wigner-Seitz primitive cell obtained from the direct lattice of graphene. Second figure depicts the reciprocal lattice of graphene, making an angle 90^0 with the direct lattice. The reciprocal lattice vectors G_1 and G_2 form the basis.

1.1.2 Honeycomb Lattice (Graphene) i.e. Nearest-Neighbor (NN) Hopping

For calculating the electronic band structure of solid materials, the tight binding (TB) method is one of the standard methods. In this method, linear combination of atomic orbitals is employed, explained in various text books [38, 39]. Localized orbitals are associated with each atomic site in this approximation. So the wave-function of the system becomes a linear combination of these basis eigenfunctions. By solving these eigenvalue equations, the energy dispersion relation may be found which determines the band structure of the given condensed matter system. By using the tight binding approximation, P. R. Wallace had obtained the electronic band structure of graphite in 1947 [40]. This enables a simple explanation of the electronic band structure of graphene [41, 42]. In the first instance, we restrict our attention to only the nearest neighbour hopping terms [43]. The nearest neighbor tight binding Hamiltonian of graphene can be written as (we use units such that $\hbar = 1$)

$$H = -t \sum_{i,j,\sigma} \left(\hat{a}^{\dagger}_{i\sigma} \hat{b}_{j\sigma} + h.c. \right). \tag{1.6}$$

If we denote the orbital on atom i with spin σ by (i, σ) then

$$\hat{a}^{\dagger}_{i\sigma} = \frac{1}{\sqrt{N}} \sum_{\mathbf{k},i} e^{-i\mathbf{k}\cdot\mathbf{R}^0_i} \hat{a}^{\dagger}_{\mathbf{k},\sigma}, \tag{1.7}$$

$$\hat{b}_{j\sigma} = \frac{1}{\sqrt{N}} \sum_{\mathbf{k}',i,j} e^{i\mathbf{k}'\cdot\left(\mathbf{R}^0_i + \boldsymbol{\delta}_j\right)} \hat{b}_{\mathbf{k}',\sigma}. \tag{1.8}$$

Here N is the number of atomic sites and $\mathbf{R}^0_i$ is the reference point within the unit cell. We have chosen atom A as reference point $\mathbf{R}^0_i$ then B type of atoms will be the nearest neighbors of A and separated by nearest neighbor vectors $\boldsymbol{\delta}_1$, $\boldsymbol{\delta}_2$ and $\boldsymbol{\delta}_3$ at an angle 120^0 with each other.

$$H = -\frac{t}{N} \sum_{\mathbf{k},\mathbf{k}',i,j,\sigma} \left(e^{-i\mathbf{k}\cdot\mathbf{R}^0_i} \hat{a}^{\dagger}_{\mathbf{k},\sigma} e^{i\mathbf{k}'\cdot\left(\mathbf{R}^0_i + \boldsymbol{\delta}_j\right)} \hat{b}_{\mathbf{k}',\sigma} + h.c. \right), \tag{1.9}$$

$$H = -\frac{t}{N} \sum_{\mathbf{k},\mathbf{k}',i,j,\sigma} \left(e^{-i(\mathbf{k}-\mathbf{k}')\cdot\mathbf{R}^0_i} \hat{a}^{\dagger}_{\mathbf{k},\sigma} e^{i\mathbf{k}'\cdot\delta_j} \hat{b}_{\mathbf{k}',\sigma} + h.c. \right). \tag{1.10}$$

If $\mathbf{k} \neq \mathbf{k}'$

$$\sum_i e^{-i(\mathbf{k}-\mathbf{k}')\cdot\mathbf{R}^0_i} = 0. \tag{1.11}$$

If $\mathbf{k} = \mathbf{k}^{'}$

$$\sum_{i} e^{-i(\mathbf{k}-\mathbf{k}^{'})\cdot\mathbf{R}_i^0} = N, \tag{1.12}$$

$$H = -t\sum_{\mathbf{k},j,\sigma}\left(e^{i\mathbf{k}\cdot\boldsymbol{\delta}_j}\hat{a}^{\dagger}_{\mathbf{k},\sigma}\hat{b}_{\mathbf{k},\sigma} + h.c.\right), \tag{1.13}$$

$$H = -t\sum_{\mathbf{k},j,\sigma}\left(e^{i\mathbf{k}\cdot\boldsymbol{\delta}_j}\hat{a}^{\dagger}_{\mathbf{k},\sigma}\hat{b}_{\mathbf{k},\sigma} + e^{-i\mathbf{k}\cdot\boldsymbol{\delta}_j}\hat{b}^{\dagger}_{\mathbf{k},\sigma}\hat{a}_{\mathbf{k},\sigma}\right). \tag{1.14}$$

In matrix form it can be written as

$$H = -t\sum_{\mathbf{k},j}\begin{bmatrix}\hat{a}^{\dagger}_{\mathbf{k},\sigma} & \hat{b}^{\dagger}_{\mathbf{k},\sigma}\end{bmatrix}\begin{bmatrix}0 & e^{i\mathbf{k}\cdot\boldsymbol{\delta}_j}\\ e^{-i\mathbf{k}\cdot\boldsymbol{\delta}_j} & 0\end{bmatrix}\begin{bmatrix}\hat{a}_{\mathbf{k},\sigma}\\ \hat{b}_{\mathbf{k},\sigma}\end{bmatrix}. \tag{1.15}$$

Nearest-neighbor distance $\boldsymbol{\delta}_1 = \frac{1}{2}d_{c-c}\hat{x} + \frac{\sqrt{3}}{2}d_{c-c}\hat{y}$, $\boldsymbol{\delta}_2 = \frac{1}{2}d_{c-c}\hat{x} - \frac{\sqrt{3}}{2}d_{c-c}\hat{y}$ and $\boldsymbol{\delta}_3 = -d_{c-c}\hat{x}$. Here d_{c-c} is carbon-carbon atom distance. This means

$$\sum_{j} -te^{i\mathbf{k}\cdot\boldsymbol{\delta}_j} = -t\left(e^{i\mathbf{k}\cdot\boldsymbol{\delta}_1} + e^{i\mathbf{k}\cdot\boldsymbol{\delta}_2} + e^{i\mathbf{k}\cdot\boldsymbol{\delta}_3}\right). \tag{1.16}$$

Then the Hamiltonian becomes

$$H = \begin{bmatrix}0 & -te^{-id_{c-c}k_x}\left(e^{i\frac{3}{2}d_{c-c}k_x}2\cos\left(\frac{\sqrt{3}}{2}d_{c-c}k_y\right)+1\right)\\ -te^{id_{c-c}k_x}\left(e^{-i\frac{3}{2}d_{c-c}k_x}2\cos\left(\frac{\sqrt{3}}{2}d_{c-c}k_y\right)+1\right) & 0\end{bmatrix}. \tag{1.17}$$

Eigenvalues of this matrix will be

$$= \pm t\sqrt{4\cos\left(\frac{3}{2}d_{c-c}k_x\right)\cos\left(\frac{\sqrt{3}}{2}d_{c-c}k_y\right) + 2\cos\left(\sqrt{3}d_{c-c}k_y\right) + 3}. \tag{1.18}$$

In order to obtain the low-energy dispersion relation, we may expand the Hamiltonian of eq.(1.17) near the Dirac point. We write the wave vector $\mathbf{k}$ as

$$\mathbf{k} = \mathbf{K} + \mathbf{p}, \quad |\mathbf{K}| >> |\mathbf{p}|. \tag{1.19}$$

By using Taylor series expansion, the expression near one of the Dirac point $\mathbf{K}$ will be

$$\sum_{\delta} e^{i\mathbf{k}\cdot\boldsymbol{\delta}} = \sum_{\delta} e^{i(\mathbf{K}+\mathbf{p})\cdot\boldsymbol{\delta}} \approx \sum_{\delta} e^{i\mathbf{K}\cdot\boldsymbol{\delta}}\left(1 + i\mathbf{p}\cdot\boldsymbol{\delta}\right) \approx \frac{3t}{2}d_{c-c}(p_x - ip_y). \tag{1.20}$$

Extracting an overall factor $-ie^{i\mathbf{K}\cdot\boldsymbol{\delta}}$ that does not affect the physical results, Hamiltonian eq.(1.17) have the form

$$H_{\mathrm{K}} = \frac{3t}{2} d_{c-c} \begin{bmatrix} 0 & (p_x - ip_y) \\ (p_x + ip_y) & 0 \end{bmatrix} = v_F \left(\boldsymbol{\sigma} \cdot \mathbf{p}\right). \tag{1.21}$$

Here, we define Fermi velocity as $v_F = \frac{3t}{2} d_{c-c}$. This is called low-energy Hamiltonian of graphene, where, $\sigma = (\sigma_x, \sigma_y)$ is the set pseudo-spin pauli matrices. The eigenvalue of above Hamiltonian is

$$E\left(\mathbf{k} = \mathbf{K} + \mathbf{p}\right) = \frac{3t}{2} d_{c-c} \sqrt{p_x^2 + p_y^2} = v_F |\mathbf{p}|. \tag{1.22}$$

Similarly, the low energy Hamiltonian near another Dirac point $\mathbf{K}'$

$$H_{\mathrm{K}'} = v_F \begin{bmatrix} 0 & (p_x + ip_y) \\ (p_x - ip_y) & 0 \end{bmatrix} = v_F \left(\boldsymbol{\sigma}^* \cdot \mathbf{p}\right). \tag{1.23}$$

Here $\sigma^* = (\sigma_x, -\sigma_y)$. Hamiltonians in eq.(1.21) and eq.(1.23) are linearly dependent on momentum and related to each other by time-reversal symmetry [23].

1.1.3 Pseudospin in Graphene

The Hamiltonian of graphene $H_{\lambda,\nu}(\mathbf{k})$ may be written as a 2×2 matrix, where λ and ν refer to sublattices A and B and $\mathbf{k}$ is the crystal momentum. Using this, valence and conduction bands of graphene are described. We consider the sublattice degree of freedom as a pseudospin, with the A sublattice represents the $|\uparrow\rangle$ pseudospin state and the B sublattice represents the $|\downarrow\rangle$ pseudospin state. There is hopping of electrons from sublattices A to B and vice versa [44]. This creates an effective magnetic field, which is proportional to magnitude and direction of momentum measured from the Brillouin-zone corners. The Hamiltonian can be defined as $H_{\lambda,\nu}(\mathbf{k}) = -h(\mathbf{k}).\boldsymbol{\sigma}_{\lambda,\nu}$, here σ represents Pauli spin matrix vector. This Hamiltonian contains momentum-dependent magnetic field $h(\mathbf{k})$, which works on the pseudospin degree of freedom. The gap between conduction and valence bands vanishes at points where the pseudospin field $h(\mathbf{k})$ is zero. The momentum can be written as a sum of wave vectors $\mathbf{p} = \mathbf{K} + \mathbf{k}$ near the $\mathbf{K}$ valley; we consider that $\mathbf{k}$ is small and can be expanded in powers of the components of this vector. The Hamiltonian of the p orbital band for each spin and valley can be written as $H = -v\mathbf{k} \cdot \boldsymbol{\sigma}$, which is the effective magnetic field, works on the pseudospin, in the direction of the momentum $\mathbf{k}$, i.e. helicity is conserved in graphene [45].

Due to this interpenetration, there is an additional degree of freedom known as pseudospin [46], which is absent in conventional 2D systems, which is the cause of its exceptional electronic properties [46]. At Dirac point **K**, the eigenvalue equation have wave function $\psi(\mathbf{k})$ contains the two component spinor function and the Hamiltonian (1.21) may be written as

$$\hat{H}_K\ \psi(\mathbf{k}) = E\ \psi(\mathbf{k}), \quad \hat{H}_K = v_F(\boldsymbol{\sigma}\cdot\mathbf{p}).$$

Here, E is the the eigenvalue of Hamiltonian, v_F denotes Fermi velocity near the Dirac point **K** and σ represents 2D pseudospin matrix corresponding to the two sublattices of honeycomb lattice. The eigenvector $\psi(\mathbf{k})$ can be written as

$$\psi(\mathbf{k}) = \begin{pmatrix} \psi_A(\mathbf{k}) \\ \psi_B(\mathbf{k}) \end{pmatrix}.$$

So the above equation becomes

$$\hbar v_F \begin{pmatrix} 0 & p_x - ip_y \\ p_x + ip_y & 0 \end{pmatrix} \begin{pmatrix} \psi_A(\mathbf{k}) \\ \psi_B(\mathbf{k}) \end{pmatrix} = E \begin{pmatrix} \psi_A(\mathbf{k}) \\ \psi_B(\mathbf{k}) \end{pmatrix}.$$

By solving above equation, the two component spinor wave function and energy eigenvalue will be

$$\psi_{\pm,K}(\mathbf{k}) = \frac{1}{\sqrt{2}} \begin{pmatrix} 1 \\ \pm e^{i\theta_k} \end{pmatrix}, \quad E = \pm\hbar v_F \sqrt{p_x^2 + p_y^2}, \tag{1.24}$$

where θ_k is the angle between between the wave vector **k** and to the x-axis and the $\pm$ sign signifies the conduction band (or π^* bond) and valence band (i.e. π bond) respectively. The wave function around the other Dirac point ($\mathbf{K}'$) can be found by similar way

$$\psi_{\pm,\mathbf{K}'}(\mathbf{k}) = \frac{1}{\sqrt{2}} \begin{pmatrix} 1 \\ \pm e^{-i\theta_k} \end{pmatrix}. \tag{1.25}$$

The projection of pseudospin along the direction of momentum called *helicity* of electron may be defined as

$$\hat{O}_{hel} = \frac{1}{\sqrt{p_x^2 + p_y^2}} (\boldsymbol{\sigma}\cdot\mathbf{p}). \tag{1.26}$$

We can see from above equation that the two component spinor wave function $\psi_K(\mathbf{k})$ is the eigenfunction of the helicity operator, it is possible to conclude that

electron and holes in graphene have definite helicity. Near Dirac points, the electronic state are configuration of states, which relates to different sublattices giving two component wave functions (spinors). These spinors needs an index to indicate sublattice 'A' and sublattice 'B' and very much similar to the spin index in quantum electrodynamics denoted as 'pseudospin'.

1.1.4 Graphene Electronic and Transport Properties

As we have described earlier, the energy spectrum of graphene near Dirac points leads to the energy-momentum relation: $E = v_F|\mathbf{k}|$, where $\mathbf{k}$ is the wave number. This energy dispersion relation is similar to a relativistic charged particle. By setting mass equal to zero and Fermi velocity equal to the velocity of light, Dirac relativistic equation leads to the graphene energy dispersion relation. There is very high electron mobility more than $15000 cm^2 V^{-1} s^{-1}$ under ambient conditions in graphene which is verified experimentally [22]. Graphene nanoribbons show the electronic resistance changes like step function, following quantum mechanical rules [47]. In conventional conductors like copper or nickel, the electrical resistance is proportional to the linear dimensions of the material (with cross-sectional area fixed) as the electrons encounter more impurities while moving through it, but in graphene nanoribbons that act like wave guide allow the electrons to flow unimpeded along the edges of the material. So resistance of the graphene nanoribbons becomes temperature independent. Also it does not depend upon the amount current flowing through it. These properties are the matter of interest for experimental and theoretical studies on graphene.

1.1.5 Graphene Optical Properties

Optical properties studied in the context of graphene are, optical conductivity, optical Stark effect and Rabi oscillations [48–50]. In graphene, minimum quantum conductivity was experimentally observed with a finite value of $\frac{e^2}{h}$, where h is the Planck constant [51]. We are not able to see single layer graphene with our bare eyes, however it can be realized experimentally. The interference based experiment has been used to detect the single layer graphene on silicon dioxide substrate [22]. Graphene layer thickness can also be detected with contrast spectroscopy [52]. For experimental detection of single layer graphene, plenty of experimental techniques have been developed [53]. Raman spectroscopy is one among them, and is accurate in detecting not only the single layer but also differentiate among the single layer, bilayer and multilayer samples [54, 55]. Many experiments have been performed

to study optical properties, such as optical Stark effect [49], optical conductivity, Rabi oscillations [49, 50, 52, 56, 57], universal optical conductance [58–60], measurement of fine structure constant [61], four wave mixing [49] and incoherent optical properties like optical dephasing [57], relaxation of charge carriers, both inter-band and intra-band in graphene and graphene based systems on various substrate has been reported experimentally by pump-probe technique [62–67].

1.2 Topological Insulator

Topological insulators are peculiar quantum systems [2], which have an insulating gap in the bulk due to the presence of spin-orbit coupling, and possess intrinsic Dirac metallic states at the surface. Physical properties of real systems are typically tied to a branch of mathematics known as (real or complex) analysis where properties depend on the precise details of the underlying Hamiltonian. These properties change significantly even due to trivial changes to the description of the system. After the discovery of the Integer Quantum Hall Effect, it was noted that there exist some physical properties that are more robust and do not change when trivial changes are made to the underlying Hamiltonian. These properties are more closely related to the branch of mathematics known as topology [68]. In topology, two geometrical objects can or cannot be smoothly deformed into one another and are consequently considered topologically equivalent or inequivalent, respectively. The eigenstates of two Hamiltonians that may be smoothly deformed into each other are regarded as being topologically equivalent to each other. A topologically trivial situation is one where the underlying space has properties that may be characterized as trivial, and hence are uninteresting from a topological point of view. The first nontrivial topological state observed in the phenomenon of Quantum Hall Effect, where a 2D electron system subject to a perpendicular magnetic field was seen to possess a quantized Hall conductivity [69].

In 2005, C. L. Kane and E. J. Mele discovered a new model to obtain a nontrivial topological states without breaking time-reversal symmetry in absence of an external magnetic field, based on the spin-orbit coupling applied to the graphene model Hamiltonian [70]. Firstly, this model shows the phenomenon of Quantum Spin Hall effect, also known as a 2D topological insulator and opens the way for the investigation of a new topological class, called Z_2 topological insulators. This concept is expanded further in the 3D topological insulator. The 3D TIs are the

systems having 2D exotic metallic states at all interfaces with vacuum or another dielectric. These topological edge states are protected by time-reversal symmetry and due to spin-orbit coupling, they are spin-momentum locked, which means that the direction of their motion uniquely determines their spin polarization and vice versa. On the edge states, the back-scattering from non-magnetic impurities is prohibited as long as time-reversal symmetry is maintained. Hence, 2D energy-momentum relation of carriers on these conducting states is linear. One or more Dirac cones of massless particles, such as the ones characterizing graphene are seen on the conducting edges. These peculiar properties are useful in applications, especially in the fields of plasmonics and spintronics [71, 72].

In following section, the history and development of Hall Effect is described in chronological order and a relation is made with topological insulators.

Hall Effect

When a conductor carrying a current subjected to a perpendicular magnetic field **B**, due to the presence of the Lorentz force, the charged particles inside the sample are deflected and accumulate near the boundary. Due to charge accumulation at the boundary, an electric field is generated. This field creates a voltage difference between the two boundaries and the value of it is $V_H = E\ W$ (W is the width of the sample), and the value of the electric current inside the sample is $I = q\ \rho_e \nu\ W$ (ρ_e is the density of the charge carriers). The ratio between the voltage to the electric current is known as the Hall resistance

$$R_H = \frac{V_H}{I} = \frac{B}{q\rho_e}. \tag{1.27}$$

R_H is linearly proportional to the magnetic field **B**. On measuring Hall resistance in ferromagnetic or even in paramagnetic metal, an additional contribution other than the linear term in the magnetic field is seen [73].

Anomalous Hall Effect

In a ferromagnetic material, Hall resistance is directly proportional to the magnetization M and the Hall effect remains even without a magnetic field and the new

Hall resistance is of the form

$$R_H = R_0 B + R_A M. \tag{1.28}$$

The second part of resistance cannot be explained by the Lorentz force on a charged particle; this arises due to the coupling of the electron's orbital motion to its spin and as such, this phenomenon is a relativistic quantum mechanical effect. In the presence of an external electric field, there is a transverse force experienced by the electron. This force is directly proportional to spin current of the electron, instead of charge current as in the Lorentz force. So in one direction of the sample, there are spin up electrons while the other direction contains spin down electrons. There is an imbalance in the number of the electrons with spin-up and spin-down. This becomes a cause for producing the anomalous Hall effect. In absence of magnetic field and magnetization in a paramagnetic metal, Hall resistance disappears. Due to spin-dependent deflected motion of electrons in solids, a new observable effect emerges that is known as the spin Hall effect [74].

Integer Quantum Hall Effect (IQHE)

A new quantum state was discovered in 1980 that was characterized by a property that was new to condensed matter physics known as the quantum Hall (QH) state. In this state, the bulk of the 2D sample is insulating, and the electric current flows only along the edge of the sample. The unidirectional flow of current averts dissipation and gives rise to a quantized Hall effect. This state is a first example of a unique quantum state, which is topologically different from all states of the matter known before. The precise quantized value of the Hall conductance is $\frac{n\,e^2}{h}$, which is a topological invariant and does not depends on material details [69, 75]. Here e is the elementary charge and h is Planck's constant and n is an integer.

In mathematics, different geometrical objects can be explained by broad classes of topology. According to the mathematical concept of topology, 2D surfaces can be classified by the number of holes or genus present inside them. Surface of an ellipsoid and surface of a perfect sphere are topologically equivalent because we can smoothly deform one into the other without creating any holes. Similarly, due to the presence of a single hole, the coffee cup is topologically equivalent to a donut. In mathematics, topological classification concentrates on the fundamental distinction of shapes and cast aside small details. In physics, a phenomenon like

Hall conductance is of topological origin, remains unaffected by small changes in the sample [68].

The specific phenomenon like QH effect works like a bridge between physics and topology. The smooth deformation works as a key concept for relating physics and topology. Smooth deformations are those that do not involve the tearing or gluing of spaces. Many topological equivalent classes are generated by the operation of smooth deformation groups [2, 3].

There was a concept of the genus, in terms of an integral over the local curvature surface introduced in Mathematics, which is a topological invariant [68]. Typically, integrals depend on details of the surface geometry, but due to the concept of genus the value of the integral over local curvature is independent of such details and depends only on the global topology. We can use this concept in physics; a topologically quantized physical quantity can be expressed as invariant integrals over the frequency-momentum space [76, 77]. The nature of the quantum state can be determined by such quantities, which works as a topological order parameter.

There is not sufficient space for electrons near the edge, so their motion can not complete a circle and hit the boundary before the circle can be completed. The electron will be reflected by the boundary and start making another circle and hit the boundary again. So electron moves in one direction near the edge state and the direction is determined by the **B** field. These edge states are responsible for quantized Hall conductivity, are known as the chiral edge states, depicted in fig.(1.4). The electrons of the bulk do not participate in the motion of electrons which move along edge states. Unlike in an ordinary 1D wire, here electrons move in one direction only while in a conventional 1D wire, electrons move both directions. The importance of this one-way current is highlighted upon including impurities. The impurity causes reflection of the electron in ordinary 1D wire and this reflection is the main reason why we have a resistivity at low temperature. However, due to one-way chiral edge state, impurity will not be able to reflect electrons, since it cannot move in the opposite direction. If impurity comes in the way of electrons, it goes around the impurity and keeps moving forward. So this is a reason behind the accuracy of quantized Hall conductivity, which becomes independent of the number of impurities.

[1]M. Z. Hasan and C. L. Kane, Reviews of Modern Physics **82**, 3045 (2010).

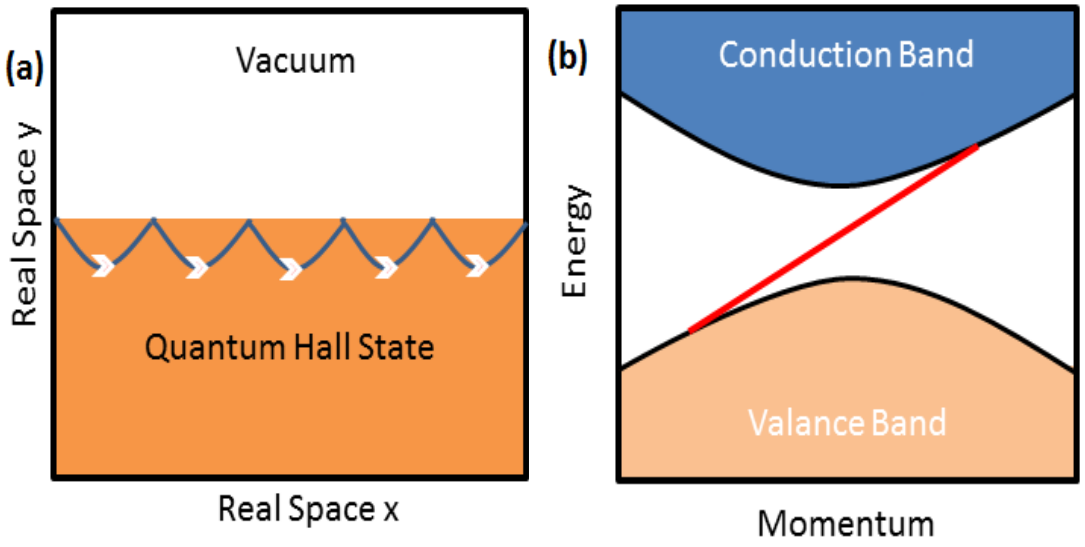

FIGURE 1.4: The figure depicts the interface between a quantum Hall state and an insulator with a chiral edge mode. **(a)** The incomplete (skipping) cyclotron orbits in quantum Hall state are seen. **(b)** The band diagram of a semi-infinite edge in a topological insulator with a Chern number of C = +1 is shown. A single edge state connects the valence band to the conduction band [1].

For the quantum Hall effect, it is necessary to suppress spin-flip scattering [2] of the conduction electrons. For this, first we require a magnetic field which is large enough to make the Zeeman energy big enough so that the up-spin and down-spin Landau levels do not overlap and very low temperature so that only one of these spin-split Landau levels has a significant thermal occupation. If we put a neutral particle in 2D then the Schrödinger equation will be in the form

$$i\partial_t\psi(x,y) = \left[\frac{1}{2m}(-i\hbar\partial_x)^2 + \frac{1}{2m}(-i\hbar\partial_y)^2\right]\psi(x,y). \tag{1.29}$$

On considering the particle with charge e then momentum operator $\mathbf{p}$ will be $\left(\mathbf{p} - \frac{e}{c}\mathbf{A}\right)$, where $\mathbf{A}$ is the vector potential, and change $i\partial_t$ will be $\left(i\partial_t - e\frac{\phi}{c}\right)$, where ϕ is the electric potential (minimal coupling). So

$$\left(i\partial_t - e\frac{\phi}{c}\right)\psi(x,y) = \left[\frac{1}{2m}\left(-i\hbar\partial_x - \frac{e}{c}A_x\right)^2 + \frac{1}{2m}\left(-i\hbar\partial_y - \frac{e}{c}A_y\right)^2\right]\psi(x,y), \tag{1.30}$$

[2]Spin-flip scattering is a process that leads to the non-conservation of the difference between the number of upspins and downspins.

$$i\partial_t\psi(x,y) = \left[\frac{1}{2m}\left(-i\hbar\partial_x - \frac{e}{c}A_x\right)^2 + \frac{1}{2m}\left(-i\hbar\partial_y - \frac{e}{c}A_y\right)^2 + e\frac{\phi}{c}\right]\psi(x,y). \tag{1.31}$$

So

$$H = \left[\frac{1}{2m}\left(-i\hbar\partial_x - \frac{e}{c}A_x\right)^2 + \frac{1}{2m}\left(-i\hbar\partial_y - \frac{e}{c}A_y\right)^2 + e\frac{\phi}{c}\right]. \tag{1.32}$$

Here $E = 0$, so $\phi = 0$. The vector potential satisfies

$$\boldsymbol{\nabla} \times \mathbf{A} = \partial_x A_y - \partial_y A_x = \mathbf{B}. \tag{1.33}$$

The vector potential $\mathbf{A}$ is not a physically observable quantity. For a particular value of $\mathbf{B}$ field, $\mathbf{A}$ is not unique. The relation between $\mathbf{B}$ and $\mathbf{A}$ is $\left(\boldsymbol{\nabla} \times \mathbf{A} = \mathbf{B}\right)$, so if we choose $\mathbf{A}' = \mathbf{A} + \boldsymbol{\nabla}\chi$ then value of $\mathbf{B}$ does not change i.e. $\boldsymbol{\nabla} \times \mathbf{A}' = \mathbf{B}$. So there are lots of choices for $\mathbf{A}$ arbitrarily and they all give the same physical results. This is known as a gauge choice. In our case $\mathbf{B}$ is a constant, so we can select $A_x = 0$ and $A_y = Bx$ (Landau gauge) and $A_x = -\frac{By}{2}, A_y = \frac{Bx}{2}$ (symmetric gauge) or any other gauge. On considering Landau gauge

$$H = \left[\frac{1}{2m}\left(-i\hbar\partial_x\right)^2 + \frac{1}{2m}\left(-i\hbar\partial_y - \frac{e}{c}Bx\right)^2\right]. \tag{1.34}$$

By solving Schrödinger equation we get the energy eigenvalues

$$\epsilon_{n,k_y} = \left(n + \frac{1}{2}\right)\frac{eB\hbar}{cm}. \tag{1.35}$$

In chiral edge states, electrons move in one direction and the quantized conductivity is determined by these edge states. The number of edge states in the top of 2D sample is

$$N = \int \frac{dp\, dr}{2\pi\hbar} = L\int \frac{dp}{2\pi\hbar}. \tag{1.36}$$

So the number of edge states per unit length will be

$$n = \frac{N}{L} = \int \frac{dp}{2\pi\hbar}. \tag{1.37}$$

$$\delta n_{top} = \int_{k_F}^{k_{F\ top}} \frac{dp}{2\pi\hbar} = \frac{k_{F\ top} - k_F}{2\pi\hbar} = \frac{\mu_{top} - \mu}{2\pi\hbar\, v_{Ftop}}. \tag{1.38}$$

Here μ is chemical potential i.e. energy required to add an electron. So net current on the top edge:

$$I_{top} = ev_{Ftop}\delta n_{top} = ev_{Ftop}\frac{\mu_{top}-\mu}{2\pi\hbar\, v_{Ftop}} = e\frac{\mu_{top}-\mu}{2\pi\hbar} = e\frac{eV/2}{2\pi\hbar} = \frac{e^2}{2\pi\hbar}\frac{V}{2}. \tag{1.39}$$

Similarly,

$$I_{bottom} = \frac{e^2}{2\pi\hbar}\frac{V}{2}. \tag{1.40}$$

It may be noticed that the currents in both edges are flowing in the same directions. The top edge has more particles moving towards right, it makes direction of total current I is right and bottom edge has less particles moving to the left, so the net current is also towards the right,

$$I = I_{top} + I_{bottom} = \frac{e^2}{2\pi\hbar}V = \frac{e^2}{h}V. \tag{1.41}$$

So the Hall conductance will be

$$\frac{1}{R_H} = \frac{I}{V} = \frac{e^2}{h} = \sigma. \tag{1.42}$$

There are n edge states, so conductivity will be

$$\sigma = \frac{I}{V} = n\frac{e^2}{h}. \tag{1.43}$$

There is only one sense of the current, so no reflection and no backward scattering are permissible. This is the reason behind quantization of σ_{xy} so precisely, hence impurities does not effect the sense of the current.

The integer quantum Hall state (QH) [69, 75] is a simplest example of a topological state. The integer C represents an integer topological invariant (also called a first Chern invariant). Later it was explained [77] that the topological invariant C (known as the TKNN invariant) can be calculated by a surface integral of the Berry flux over the Brillouin zone (BZ),

$$\mathrm{C} = \frac{1}{2\pi}\sum_i \int_{BZ} \boldsymbol{\nabla} \times \mathcal{A}_i \, d^2k, \tag{1.44}$$

where $\mathcal{A}_i = i\langle u_i|\boldsymbol{\nabla}_k|u_i\rangle$ denotes the Berry curvature, $|u_i\rangle$ are the Bloch wave functions, and the sum runs over the contributions from all occupied bands. Due to the honeycomb lattice, graphene was initially regarded as a good candidate for

the first realization of a 2D TI, but due to weak spin orbit coupling, it is impossible for it to support topological order [78, 79]. The material which possesses stronger spin orbit coupling can be considered a TI [80, 81].

Spin Hall Effect and Quantum Spin Hall Effect

In 1971 Russian physicists Dyakonov and Perel proposed the spin version of the Hall effect, known as spin Hall effect. There is spin accumulation of electrons on the lateral surfaces of a current-carrying sample, the signs of the spin orientations being opposite on two opposite boundaries. On reversing the direction of the current, the direction of spin orientation is also reversed. This effect has been verified experimentally in GaAs and InGaAs thin film and spin light-emitted diode of p-n junction [82].

The presence of external magnetic field is necessary for Quantum Hall Effect. A new phenomenon has been discovered which is quite similar to Quantum Hall (QH) Effect, but it is time reversal invariant and does not require an applied field is called quantum spin Hall effect (QSHE). This peculiar phenomenon is found in some specific materials and only depends on its topology and not on microscopic details. Due to topological distinction from all previously known states of matter, these materials are known as a topological insulator. QSHE is a state of matter that exists in special 2D semiconductors, possess a quantized spin-Hall conductance and a vanishing charge-Hall conductance. The integer quantum Hall state and quantum spin Hall state are closely related to each other. Both states can be realized on a lattice without the application of a large magnetic field [70, 83].

The time reversal (TR) symmetry breaks explicitly in QH states due to the presence of magnetic field and each QH state belongs to a particular topological class. A new topological class of material has been developed recently, which is invariant under TR, and where spin-orbit coupling (SOC) plays an important role [80, 81, 84], known as Topological Insulator (TI). These are peculiar materials of condensed matter physics which are insulators in the bulk but have exotic metallic states present at their surfaces. In such materials, there is quantum-Hall-like behavior in the absence of a magnetic field. There are two distinct classes for all TR invariant insulators in nature (without ground state degeneracy), classified by a Z_2 topological order parameter. There are gapless edge or surface states with an odd number of Dirac fermions and a full insulating gap in the bulk in the topologically nontrivial state. If time reversal symmetry preserved in bulk

but broken on the surface, the topological property is seen more dramatically in which case the material is fully insulating both inside the bulk and on the surface. The 2D version of the topological insulator, addressed as the quantum spin Hall (QSH) insulator, was first theoretically predicted in 2006 [80, 81] and experimentally observed [85] in HgTe/CdTe quantum wells (QW). The salient predictions of experimentally measurable topological effects can be done by using Topological Field Theory (TFT), which works in the long-wavelength and low-energy limits [86]. Thus we can say QSH state in 2D can be assumed as two copies of the QH state, where states with opposite spin counter-propagate at the edge. A big question is regarding the stability of edge states in the QSH state. In 2005, Kane and Mele has shown, the stability depends on the number of pairs of edge states. If there are the odd number of pairs, then it is stable, whereas in the presence of the even number of pairs is unstable [70, 83]. A Z_2 classification was proposed by them for TR invariant 2D insulators. The above information is taken from article of Xiao-Liang Qi [3]. The development of quantum Hall effect in the following section is important to understand the theory of TI.

1.2.1 Honeycomb Lattice (Graphene) i.e. Next Nearest Neighbors (NNN) Hopping

Topological insulator was first described in Haldane model beyond quantum Hall effect [36]. Haldane had taken next nearest neighbors (NNN) hoppings in honeycomb model of graphite and assumed their hopping amplitudes are complex. For making simple model, we have chosen all NNN bonds have same amplitude and same complex phase. Hopping strength phase is ϕ in forward direction and $-\phi$ in an backward direction. By applying staggered magnetic field $\mathbf{B}$, complex phases can be raised. $\mathbf{B}$ is positive in the vicinity of the center of the hexagons and negative near the edges. If we move a particle around a closed contour, the phase difference between the final and initial states is proportional to the magnetic flux enclosed by the contour $\phi = \frac{e}{\hbar}\iint \mathbf{B}\cdot\mathbf{dS} = \frac{e}{\hbar}\oint \mathbf{A}\cdot\mathbf{dl}$, this effect is known as Aharonov-Bohm effect. Consider three lattice sites a, b and c possessing hopping strengths t_{ab}, t_{bc} and t_{ca} respectively. When the particle goes from a to b, from b to c, and back from c to a. The total hopping strength around the loop will be

$$t_{ab}t_{bc}t_{ca} = |t_{ab}|e^{i\phi_{ab}} * |t_{bc}|e^{i\phi_{bc}} * |t_{ca}|e^{i\phi_{ca}} = |t_{ab}\ t_{bc}\ t_{ca}|e^{i(\phi_{ab}+\phi_{bc}+\phi_{ca})}. \qquad (1.45)$$

Then electron has phase:

$$\phi_{ab} + \phi_{bc} + \phi_{ca} = \frac{e}{\hbar} \iint \mathbf{B} \cdot \mathbf{dS}. \tag{1.46}$$

For making above phase nonzero, $\mathbf{B}$ should be non-zero inside the triangle made by these three sites. There is no physical meaning of individual phases for t_{ab}, t_{bc} and t_{ca}, they are actually gauge dependent. Only the total phase on a loop possesses physical meaning. The phase along one segment is

$$\phi_{ab} = \frac{e}{\hbar} \int_a^b \mathbf{A} \cdot \mathbf{dl}. \tag{1.47}$$

Using gauge transformation: $\mathbf{A} \to \mathbf{A} + \boldsymbol{\nabla}\chi$

$$\phi_{ab} \to \phi'_{ab} = \frac{e}{\hbar} \int_a^b (\mathbf{A} + \boldsymbol{\nabla}\chi) \cdot \mathbf{dl} = \phi_{ab} + (\chi_b - \chi_a)\frac{e}{\hbar}. \tag{1.48}$$

Due to dependence on gauge choice, physical observation of ϕ_{ab} is not possible. The total phase around a loop is different, which is a loop integral of $\mathbf{A}$ and gauge independent because $\frac{e}{\hbar} \oint \boldsymbol{\nabla}\chi \cdot \mathbf{dl} = 0$ and the physical meaning of this integral is the magnetic flux. The complex hopping strength is due to $\mathbf{B}$ fields and breaks the time-reversal symmetry because of $\mathbf{B} \to -\mathbf{B}$ under time reversal (so we can say, under time-reversal, there should be flip in the sign of all these phases).

When there are hoppings from an A-site to an A-site (and from a B-site to a B-site), we called it NNN hoppings. In case of A-to-A hoppings, the three different types of NNN bonds are formed, along $\theta = 0, \frac{2\pi}{3}, \frac{4\pi}{3}$. Similarly it is true for B-to-B hoppings. So the Hamiltonian becomes

$$\begin{aligned} H_{NNN} = \quad & -t' e^{i\phi} \sum_i a^\dagger_{\mathbf{r_i}} a_{\mathbf{r_i}+\boldsymbol{\nu}_1} - t' e^{i\phi} \sum_i a^\dagger_{\mathbf{r_i}+\boldsymbol{\nu}_1} a_{\mathbf{r}_i-\boldsymbol{\nu}_3} - t' e^{i\phi} \sum_i a^\dagger_{\mathbf{r_i}-\boldsymbol{\nu}_3} a_{\mathbf{r_i}} \\ & + h.c. + \big(a \to b \text{ and } \phi \to -\phi\big). \end{aligned} \tag{1.49}$$

Here, $\boldsymbol{\nu}_1 = \big(\sqrt{3}a, 0\big) \to (2a\cos(30^o), 0)$ and $\boldsymbol{\nu}_2 = \left(-\frac{\sqrt{3}}{2}a, \frac{3}{2}a\right)$ and $\boldsymbol{\nu}_3 = \left(-\frac{\sqrt{3}}{2}a, -\frac{3}{2}a\right)$. So in momentum space

$$\begin{aligned} H_{NNN} = \quad & -t' e^{i\phi} \sum_{\mathbf{k}} a^\dagger_{\mathbf{k}} a_{\mathbf{k}} \left(e^{-i\mathbf{k}\cdot\boldsymbol{\nu}_1} + e^{-i\mathbf{k}\cdot\boldsymbol{\nu}_2} + e^{-i\mathbf{k}\cdot\boldsymbol{\nu}_3}\right) + h.c. \\ & + \big(a \to b \text{ and } \phi \to -\phi\big) \end{aligned} \tag{1.50}$$

After writing Hermitian conjugate properly, we got

$$\begin{aligned} H_{NNN} = \quad & -2t^{'} \sum_{\mathbf{k}} a_{\mathbf{k}}^{\dagger} a_{\mathbf{k}} \left[\cos(\mathbf{k}\cdot\boldsymbol{\nu}_1 - \phi) + \cos(\mathbf{k}\cdot\boldsymbol{\nu}_2 - \phi) + \cos(\mathbf{k}\cdot\boldsymbol{\nu}_3 - \phi)\right] \\ & -2t^{'} \sum_{\mathbf{k}} b_{\mathbf{k}}^{\dagger} b_{\mathbf{k}} \left[\cos(\mathbf{k}\cdot\boldsymbol{\nu}_1 + \phi) + \cos(\mathbf{k}\cdot\boldsymbol{\nu}_2 + \phi) + \cos(\mathbf{k}\cdot\boldsymbol{\nu}_3 + \phi)\right]. \end{aligned} \tag{1.51}$$

$$H = H_{NN} + H_{NNN} = \sum_{k} \begin{pmatrix} a_k^{\dagger} & b_k^{\dagger} \end{pmatrix} \begin{pmatrix} H_{11}(\mathbf{k}) & H_{12}(\mathbf{k}) \\ H_{21}(\mathbf{k}) & H_{22}(\mathbf{k}) \end{pmatrix} \begin{pmatrix} a_k \\ b_k \end{pmatrix}. \tag{1.52}$$

Here

$$H_{12}(\mathbf{k}) = -t\left(e^{-i\mathbf{k}.\boldsymbol{\delta}_1} + e^{-i\mathbf{k}.\boldsymbol{\delta}_2} + e^{-i\mathbf{k}.\boldsymbol{\delta}_3}\right), \tag{1.53}$$

$$H_{21}(\mathbf{k}) = H_{12}(\mathbf{k})^{*} = -t\left(e^{i\mathbf{k}.\boldsymbol{\delta}_1} + e^{i\mathbf{k}.\boldsymbol{\delta}_2} + e^{i\mathbf{k}.\boldsymbol{\delta}_3}\right), \tag{1.54}$$

$$H_{11}(\mathbf{k}) = -2t^{'} \sum_{\mathbf{k}} a_{\mathbf{k}}^{\dagger} a_{\mathbf{k}} [\cos(\mathbf{k}\cdot\boldsymbol{\nu}_1 - \phi) + \cos(\mathbf{k}\cdot\boldsymbol{\nu}_2 - \phi) + \cos(\mathbf{k}\cdot\boldsymbol{\nu}_3 - \phi)], \tag{1.55}$$

$$H_{22}(\mathbf{k}) = -2t^{'} \sum_{\mathbf{k}} b_{\mathbf{k}}^{\dagger} b_{\mathbf{k}} [\cos(\mathbf{k}\cdot\boldsymbol{\nu}_1 + \phi) + \cos(\mathbf{k}\cdot\boldsymbol{\nu}_2 + \phi) + \cos(\mathbf{k}\cdot\boldsymbol{\nu}_3 + \phi)]. \tag{1.56}$$

On computing the eigenvalues of $H(\mathbf{k})$, it is found that the two bands never overlap each other for any $\mathbf{k}$ (when $t^{'}$ becomes non-zero and ϕ is not an integer times π). Using Pauli matrices:

$$H = H_0(\mathbf{k})I + H_x(\mathbf{k})\sigma_x + H_y(\mathbf{k})\sigma_y + H_z(\mathbf{k})\sigma_z, \tag{1.57}$$

$$H_0 = \frac{H_{11}(\mathbf{k}) + H_{22}(\mathbf{k})}{2} = -2t^{'}\cos\phi[\cos(\mathbf{k}\cdot\boldsymbol{\nu}_1) + \cos(\mathbf{k}\cdot\boldsymbol{\nu}_2) + \cos(\mathbf{k}\cdot\boldsymbol{\nu}_3)], \tag{1.58}$$

$$H_z = \frac{H_{11}(\mathbf{k}) - H_{22}(\mathbf{k})}{2} = -2t^{'}\sin\phi[\sin(\mathbf{k}\cdot\boldsymbol{\nu}_1) + \sin(\mathbf{k}\cdot\boldsymbol{\nu}_2) + \sin(\mathbf{k}\cdot\boldsymbol{\nu}_3)], \tag{1.59}$$

$$H_x = Re[H_{21}(\mathbf{k})] = -t[\cos(\mathbf{k}\cdot\boldsymbol{\delta}_1) + \cos(\mathbf{k}\cdot\boldsymbol{\delta}_2) + \cos(\mathbf{k}\cdot\boldsymbol{\delta}_3)], \tag{1.60}$$

$$H_y = Im[H_{21}(\mathbf{k})] = -t[\sin(\mathbf{k}\cdot\boldsymbol{\delta}_1) + \sin(\mathbf{k}\cdot\boldsymbol{\delta}_2) + \sin(\mathbf{k}\cdot\boldsymbol{\delta}_3)]. \tag{1.61}$$

The energy dispersion is

$$\epsilon_{\pm}(\mathbf{k}) = H_0(\mathbf{k}) \pm \sqrt{H_x(\mathbf{k})^2 + H_y(\mathbf{k})^2 + H_z(\mathbf{k})^2}. \tag{1.62}$$

In absence of the complex NNN hoppings $H_0 = H_z = 0$, so the dispersion

$$\epsilon_{\pm}(\mathbf{k}) = \pm\sqrt{H_x(\mathbf{k})^2 + H_y(\mathbf{k})^2}. \tag{1.63}$$

$H_x = H_y = 0$ at $\mathbf{K}$ and $\mathbf{K}'$, therefore the two bands become degenerate (in

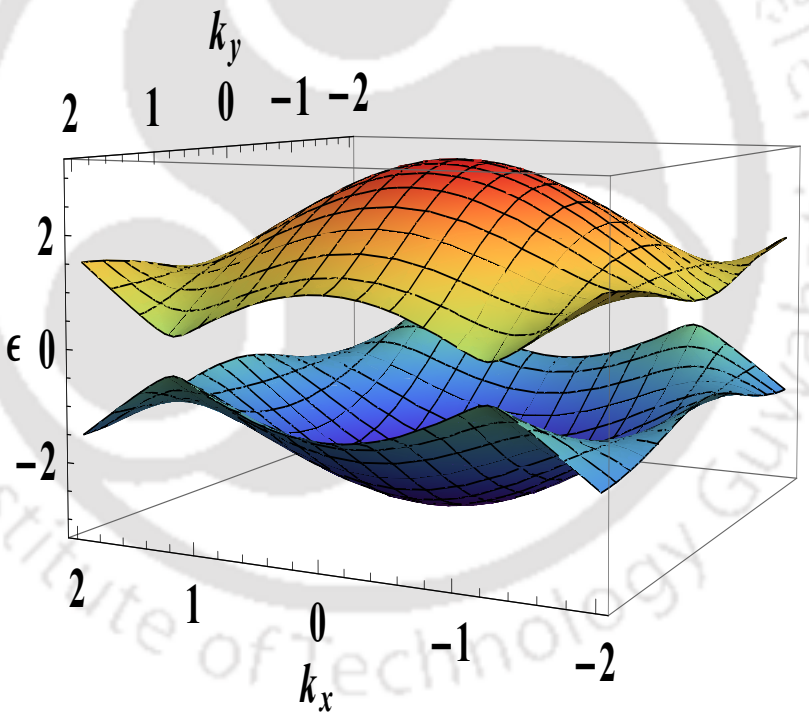

FIGURE 1.5: The plot between energy dispersion $\epsilon_{\pm}$ and k_x and k_y for both bands in the first Brillouin zone.

absence of the complex NNN hoppings), so

$$\epsilon_{\pm}(\mathbf{k}) = 0 \quad \text{which denotes the Dirac points.} \tag{1.64}$$

So in the presence of complex NNN hoppings, at $\mathbf{K}$ and $\mathbf{K}'$, $H_x = H_y = 0$ but $H_z \neq 0$. The two bands have gap

$$\epsilon_+(\mathbf{k}) - \epsilon_-(\mathbf{k}) = 2\sqrt{H_x(\mathbf{k})^2 + H_y(\mathbf{k})^2 + H_z(\mathbf{k})^2} = 2 \mid H_z(\mathbf{k} = \mathbf{K}) \mid$$
$$= 6\sqrt{3}t' \sin\phi. \quad (1.65)$$

The above eq.(1.65) calculates the gap is shown pictorially in fig.(1.5). In fact, at the $\mathbf{K}$ point

$$H_z = -3\sqrt{3}t' \sin\phi. \quad (1.66)$$

At the $\mathbf{K}'$ point

$$H_z = 3\sqrt{3}t' \sin\phi \text{ They possess opposite signs (as long as } \phi \text{ is not } n\pi). \quad (1.67)$$

1.2.1.1 Potential Energy (Breaking Inversion Symmetry)

Consider the following choice where the NNN hopping terms are set to zero

$$H_{\text{Potential}} = (V + M)\sum_i a_i^\dagger a_i + (V - M)\sum_i b_i^\dagger b_i,$$

$$H_{\text{Potential}} = V\left(\sum_i a_i^\dagger a_i + \sum_i b_i^\dagger b_i\right) + M\left(\sum_i a_i^\dagger a_i - \sum_i b_i^\dagger b_i\right),$$

$$= VN + M\sum_i a_i^\dagger a_i - M\sum_i b_i^\dagger b_i. \quad (1.68)$$

We add just a constant term M in potential energy V (average potential between A and B sites), due to conservation of total particle number N. Therefore the V term can be left out and the difference between the potential energies at A and B sites (M) is considered. In k-space

$$H_{\text{Potential}} = M\sum_i a_i^\dagger a_i - M\sum_i b_i^\dagger b_i = M\sum_k a_k^\dagger a_k - M\sum_k b_k^\dagger b_k, \quad (1.69)$$

$$= \sum_k \begin{pmatrix} a_k^\dagger & b_k^\dagger \end{pmatrix} M\sigma_z \begin{pmatrix} a_k \\ b_k \end{pmatrix}. \quad (1.70)$$

So the σ_z component of the Hamiltonian becomes a cause of gap opening at the Dirac point as in NNN complex hopping. In absence of the complex NNN hoppings, the gap is $2M$ at $\mathbf{K}$ and $\mathbf{K}^{'}$, and the system becomes a trivial insulator at half-filling.

1.2.1.2 Joint Presence of $H_{Potential}$ and H_{NNN}

If H_z has the same sign at $\mathbf{K}$ and $\mathbf{K}^{'}$ points, only one wave function is sufficient to cover the whole BZ, so the Chern number C = 0 (trivial insulator). When H_z has opposite signs at $\mathbf{K}$ and $\mathbf{K}^{'}$, the system becomes a topological insulator with C = $\pm$1. So value of H_z at the Dirac point $\mathbf{K}$ is

$$H_z = M - 3\sqrt{3}t^{'}\sin\phi. \tag{1.71}$$

At the $\mathbf{K}^{'}$ point

$$H_z = M + 3\sqrt{3}t^{'}\sin\phi. \tag{1.72}$$

If $|M| < 3\sqrt{3}t^{'}\sin\phi$, the system becomes a topological insulator (H_z changes it's sign). When $|M| > 3\sqrt{3}t^{'}\sin\phi$, H_z is always positive (or negative) and thus the system becomes topologically trivial. When value of $|M|$ becomes $3\sqrt{3}t^{'}\sin\phi$, there is a topological transition. So H_z becomes zero at either the $\mathbf{K}$ point or the $\mathbf{K}^{'}$ point. The value of $H_x = H_y = 0$ at these two points, so the gap must vanish at one of the two points. There is a band crossing in the system (either at $\mathbf{K}$ or $\mathbf{K}^{'}$, depending on the sign of M and $t^{'}\sin\phi$) at the transition point and the system is not an insulator. At the topological transition point, the insulating gap closes. This derivation is taken from reference given in footnote[3].

So the two basic differences between the model of Haldane and the quantum Hall effect are: (1)In the Haldane model, the Magnetic field $\mathbf{B}$ is on average zero but in the QHE, it is a uniform $\mathbf{B}$ field (2) In the Haldane model, the lattice background potential is very strong but in the QHE, there is a weak lattice potential. By using Haldane's model, time-reversal invariant topological insulators was proposed. These materials have been theoretically predicted and experimentally realized in Cr-doped $(Bi_{1-x}Sb_x)_2Te_3$ thin films [87] and in ultracold fermion systems [88].

[3] http://www-personal.umich.edu/~sunkai/teaching/Fall_2012/chapter3_part7.pdf

1.2.2 Kane-Mele Model

Haldane has proposed his model for spinless fermions. This model can be generalized for an electron system with spin, which becomes doubly degenerate if fermion-fermion interactions are ignored. At the edge channel, electrons become chiral, start to flow around the boundary in the counterclockwise direction for Chern number $\mathrm{C} = 1$ and in the clockwise direction for $\mathrm{C} = -1$, which is characteristic of Quantum Hall Effect. In 2005, Kane and Mele [70] proposed a generalized Haldane model for the graphene lattice model of electrons with spin $\frac{1}{2}$. A new quantum phenomenon has been predicted viz. the Quantum Spin Hall effect, to replace the periodic magnetic flux by the spin-orbit coupling between electron spin and momentum. When system possesses time reversal symmetry, electrons with spin-up in the edge channel flow in one direction, while electrons with spin-down in the edge channel flow in opposite direction, $I_\uparrow = -I_\downarrow$. So net charge current in two edge channels becomes zero, $I_c \equiv I_\uparrow + I_\downarrow = 0$ as a net charge current breaks time reversal symmetry. Only a pure spin current circulates around the boundary of system, $I_s = \frac{\hbar}{2e}(I_\uparrow - I_\downarrow)$. In the Quantum Hall Effect, time reversal symmetry is broken due to the magnetic field, but due to the spin-orbit coupling, this symmetry is preserved in Quantum Spin Hall effect since the momentum $p \to -p$ and spin $\sigma \to -\sigma$ under the time reversal (the description in this section is taken from the book [4]).

Quantum Hall insulators are formed using a $\mathbf{B}$ field (uniform or staggered). Spin-orbit effect and external $\mathbf{B}$ field are really similar to each other, $\mathbf{B}$ for spin up electron and $-\mathbf{B}$ for spin down electron. We may consider Kane-Mele's model as two copies of the Haldane model, one for spin up and one for spin down configurations. There are opposite phases in complex hoppings for spin up and down electrons. Chern number $\mathrm{C} = 1$ for spin-up quantum Hall state and $\mathrm{C} = -1$ for spin down quantum Hall state and whole system posses $\mathrm{C} = 0$ (no Hall effect), but this is an insulator with metallic edge states. Haldane model uses staggered magnetic field for complex hopping terms. But in Kane-Mele model, the the complex hopping terms was induced by spin-orbit coupling terms (spin-dependent hopping). So time-reversal symmetry is preserved. So

$$H = \sum_k \begin{pmatrix} a^\dagger_{k\uparrow} & b^\dagger_{k\uparrow} & a^\dagger_{k\downarrow} & b^\dagger_{k\downarrow} \end{pmatrix} \begin{pmatrix} H_{11}(\mathbf{k}) & H_{12}(\mathbf{k}) & 0 & 0 \\ H_{21}(\mathbf{k}) & H_{22}(\mathbf{k}) & 0 & 0 \\ 0 & 0 & H_{11}(\mathbf{k}) & H_{21}(\mathbf{k}) \\ 0 & 0 & H_{12}(\mathbf{k}) & H_{22}(\mathbf{k}) \end{pmatrix} \begin{pmatrix} a_{k\uparrow} \\ b_{k\uparrow} \\ a_{k\downarrow} \\ b_{k\downarrow} \end{pmatrix}. \quad (1.73)$$

In an ideal model, hybridization between spin up and down electrons is taken to be zero (the lower-left and upper-right corners of Hamiltonian are assumed to be

zero). In a realistic system, there are additional terms that hybridize the spin up and down electrons (additional terms in the Hamiltonian)[4]. By including these extra terms in the model, Kane and Mele found:

- Time reversal symmetry is the cause of edge states protection. When time-reversal symmetry is broken, edge states disappear and the system reverts to a trivial insulator.

- This means there are two types of insulators: no edge states (trivial) or 1 pair of edge states (topological). This is to be distinguished from integer quantum Hall effect (IQHE), which possess any number of edge states. Due to presence of 0 or 1 pair of edge states, we called these insulators as Z_2 topological insulators.

If we include Rashba term, the system becomes complicated since σ_z is no longer conserved and the electrons with spin-up and spin-down are coupled together. There is a mixing of electrons with spin-up and spin-down in Kane-Mele model; it is not possible to separate the whole system into two independent parts as in the case of Haldane Model. It is not possible to introduce a spin-dependent Chern number to describe this new phase. So Kane and Mele introduced Z_2 invariant to describe it.

The first proposal of QSHE state was in graphene, due to it's huge theoretical contribution to the discovery of this new topological phase. However, it was soon found to be unrealistic due to the weakness of spin orbit coupling (SOC) in graphene (the gap opened by SOC in graphene is on the order of 10^{-3} eV [78]). This type of material is experimentally realized in heavy elements, which would show stronger SOC. Firstly, it was proposed by B. Bernevig *et al.* in 2006, which predicted QSH effect in HgTe-CdTe semiconductor quantum wells [80]. There was a proposal of Z_2 topological invariant of the QSHE in 3D systems in 2007 [89]. After one year in 2008, D. Hsieh *et al.* reported the first experimental observation of a 3D topological insulator in $Bi_{1-x}Sb_x$ [90].

1.2.3 Terahertz and Infrared Study of Topological Insulators

The dynamics of charge carriers can be well measured by infrared spectroscopy - a powerful tool for this measurement. By this measurement, it is possible to study

[4] http://www-personal.umich.edu/~sunkai/teaching/Fall_2013/chapter7.pdf

low-energy electronic excitations and their interaction with other excitations of the system (eg. phonons). Due to residual conductivity associated with the bottom of the bulk conduction band, reflectivity measurements on TI single crystals creates the same problems as transport measurements to detect the surface states signal. This problem is solved for instance by Di Pietro *et al.* [91], A. D. LaForge *et al.* [92] and A. B. Sushkov *et al.* [93].

However, when we deal with thin films, the situation is different. In 2012, N. P. Armitage's group [94], have done an optical characterization of Bi_2Se_3 molecular beam epitaxy grown thin films. They reported [95] time-domain terahertz spectroscopy measurements on films with thickness ranging from 2 to 128 QL, the spectra at 5K. This data shows a distinctive Drude-Lorentz behavior, indicating a contribution from both free carriers and crystal vibrations. Using Drude Lorentz analysis, these authors found the free carrier and phonon 2D spectral weight separately, defined as $(\omega_p/2\pi)^2 d$ and $(S_{ph}/2\pi)^2 d$, where ω_p is the plasma frequency, S_{ph} is the phonon intensity and d is the film thickness. The values found are plotted in fig.(2c) as a function of the film thickness in that article [95]. From the plots, it can be seen that the Drude term is almost thickness-independent and the integrated spectral weight, describes it is related to surface free carriers. However, the phonon spectral function is proportional to thickness which is characteristic of bulk response. The big advantage of THz spectroscopy is that it can detect topological surface states and distinguish the surface states from bulk states in topological insulators. The important properties of topological insulators lie on the surface which is protected by time-reversal symmetry. So a study of surface states of topological insulators has been a major goal for researchers. Most signatures of topological nontrivial surface states have been detected by surface techniques, such as angle-resolved photoemission spectroscopy (ARPES) and scanning tunneling spectroscopy (STS) [84, 90, 96–98].

1.3 Weyl Semimetal

There is a new class of unconventional and topological (somewhat different from topological insulators) phase semimetal has been studied in the last couple of years known as Weyl semimetal (WSM). Closely related to graphene, its band structure contains a pair of bands crossing at certain points in momentum space; in other words it is a 3D system analogous to graphene. The properties of WSM are strongly influenced by spin orbit coupling. Actually, WSM is a novel topological

phase of 3D materials. It is represented by the existence of a set of linear-dispersive band-touching points, called Weyl nodes. They are protected against small perturbations and disorder. All this information has been taken from the review article of P. Hosur [99].

In following section, we describe the journey of topological phenomena in condensed matter from Dirac fermions to Weyl fermions and finally to Weyl semimetals step by step.

1.3.1 Dirac Fermions

Graphene and topological insulators are often termed Dirac materials due to emergence of Dirac fermions [100] in their low energy description. In the vicinity of Fermi energy, the Dirac equation is used for their description

$$(-i\boldsymbol{\alpha}\cdot\boldsymbol{\nabla}+\beta m)\,\psi = i\frac{\partial\psi}{\partial t}, \tag{1.74}$$

where ψ is the four-component Dirac spinor, and α, β are the 4×4 Dirac gamma matrices:

$$\boldsymbol{\alpha} = \begin{bmatrix} 0 & \boldsymbol{\sigma} \\ \boldsymbol{\sigma} & 0 \end{bmatrix}, \quad \boldsymbol{\beta} = \begin{bmatrix} I & 0 \\ 0 & -I \end{bmatrix}. \tag{1.75}$$

In order to obtain plane wave solutions, we write the four component Dirac spinor ψ as

$$\psi(\mathbf{r},t) = u(\mathbf{p})e^{-i(Et-\mathbf{p}\cdot\mathbf{r})} = \begin{bmatrix}\chi\\ \phi\end{bmatrix} e^{-i(Et-\mathbf{p}\cdot\mathbf{r})}. \tag{1.76}$$

Here, $u(\mathbf{p})$ is a four-component spinor and both χ and ϕ are two-component spinors. So the Dirac equation becomes

$$\begin{bmatrix} m & \boldsymbol{\sigma}\cdot\mathbf{p} \\ \boldsymbol{\sigma}\cdot\mathbf{p} & -m \end{bmatrix}\begin{bmatrix}\chi\\ \phi\end{bmatrix} = E\begin{bmatrix}\chi\\ \phi\end{bmatrix}. \tag{1.77}$$

After dropping the exponential factors, the general solution of above equation is

$$\chi = \frac{\boldsymbol{\sigma}\cdot\mathbf{p}}{E-m}\phi, \tag{1.78}$$

$$\phi = \frac{\boldsymbol{\sigma} \cdot \mathbf{p}}{E + m}\chi. \tag{1.79}$$

The energy eigenvalues from above equation

$$E^2 = |\mathbf{p}|^2 + m^2. \tag{1.80}$$

When fermions become massless, above energy dispersion is a linear function of momentum. This dispersion relation is true for graphene and topological insulators in case of low energy physics.

For massless system above eq.(1.77) becomes

$$\begin{bmatrix} 0 & \boldsymbol{\sigma} \cdot \mathbf{p} \\ \boldsymbol{\sigma} \cdot \mathbf{p} & 0 \end{bmatrix} \begin{bmatrix} \chi \\ \phi \end{bmatrix} = E \begin{bmatrix} \chi \\ \phi \end{bmatrix}. \tag{1.81}$$

Therefore

$$(\boldsymbol{\sigma} \cdot \mathbf{p})\, \chi = E\phi, \tag{1.82a}$$

$$(\boldsymbol{\sigma} \cdot \mathbf{p})\, \phi = E\chi. \tag{1.82b}$$

From above equation, we can say that χ and ϕ are not independent of each other. But a linear combination of χ and ϕ has the following form

$$\psi_R = \frac{1}{2}(\chi + \phi), \tag{1.83a}$$

$$\psi_L = \frac{1}{2}(\chi - \phi), \tag{1.83b}$$

yields

$$+ (\boldsymbol{\sigma} \cdot \mathbf{p})\, \psi_R = E\psi_R, \tag{1.84a}$$

$$- (\boldsymbol{\sigma} \cdot \mathbf{p})\, \psi_L = E\psi_L. \tag{1.84b}$$

These two new redefined two-component spinors, ψ_R and ψ_L are called Weyl spinors. These spinors decoupled from each other and are considered independent particles. They are represented by a conserved quantum number, known as chirality [101]. Eigenstates of the operator $\frac{\boldsymbol{\sigma}\cdot\mathbf{p}}{|\mathbf{p}|}$, chirality is the projection of

angular momentum $\boldsymbol{\sigma}$ on the momentum $\hat{p}$. If angular momentum parallel to linear momentum, the chirality becomes $+$, for antiparallel alignment becomes $-$. Chirality is conserved, in case of massless particles.

1.3.2 Weyl Fermions

The 'Weyl equation' belongs to high energy physics [102]. German physicist Hermann Weyl had introduced this equation, as a relativistic wave equation for describing massless spin-1/2 particles [9]. From last decade, Dirac equation has been introduced in condensed matter physics, Weyl fermions have also gained prominence over the past couple of years. Due to coming of Weyl fermions in condensed matter physics, growing list of topologically nontrivial phenomena have become possible. If particle has massless nature then the relativistic fermions can be described by only two component spinor rather than four component Dirac spinor, was first noticed by Hermann Weyl. These types of fermions are called Weyl fermions and they obey the Weyl equation $H\psi = E\psi$ generated by the Weyl Hamiltonian

$$H_{\text{Weyl}} = v_F(p_x\sigma_x + p_y\sigma_y + p_z\sigma_z), \tag{1.85}$$

$$E_{\text{Weyl}} = \pm v_F\sqrt{p_x^2 + p_y^2 + p_z^2}. \tag{1.86}$$

All Pauli matrices σ are already coupled to all three momenta, so no other anticommuting 2×2 matrices are available. This implies that one cannot open a gap and the fact that the bands touch in some points is stable. So these 3D Weyl fermions may be expected to be more protected against small perturbations than the Dirac fermions in graphene and this 3D phase of matter is called Weyl semimetal. Due to the two-component description by two-component wave functions rather than four-component Dirac spinors, Weyl fermions occur in systems where two nondegenerate bands meet with each other at a limited number of isolated points in the Brillouin zone. In case of a Weyl semimetal, systems are robust to most translationally-invariant interactions. The reason behind this property is chirality, which is conserved in three dimensions, while in two dimensions it is not a conserved quantum number. Due to chirality conservation, there is linear dispersing massless fermions in three dimensions, so only those interactions which could couple different fermions with opposite chirality can open a uniform gap at

the Weyl nodes in Weyl semimetals. Another property which leads to a difference between graphene and Weyl semimetal is spin degeneracy. There is inversion symmetry and time-reversal symmetry in graphene, which ensures two-fold spin degeneracy in graphene's 2D energy spectrum, while in case of Weyl semimetal, either inversion symmetry or time-reversal symmetry is broken, so that their energy spectra are non-degenerate.

There are significant differences between graphene and WSMs due to their different dimensionality. Since all three Pauli matrices are present in the Hamiltonian $H = v_F \boldsymbol{\sigma} \cdot \mathbf{p}$ of WSM and absence of such a matrix that anticommutes with Hamiltonian of Weyl, gaps out the spectrum. There are only two ways of a destroying Weyl point, **(i)** By neutralizing it with another Weyl point of opposite chirality either by purposely shifting the Weyl points around in momentum space and merging them or by allowing for scattering to take place between different Weyl nodes - the latter requires the violation of translational symmetry **(ii)** By spoiling charge conservation using superconductivity. In presence of charge conservation and translational invariance, the Weyl nodes are stable to arbitrary perturbations. In case of graphene, Dirac nodes can be demolished individually by breaking lattice point group symmetries.

A crucial quantity characterizing massless Weyl fermions is, helicity. The projection of spin $\mathbf{s}$ on the direction of momentum $\mathbf{p}$ of the particle known as helicity

$$\chi = \frac{\mathbf{p} \cdot \mathbf{s}}{|p||s|}. \tag{1.87}$$

For a spin $\frac{1}{2}$ fermion, the spin operator $\hat{s} = \frac{\hbar \boldsymbol{\sigma}}{2}$, the helicity operator for a Weyl fermion is $\hat{\chi} = \frac{\mathbf{p} \cdot \boldsymbol{\sigma}}{|p|}$. Due to commutation of the helicity operator with the Weyl Hamiltonian $H = v_F \mathbf{p} \cdot \boldsymbol{\sigma}$ helicity becomes a conserved quantity and hence a good quantum number. Helicity operators has eigenvalues ± 1, $+1$ depicts a fermion with the spin vector aligned along the momentum, -1 in the opposite direction. The energy of a Weyl fermion is $E = \pm v_F |\mathbf{p}|$, can be written as helicity operator times the energy

$$H = v_F \mathbf{p} \cdot \boldsymbol{\sigma} = sgn(v_F)|E|\hat{\chi}. \tag{1.88}$$

From above expression, a picture may be drawn, where a Weyl node looks like a hedgehog or a magnetic monopole in momentum space, have spin vectors in the direction of the Weyl node or in the opposite direction.

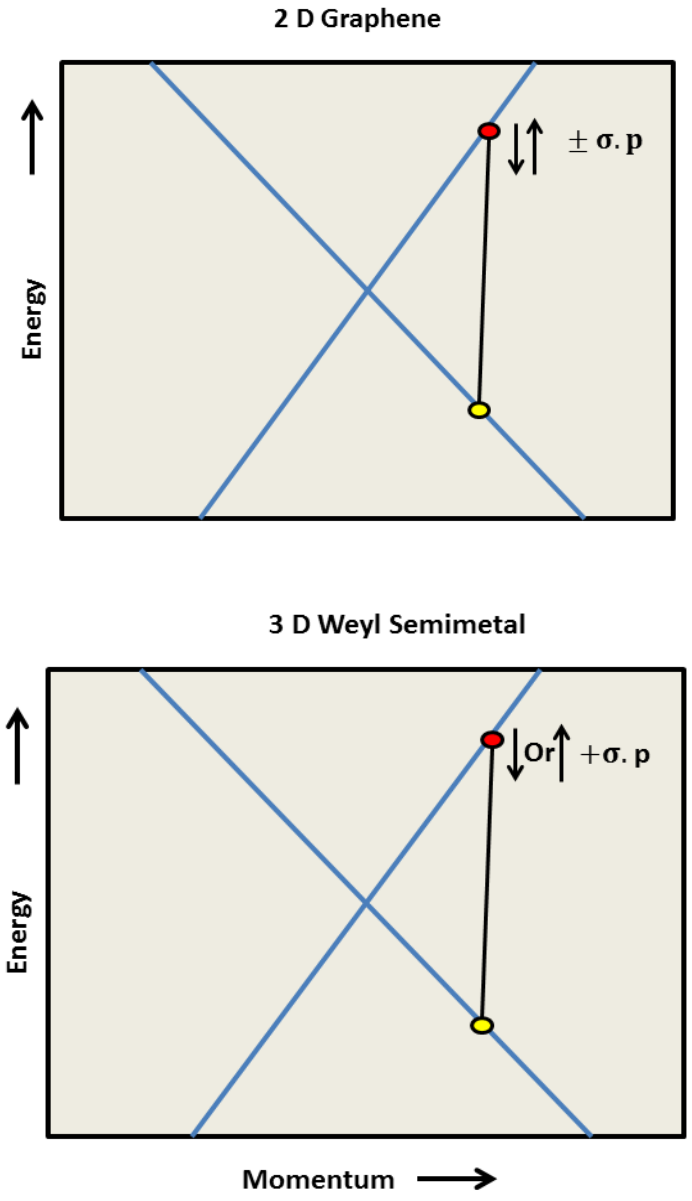

FIGURE 1.6: Band structure comparison between 2D graphene and 3D Weyl Semi-Metal system. Detailed degeneracy properties in both cases are indicated explicitly. In order to highlight the key point, we only plot dispersion near one node in each case, however, in the Weyl systems, Weyl nodes always appear in pairs with opposite chiralities.

1.3.3 Possible Realization of Weyl semimetals

Firstly, Weyl fermion has been studied in case of liquid He^3, where these fermions are generated in a certain phase of this system [103, 104]. Weyl fermions are an active area of research [1, 105–110]. These works proved the existence of

[5]X. Wan, A. M. Turner, A. Vishwanath, and S. Y. Savrasov, Physical Review B 83, 205101 (2011).

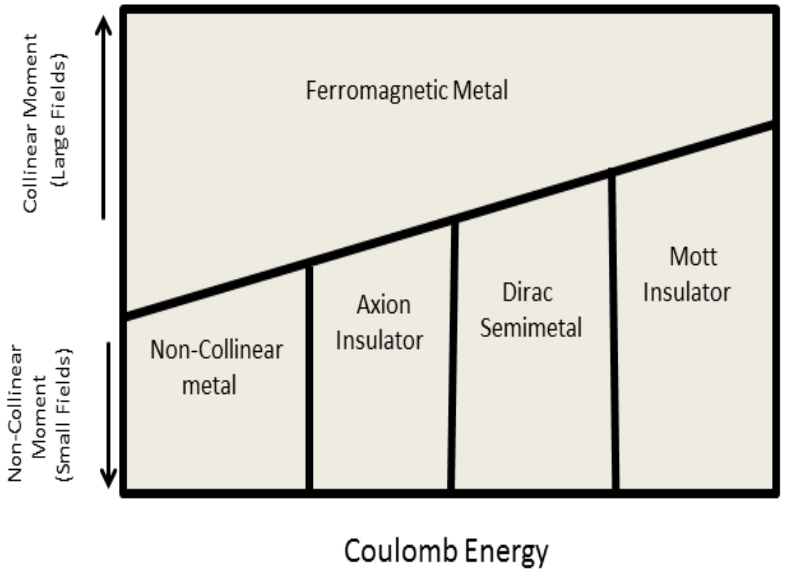

FIGURE 1.7: Figure shows predicted phase diagram for Pyrochlore Iridates: horizontal axis represents the increasing interaction among Ir $5d$ electrons; the vertical axis represents the external magnetic field, which could cause a transition out of the noncollinear all-in/all-out ground state possessing several electronic phases[5].

Weyl semimetal in nature. It is conjectured that Weyl fermions are the low energy excitations of two types of possible Weyl semimetal structures: Pyrochlore Iridates [105] and Topological-Normal Insulator heterostructures [1]. The semimetallic nature of these materials is preserved by the touching of two non-degenerate bands at even numbers of Weyl nodes. Due to the conservation of chirality at each node, only interactions that couple nodes can open gaps. So this system gives an interesting podium for studying, the interplay of interaction and spin orbit in establishing new states of matter. Pyrochlore Iridates is considered as the first possible realization of Weyl semimetal. There are three Weyl points at each hexagonal zone boundary, so total becomes 24 [105]. The fig.(1.7) depicts phase diagram of $Y_2Ir_2O_7$. For each pair of Weyl nodes with opposite chiralities, there is perfect nesting. Refs.[105] focused on the pyrochlore iridates, which have the general formula $A_2Ir_2O_7$, where A=yttrium or a lanthanide element.

In this structure, inversion symmetry is preserved as the electronic properties evolve with correlation strength. In case of weak correlations, or in the absence of magnetic order, a metal is obtained. With strong correlations, a Mott insulator with all-in/all-out magnetic order is obtained. Between these two limits,

with intermediate correlations, the electronic ground state is found to be a Weyl semimetal. This state has linearly dispersing nodes at the chemical potential, phase time-reversal symmetry is broken and inversion symmetry is preserved. In

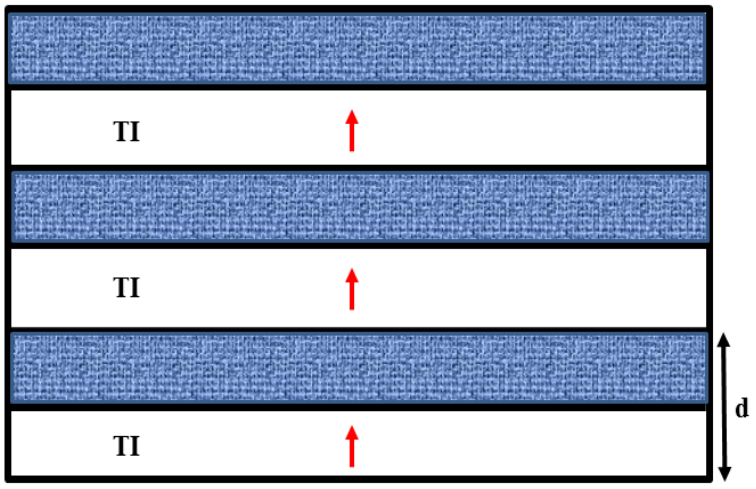

FIGURE 1.8: Schematic diagram of the 3D multilayer heterostructures, which is found by alternating Topological Insulator(TI) layers and Normal Insulator(NI) layers. In all TI layers, their surface states time-reversal symmetry is broken caused by doping magnetic impurities inside TI layers. Unhashed layers represent the TI layers, while hashed layers represent the NI spacers. The arrow of each TI layer represents the magnetization direction. Only three periods of the superlattice are shown in the schematic[6].

the superlattice heterostructures, there is a second possible realization of a Weyl semimetal system [1]. This is constructed by alternating layers of topological insulator and normal insulator. The simplest realization of the three dimensional Weyl semimetal phase is proposed in the topological-normal insulator heterostructures. They have only two Weyl nodes carrying opposite chirality separated in momentum space. The simplest realization of a three dimensional Weyl semimetal is achieved by composing identical thin films of a magnetically doped 3D topological insulator layers separated by ordinary insulator spacer layers, depicted in fig.(1.8). The spin splitting of the surface states is achieved due to doped magnetic impurities in layers of topological insulator. This becomes a cause for time-reversal breaking in the Weyl System because magnetic impurities ferromagnetically ordered with magnetization along the growth direction of the heterostructures.

[6] A. Burkov and L. Balents, Physical Review Letters 107, 127205 (2011).

1.3.4 Chiral Anomaly in Weyl semimetal

A peculiar nonconservation of chiral charge is known as a chiral anomaly and has been well described in high-energy physics. Due to the emergence of new materials like TI, graphene and Weyl semimetals, many high energy phenomena have been described in condensed matter physics. The chiral anomaly has been realized in Weyl semimetal. This property can be used for detection of Weyl semimetal. Many research articles have been published regarding chiral anomaly recently [106, 111–115]. The continuity equation for a Weyl point in presence chirality χ and external electric $\mathbf{E}$ and magnetic field $\mathbf{B}$:

$$\frac{\partial \rho}{\partial t} + \nabla \cdot \mathbf{j} = \frac{\chi}{4\pi^2} \mathbf{E} \cdot \mathbf{B}. \tag{1.89}$$

Here ρ is charge density and $\mathbf{j}$ is current density.

This equation shows charge is not conserved at a single Weyl point with parallel $\mathbf{E}$ and $\mathbf{B}$ fields. To compensate for this excess/deficit charge, there is another Weyl point of the opposite chirality to ensure the overall conservation of charge in the system. So by using parallel $\mathbf{E}$ and $\mathbf{B}$ fields, we can drive charge between Weyl points of opposite chirality. The experiment proposed for detection of Weyl semimetal is focused around chiral anomaly in some form. The large longitudinal magnetoconductivity is one of the transport properties which arise due to chiral anomaly [116]. The phenomenon like chiral magnetic effect is generated by the chiral anomaly, where current flows parallel to an applied magnetic field [117, 118].

1.3.5 Electronic Properties of Weyl Semimetal

While the conductivity of Weyl semimetal (WSMs) is similar to graphene and 3D Dirac semimetals [119], it demonstrates behavior that neither metals nor insulators do. Such systems have a particle-hole symmetry about the charge neutrality locations, so there are states with of electrons and holes moving with equal and opposite momenta that carry current. Due to this, the total momentum becomes vanishes and Coulomb interactions can in fact cause dephasing (relaxation) of these states.

These non-interacting WSMs with chemical potential disorder show bad metals behavior in some of their transport properties [1, 119, 120]. The optical conductivity of disordered WSMs is calculated within a Born approximation by Hosur

et al.[119] that shows temperature and frequency dependence. It contains Drude peak whose height is set by the disorder strength. In case of metal, peak width has a weaker dependence $\sqrt{T}$ on temperature but here the width of the peak goes as T^2. So on lowering the temperature, the conductivity at small non-zero frequency falls rapidly in WSMs as compared to ordinary metals. On going beyond Born approximation, there are rare regions of disorder found in a WSM near the Weyl points that induce a small density of states, and hopping between rare regions results in a finite DC conductivity even at zero temperature [121]. At high frequencies $\hbar\omega >> k_B T$, the conductivity varies linearly with the frequency: $\sigma_{xx}(\omega) = \frac{e^2}{12h}\frac{\omega}{v_F}$ per Weyl node. Importantly, these features are not present in either metals or insulators. So we can say, WSMs are in between metals and insulators in their electric transport properties. But they are closer to being (bad) metals than (bad) insulators [99, 119].

1.3.6 Optical Properties of Weyl Semimetal

The Weyl fermion exhibits novel linear and nonlinear optical properties due to linear dispersion of low energy excitations and poor screening. The Weyl fermion in two dimensions possesses giant nonlinear responses to electromagnetic fields in the terahertz (THz) regime [96]. Due to the promotion of the intensive THz excitations and good coupling between THz fields and free carriers in semiconductors, we study nonlinear electromagnetic responses in the THz region [96, 122–125]. The bound excitons exist in one-dimensional (1D) metallic carbon nanotubes and graphene (possess Weyl Fermions) [23, 45], predicted by ab initio calculations [126–129] and subsequent experiments [130]. In terms of electronic dispersions, carbon nanotubes and graphene may be thought of as two dimensional (2D) analogs to Weyl semimetals . The density of states disappear at the Fermi energy in Weyl fermions, so electrostatic screening becomes weak[96] (for more details see [17]).

1.4 Applications

1.4.1 Graphene

There are a number of applications of graphene in mechanical engineering, electrical engineering and micro-electronics. It has become an important material due to its wide range of applications in electronics engineering as a component

material. Graphene is a good candidate for replacing indium-based electrodes in organic light emitting diodes (OLED). These OLED can be used in mobile display screens due to diminished power consumption. Graphene is cheap, thin and see-through and critically is electrically conductive [131]. So it becomes a good candidate for the flat-screen displays used on smart phones that need electricity to power the optical elements, and to respond to the user touch. By using graphene in the place of indium not only cuts the cost but eliminates the use of metals in the OLED, which may make devices better for recycling. If we use graphene on the surface of the anode in Lithium-ion batteries, lithium ions start to attach with the anode substrate due to defects in the graphene sheet (introduced using a heat treatment). This battery recharges very quickly compared to conventional lithium-ion batteries. There are 2,600 square meters area in a gram of graphene - an equivalent of about ten tennis courts, which provides more opportunities for a reaction to occur in the battery[7]. The ease with which large surface areas of graphene sheets can be produced means that they can be used in the fabrication of capacitors. This will provide avenues for recharging batteries in minutes instead of hours. It is possible to produce a thin membrane by using graphene oxide. It can be used in water desalination because this membrane can block harmful particles and gases. The process of desalinating sea water from this will be cheapest compared to others [132]. To produce a working transistor with graphene is a big achievement because graphene is not a natural semiconductor. It was a significant technical challenge, but this transistor is twice as fast as a silicon transistor with commensurate features. A broadband radio frequency mixer has been designed, which is used in radio applications to process signals at a range of frequencies. This is effectively a solo IC component which shows that graphene transistors can be used reliably in more complicated systems [133]. High-frequency transistors made from graphene are a promising application because of the higher mobility of electrons in graphene move as compared to electrons in silicon. The processes for developing of lithography techniques, which is used to fabricate integrated circuits is based on graphene are growing rapidly [134, 135]. Graphene can be used as corrosion-resistive coatings to protect important buildings and machine parts from corrosion [136].

[7] `http://www.bbc.com/future/story/20130306-bend-and-flex-for-mobile-phones`

1.4.2 Topological Insulator

A fermion which is it's own antiparticle is known as a Majorana fermion. Majorana fermion is true for spin-1 photon and spin-0 neutral pions and has not been yet detected in any known half-spin integral particle. This type of state is present on treating the Dirac equation for real field solutions in the place of complex field for electrons/positrons [137]. Firstly, the existence of a Majorana particle was imagined in neutral neutrino or anti-neutrino and the double-beta decay for a long time. This particle could be a supersymmetry partner of neutral bosonic fields, e.g. the superpartner photino for photons has been confirmed in recent large hadron collider (LHC) experiment going on in CERN, Geneva. In the presence of a topological defect, a bound, isolated, zero-energy mode can exist obeying a Dirac-type equation, apart from the positive and negative energy eigenvalues [138, 139]. When there is conventional Dirac representation this zero mode gives rise to charge fractionalization ($\pm 1/2$), but when we consider Majorana representation [137] the field operator becomes real, zero modes with chargeless (neutral) Majorana fermions are seen. Read and Green [140], proposed such Majorana bound states (MBS) for the $p_x + ip_y$ wave superconductor, e.g. in Sr_2RuO_4 [141] and in cold-atoms [142] while conventional s-wave superconductors do not give a signature of zero modes. Topological superconductors show presence of MBS. MBS developes only in a strong TI because of the proximity effect when the TI's surface is close to that of a superconductor. There are some techniques to produce them in real experiments suggested by Fu and Kane [143].

Axion Electrodynamics

Lagrangian density has following form in electromagnetic field theory

$$\mathcal{L}_0 = \frac{1}{8\pi}\left(\epsilon E^2 - \frac{1}{\mu}B^2\right).$$

When we have electromagnetic coupling, there will be an additional term with invariance under $\theta \to \theta + 2\pi$. So

$$\mathcal{L}_\theta = \frac{\theta e^2}{2\pi h}\mathbf{E}\cdot\mathbf{B}. \tag{1.90}$$

This term is called axion field term. It has been introduced for solving strong CP violation problem in particle physics [144, 145]. Electric field E is TR invariant and magnetic field B is odd to TR symmetry. So the Lagrangian in eq.(1.90) loses

the TR symmetry unless θ is odd to TR as well. But the distinction between trivial topological insulator and nontrivial (strong) topological insulator depends on the choice of $\theta = 0$ and $\theta = \pi$ respectively [146, 147]. So they are related to the Z_2 invariant class and θ/π is identical to the invariant ν_0. From topological field theory, the coefficient of the axion term (eq.(1.90) denotes the value of the Hall conductance [86]. On taking $\theta = \pi$, eq.(1.90) gives a coefficient $1/2(e^2/h)$ which can only be shifted by an integer due to disorders. By measuring surface Hall conductivity in the strong topological insulator, it confirms topological robustness and the axion electrodynamics as well.

Due to protected surface/edge states in TI, there is absence of decoherence in the spin current. Spin current is very important for quantum computation. If there are bound Majorana fermions in TI, their non-Abelian statistics will form the qubits, which is essential for quantum computation [148]. It is found that topological surface states can facilitate surface reaction by promoting different directions of static electron transfer. In theory, this surface reaction suggests that topological insulators can be used as high-performance catalyst [149]. Zhang *et al.* suggested application of Bi_2Se_3 in wide band-width, high performance photodetector, which works between terahertz to infrared frequency range [150]. Peng *et al.* designed near infrared transparent flexible electrode, which show low resistance and high transparency with Bi_2Se_3 grown on mica [151]. The advantage of the unique surface electrons of topological insulators can be used in the future electronic device for energy utilization. The above information is taken from the source given in footnote[8].

1.4.3 Weyl Semimetal

A Weyl semimetal comprises Weyl fermions, which could be very useful in electrical conduction due to it's massless nature. Weyl electrons have higher mobility than normal electrons-which could be used to create faster electronic circuits. The electron in graphene is also massless but Weyl fermions are topologically protected from scattering, which means that they could be useful in quantum computers. Weyl semimetal has high mobility with topological protection, so it can become motherboard for future electronic devices [9].

[8] http://www.jncasr.ac.in/hbar/PDF/ti.pdf
[9] http://physicsworld.com/cws/article/news/2015/jul/23/weyl-fermions-are-spotted-at-long-last

1.5 Rabi Oscillations in Two-Levels

In order to understand the phenomenon of Rabi oscillations in a two-level system, take an example of the hydrogen atom interacting with an electromagnetic field. the time evolution has the form [49]

$$i\hbar\frac{\partial}{\partial t}\psi(\mathbf{r},t) = [H_0 + H_i(t)]\psi(\mathbf{r},t). \tag{1.91}$$

Here H_0 is the unperturbed Hamiltonian of the hydrogen atom, $\hat{H}_i = e\mathbf{D}\cdot\mathbf{E_0}\cos(\omega\mathbf{t})$ is the interacting Hamiltonian with $\mathbf{D}$ dipole moment operator, $\mathbf{E}(t) = \mathbf{E}_0\cos(\omega t)$ is monochromatic incident electric field and $\psi(\mathbf{r},t)$ is the time dependent wave function, which can be further written in form of stationary eigenfunctions for two level system as follows

$$\psi(\mathbf{r},t) = c_1(t)\psi_1(\mathbf{r},t) + c_2(t)\psi_2(\mathbf{r},t). \tag{1.92}$$

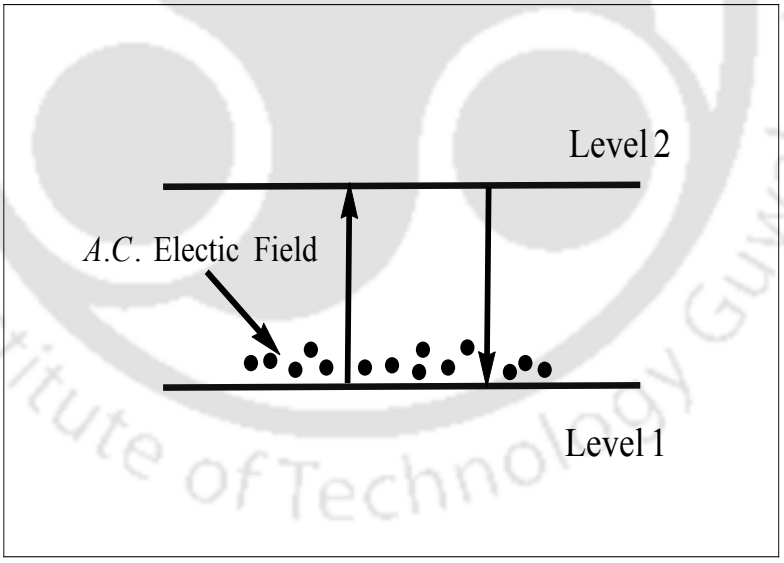

FIGURE 1.9: A schematic diagram of atomic oscillations (Rabi oscillations) between two level systems in presence of applied A.C. electric field.

We defined

$$\psi_n(\mathbf{r},t) = e^{-\frac{iE_nt}{\hbar}}\psi_n(\mathbf{r}), \tag{1.93}$$

$$\psi(\mathbf{r},t) = c_1(t)e^{-\frac{iE_1t}{\hbar}}\psi_1(\mathbf{r}) + c_2(t)e^{-\frac{iE_2t}{\hbar}}\psi_2(\mathbf{r}). \tag{1.94}$$

Inserting eq.(1.94) in eq.(1.91), from eq.(1.91) the equation of motion for the probability amplitude we obtain

$$i\hbar\frac{\partial}{\partial t}\left(c_1(t)e^{-\frac{iE_1t}{\hbar}}\psi_1(\mathbf{r}) + c_2(t)e^{-\frac{iE_2t}{\hbar}}\psi_2(\mathbf{r})\right)$$

$$= [H_0 + H_I(t)]\left(c_1(t)e^{-\frac{iE_1t}{\hbar}}\psi_1(\mathbf{r}) + c_2(t)e^{-\frac{iE_2t}{\hbar}}\psi_2(\mathbf{r})\right), \tag{1.95}$$

$$i\hbar\left[\left(\frac{\partial c_1(t)}{\partial t}e^{-\frac{iE_1t}{\hbar}} - \frac{iE_1}{\hbar}e^{-\frac{iE_1t}{\hbar}}c_1(t)\right)\psi_1(\mathbf{r}) + \left(\frac{\partial c_2(t)}{\partial t}e^{-\frac{iE_2t}{\hbar}} - \frac{iE_2}{\hbar}e^{-\frac{iE_2t}{\hbar}}c_2(t)\right)\psi_2(\mathbf{r})\right]$$

$$= [H_0 + H_I(t)]\left(c_1(t)e^{-\frac{iE_1t}{\hbar}}\psi_1(\mathbf{r}) + c_2(t)e^{-\frac{iE_2t}{\hbar}}\psi_2(\mathbf{r})\right), \tag{1.96}$$

$$i\hbar\left[\left(\frac{\partial c_1(t)}{\partial t}e^{-\frac{iE_1t}{\hbar}}\right)\psi_1(\mathbf{r}) + \left(\frac{\partial c_2(t)}{\partial t}e^{-\frac{iE_2t}{\hbar}}\right)\psi_2(\mathbf{r})\right]$$

$$= H_I(t)\left(c_1(t)e^{-\frac{iE_1t}{\hbar}}\psi_1(\mathbf{r}) + c_2(t)e^{-\frac{iE_2t}{\hbar}}\psi_2(\mathbf{r})\right). \tag{1.97}$$

Multiply by $e^{\frac{iE_1t}{\hbar}}\psi_1^*(\mathbf{r})$

$$i\hbar\left[\left(\frac{\partial c_1(t)}{\partial t}e^{-\frac{iE_1t}{\hbar}}\right)e^{\frac{iE_1t}{\hbar}}\psi_1^*(\mathbf{r})\psi_1(\mathbf{r}) + \left(\frac{\partial c_2(t)}{\partial t}e^{-\frac{iE_2t}{\hbar}}\right)e^{\frac{iE_1t}{\hbar}}\psi_1^*(\mathbf{r})\psi_2(\mathbf{r})\right]$$

$$= e^{\frac{iE_1t}{\hbar}}\psi_1^*(\mathbf{r})H_I(t)\left(c_1(t)e^{-\frac{iE_1t}{\hbar}}\psi_1(\mathbf{r}) + c_2(t)e^{-\frac{iE_2t}{\hbar}}\psi_2(\mathbf{r})\right). \tag{1.98}$$

Integrating w.r.t. $\mathbf{r}$

$$i\hbar\left(\frac{\partial c_1(t)}{\partial t}\right) = c_1(t)\int\psi_1^*(\mathbf{r})H_I(t)\psi_1(\mathbf{r})d\mathbf{r}$$
$$+e^{\frac{i(E_1-E_2)t}{\hbar}}c_2(t)\int\psi_1^*(\mathbf{r})H_I(t)\psi_2(\mathbf{r})d\mathbf{r}. \tag{1.99}$$

We define $\omega_0 = \frac{i(E_2-E_1)t}{\hbar}$

$$i\hbar\frac{\partial c_1(t)}{\partial t} = c_1(t)M_{11} + e^{-i\omega_0 t}c_2(t)M_{12}. \tag{1.100}$$

The transition matrix elements M_{mj} are given by

$$\hbar M_{mj} = \int \psi_m^* \hat{H}_i \psi_j dV = \langle \psi_m | \hat{H}_i | \psi_j \rangle. \tag{1.101}$$

Similarly

$$i\hbar \frac{\partial c_2(t)}{\partial t} = e^{i\omega_0 t} c_1(t) M_{21} + c_2(t) M_{22}. \tag{1.102}$$

We defined $\hat{H}_i = e\mathbf{D} \cdot \mathbf{E_0} \cos(\omega \mathbf{t})$. From symmetry

$$M_{11} = M_{22} = 0, \tag{1.103}$$

$$M_{12} = M_{21}^* = \frac{1}{\hbar} e E_0 X_{12} \cos(\omega t). \tag{1.104}$$

Here,

$$X_{12} = \int \psi_1^* X \psi_2 dV = \langle \psi_1 | X | \psi_2 \rangle, \tag{1.105}$$

is the dipole matrix element. We defined the Rabi frequency Ω_{Rabi} as

$$\Omega_{\text{Rabi}} = \frac{1}{\hbar} e E_0 X_{12}, \tag{1.106}$$

$$M_{12} = M_{21}^* = \Omega_{\text{Rabi}} \cos(\omega t), \tag{1.107}$$

$$i\hbar \frac{\partial c_1(t)}{\partial t} = e^{-i\omega_0 t} c_2(t) \Omega_{\text{Rabi}} \cos(\omega t) = e^{-i\omega_0 t} c_2(t) \Omega_{\text{Rabi}} \frac{1}{2} \left(e^{i\omega t} + e^{-i\omega t} \right), \tag{1.108}$$

$$i\hbar \frac{\partial c_2(t)}{\partial t} = e^{i\omega_0 t} c_1(t) \Omega_{\text{Rabi}}^* \cos(\omega t) = e^{i\omega_0 t} c_1(t) \Omega_{\text{Rabi}}^* \frac{1}{2} \left(e^{i\omega t} + e^{-i\omega t} \right), \tag{1.109}$$

$$i\hbar \frac{\partial c_1(t)}{\partial t} = c_2(t) \Omega_{\text{Rabi}} \frac{1}{2} \left(e^{i(\omega - \omega_0)t} + e^{-i(\omega + \omega_0)t} \right), \tag{1.110a}$$

$$i\hbar \frac{\partial c_2(t)}{\partial t} = c_1(t) \Omega_{\text{Rabi}}^* \frac{1}{2} \left(e^{i(\omega + \omega_0)t} + e^{-i(\omega - \omega_0)t} \right). \tag{1.110b}$$

The eq.(1.110a) and eq.(1.110b) are known as optical Bloch equations. When

light interacts with the hydrogen atom near resonance i.e. $|\omega - \omega_0| << \omega_0$, the exponential factor $e^{i(\omega-\omega_0)t}$ is almost time independent and complementary term viz. $e^{i(\omega+\omega_0)t}$ oscillates very fast with almost double the incident frequency. After few time periods, the average contribution of the fast oscillating term will nearly vanishes. In quantum optics this approximation has a specific name called 'rotating wave approximation' (RWA). On applying this approximation to the above equation

$$i\hbar\frac{\partial c_1(t)}{\partial t} = c_2(t)\Omega_{\text{Rabi}}\frac{1}{2}e^{i(\omega-\omega_0)t}, \tag{1.111a}$$

$$i\hbar\frac{\partial c_2(t)}{\partial t} = c_1(t)\Omega^*_{\text{Rabi}}\frac{1}{2}e^{-i(\omega-\omega_0)t}. \tag{1.111b}$$

We consider zero detuning: $\omega = \omega_0$ where the well-known Rabi oscillations between the ground and excited state of the driven two-level system are seen. On choosing initial conditions $|c_1|^2 = 1$ and $|c_2|^2 = 0$ we found

$$|c_1|^2 = \cos^2\left(\frac{\Omega_{\text{Rabi}}t}{2}\right) \text{ and } |c_2|^2 = \sin^2\left(\frac{\Omega_{\text{Rabi}}t}{2}\right). \tag{1.112}$$

The frequency Ω_{Rabi} depends only upon the intensity of the applied optical field and is independent of the applied frequency. In most cases, the Rabi frequency Ω_{Rabi} is always less than the frequency of incident applied optical field. This phenomenon was predicted theoretically a long time ago, but was observed experimentally in conventional semiconductors (bands instead of levels) only in the 1980's. In case of graphene and TI, coherent optical properties have been studied in presence of classical [152–154] and quantum fields [155] in various regimes with various approximations. The observed Rabi oscillations in the presence of a quantum EM field [155] are quite different from those observed in presence of a classical field [152]. Incoherent effects like optical dephasing and relaxation of band electrons (intra-band as well as inter-band) have also been studied by various authors [62, 63].

Chapter 2

Rabi Oscillations in Dirac-Weyl Fermionic Systems

2.1 Introduction

The light matter interaction is an important part of physics. Newton saw that visible light separates into its constituent colors upon passing through a prism. There are two reasons behind this phenomenon **(i)** white light has many frequencies, in other words it is non-monochromatic, and **(ii)** interaction of light with matter causes dispersion of white light into different frequency components. There are many new phenomena resulting from light-matter interactions like the change in refractive index, scattering, diffraction, dispersion, etc [156]. One such phenomenon is Rabi oscillation, a familiar theme in nonlinear optics, which comes due to light matter interaction. It is the slow periodic oscillation of the amplitudes of the population and polarization of a system with two levels or bands when these quantities themselves oscillate rapidly with the frequency of the externally applied optical field. It is also the periodic exchange of energy between the electromagnetic field and the system. This slow frequency ω_R, known as the Rabi frequency, which is typically much smaller than the optical frequency ω itself. Generally, we study this phenomenon in a two-level system of atomic physics. Rabi oscillations are also seen in semiconductors, which have bands instead of energy levels, and where there is a mixing of these energies due to long-range Coulomb interactions [19, 49, 157–162]. This enables understanding of other effects, such as the phenomenon of excitonic quantum beats and excitonic optical Stark effect [49]. So it is natural to investigate the same effects in TI and Weyl semimetal,

where a Dirac cone exists, i.e. the bands are linear instead of parabolic. With the emergence of new Dirac-Weyl fermionic systems in condensed matter, many works have emerged that compare and contrast conventional semiconductors/metals and Dirac-Weyl fermionic systems. This type of study has been performed in several research articles [153, 154, 160, 163–168].

Conventional Rabi oscillations are studied using the rotating wave approximation (RWA). It is an approximation used for the approximate analytic solution of time dependent evolution eqn. of a two level system coupled to a weak electric field in resonance with the transition. In this approximation, we remove rapidly oscillating terms of the effective Hamiltonian, but its validity is limited to only when the internal frequency of the two-level system is close to the external frequency of field, i.e. in case of resonance [49, 157]. We wish to see if something new can be learned by studying Rabi oscillations in these Dirac-Weyl systems. Nonlinear optics in these systems is poorly studied and few interesting articles have been published till now [165, 166, 169–174].

In this chapter, we have reported a new approach, which is basically an advancement of RWA, we called it 'asymptotic rotating wave approximation (ARWA)' [152, 155, 175–178] (otherwise known as Floquet approximation [179–181]). The numerically exact solution of coherent Bloch equations also reconfirm these findings.

2.2 Problem Formulation

In this chapter, we have described one of the most significant optical property in relativistic fermionic systems- Rabi oscillations. As we described earlier, Rabi oscillations have been analyzed in graphene by Mishchenko using the well known rotating wave approximation (RWA) [153] and this is applicable only near the conventional resonance condition, when the frequency of the incident optical field is comparable to the frequency corresponding to particle hole energy. Far from conventional resonance, only relativistic fermionic systems exhibit a new type of Rabi oscillation, which is absent in conventional semiconductors and two-level systems [152, 155, 175–178]. Our aim is to study nonlinear optics of these systems at the Weyl (Dirac) node, since all interesting physics at low energy occurs in the vicinity of the Weyl(Dirac) node - particularly the phenomenon of anomalous Rabi oscillation (ARO), which has been predicted theoretically in single layer graphene

by our group [152]. In order to study this, we employ an approximation known as asymptotic rotating wave approximation (ARWA) [152, 155, 175–178]. In this chapter a new kind of slow oscillation in population and polarization densities that is present only in relativistic fermionic systems, is seen far from conventional resonance. We have studied this phenomenon as well as the conventional close to resonance Rabi oscillations and verified the claims numerically.

We use the velocity gauge (only vector potential is present but no scalar potential) in the calculations. We will, of course, obtain the same results upon using the other extreme choice namely - the length gauge, i.e. including only a scalar potential. The relative benefits of these choices are well described in these references [168, 182].

2.3 Weyl Semimetal Hamiltonian in Second Quantized Form

If the particles are massless, then relativistic fermions are described by a two-component spinor explained by Hermann Weyl in 1929 [183] in contrast to the four-component Dirac spinor. This analysis leads to the Weyl equation $H\psi = E\psi$ generated by the Weyl Hamiltonian

$$H = v_F(p_x\sigma_x + p_y\sigma_y + p_z\sigma_z), \tag{2.1}$$

$$E = \pm v_F\sqrt{|p_\parallel|^2 + p_z^2}. \tag{2.2}$$

Here $|p_\parallel| = \sqrt{p_x^2 + p_y^2}$, v_F is hopping velocity between nearest neighbors. Due to the massless nature, it is the Pauli matrices that enter into the formalism rather than Dirac matrices. The minimal matrix representation of these matrices is two dimensional. This aspect may be further clarified by noting that all three σ matrices are already coupled to all three components of the momentum $\mathbf{p}$, and there is no other anticommuting 2×2 matrix available for the mass to couple to momentum. Since an energy gap cannot be opened in such systems, the fact that the bands touch is a stable notion. Hence in such materials, 3D Weyl fermions are expected to be more protected against small perturbations than the Dirac fermions in graphene. Due to commutation of helicity operator with the Weyl Hamiltonian $H = v_F\mathbf{p}\cdot\boldsymbol{\sigma}$, helicity is a conserved quantity and becomes a good quantum number.

Using the tight binding approximation, the low-energy Hamiltonian of Weyl metals in momentum space with hopping and interaction with electromagnetic radiation (in the radiation gauge with vector potential $\mathbf{A}(t)$) in second quantized form

$$H = \sum_{\alpha,\beta} v_F \boldsymbol{\sigma}_{\alpha,\beta} \cdot \left(\mathbf{p} - \frac{e}{c}\mathbf{A}(t)\right) c^{\dagger}_{p,\alpha} c_{p,\beta}, \tag{2.3}$$

where the Greek indices stand for either spin up or spin down and $c^{\dagger}(c)$ is the creation (annihilation) operator. We have taken $\mathbf{A}(t) = \mathrm{Re}(\mathbf{A_0} e^{-i\omega t})$ i.e. $\mathbf{A}(t) = \frac{1}{2}\mathbf{A_0} e^{-i\omega t} + \frac{1}{2}\mathbf{A_0^*} e^{i\omega t}$.

2.4 Rabi Oscillations in Weyl

Consider the evolution equation

$$i\frac{\partial}{\partial t}\psi(p,t) = H\psi(p,t) \text{ on setting } \hbar = 1. \tag{2.4}$$

Insistence on analytical solutions to the above Weyl equation necessitate the use of approximations. When the driving frequency is close to one of the excitation or resonant frequencies of the system we use RWA where the time dependence of the dynamical quantities are factored into fast and slow variables: fast means the external frequency, and slow being the difference between the external frequency and the resonant frequency [19]. In the off-resonant case, we use ARWA [152, 155, 175–178], where we consider the limit in which the external driving frequency ω is always much greater than the Rabi frequency ω_R and the resonant frequency for the creation of particle hole pairs namely $2v_F\sqrt{|p_\parallel|^2 + p_z^2}$, ($\omega >> \omega_R$ and $\omega >> 2v_F\sqrt{|p_\parallel|^2 + p_z^2}$). This is quite different from the usual condition used in rotating wave approximation (RWA) namely $\mid \omega - 2v_F\sqrt{|p_\parallel|^2 + p_z^2} \mid << \omega$. We rewrite H and $\psi(p,t)$ in terms of slow and fast parts

$$H = H_0 + e^{-i\omega t}\, V_+ + e^{i\omega t}\, V_- \ , \tag{2.5}$$

$$\psi = \psi_0 + e^{-i\omega t}\, \psi_+ + e^{i\omega t}\, \psi_- + ... \tag{2.6}$$

Here, H_0 and ψ_0 are slow parts, while V_+, V_- and ψ_+, ψ_- are the (coefficients of)

fast parts of the full Hamiltonian and wavefunction respectively. Upon decomposing the Hamiltonian in eq.(2.3) in the above form we obtain

$$H_0 = v_F \begin{bmatrix} p_z & (p_x - ip_y) \\ (p_x + ip_y) & -p_z \end{bmatrix}, \tag{2.7}$$

$$V_+ = v_F \begin{bmatrix} -\frac{e}{2c}A_{z0} & -\frac{e}{2c}(A_{x0} - iA_{y0}) \\ -\frac{e}{2c}(A_{x0} + iA_{y0}) & \frac{e}{2c}A_{z0} \end{bmatrix}, \tag{2.8}$$

$$V_- = v_F \begin{bmatrix} -\frac{e}{2c}A^*_{z0} & -\frac{e}{2c}(A^*_{x0} - iA^*_{y0}) \\ -\frac{e}{2c}(A^*_{x0} + iA^*_{y0}) & \frac{e}{2c}A^*_{z0} \end{bmatrix}. \tag{2.9}$$

The "Rabi landscape", which is a plot of the generalized Rabi frequency versus wave vector has two local minima - one corresponding to conventional Rabi oscillations and the other, even lower minimum corresponding to anomalous Rabi oscillations. We also showed that the anomalous Rabi frequency is absent in conventional systems. But there is a limit in which the Weyl-graphene-like system can be made to resemble more conventional two-level systems. This is the limit where the Hamiltonian become diagonal which leads to emergence of a new symmetry which may be used to generate a Noether constant, making the model soluble [152]. In this limit, the term involving the anomalous Rabi frequency drops out making the solutions resemble that of two-level systems. But when the free theory includes terms with two or more non-commuting Pauli matrices, this symmetry is gone and the anomalous Rabi oscillations reappear. Conventional Rabi oscillations however are always present in all these systems. This is the reason, why we insist that, anomalous Rabi oscillations are due to "pseudo-spin" meaning that the presence of two or more non-commuting Pauli matrices (even in the absence of an external field) is a must for anomalous Rabi oscillations to be seen (upon inclusion of the external time dependent fields). Furthermore, unlike conventional Rabi oscillations, anomalous Rabi oscillations are sensitive to the polarization of radiation. For a real vector potential and linear polarization, anomalous Rabi oscillations are absent and are most prominent for circular polarization [155]. We now exploit this observation to recast the above model using a solvable basis namely one that ignores the off-diagonal parts of the time independent Hamiltonian- an approach that complements all the other approaches. This effort is best able to motivate the need for the new technique of ARWA. For a plane electromagnetic wave we may choose the direction of propagation to be the z direction so that $A_z = 0$ without

loss of generality. We notice that there is a limit in which the above equations become soluble. This is the limit in which $p_x = p_y = 0$ and $A_z = 0$ and circular polarization $A_{x0} = -iA_{y0} = A$. In this case

$$i\frac{\partial}{\partial t}\psi_\uparrow = v_F p_z \psi_\uparrow - v_F e^{-i\omega t}\frac{e}{c}A\ \psi_\downarrow, \tag{2.10a}$$

$$i\frac{\partial}{\partial t}\psi_\downarrow = -v_F p_z \psi_\downarrow - v_F e^{i\omega t}\frac{e}{c}A\ \psi_\uparrow. \tag{2.10b}$$

Make the substitutions $\psi_\uparrow = \psi_{\uparrow,1}\ e^{-iv_F p_z t}$ and $\psi_\downarrow = \psi_{\downarrow,1}\ e^{iv_F p_z t}$ where $\delta^{'} = \omega - 2v_F p_z$ is the detuning and $\omega_R^{'} = \frac{2ev_F A}{c}$ is the Rabi frequency.

$$i\frac{\partial}{\partial t}\psi_{\uparrow,1} = -\frac{\omega_R^{'}}{2}\ e^{-i\delta^{'}t}\ \psi_{\downarrow,1}\ ;\ \ i\frac{\partial}{\partial t}\psi_{\downarrow,1} = -\frac{\omega_R^{'}}{2}\ e^{i\delta^{'}t}\ \psi_{\uparrow,1}. \tag{2.11}$$

$$\psi_{\downarrow,1}(t) = e^{-\frac{1}{2}it\left(\sqrt{\delta^{'2}+\omega_R^{'2}}-\delta^{'}\right)}\left(c_1 + c_2\ e^{it\sqrt{\delta^{'2}+\omega_R^{'2}}}\right), \tag{2.12}$$

$$\psi_{\uparrow,1}(t) = \frac{e^{-\frac{1}{2}it\left(\sqrt{\delta^{'2}+\omega_R^{'2}}+\delta^{'}\right)}}{\omega_R^{'}}\left[\sqrt{\delta^{'2}+\omega_R^{'2}}\left(-c_1 + c_2\ e^{it\sqrt{\delta^{'2}+\omega_R^{'2}}}\right) + \delta^{'}\left(c_1 + c_2\ e^{it\sqrt{\delta^{'2}+\omega_R^{'2}}}\right)\right]. \tag{2.13}$$

We may see from these solutions that only conventional Rabi oscillations are seen. This is because this system resembles a two-level atom with the time independent part of the Hamiltonian involving just the σ_z Pauli matrix. The coefficient of the rapidly varying portion of the current (Fermi bilinear) is slowly oscillating with a frequency $\sqrt{\delta^{'2}+\omega_R^{'2}}$ which goes through a minimum when $\delta^{'} = \omega - 2v_F p_z = 0$ indicating that this corresponds to conventional Rabi oscillation rather than anomalous Rabi oscillation. In what follows, we wish to convince the reader that even a small non-zero contribution from p_x, p_y yields, in addition, a new slow oscillation known as anomalous Rabi oscillation. Upon restoring p_x, p_y, we get

$$i\frac{\partial}{\partial t}\psi_\pm = p_z\psi_\pm + v_F(p_x \mp ip_y)\psi_\mp - v_F e^{\mp i\omega t}\frac{ev_F}{c}A\ \psi_\mp. \tag{2.14}$$

Here "+" for up spin and "−" for down spin. We use the solutions in eq.(2.12) and eq.(2.13) by imagining the integration constants to be now time dependent and

substitution into the above equations which gives

$$-i\left[\left(\sqrt{\delta'^2+\omega_R'^2}-\delta'\right)c_1'(t)-\left(\sqrt{\delta'^2+\omega_R'^2}+\delta'\right)c_2'(t)e^{it\sqrt{\delta'^2+\omega_R'^2}}\right]= v_F\omega_R'(p_x-ip_y)e^{it\omega}\left(c_1(t)+c_2(t)e^{it\sqrt{\delta'^2+\omega_R'^2}}\right), \tag{2.15a}$$

$$i\omega_R' e^{it\omega}\left(c_1'(t)+c_2'(t)e^{it\sqrt{\delta'^2+\omega_R'^2}}\right)=v_F(p_x+ip_y)\left[-c_1(t)\left(\sqrt{\delta'^2+\omega_R'^2}-\delta'\right)+c_2(t)\left(\sqrt{\delta'^2+\omega_R'^2}+\delta'\right)e^{it\sqrt{\delta'^2+\omega_R'^2}}\right]. \tag{2.15b}$$

It may be shown that the eq.(2.15a) and eq.(2.15b) show a new kind of Rabi oscillation far from resonance $\omega >> 2v_F|p_z|$. This is also seen through a fully numerical solution of the Floquet-Bloch equations which are the equations for the Fermi bilinears deduced from eq.(2.14). First, we establish the presence of anomalous Rabi oscillations using the analytical method of ARWA.

2.4.1 Off-Resonance Case (ARWA)

The fundamental idea behind this off-resonance technique is that the unknown wave function is taken to be a series involving harmonics of the largest of the frequencies - in the present case, the external driving frequency ω. The coefficients ψ_0, ψ_+ and ψ_- are assumed to be slowly varying on the scale of external driving frequency ω. We ignore higher harmonics of ω in the field eq.(2.6) as including them amounts to studying higher order effects known as the Bloch Siegert shift [175]. Hence, eq.(2.4) is solved by retaining only the leading harmonics, i.e. in terms of ψ_0 and H_0 where we neglect terms of order of $\frac{1}{\omega^2}$. This method is in fact quite well-known and not particularly new. It goes under the name of Floquet theory (derived in appendix (section 2.8.1.2)). The evolution equation simplifies as follows

$$i\frac{\partial}{\partial t}\psi_0 = H_{eff}\ \psi_0, \tag{2.16}$$

where,

$$H_{eff} \equiv \left(H_0\ +\frac{1}{\omega}\left[V_-,\ V_+\right]\right), \tag{2.17}$$

and $\omega\ \psi_+ = V_+\ \psi_0; \quad -\omega\ \psi_- = V_-\ \psi_0$. In ARWA, we consider the limit $\omega \to \infty$, in such a way that $\omega v_F|p| = \delta < \infty$. The eigenvalues of H_{eff} are the anomalous Rabi frequency of the wave function. We denote them as $\pm\frac{1}{2}\Omega_{ARWA}$, since H_{eff} is

traceless. In fact we may write $H_{eff} = \frac{1}{2}\Omega_{ARWA}(p)\ \hat{e}(p)\cdot\boldsymbol{\sigma}$ for some unit vector $\hat{e}(p)$. Therefore, we are entitled to assert

$$\psi_0(\mathbf{p},t) = \ -\frac{2i}{\Omega_{ARWA}(p)}\ \sin\left(\frac{1}{2}\Omega_{ARWA}(p)t\right)\ H_{eff}\psi_0(\mathbf{p},0) + \cos\left(\frac{1}{2}\Omega_{ARWA}(p)t\right)\ \psi_0(\mathbf{p},0). \tag{2.18}$$

We choose an initial state corresponding to the lowest energy of H_0 viz. $-v_F p = -v_F\sqrt{p_x^2+p_y^2+p_z^2}$ in which case

$$\psi_0(\mathbf{p},0) = \begin{pmatrix} -\frac{(p_x - ip_y)}{\sqrt{2p(p+p_z)}} \\ \sqrt{\frac{(p+p_z)}{2p}} \end{pmatrix}. \tag{2.19}$$

This state ensures that the net current $\mathbf{J} = \sum_{\mathbf{p}}\psi_0^\dagger(\mathbf{p},0)\boldsymbol{\sigma}\psi_0(\mathbf{p},0) = 0$. Here $\Omega_{ARWA}(p)$ is the frequency of oscillation of the amplitudes of observables such as polarization, densities, current, etc. A general formula for this may be obtained as follows

$$\Omega_{ARWA}(p) = 2v_F\ \left[-\frac{e^4v_F^2}{4c^4\omega^2}\ \mathbf{A}_0^{*2}\mathbf{A}_0^2 + \frac{e^4v_F^2}{4c^4\omega^2}(\mathbf{A}_0^*\cdot\mathbf{A}_0)^2 + \frac{ie^2v_F}{c^2\omega}(\mathbf{A}_0^*\times\mathbf{A}_0)\cdot\mathbf{p} + p^2\right]^{\frac{1}{2}}. \tag{2.20}$$

It is not possible to measure the wave function directly in laboratory, but we can measure observables such as current density which is a bilinear in the fields. The frequency of the observables such as the current is twice the frequency of the wave function. We are interested in that result which is analogous to what we obtained in graphene, so we impose the condition $A_{x0} = A_{x0}^* = A$, $A_{y0} = Ae^{i\gamma}$, $A_{y0}^* = Ae^{-i\gamma}$ and $A_{z0} = 0, A_{z0}^* = 0$ - the z-component of the vector potential is chosen to be zero thereby eventually enabling a comparison with two dimensional graphene (when the z-component of the momentum is also set to zero). We obtain the off resonance frequency of the slow part of the current density as

$$\Omega_{ARWA} = 2\sqrt{\left(v_F p_\parallel\right)^2 + \left(v_F p_z - \frac{A^2e^2v_F^2}{c^2\omega}\sin\gamma\right)^2}. \tag{2.21}$$

Here γ is the polarization of the incident radiation and A is amplitude of electromagnetic vector potential and $p_\parallel = \sqrt{p_x^2+p_y^2}$. Now we go on to examine various limiting cases of these expressions with respect to polarization. Linear polarization: in this case, we choose $\gamma = 0, \pm\pi, \pm 2\pi, ...$ The anomalous Rabi frequency in this case vanishes at the Weyl node. It shows that there are no anomalous Rabi oscillations at the Weyl node if light is linearly polarized which is also the case in graphene [155].

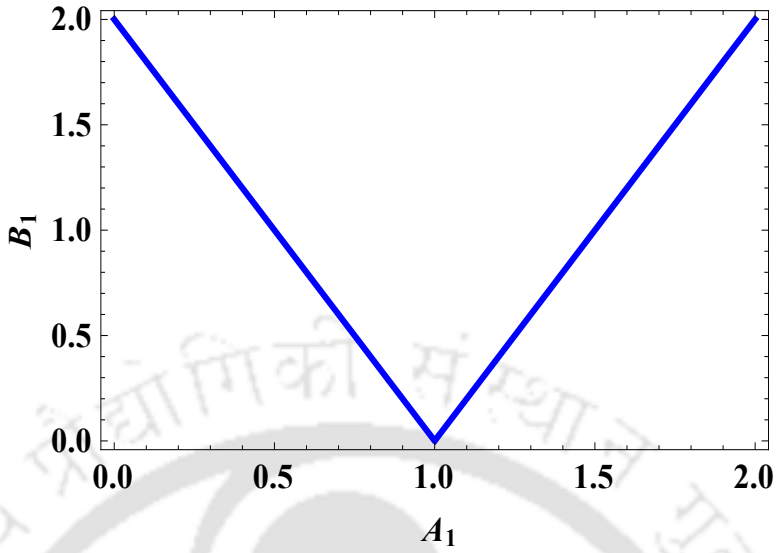

FIGURE 2.1: The plot belongs from eq.(2.22), depicts the anomalous Rabi frequency versus the component of the wave vector p_z upon setting $p_x = 0$ and $p_y = 0$ where $A_1 = \frac{v_F p_z \omega}{\omega_R'^2}$ and $B_1 = \frac{\Omega_{ARWA}\ \omega}{\omega_R'^2}$. For plotting we consider $\frac{\omega_R'}{\omega} = 0.1$, $v_F = 1$ and $\hbar = 1$.

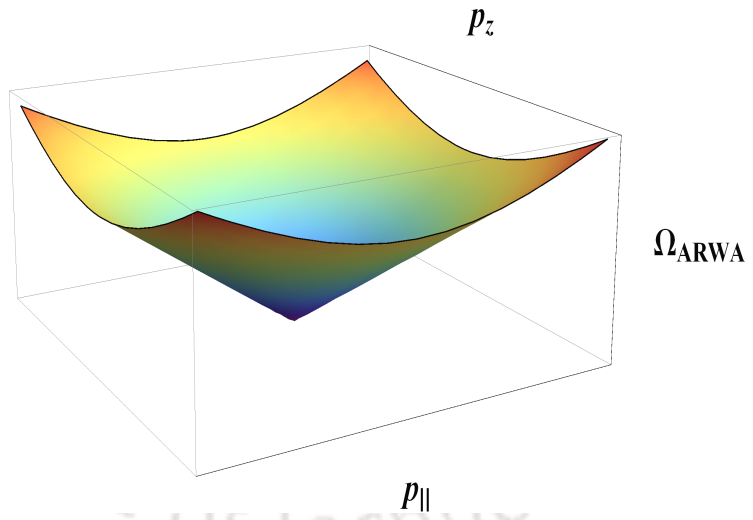

FIGURE 2.2: The plot shows the anomalous Rabi frequency versus wave vector (qualitatively) in 3D with $\sqrt{p_x^2 + p_y^2} = |p_{||}|$, plot is for circularly polarized light.

Circular polarization: in this case $\gamma = \frac{m\pi}{2}$, where $m = \pm 1, \pm 3, ...$ Suppose we choose $\gamma = \frac{\pi}{2}$, the anomalous Rabi frequency will be

$$\Omega_{ARWA} = 2\sqrt{\left(v_F p_{\parallel}\right)^2 + \left(v_F p_z - \frac{\omega_R'^2}{\omega}\right)^2}, \tag{2.22}$$

where $\omega_R' = \frac{e v_F}{c} A$ is a parameter which is of the order of the conventional Rabi

frequency. In Weyl metals, the anomalous Rabi frequency is peculiar and shows considerable departure from the form of this quantity seen in graphene. In single layer graphene we have seen [152] that the anomalous Rabi frequency is $\Omega_{ARWA} = 2\sqrt{\left(v_F p_\parallel\right)^2 + \left(\frac{\omega_R^2}{\omega}\right)^2}$. This result is reproduced if we "flatten" the spherically symmetric Weyl metal by setting $p_z = 0$. However, in general, the two formulas differ. While the modes of anomalous Rabi oscillation in graphene always manifest themselves in a form that resembles massive Dirac particles (with mass $\sim \frac{2\omega_R^2}{\omega}$), in Weyl metals, we see a form that resembles massless Dirac particles at certain points in the reciprocal space. This conclusion follows from the observation of eq.(2.22).

For instance, in the vicinity of the point $p_x = 0$, $p_y = 0$ and $v_F p_z \sim \frac{\omega_R'^2}{\omega}$ in reciprocal space, we see that the anomalous Rabi frequency is a linear function of p_z, indicating the presence of massless modes (shown in fig.(2.1) and fig.(2.2)). On the other hand, if $p_x, p_y \neq 0$, then these modes acquire a "mass" equal to $v_F|p_\parallel|$. This is unlike in graphene where anomalous Rabi oscillations are always "massive".

2.4.2 Resonance Case(RWA)

Close to conventional resonance, we may solve the Weyl equation by the usual method described in many books on quantum optics [49, 157]. In the general case, we obtain a value for the conventional Rabi frequency as $\Omega_{RWA} = \sqrt{\delta'^2 + \omega_R^2}$, where the conventional Rabi frequency ω_R comes out as

$$\omega_R = \frac{ev_F}{c}\left(\mathbf{A}_0^* \cdot \mathbf{A}_0 + \frac{i}{|\mathbf{p}|}\mathbf{p} \cdot (\mathbf{A}_0^* \times \mathbf{A}_0) - \frac{|(\mathbf{A}_0 \cdot \mathbf{p})|^2}{p^2}\right)^{\frac{1}{2}}, \tag{2.23}$$

where $\delta' = \left(\omega - 2v_F\sqrt{p_\parallel^2 + p_z^2}\right)$ is the detuning. We now want to study the effects of polarization as done in the earlier ARWA subsection. For this we use the same field configurations used earlier in case of ARWA : i.e. $A_{x0} = A_{x0}^* = A$, $A_{y0} = Ae^{i\gamma}$, $A_{y0}^* = Ae^{-i\gamma}$ and $A_{z0} = 0, A_{z0}^* = 0$. In this case,

$$\omega_R = \frac{ev_F}{c}\left(A^2 - \frac{2p_z}{p}A^2 \sin\gamma + \frac{p_z^2 A^2 - 2p_x p_y A^2 \cos\gamma}{p^2}\right)^{\frac{1}{2}}. \tag{2.24}$$

A choice of $\gamma = 0$ leads to an expression which is not particularly illuminating since it does not enable a straightforward comparison with the graphene result. The above peculiar result (eq.(2.24)) is because a choice of $\gamma = 0$ leads to a vector potential that points midway between the x and y axes which explains the origin of a term involving $p_x p_y$. To get rid of this we could choose $\gamma = \infty$ which is also

linear polarization but this choice makes $A_{y0} = 0$ (since $e^{i\gamma}$ averages out to zero due to rapid oscillations) and $A_{x0} = A$ and therefore $\omega_R = \frac{ev_F}{c}\left(A^2 + \frac{p_z^2 A^2}{p^2}\right)^{\frac{1}{2}}$. Lastly, setting $p_z = 0$ makes the system truly two dimensional and we expect the result to be identical to that of graphene and indeed it is $\Omega_{RWA} = \sqrt{\delta'^2 + \left(\frac{ev_F A}{c}\right)^2}$ [152]. A choice of $\gamma = \frac{\pi}{2}$ corresponding to circular polarization leads to $\omega_R = \frac{ev_F A}{c}\left(1 - \frac{p_z}{p}\right)$.

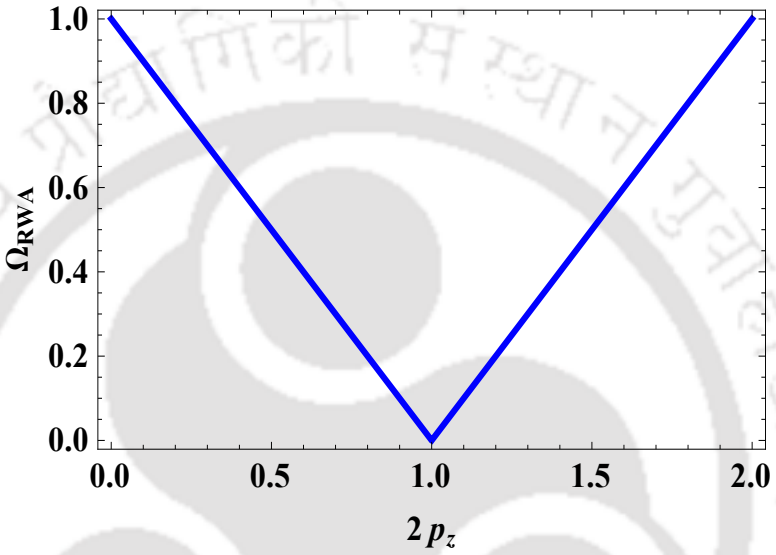

FIGURE 2.3: Plot of conventional Rabi frequency from eq.(2.25) is shown for circularly polarized light. Parameters are plotted in units of ω and for plotting we consider $\frac{\omega_R'}{\omega} = 0.1$, $v_F = 1$ and $\hbar = 1$. As before, in the first plot the values of p_x and p_y are zero.

Unlike in graphene, where the conventional Rabi frequency has a form identical to that seen in two-level systems and semiconductors close to resonance - in Weyl metals, as we may see from the formulas above, this quantity shows a pronounced anisotropy in the reciprocal lattice space near the Weyl nodes. As pointed out earlier, this may be attributed to a combination of the three dimensional nature of the reciprocal space and the transverse nature of the electromagnetic field - a feature not shared by graphene since both the graphene sheet and the plane electromagnetic wave being two dimensional, lead to an isotropic conventional Rabi frequency. As usual, setting $p_z = 0$ renders the system effectively two dimensional and we recover the familiar result viz. $\Omega_{RWA} = \sqrt{\left(\delta'^2 + \omega_R'^2\right)}$. More interestingly, setting $p_x = p_y = 0$ causes the conventional Rabi frequency of the Weyl metal to

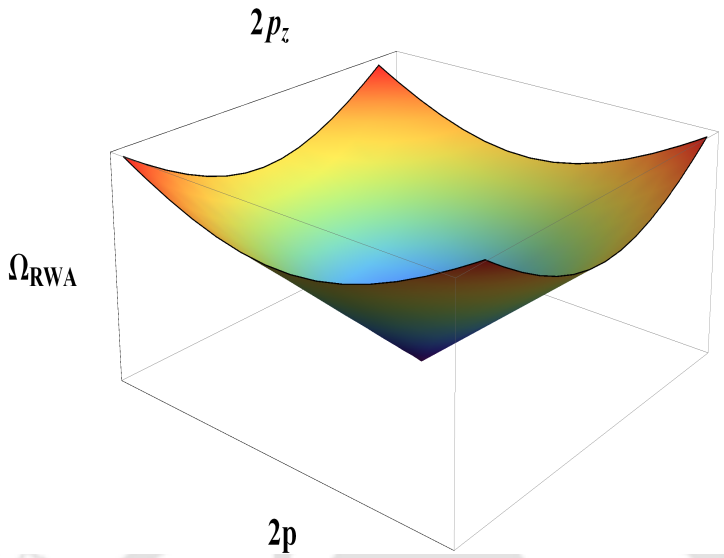

FIGURE 2.4: 3D plot of conventional Rabi frequency (qualitatively) from eq.(2.25) is shown for circularly polarized light.

take on a massless character (shown in fig.(2.3) and fig.(2.4)).

$$\Omega_{RWA}(p_x = 0, p_y = 0) = \Big|\omega - 2v_F|p_z|\Big|;$$
$$\Omega_{RWA} = \sqrt{\delta'^2 + \omega_R'^2 \left(1 - \frac{p_z}{p}\right)^2}. \tag{2.25}$$

Which indicates that the Rabi frequency at conventional resonance is zero and close to it, the dispersion relation of the quanta of conventional Rabi oscillations are linear instead of being parabolic, indicating the presence of massless modes.

2.5 Fully Numerical Solution

In this section, we wish to ascertain unequivocally that the phenomenon of anomalous Rabi oscillation is not an artifact of the approximations used. The only way to do this is to solve e.g. the Floquet-Bloch equations fully numerically and examine the plots for slowly oscillating amplitudes and verify that their frequency matches the one shown in eq.(2.21). This has been done in this section and an inspection of the table (2.1) shows that the approximation scheme we are using viz. ARWA is indeed reliable. The Floquet-Bloch equations are,

$$i\frac{d}{dt}n_{diff}(\mathbf{p}, t) = 2v_F\boldsymbol{\sigma}_{AB} \cdot \left(\mathbf{p} - \frac{e}{c}\mathbf{A}^*(t)\right) P(\mathbf{p}, t) - c.c.\ , \tag{2.26}$$

$$i\frac{d}{dt}P(\mathbf{p},t) = v_F\boldsymbol{\sigma}_{BA}\cdot\left(\mathbf{p}-\frac{e}{c}\mathbf{A}(t)\right)n_{diff}(\mathbf{p},t) + v_F\boldsymbol{\sigma}_{BB}P(\mathbf{p},t), \tag{2.27}$$

where $v_F\boldsymbol{\sigma}_{AB}\cdot\mathbf{p} = v_F(p_x - ip_y)$, $v_F\boldsymbol{\sigma}_{BB}\cdot\mathbf{p} = v_Fp_z$, $n_{diff}(\mathbf{p},t) = \psi^\dagger_\uparrow(\mathbf{p},t)\psi_\uparrow(\mathbf{p},t) - \psi^\dagger_\downarrow(\mathbf{p},t)\psi_\downarrow(\mathbf{p},t)$, $P(\mathbf{p},t) = \psi^\dagger_\downarrow(\mathbf{p},t)\psi_\uparrow(\mathbf{p},t)$. The time period of slow oscillations of

$\frac{v_Fp_z}{\omega}$	Time Period (fully analytical)	Time Period (fully numerical)
0.350	1.67	1.74
0.400	2.5	2.45
0.450	5.0	5.14
0.550	5.0	5.15
0.600	2.5	2.54
0.650	1.67	1.69

TABLE 2.1: Time periods are in units of $\frac{2\pi\omega}{\omega_R'^2}$ and $v_Fp_\parallel = (0.002)\frac{\omega_R'^2}{\omega}$.

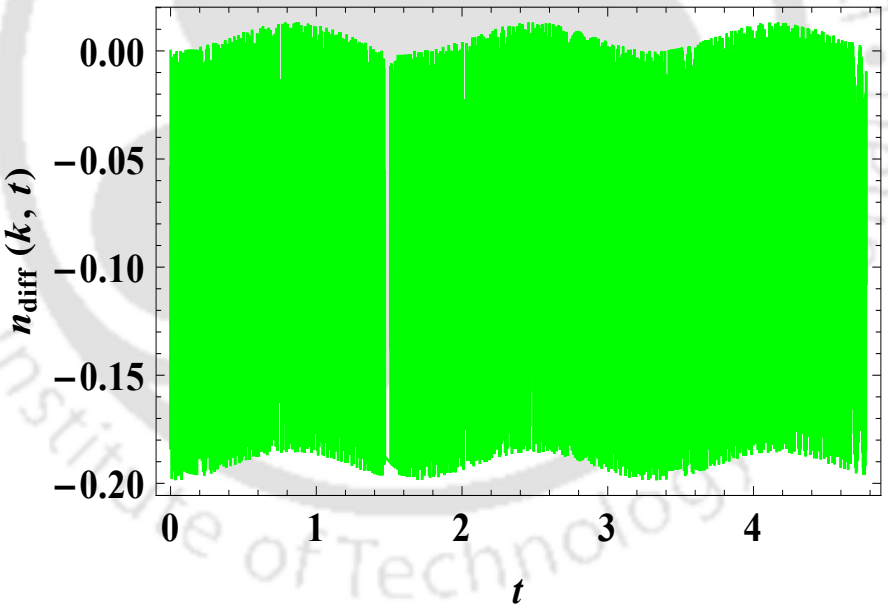

FIGURE 2.5: Slow oscillations plot correspond to an anomalous Rabi frequency with theoretical periods of 1.67 $\left(\text{time is in unit of } \frac{2\pi\omega}{\omega_R^2}\right)$.

these observables are tabulated in table(2.1), both by solving the above Floquet-Bloch equations fully numerically using the NDSolve routine of Mathematica [184] and also by the analytical approach described earlier. The analytical calculation for the time period is the reciprocal of eq.(2.21).

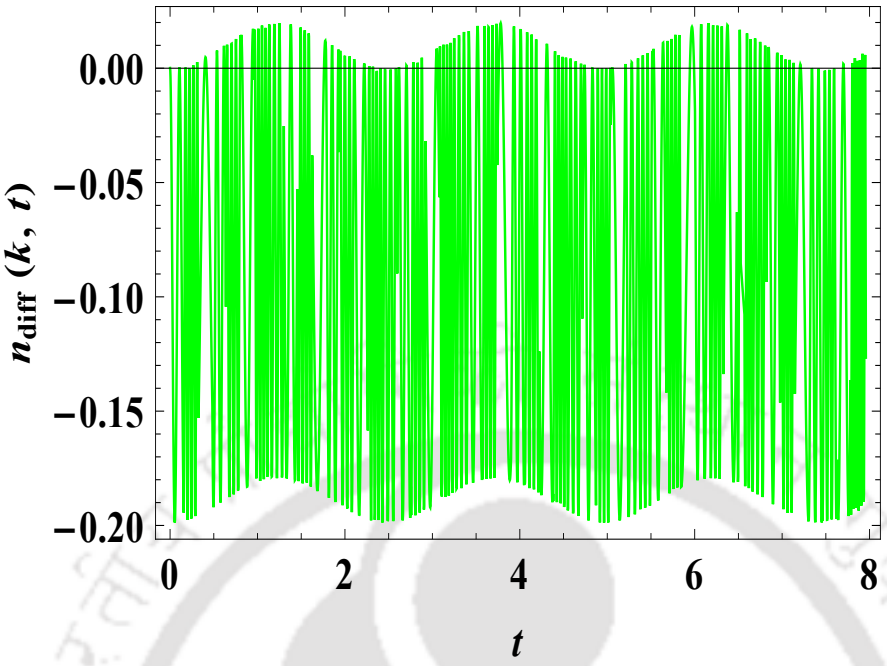

FIGURE 2.6: Slow oscillations plot correspond to an anomalous Rabi frequency with theoretical periods of 2.5 $\left(\text{time is in unit of } \frac{2\pi\omega}{\omega_R^2}\right)$.

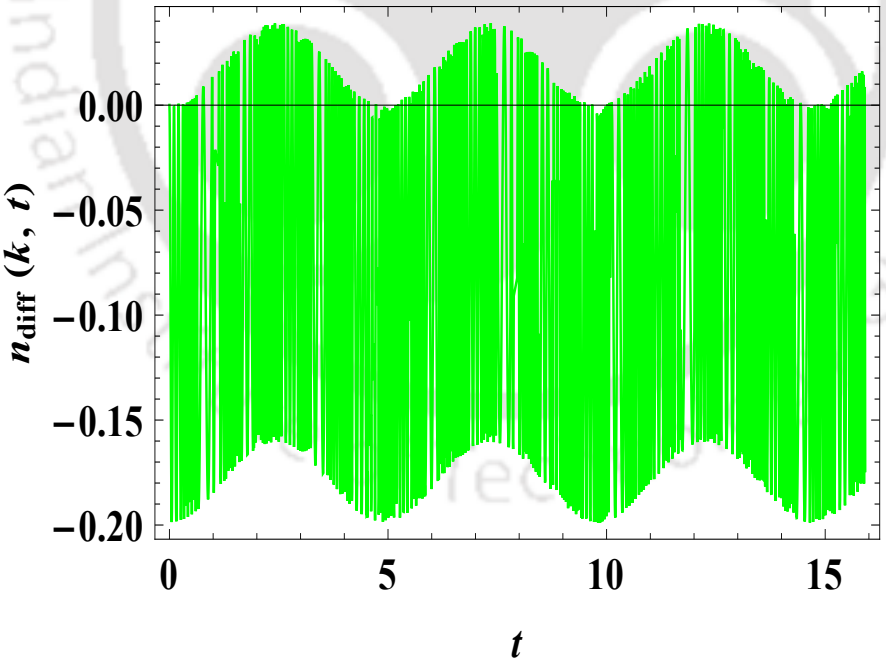

FIGURE 2.7: Slow oscillations plot correspond to an anomalous Rabi frequency with theoretical periods of 5.0 $\left(\text{time is in unit of } \frac{2\pi\omega}{\omega_R^2}\right)$.

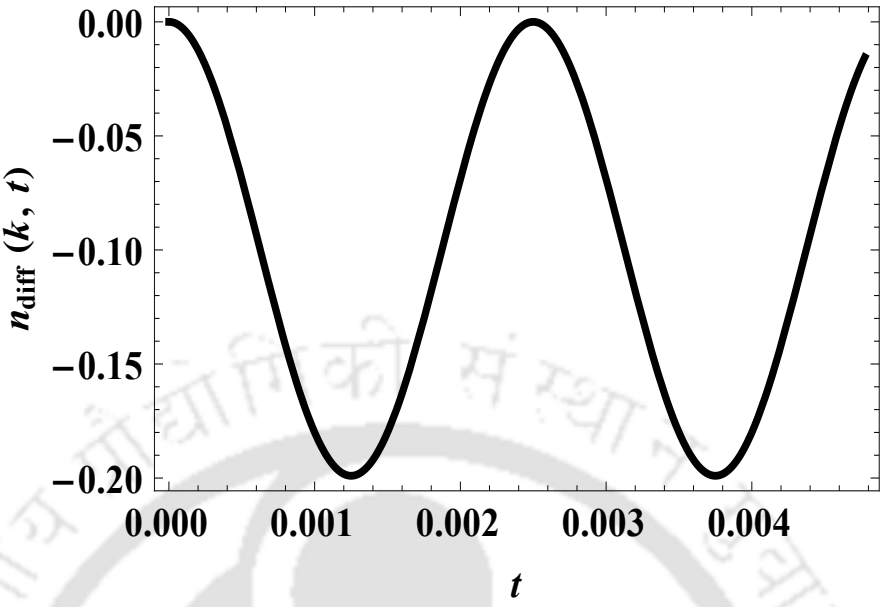

FIGURE 2.8: This plot depicts fast oscillations in earlier plots that makes the latter appear to have a thick green line. The fast oscillations have a frequency equal to the frequency of external radiation, time is in unit of $\frac{2\pi\omega}{\omega_R^2}$.

2.6 Surface States in a 3D Topological Insulator

In this section, we study anomalous Rabi oscillations on the surface of 3D TI. In this case, the wavevector dependence of the Rabi frequencies is going to be anisotropic, due to the coupling of the electron spin to the applied a.c. magnetic field (EM field). It is interesting that this anisotropy also leads to a vanishing Rabi frequency at certain points in the reciprocal space. Furthermore, the qualitative behavior of the Rabi frequency in the vicinity of these points is unique as well. In case of graphene, spin orbit coupling is very weak [78, 185, 186] so we do not need to consider the Zeeman term, but in case of TI it is quite strong [80, 146, 187], so we cannot neglect it.

The two-dimensional Hamiltonian for these Dirac fermions with hybridization due to quantum tunneling between the top and bottom surfaces of the bulk TI is given by [188, 189]

$$H = \int d^2r\ \psi^\dagger(\mathbf{r}) \left[v_F \tau_z (\hat{z} \times \sigma).\left(\mathbf{p} + \frac{e}{c}\mathbf{A}\right) + \boldsymbol{\Delta}\cdot\boldsymbol{\sigma} + \Delta_t \tau_x \right] \psi(\mathbf{r}). \tag{2.28}$$

Here Δ_t is the hybridization matrix element between the states of the top and bottom surfaces of the TI [190]. Its value depends on the thickness of the 3D TI, a typical value of Δ_t varies from 0 to 10^2 meV depending on the thickness

of the 3D TI [191]. The Pauli matrices σ and τ describe the real spin and the surface pseudospin degrees of freedom. The Zeeman energy is the projection of $\mathbf{\Delta} = \frac{1}{2}g\mu_B\mathbf{B}(t) = \frac{1}{2}\mathbf{\Delta}_0\, e^{i\omega t} + \frac{1}{2}\mathbf{\Delta}_0^*\, e^{-i\omega t}$ on the spin, where g is the effective Lande-g factor and μ_B is the Bohr magneton. We also write the vector potential as $\mathbf{A}(t) = \frac{1}{2}\mathbf{A}_0\, e^{i\omega t} + \frac{1}{2}\mathbf{A}_0^*\, e^{-i\omega t}$ so that $\mathbf{\Delta}_0 = \frac{1}{2}g\mu_B(-i\mathbf{k}\times\mathbf{A}_0)$. Without loss of generality we may assume that the surfaces of the TI are in the $x-y$ plane.

We wish to study anomalous Rabi oscillations in this system. The technique of ARWA we use may be described mathematically as the limit $\omega\to\infty$, $|p|\to 0$ and $\Delta_t\to 0$ in such a way that $\omega\Delta_t = \kappa < \infty$ and $\omega v_F|p| = \delta < \infty$. Physically, ARWA is the regime where $v_F|p| << \omega$. This in contrast to the conventional RWA which mathematically may be described as the limit $\omega, v_F|p|\to\infty$ in such a way that the detuning $\delta' \equiv |\omega - 2v_F|p|| < \infty$. Physically, RWA is the regime where $2v_F|p| \sim \omega$. In the results that follow, the ARWA frequency may be written as $\Omega_{ARWA} = \frac{\omega_{red}^2}{\omega}$ where, mathematically, ω_{red} remains fixed as ω is made large.

We first focus on the case of linear polarization. We have seen in earlier works that anomalous Rabi oscillations are absent in two-dimensional graphene when radiation is linearly polarized. Here too the situation is similar except that the hybridization induces an intrinsic frequency scale which cannot be thought of Rabi oscillation. In presence of hybridization it may be seen that,

(i) EM Wave propagation $\mathbf{k}$ in z direction, $\mathbf{A}_0$ in x direction, $\mathbf{\Delta}_0$ in y direction then, $\Omega_{ARWA} = \sqrt{\Delta_t^2 + v_F^2(p_x^2+p_y^2)}$.

(ii) EM wave propagation $\mathbf{k}$ in x direction, $\mathbf{A}_0$ in y direction, $\mathbf{\Delta}_0$ in z direction. Here $\omega_R' = \frac{ev_F}{c}A$ is the scale of the conventional Rabi frequency and A is the magnitude of the vector potential then

$$\Omega_{ARWA} = \sqrt{\left(v_F p_x - \frac{g\mu_B\omega_R'^2}{2ev_F}\right)^2 + \Delta_t^2 + v_F^2 p_y^2}. \tag{2.29}$$

The anisotropic dependence of the frequency on the wave vector due to the coupling of the spin with the magnetic field is clearly seen. We may also note that in a system with vanishing hybridization (thick samples) and in the region $v_F p_y = 0$, this frequency has a massless character i.e., the dispersion relation with the remaining component p_x is linear and the frequency vanishes at $v_F p_x = \frac{g\mu_B\omega_R'^2}{2ev_F} \equiv \epsilon_0$ which is the Zeeman energy scale, rather than at $v_F p_x = 0$. To be consistent, we have to ensure that this point is in the ARWA regime. This is possible only if $\frac{g\mu_B\omega_R'^2}{2ev_F} << \omega$. The table 2.2 assures us that this is the case. Next, we focus on

Quantity	Numerical value
$\nu = \frac{\omega}{2\pi}$	$500 \times 10^{12} Hz$
$\omega = 2\pi\nu$	$3.14 \times 10^{15} Hz$
E_{max}	750×10^{5}statvolt/cm
ω_R	$1.21 \times 10^{13} rad/sec$
$\frac{\omega_R}{\omega}$	3.85×10^{-3}
v_F	$1 \times 10^{8} cm/sec$
e	4.80×10^{-10} statcoulombs
$\frac{\epsilon_0}{\omega}$	9.0×10^{-9}

TABLE 2.2: Table of realistic numerical values of parameters used.

the case of circular polarization and grazing incidence (direction of propagation radiation is taken to be x-direction and the surfaces are in the xy plane). In graphene, in this case, no anomalous Rabi oscillations are seen. However, in the present example, we do see anomalous Rabi oscillations with an anisotropic dependence on the wavevector due to the coupling of spin with the magnetic field (EM field).

(iii) EM wave propagation in x-direction (grazing incidence) with beam circularly polarized in the $y-z$ plane. In this case, we see two branches in the anomalous Rabi frequency

$$\Omega_{ARWA} = \frac{1}{\omega}\left[\pm\frac{2(\epsilon_0\omega)^2}{\omega_R'^2}\sqrt{\kappa^2+\delta^2\frac{p_y^2}{p^2}} + (\epsilon_0\omega)^2\left[1+\left(\frac{\epsilon_0\omega}{\omega_R'^2}\right)^2\right] + 2\delta(\epsilon_0\omega)\frac{p_x}{p} + \kappa^2 + \delta^2\right]^{\frac{1}{2}}, \tag{2.30}$$

where $\left(\epsilon_0 = \frac{g\mu_B\omega_R'^2}{2ev_F}\right)$. The form of eq.(2.30) is quite illuminating. From case **(ii)** we know that $\epsilon_0 \sim v_F p_x \to 0$ in the limit $\omega \to \infty$ such that $0 < \epsilon_0\omega < \infty$. Of course in ARWA: $0 < \kappa, \delta < \infty$ as $\omega \to \infty$. Hence the form of eq.(2.30) is consistent with ARWA which demands $\Omega_{ARWA} \sim \frac{const.}{\omega}$ as $\omega \to \infty$. In addition, the anisotropic dependence of this Rabi frequency on the wavevector is also apparent. It is interesting to consider the special case of vanishing hybridization $\kappa = 0$ and $v_F p_y = 0$. In this case

$$\Omega_{ARWA} = \sqrt{\left(\frac{z_0^2}{\omega}\right)^2 + (v_F p_x + \epsilon_0)^2}, \tag{2.31}$$

where $z_0 = \frac{\epsilon_0\omega}{\omega_R'}$. In this case we see that there is a nonvanishing minimum anomalous Rabi frequency viz. $\frac{z_0^2}{\omega}$. This minimum is not at the Dirac point $p_x = p_y = 0$ but shifted relative to this point $v_F p_x = -\epsilon_0$. This is a feature we also saw in

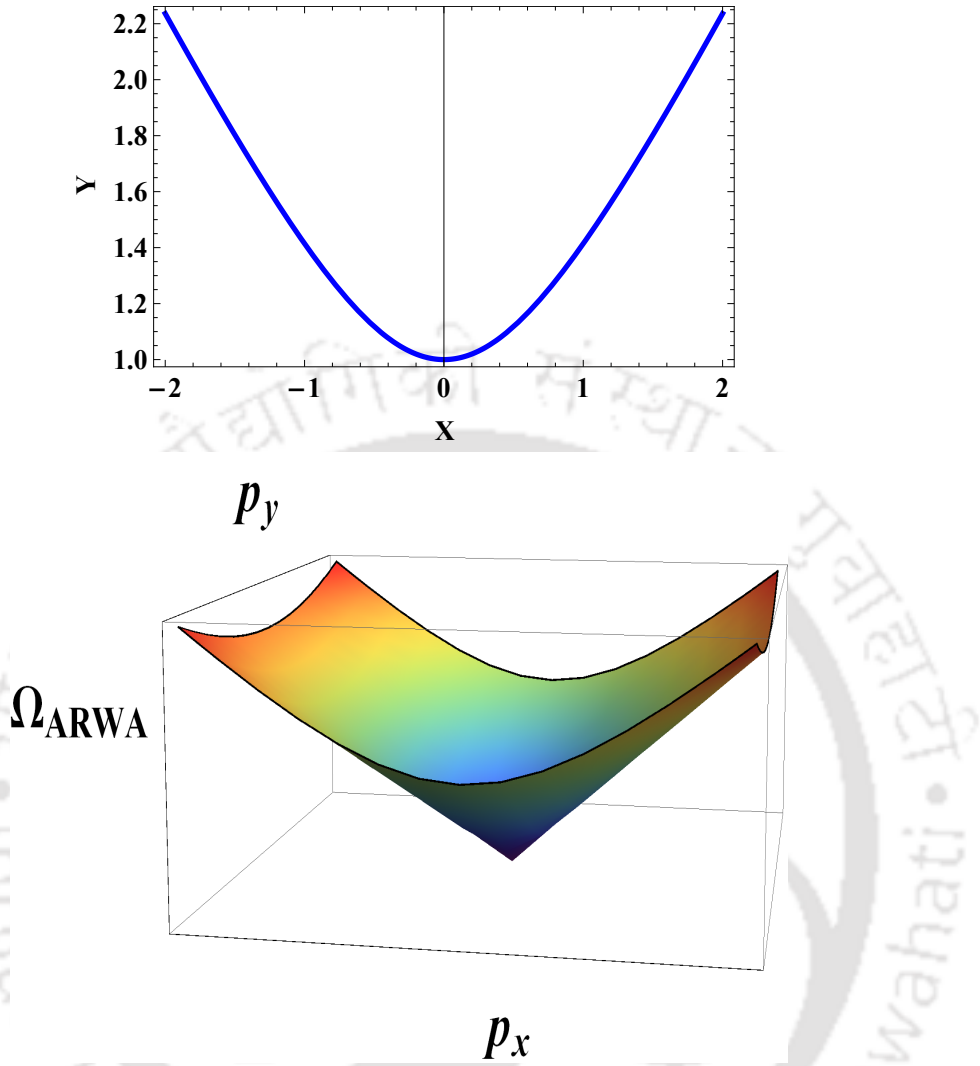

FIGURE 2.9: Top figure demonstrates (eq.(2.31)) the anomalous Rabi frequency versus the x-component of the wavevector when the y-component is made zero. Even though the plot amplifies the massive character of this Rabi mode, it is nearly massless and the small non-zero minimum value is due to the Zeeman energy. The labels in this plot are $Y = \frac{\Omega_{ARWA}}{5.45\times10^{-12}\omega}$, $\frac{v_F p_x}{\omega} = 5.45 \times 10^{-12}\,(X - 1652.0)$. The 3D plot on the bottom (eq.(2.32)) depicts the massless Dirac-like cone of the anomalous Rabi frequency at a shifted point in the wavevector space determined by the Zeeman energy scale.

Weyl materials but not in graphene. We may think of this feature as a kind of intrinsic Bloch-Siegert shift [175] not brought about by frequency doubling or the inclusion of counter rotating terms, but by the Zeeman term. In general however, whenever hybridization may be ignored. So

$$\Omega_{ARWA} = \frac{\sqrt{\left(\omega v_F p_y + \frac{(\epsilon_0\omega)^2}{\omega_R'^2}\right)^2 + \omega^2(v_F p_x + \epsilon_0)^2}}{\omega}. \tag{2.32}$$

A plot of eq.(2.32) shows the massless character of the Rabi modes on the surface

of topological insulators in the special case of grazing incidence and circularly polarized light in the vicinity of the point $(v_F p_x, v_F p_y) = \left(-\epsilon_0, -\frac{(\epsilon_0\omega)^2}{\omega\omega_R'^2}\right)$. Lastly, we focus on the case of circular polarization but normal incidence.

(iv) In the case of circular polarization and normal incidence, the anomalous Rabi frequency $\sqrt{\left(\frac{\omega_{R,*}^2}{\omega}\right)^2 + (v_F p)^2}$ is isotropic and closely resembles the form seen in graphene, where $\omega_{R,*} = \sqrt{\omega_R'^2 \pm \Delta_t\omega + \left(\frac{\epsilon_0\omega}{\omega_R'}\right)^2}$.

As a comparison, we now wish to study conventional Rabi oscillations in this system as well. As usual, the interesting phenomena take place when the hybridization is vanishingly small ($\Delta_t = 0$). It so happens that this limit is mathematically simpler as well. In the case studied earlier viz. grazing incidence and circular polarization, and when in addition we set $v_F p_y = 0$, the *anomalous* Rabi frequency is given by eq.(2.31) which shows that the small mass in these modes is purely due to the Zeeman term and it is massless when the Zeeman term is absent. On the other hand, in this case, the conventional Rabi frequency is found to be

$$\Omega_{RWA} = \sqrt{\left(\omega_R' \pm \frac{\epsilon_0\omega}{\omega_R'}\right)^2 + \delta'^2}, \tag{2.33}$$

where $\delta' = \omega - 2v_F p$ is the detuning. This eq.(2.33) shows that the modes are massive even in the absence of the Zeeman term. This observation reinforces the point we have made in our earlier works as well, viz. it is the *anomalous* Rabi oscillation that is sensitive to qualitative changes in the low-energy band structure rather than the conventional Rabi oscillation.

2.7 Conclusions

The main idea we have been trying to promote is - the presence of two distinct resonances in the "Rabi Landscape" which is the plot of the generalized Rabi frequency versus the wave vector. The resonances are local minima in this plot. Unlike in graphene, where the conventional Rabi frequency has a form identical to those seen in two-level systems and semiconductors close to resonance - in Weyl metals, this quantity shows a pronounced anisotropy in reciprocal space near the Weyl nodes. This may be attributed to a combination of the three-dimensional nature of the Brillouin zone and the transverse nature of the electromagnetic field- a feature not shared by graphene since both the graphene sheet and the plane electromagnetic wave being two dimensional, lead to an isotropic conventional Rabi

frequency. In Dirac fermion systems, in addition to the conventional resonance located at the usual spot namely when the energy of the external photon matches the particle-hole energy, there is an anomalous resonance close to the Dirac points and far from conventional resonance. In Weyl metals and surface states of topological insulators, the location in wave vector space of this anomalous resonance is sometimes seen to be shifted relative to its location in graphene. Moreover, unlike in graphene, where the anomalous Rabi frequency has a non-zero minimum value, in these systems, this minimum value vanishes making the modes of anomalous Rabi oscillations themselves ultra-relativistic.

In the surface states of topological insulators, the presence or absence of the Zeeman term has no qualitative impact on conventional Rabi oscillations. However, it has a qualitative effect on *anomalous* Rabi oscillations despite the smallness of the Zeeman energy scale relative to the conventional Rabi energy. The qualitative effect includes making the anomalous Rabi modes massless if the Zeeman term is absent.

The presence of anomalous Rabi oscillations in Dirac-Weyl systems have been unequivocally demonstrated in this work and earlier works by a fully numerical solution of the Floquet-Bloch equations. The detailed quantitative and qualitative agreement with these numerical simulations with the analytical method introduced to study this new phenomenon viz. asymptotic rotating wave approximation (ARWA) validates these analytical schemes and conclusions that are drawn using them.

Therefore, it is no exaggeration to say that the anomalous Rabi oscillation is a phenomenon that is uniquely suited to study condensed matter realizations of relativistic systems.

We have proposed a pump-probe experiment to detect anomalous Rabi oscillation (chapter 4). This simply involves looking for periodic oscillations in the differential transmission coefficient versus pump pulse duration. When all else remains fixed (including pump-probe delay), this plot exhibits oscillations with a frequency corresponding to the anomalous Rabi frequency.

2.8 Appendix

2.8.1 Methods for Obtaining Anomalous Rabi Frequency

2.8.1.1 Current Density Method

1. With the help of Heisenberg's equation (Bloch equation in optics) ($i\hbar\frac{\partial}{\partial t}\langle\hat{O}\rangle = \langle[\hat{H},\hat{O}]\rangle$) followed by anti-commutation relations ($\{\hat{x},\hat{y}\} = \hat{x}\hat{y}+\hat{y}\hat{x}$), we have derived the equation of motion for the following physical quantities,

$$n_{diff}(\boldsymbol{k},t) = n_A(\boldsymbol{k},t) - n_B(\boldsymbol{k},t) = \langle c^{\dagger}_{k,A}(t)c_{k,A}(t)\rangle - \langle c^{\dagger}_{k,B}(t)c_{k,B}(t)\rangle, \quad (2.34)$$

and

$$p(\boldsymbol{k},t) = \langle c^{\dagger}_{k,A}(t)c_{k,B}(t)\rangle. \quad (2.35)$$

where, $n_{diff}(\boldsymbol{k},t)$ is the population excess between sublattice 'A' and sublattice 'B' in graphene or spin up $\uparrow$ or spin down $\downarrow$ for TI of Weyl semimetal and $p(\boldsymbol{k},t)$ is defined as polarization density in similar way.

2. First we try to solve the unknowns in the problem namely the population excess $n_{diff}(\boldsymbol{k},t)$ and polarization density $p(\boldsymbol{k},t)$, by expressing them as a harmonic series involving the largest of the frequencies, viz. the frequency of the applied field ω. We consider the coefficients as slowly varying, compared to ω. We assert that the external driving frequency ω is always much greater Rabi frequency ω_R which we assume is, in turn, much greater than the 'resonant' frequency for the creation of particle hole pairs namely $2v_F|k|$ ($\omega >> \omega_R >> 2v_F|k|$). Now we assume number density $n_{diff}(\boldsymbol{k},t)$ and polarization density $p(\boldsymbol{k},t)$ in term of slow and fast part

$$n_{diff}(\boldsymbol{k},t) = n_s(\boldsymbol{k},t) + n_+(\boldsymbol{k},t)e^{-i\omega t} + n_-(\boldsymbol{k},t)e^{i\omega t}, \quad (2.36)$$

$$p(\boldsymbol{k},t) = p_s(\boldsymbol{k},t) + p_+(\boldsymbol{k},t)e^{-i\omega t} + p_-(\boldsymbol{k},t)e^{i\omega t}. \quad (2.37)$$

Here $n_s(\boldsymbol{k},t)$ and $p_s(\boldsymbol{k},t)$ are slow part. n_+, n_-, p_+, p_- are fast part.

3. Now we compare slow and fast parts of equation from both sides, making equation of $i\frac{dn_s(\boldsymbol{k},t)}{dt}$, $i\frac{dp_s(\boldsymbol{k},t)}{dt}$, $i\frac{dn_\pm(\boldsymbol{k},t)}{dt}$ and $i\frac{dp_\pm(\boldsymbol{k},t)}{dt}$. We neglect $\frac{dX(\boldsymbol{k},t)}{dt}$ in comparison with $\omega\ X(\boldsymbol{k},t)$ and term of $O(\frac{1}{\omega^2})$, due large value of external

frequency ω in comparison with all other frequency scales. This enables us to recast these equations in terms of the slow parts only.

4. After solving these equations, the (anomalous) Rabi frequency is obtained in the off-resonance situation.

2.8.1.2 Wave Function Method

When we apply potential in form of $A_0 e^{\pm i\omega t}$ in Hamiltonian, it will change in following form

$$H = H_0 + e^{-i\omega t}\, V_+ + e^{i\omega t}\, V_-, \tag{2.38}$$

We can write wave function in harmonic series form

$$\psi = \psi_0 + e^{-i\omega t}\, \psi_+ + e^{i\omega t}\, \psi_- + ... \tag{2.39}$$

Here H_0 and ψ_0 are slow parts, while V_+, V_- and ψ_+, ψ_- are the (coefficients of) fast parts of the full Hamiltonian and wavefunction respectively. By evolution equation

$$i\frac{\partial}{\partial t}\psi = H\psi, \tag{2.40}$$

$$i\frac{\partial}{\partial t}(\psi_0 + e^{-i\omega t}\, \psi_+ + e^{i\omega t}\, \psi_-) = \left(H_0 + e^{-i\omega t}\, V_+ + e^{i\omega t}\, V_-\right) \left(\psi_0 + e^{-i\omega t}\, \psi_+ + e^{i\omega t}\, \psi_-\right), \tag{2.41}$$

$$i\frac{\partial}{\partial t}\left(\psi_0 + e^{-i\omega t}\, \psi_+ + e^{i\omega t}\, \psi_-\right) = H_0\left(\psi_0 + e^{-i\omega t}\, \psi_+ + e^{i\omega t}\, \psi_-\right) + e^{-i\omega t}\, V_+ \left(\psi_0 + e^{-i\omega t}\, \psi_+ + e^{i\omega t}\, \psi_-\right) + e^{i\omega t}\, V_-\left(\psi_0 + e^{-i\omega t}\, \psi_+ + e^{i\omega t}\, \psi_-\right), \tag{2.42}$$

$$i\frac{\partial}{\partial t}\left(\psi_0 + e^{-i\omega t}\, \psi_+ + e^{i\omega t}\, \psi_-\right) = H_0\left(\psi_0 + e^{-i\omega t}\, \psi_+ + e^{i\omega t}\, \psi_-\right) + V_+ \left(\psi_0 e^{-i\omega t} + e^{-2i\omega t}\, \psi_+ + \psi_-\right) + V_-\left(\psi_0 e^{i\omega t} + \psi_+ + e^{2i\omega t}\, \psi_-\right). \tag{2.43}$$

Coefficient of constant

$$i\frac{\partial}{\partial t}\psi_0 = H_0\ \psi_0 + \ V_+\ \psi_- + \ V_-\ \psi_+. \tag{2.44}$$

Coefficient of $e^{i\omega t}$ and taking ω is large

$$-\omega\ \psi_- = H_0\ \psi_- + \ V_-\psi_0 \Rightarrow \ \psi_- = -\left(\frac{V_-\psi_0}{\omega}\right). \tag{2.45}$$

Coefficient of $e^{-i\omega t}$ and taking ω is large

$$\omega\ \psi_+ = H_0\ \psi_+ + \ V_+\ \psi_0 \Rightarrow \ \psi_+ = \left(\frac{V_+\ \psi_0}{\omega}\right). \tag{2.46}$$

On substituting eq.(2.45) and eq.(2.46) in equation of constant eq.(2.44), we get

$$i\frac{\partial}{\partial t}\psi_0 = H_0\ \psi_0 + \ V_+\ \psi_- + \ V_-\ \psi_+, \tag{2.47}$$

$$i\frac{\partial}{\partial t}\psi_0 = H_0\ \psi_0 - \ V_+\ \left(\frac{V_-\psi_0}{\omega}\right) + \ V_-\ \left(\frac{V_+\ \psi_0}{\omega}\right), \tag{2.48}$$

$$i\frac{\partial}{\partial t}\psi_0 = H_0\ \psi_0 + \frac{\psi_0}{\omega}\left(-\ V_+\ V_- + \ V_-\ V_+\right), \tag{2.49}$$

$$i\frac{\partial}{\partial t}\psi_0 = H_0\ \psi_0 + \frac{\psi_0}{\omega}\Big[V_-,\ V_+\Big], \tag{2.50}$$

$$i\frac{\partial}{\partial t}\psi_0 = \left(H_0\ + \frac{1}{\omega}\Big[V_-,\ V_+\Big]\right)\psi_0, \tag{2.51}$$

$$i\frac{\partial}{\partial t}\psi_0 = H_{eff}\ \psi_0. \tag{2.52}$$

So we define

$$H_{eff} = \left(H_0\ + \frac{1}{\omega}\Big[V_-,\ V_+\Big]\right). \tag{2.53}$$

The eigenvalue of H_{eff} will be anomalous Rabi frequency.

2.8.1.3 Fourier Transform method

1. First we take Bloch eqution and solve this using the Fourier transform method,

$$X(t) = \int_{-\infty}^{\infty} \frac{d\omega^{'}}{2\pi} e^{-i\omega^{'}t}\ \tilde{X}(\omega^{'}), \tag{2.54}$$

   where $X = p, n_{diff}$.

2. We neglect a term such as $\tilde{X}(\omega \pm 2\omega^{'})$ i.e. leaving higher order harmonics $\tilde{X}(\omega \pm 3\omega^{'})$ and others. The equation for $\omega^{'}$ we obtain will be of the form, $W(\omega^{'}, \omega, \omega_R, |z_k|) = 0$,$z_k = v_F \boldsymbol{\sigma}_{AB} \cdot \boldsymbol{k} = v_F(k_x - ik_y)$ for graphene . In this case we find $lim_{|z_k|\to\infty} W(\omega^{'}, \Delta + 2|z_k|, \omega_R, |z_k|)$, holding $\Delta \equiv \omega - 2|z_k|$ fixed, and then set this function to zero. This leads to an expression for the conventional Rabi frequency $\omega^{'}$.

3. For studying off resonance case i.e. ARWA limit, we hold $c^2 = |z_k|^2\omega^2$ and ω_R fixed, $\omega^{'} = \frac{\omega^{''}}{\omega}$ and find $lim_{\omega\to\infty} W(\frac{\omega^{''}}{\omega} + \omega, \omega, \omega_R, \frac{c}{\omega})$ and setting this function to zero, we get value of $\omega^{'}$ will be anomalous Rabi frequency.

2.8.1.4 Numerical Simulation Method

We can also solve above Bloch equations fully numerically using the NDSolve routine of Mathematica [184], we obtain results for both types of Rabi frequency which exactly matches with the result obtained earlier using analytical method.

Chapter 3

Band-Anisotropy Induced Bloch-Siegert Shift in Graphene

3.1 Introduction

The periodic exchange of energy between a radiation field and a two-level system is known as (conventional) Rabi oscillation [19]. The population and polarization of carriers oscillate with the frequency ω of the radiation field. The amplitude of these oscillations themselves oscillates much more slowly with a frequency $\omega_R << \omega$ known as the Rabi frequency [157]. Conventional Rabi oscillations are studied using the rotating wave approximation (RWA), which involves asserting that the detuning $\Delta \equiv \hbar\omega - \epsilon$ is much smaller than the transition energy, i.e. $|\Delta| << \epsilon$, where ϵ is the energy separation of the two levels (or in case of bands, it is the energy of the particle-hole pair) [49]. Semiconductors have bands instead of energy levels and there is a mixing of these energies due to long-range Coulomb interactions. This leads to, among other effects, the phenomenon of excitonic quantum beats and excitonic optical Stark effect [158–162, 192–196].

Graphene was first studied theoretically by P. R. Wallace [40] in 1946. Graphene is the first 2D material to be synthesized. Graphite can be built by stacking 2D graphene sheets one on top of another separated by a distance of $0.335nm$. Graphene is a honeycomb lattice formed by two interpenetrating triangular sublattices. It was made by micromechanical cleavage of graphite in 2004. The energy versus momentum relation for graphene shows a linear dispersion near the six corners of the two-dimensional hexagonal Brillouin zone. The most peculiar property of graphene is that at low energies, electrons and holes near these six points, two

of which are inequivalent, behave like massless relativistic particles described by the Dirac equation for spin 1/2 particles. The six corners of the Brillouin zone are called the Dirac points [22, 23]. As we move further away from the Dirac points, the energy dispersion becomes both nonlinear in the momentum as well as anisotropic.

Band anisotropy in single layer graphene has another possible origin known as the Rashba effect [70, 197–199]. Single layer graphene on a substrate, lacks inversion symmetry in a direction perpendicular to the plane of the graphene sheet. The lack of inversion symmetry may be taken into account by postulating an effective electric field perpendicular to the graphene sheet. What is an electric field to a static electron, is also partly a magnetic field to a moving one and this magnetic field in turn couples to the intrinsic magnetic moment of the electron leading to the Rashba effect. This account is somewhat oversimplified [200] but will suffice for the present purposes. In the presence of Rashba spin orbit interaction, the low energy electronic bands of monolayer graphene deform and undergo trigonal-warping deformation for energies smaller than the Lifshitz energy [197]. At low energy, bilayer graphene also shows a very similar effect although for different reasons [201].

Graphene has an intrinsic pseudo-spin. Like ordinary spin that has two possible projections on any given axis, pseudo-spin also has two different eigenvalues that label the two triangular sublattices. Due to pseudo-spin, in the off-resonance case, a new kind of Rabi oscillation is seen which we refer to as anomalous Rabi oscillation (ARO). To study this, we employ an approximation known as asymptotic rotating wave approximation (ARWA) [152]. It appears that the ARO has already been seen in the experimental data of Breusing *et al* [63]. The pump probe spectra presented in this work has been theoretically derived [202].

Earlier works on Rabi oscillations in graphene by other authors such as Mishchenko [153], Mikhailov [164, 167, 203] and Ishikawa [154] have focussed on resonant excitations which are studied using the conventional rotating wave approximation. As we alluded to in the above paragraph, earlier works [152, 178, 202] have shown that in addition to these conventional Rabi oscillations, graphene also exhibits anomalous Rabi oscillations far from resonance. The present work is an attempt to extend the domain of validity of these works by exploring the consequences of a strong electromagnetic field on these Rabi oscillations.

3.2 Problem Formulation

In two-level systems, it is recognized that conventional Rabi oscillations undergo a shift in the resonant frequency which is the Bloch-Siegert shift. This shift is quite small in such systems and hence largely of academic interest. The present work shows that in graphene, such shifts can be substantial - especially upon the inclusion of band curvature effects and Rashbha coupling.

Both conventional and anomalous Rabi oscillations are resonance phenomena, in other words, the amplitude of these oscillations peak when the condition for resonance is obeyed. The purpose of this chapter is to study the shift in the conditions for resonance brought about by **(a)** the presence of strong fields upon the inclusion of frequency doubling effects or **(b)** band anisotropy due to next nearest neighbor hopping or Rashba effect. We refer to both these shifts as Bloch-Siegert shifts, although only **(a)** was envisaged by Bloch and Siegert.

Bloch and Siegert studied the behavior of a spin $\frac{1}{2}$ particle, in a constant field H_0 at magnetic resonance, by choosing an arbitrary alternating field with circular frequency ω perpendicular to H_0. They had shown that to lowest order, the correction to the shape of the resonance curve is constant but shifted by a percentage amount $\frac{H_1^2}{16H_0^2}$ where H_1 is the effective amplitude of the oscillating field. Due to that, there is a correction to the magnetic moment towards smaller values. This correction for all practical purposes, is too small [204]. The Bloch-Siegert shift is used to characterize the amplitude and homogeneity of the proton-decoupling field, and to monitor probe performance [205]. In the presence of a strong pump, on calculating the probe response of a homogeneously broadened two-level transition, using a generalized interaction Hamiltonian, one finds a common description of both the Bloch-Siegert shift and dynamic Stark splitting. The Bloch-Siegert shift can be viewed as an extreme situation of the dynamic Stark splitting, commonly known as a light shift in that literature [206]. In the limit of vanishing natural line width, Stenholm [207] derived exact semiclassical expressions for the generalized Bloch-Siegert shift of the main RF resonances. Their power series expansion has good agreement with quantum electrodynamic calculations, but a truncated continued fraction expression is shown to represent the exact values much better. The Bloch-Siegert shifts for multiphoton resonances at the inhomogeneous broadening of spectral lines reduce only the nutation amplitude but do not change their frequencies [208]. Beijersbergen *et al.* [209] observe multiphoton resonances and Bloch-Siegert shifts in a strongly driven classical two-level system which is an

optical ring resonator where the levels are two orthogonal linear polarizations. On measuring the Rabi frequency and the Bloch-Siegert shift for both the one- and three-photon cases it is shown that these coherent phenomena can be observed in a purely classical system. For measuring Bloch-Siegert shifts and widths of multiphoton resonances in a two-state system for the in-plane configuration of fields, Ostrovsky *et al.* [210] derive a convenient working formula. The final results have a simple form in case of a weak driving field. There is a drastic change in width compared to the conventional perpendicular field configuration, while the shift is only weakly affected.

Given this literature, it is fair to say that the Bloch-Siegert shift is an interesting problem to study. We study this problem in graphene especially with an anisotropic band structure and find several interesting features, the most prominent being a large Bloch-Siegert shift associated with anomalous Rabi oscillations in anisotropic graphene.

3.3 Bloch-Siegert Shift in a Two-level System

In this section, we revisit the well-known analysis of the Bloch-Siegert shift in two-level systems. This is described well in many books such as Allen and Eberly [157]. In order to maintain a close similarity with the discussion for graphene, we rephrase the problem in a two-level system as follows. Given a Hamiltonian

$$H = \frac{\hbar\omega_0}{2}\sigma_z - \hbar\kappa\mathcal{E}\sigma_x cos(\omega t), \tag{3.1}$$

that describes say a spin 1/2 particle in a constant magnetic field in the z-direction and a time varying electromagnetic field polarized in the x direction, the problem is to find the average magnetization.

$$\vec{M}(t) = \langle\Phi(t)|\boldsymbol{\sigma}|\Phi(t)\rangle. \tag{3.2}$$

It is usual to use the spherical vector form of the magnetization

$$M_0(t) = \langle\Phi(t)|\sigma_z|\Phi(t)\rangle; \quad M_\pm(t) = \langle\Phi(t)|\sigma_\pm|\Phi(t)\rangle, \tag{3.3}$$

where $\sigma_\pm = \sigma_x \pm i\sigma_y$. Here the state vector obeys

$$i\hbar\partial_t|\Phi(t)\rangle = \left(\frac{\hbar\omega_0}{2}\sigma_z - \hbar\kappa\mathcal{E}\sigma_x cos(\omega t)\right)|\Phi(t)\rangle. \tag{3.4}$$

Therefore,

$$i\hbar\partial_t M_0(t) = -\hbar\kappa\mathcal{E}\ cos(\omega t)(M_+(t) - M_-(t)), \tag{3.5}$$

$$i\hbar\partial_t M_\pm(t) = \mp\hbar\omega_0\ M_\pm(t) \mp 2\hbar\kappa\mathcal{E}cos(\omega t)M_0(t). \tag{3.6}$$

Instead of following the customary route of solving with rotating wave approximation, we use the Fourier transform method.

$$M_a(t) = \int_{-\infty}^{\infty}\frac{d\omega^{'}}{2\pi}\ e^{-i\omega^{'}t}\tilde{M}_a(\omega^{'}). \tag{3.7}$$

$$\begin{aligned}\hbar\omega^{'}\ \tilde{M}_0(\omega^{'}) = &-\frac{1}{2}\hbar\kappa\mathcal{E}\ \left(\tilde{M}_+(\omega^{'}+\omega) - \tilde{M}_-(\omega^{'}+\omega)\right)\\ &-\frac{1}{2}\hbar\kappa\mathcal{E}\ \left(\tilde{M}_+(\omega^{'}-\omega) - \tilde{M}_-(\omega^{'}-\omega)\right),\end{aligned} \tag{3.8}$$

$$\tilde{M}_\pm(\omega^{'}) = \mp\frac{\hbar\kappa\mathcal{E}}{\hbar(\omega^{'}\pm\omega_0)}\ \tilde{M}_0(\omega^{'}+\omega) \mp \frac{\hbar\kappa\mathcal{E}}{\hbar(\omega^{'}\pm\omega_0)}\ \tilde{M}_0(\omega^{'}-\omega). \tag{3.9}$$

These are coupled recursion relations with non-constant coefficients. They imply that $\omega^{'}$ takes a restricted number of values determined by the condition that non-trivial solutions to these homogeneous equations exist. However no exact solution is possible since the coefficients are not constants. Approximate solutions may be given by asserting that only a finite number of harmonics in ω are important. Practically, this means asserting that $\tilde{M}_0(\omega^{'}\pm n\omega) \equiv 0$ and $n \geq N$ for some N. The present exercise (see below) also shows that there is nothing like an anomalous Rabi oscillation in case of the two-level system. We define

$$\epsilon(\omega^{'}) = \left[\omega^{'} - \frac{(\kappa\mathcal{E})^2(\omega^{'}+\omega)}{[(\omega^{'}+\omega)^2-\omega_0^2]} - \frac{(\kappa\mathcal{E})^2(\omega^{'}-\omega)}{[(\omega^{'}-\omega)^2-\omega_0^2]}\right]. \tag{3.10}$$

Combining the equations (3.8), (3.9) and (3.10) into one means we have to deal with the following recursion relation for $\tilde{M}_0$.

$$\epsilon(\omega^{'})\ \tilde{M}_0(\omega^{'}) = \frac{(\kappa\mathcal{E})^2(\omega^{'}+\omega)}{[(\omega^{'}+\omega)^2-\omega_0^2]}\ \tilde{M}_0(\omega^{'}+2\omega) + \frac{(\kappa\mathcal{E})^2(\omega^{'}-\omega)}{[(\omega^{'}-\omega)^2-\omega_0^2]}\ \tilde{M}_0(\omega^{'}-2\omega). \quad (3.11)$$

The simplest case is to ignore second harmonics viz. set $\tilde{M}_0(\omega^{'}\pm 2\omega)=0$. In this case nontrivial solutions exist for $\omega^{'}$ such that

$$\epsilon(\omega^{'})=0. \quad (3.12)$$

Of the five solutions, the one that is positive and reduces to the rotating wave approximation (RWA) result in the limit $|\Delta|=|\omega-\omega_0| << \omega_0$ is

$$\omega^{'}=\sqrt{(\kappa\mathcal{E})^2+\omega^2+\omega_0^2-\sqrt{(\kappa\mathcal{E})^4+4\omega^2\omega_0^2}}. \quad (3.13)$$

In the RWA limit, this reduces to

$$\omega^{'}=\sqrt{(\Delta^2+(\kappa\mathcal{E})^2)-\frac{(\kappa\mathcal{E})^4}{(2\omega_0)^2}+...} \quad (3.14)$$

Now we are entitled to ask what happens in the other extreme case - the limit we have referred to as asymptotic rotating wave approximation (ARWA) [152]. In this limit, $\omega >> \omega_0, \kappa\mathcal{E}$. As we have pointed out there, this limit is most illuminating when in eq.(3.13) we examine the limit, $\omega_0 \to 0$. In this case

$$\omega^{'}=\omega+O(\omega_0^2)+... \quad (3.15)$$

indicating that $\omega^{'}$ and ω differ by a term of order ω_0^2. Thus the Rabi frequency that was small compared to ω in the resonant case 'crosses over' to a frequency which is of the same order as the external frequency. This is in stark contrast to the graphene case as we have seen in the earlier work [152] as shall do so again below where the Rabi frequency crosses over from the conventional RWA to the anomalous result which continues to be small compared to ω. To see why this is important, we note that the present model is meant as a caricature to the simple two band model of a semiconductor where there is no such thing as pseudo-spin - to begin with, the unperturbed Hamiltonian is diagonal. In this case, the time dependent part may be identified with the external time dependent field coupling to the current operator. Thus the optical response is measured by the time dependence of $M_{\pm}(t)$. Given that $M_0(t)$ is oscillating with frequency $\pm\omega$

in the ARWA limit, an examination of eq.(3.6) in the limit $\omega_0 \to 0$, forces us to conclude that there is no component of $M_{\pm}(t)$ that oscillates with frequency ω (it is either small compared to ω or it is of order 2ω). Thus the amplitude of the induced current that oscillates with the external frequency is nearly independent of time - a sign that there is no such thing as an anomalous Rabi oscillation in this case. This is a contrast to graphene where there is such an anomalous Rabi frequency.

Getting back to the topic of the present chapter which is Bloch-Siegert shift, one may derive a formula for this. As pointed out in the introduction, Shirley [211], Swain [212, 213] and others have provided a rather complete description of the phenomenon in case of the two-level system. Indeed, iteration of the recursion eq.(3.11) leads to precisely the sort of continued fraction expressions for the Rabi frequency found in the work by Swain. We shall however be content at deriving the leading corrections to the Bloch-Siegert shift as we are merely interested in calibrating the Fourier transform method against well-understood problems so that we may then apply the technique to graphene. Bloch-Siegert shift is obtained by retaining the second harmonic terms (and beyond, for more accuracy see e.g. Shirley [211] or Swain [212, 213]). We will iterate eq.(3.11) once and ignore the term $M_0(\omega' \pm 4\omega)$

$$\tilde{M}_0(\omega' \pm 2\omega) = \frac{(\kappa\mathcal{E})^2(\omega' \pm \omega)}{\epsilon(\omega' \pm 2\omega)\ [(\omega' \pm \omega)^2 - \omega_0^2]}\ \tilde{M}_0(\omega'). \tag{3.16}$$

We now substitute these into eq.(3.11) to obtain an equation for the eigenfrequency.

$$\epsilon(\omega') = \frac{(\kappa\mathcal{E})^4(\omega' + \omega)^2}{\epsilon(\omega' + 2\omega)\ [(\omega' + \omega)^2 - \omega_0^2]^2} + \frac{(\kappa\mathcal{E})^4(\omega' - \omega)^2}{\epsilon(\omega' - 2\omega)\ [(\omega' - \omega)^2 - \omega_0^2]^2}. \tag{3.17}$$

Set $\omega = \omega_0 + \Delta$ and expand the left hand side of the above equation in powers of ω_0^{-1} keeping Δ fixed (this is the RWA regime). This leads to

$$\frac{\omega'(\Delta^2 + (\kappa\mathcal{E})^2 - \omega'^2)}{\Delta^2 - \omega'^2} + \frac{\Delta(\kappa\mathcal{E})^4\omega'}{2\omega_0(\Delta^2 - \omega'^2)^2} \approx 0. \tag{3.18}$$

This means

$$\omega'^2 = \Delta^2 + (\kappa\mathcal{E})^2 - \frac{\Delta(\kappa\mathcal{E})^2}{2\omega_0}. \tag{3.19}$$

Completing the square we get, $\omega'^2 = \left(\Delta - \frac{(\kappa\mathcal{E})^2}{4\omega_0}\right)^2 + (\kappa\mathcal{E})^2 - \frac{(\kappa\mathcal{E})^4}{16\omega_0^2}$. Therefore the new resonance frequency is

$$\omega = \omega_* \equiv \omega_0 + \frac{(\kappa\mathcal{E})^2}{4\omega_0}. \tag{3.20}$$

This expression is identical to what may be found in the text-books (see e.g. Allen and Eberly [157]). The series obtained by Shirley [211] (which may also be obtained by iterating eq.(3.11)) is

$$\omega = \omega_* \equiv \omega_0 + \frac{(\kappa\mathcal{E})^2}{4\omega_0} + \frac{(\kappa\mathcal{E})^4}{(4\omega_0)^3} - \frac{35}{32}\frac{(\kappa\mathcal{E})^6}{2^6\omega_0^5} - ... \tag{3.21}$$

The main motivation for this section is of course not to reproduce well-known results such as the one above but rather to use them to calibrate the technique we are going to employ throughout this chapter namely writing the Bloch equation in the frequency domain where it has the appearance of a recursion relation, then suitably truncating the recursion to convert it into an eigenvalue equation for the frequencies involved, which in turn yields the Rabi frequencies along with the Bloch-Siegert shift in the different domains of interest.

Now we proceed to describe Bloch-Siegert shift in graphene. In graphene, we have a situation where close to the Dirac point the quasiparticles are chiral massless Dirac fermions with linear dispersion, but the dispersion acquires curvature as one moves away from the Dirac point. We study the nature of the Bloch-Siegert shift by assuming a strictly linear dispersion first followed by a more realistic and logically consistent calculation that includes non-linearities in the dispersion. These two studies are aimed at pinpointing the role played by band structure effects on the Bloch-Siegert shift in graphene.

3.4 Bloch-Siegert Shift in Graphene - Linear Dispersion

As usual, we start with the Bloch equations for graphene (derived in the appendix (section 3.9.1)). The massless Dirac Hamiltonian is

$$H = \sum_{\mathbf{p}} \left[v_F(p_x - ip_y)c_A^\dagger(\mathbf{p})c_B(\mathbf{p}) + c.c. \right]. \tag{3.22}$$

$P(\mathbf{p},t) = c_A^\dagger(\mathbf{p})c_B(\mathbf{p})$ and $n_{diff}(\mathbf{p},t) = c_A^\dagger(\mathbf{p})c_A(\mathbf{p}) - c_B^\dagger(\mathbf{p})c_B(\mathbf{p})$ are the popula-

tion excess and polarization respectively, so that

$$i\frac{d}{dt}n_{diff}(t) = 2v_F\boldsymbol{\sigma}_{AB}\cdot\left(\mathbf{p}-\frac{e}{c}\mathbf{A}^*(t)\right)P(t) - c.c.\ , \tag{3.23}$$

$$i\frac{d}{dt}P(t) = v_F\boldsymbol{\sigma}_{BA}\cdot\left(\mathbf{p}-\frac{e}{c}\mathbf{A}(t)\right)n_{diff}(t). \tag{3.24}$$

$z_k = v_F\boldsymbol{\sigma}_{AB}\cdot\mathbf{p} = v_F(p_x - ip_y)$, $z_R = \frac{e}{c}v_F\boldsymbol{\sigma}_{BA}\cdot\mathbf{A}(0), p_x = p\cos(\theta_k)$ and $p_y = p\sin(\theta_k)$. As we did in case of the two-level system, we solve this using the Fourier transform method, $X(t) = \int_{-\infty}^{\infty}\frac{d\omega}{2\pi}e^{-i\omega t}\ \tilde{X}(\omega)$ where $X = P, n_{diff}$.

$$n_{diff}(t) = \int_{-\infty}^{\infty}\frac{d\omega^{'}}{2\pi}e^{-i\omega^{'}t}\ N_{diff}(\omega^{'}); \tag{3.25}$$

$$P(t) = \int_{-\infty}^{\infty}\frac{d\omega^{'}}{2\pi}e^{-i\omega^{'}t}\ P(\omega^{'}) \tag{3.26}$$

This yields

$$\omega^{'}\ N_{diff}(\omega^{'}) = \ 2z_k\ P(\omega^{'}) - 2z_R^*\ P(\omega^{'}+\omega) - 2z_k^*\ P^*(-\omega^{'}) + 2z_R\ P^*(\omega-\omega^{'}), \tag{3.27}$$

$$\omega^{'}\ P(\omega^{'}) = z_k^*\ N_{diff}(\omega^{'}) - z_R N_{diff}(\omega^{'}-\omega). \tag{3.28}$$

Inserting the second of the above equations into the first we get a recursion relation exclusively for $N_{diff}(\omega^{'})$.

$$\left(\omega^{'} - \frac{4\omega^{'}\omega_R^2}{\omega^{'2}-\omega^2}\right)N_{diff}(\omega^{'}) = \frac{2z_kz_R(2\omega^{'}-\omega)N_{diff}(\omega^{'}-\omega)}{\omega^{'}(\omega-\omega^{'})} - 2z_R^*z_k^*\frac{(2\omega^{'}+\omega)}{(\omega^{'}+\omega)\omega^{'}}N_{diff}(\omega^{'}+\omega). \tag{3.29}$$

Iterating this equation leads to expressions for the eigen-frequencies. We are particularly interested in the one that approaches $\sqrt{\Delta^2+\omega_R^2}$ as $|z_k| \to \infty$ keeping $\Delta \equiv \omega - 2|z_k|$ fixed. Having obtained a general expression for this frequency, we will then examine the other limit viz. when $\omega \to \infty$, $|z_k| \to 0$, keeping $\omega|z_k|$ fixed (we have called this ARWA). Iterating the above eq.(3.29) and throwing away $N_{diff}(\omega^{'} \pm 3\omega)$ and beyond allows us to capture the lowest order Bloch-Siegert shift since we are including the first counter rotating term $N_{diff}(\omega^{'} \pm 2\omega)$. The

equation for $\omega^{'}$ we obtain will be of the form, $W(\omega^{'}, \omega, \omega_R, |z_k|) = 0$. Thus we obtain the following two kinds of Bloch-Siegert shifts. The first one is deduced from the conventional Rabi frequency near resonance $|\Delta| << \omega$. In this case we find $lim_{|z_k|\to\infty} W(\omega^{'}, \Delta + 2|z_k|, \omega_R, |z_k|)$, holding Δ fixed, and then set this function to zero. This leads to an expression for the conventional Rabi frequency with Bloch-Siegert shift

$$\omega^{'} \equiv \Omega_{RWA} = \sqrt{\omega_R^2 - \frac{\omega_R^4}{64|z_k|^2} + \left(\Delta - \frac{\omega_R^2}{8|z_k|}\right)^2}, \tag{3.30}$$

as $\omega_{shift} = \frac{\omega_R^2}{4|2z_k|}$. This expression is identical to what may be found in the textbooks on two-level systems (e.g. Allen and Eberly). The second one employs the ARWA limit where we hold $c^2 = |z_k|^2\omega^2$ and ω_R fixed and find $lim_{\omega\to\infty} W(\frac{\omega^{''}}{\omega} + \omega, \omega, \omega_R, \frac{c}{\omega})$ before setting this function to zero. Then the Rabi frequency is going to be $\omega^{'} = \frac{\omega^{''}}{\omega}$. We have to shift by ω in order to extract the Rabi frequency associated with the single harmonic in the external field (the series below required six iterations of eq.(3.29) to obtain).

$$\Omega_{ARWA} = \frac{1}{\omega}\left(4\omega^2|z_k|^2 + 4\omega_R^4 - \frac{8\omega_R^2(\omega^2|z_k|^2 + \omega_R^4)}{\omega^2} + \frac{4\omega_R^4(7\omega^2|z_k|^2 + 5\omega_R^4)}{\omega^4} + ...\right)^{\frac{1}{2}}. \tag{3.31}$$

One may see here that this result is not too different from the simple result obtained by ignoring frequency doubling [152]. In particular, unlike in case of the rotating wave approximation, where resonance occurs at a shifted value of $|z_k| = \frac{\omega}{2} + (shift)$ (at which value of the Rabi frequency is a minimum), here the anomalous Rabi frequency is minimum when $|z_k| = 0$ both in the simple case and when Bloch-Siegert like corrections are included. Therefore in the ARWA case for isotropic graphene, we do not have a Bloch-Siegert shift but merely a change in the effective Rabi frequency. This uninteresting result motivates us to include band curvature effects. It is also worthwhile to note that it is logically inconsistent to explore the high field effects which involve higher and higher powers of the field while ignoring such higher order effects in the band dispersion. We now wish to set this right by including the band curvature effects.

3.5 Bloch-Siegert Shift in Graphene - Band Curvature Effects

Using the Hamiltonian for graphene that includes nearest and next nearest neighbor (nnn) hopping (derived in appendix (section 3.9.2)), we may evaluate corrections to the Bloch equation brought about by band curvature effects ($z_k =$

$v_F\boldsymbol{\sigma}_{AB}\cdot\mathbf{p}$, $z_R=\frac{e}{c}v_F\boldsymbol{\sigma}_{BA}\cdot\mathbf{A}(0)\big)$

$$i\frac{dP(\mathbf{p},t)}{dt}=-\frac{a_{cc}i}{4v_F}\left(z_k^2+z_R^{*2}e^{2i\omega t}-2z_kz_R^*e^{i\omega t}\right)n_{diff}(\mathbf{p},t)+\left(z_k^*-z_R\,e^{-i\omega t}\right)n_{diff}(\mathbf{p},t),\tag{3.32}$$

$$i\frac{dn_{diff}(\mathbf{p},t)}{dt}=\frac{a_{cc}i}{2v_F}\left(z_k^{*2}+z_R^2e^{-2i\omega t}-2z_k^*z_Re^{-i\omega t}\right)\;P(\mathbf{p},t)+2\left(z_k-z_R^*\,e^{i\omega t}\right)P(\mathbf{p},t)-c.c.\tag{3.33}$$

This is also solved using the Fourier transform method where we first write $X(t)=\int_{-\infty}^{\infty}\frac{d\omega}{2\pi}e^{-i\omega t}\;\tilde{X}(\omega)$ where $X=p,n_{diff}$. Then the formula for the variable $\tilde{p}$ in terms of $\tilde{n}_{diff}$ is substituted into the equation for $\tilde{n}_{diff}$ and a recursion relation is formed. This recursion is iterated twice so that equations for $\tilde{n}_{diff}(\mathbf{p},\omega^{'}+n\omega)$, $n=0,\pm1,\pm2$ are obtained. These will involve higher harmonics such as $n=\pm3,\pm4$ and so on. We drop these terms to obtain a closed set of five homogeneous linear equations which defines an eigenvalue problem. The reason why we include terms only up to the second harmonic is because the corrections to the Bloch equations only involve terms to that order. The eigenfrequencies are precisely the Rabi frequencies. We now list the final results for the Rabi frequencies in various cases. These outcomes are a result of rather involved analytical calculations made possible largely due to the availability of symbolic computation packages such as Mathematica [184]. We have made extensive use of Mathematica [184] in this work.

(i) No nonlinearities ($q=\frac{a_{cc}}{v_F}\to0$) in the dispersion, frequency doubling effects ignored ($\omega\to\infty$). This is the simplest case and leads to the following results for the conventional and anomalous Rabi frequencies ($\delta^2=|z_k|\omega$).

$$\Omega_{RWA}=\sqrt{\omega_R^2+\Delta^2};\quad\Omega_{ARWA}=\frac{2\sqrt{\omega_R^4+\delta^4}}{\omega}.\tag{3.34}$$

where $\Delta=\omega-2|z_k|$ is the detuning.

(ii) No nonlinearities in the dispersion ($q=0$) but frequency doubling effects included ($\omega<\infty$, see earlier section).

$$\Omega_{RWA}=\sqrt{\omega_R^2+O\left(\frac{1}{|z_k|^2}\right)+\left(\Delta-\frac{\omega_R^2}{8|z_k|}\right)^2},\tag{3.35}$$

$$\Omega_{ARWA} = \frac{2\sqrt{\omega_R^4 + \delta^4}}{\omega}\left(1 - \frac{\omega_R^2}{\omega^2}\right). \tag{3.36}$$

(iii) Leading nonlinearities in the dispersion included ($q \neq 0$) but frequency doubling effects ignored ($\omega \to \infty$).

$$\Omega_{RWA} = \sqrt{(\omega_R^2 + \Delta^2) + sin(3\theta_k)\ |z_k|\ \omega_R^2\ q}; \tag{3.37}$$

$$\Omega_{ARWA} = \frac{2\sqrt{\omega_R^4 + \delta^4}}{\omega}\left(1 + \frac{\omega_R^8 \delta^8 q^4}{2^{11}(\omega_R^4 + \delta^4)^3} + O(q^8)\right). \tag{3.38}$$

(iv) General case $\left[q \neq 0, \omega < \infty, \tau = \frac{1}{(E_k + \Delta)}, E_k = 2v_F|p|\sqrt{1 + \frac{qv_F}{16}(p^2 q v_F + 8|p| sin(3\theta_k))}\ \right]$

$$\Omega_{RWA} = \left[\left(\omega_R^2 - \frac{23\omega_R^4\tau^2}{8} + \left(\Delta - \frac{\tau\omega_R^2}{4}\right)^2\right)\left(1 - \frac{(\tau^2\omega_R^2)}{4}\right) + sin(3\theta_k)\ |z_k|\ \omega_R^2\ q\right]^{\frac{1}{2}}, \tag{3.39}$$

$$\Omega_{ARWA} = \frac{\sqrt{2}}{\omega^2}\left[2(\omega_R^4 + \delta^4)(-2\omega_R^2 + \omega^2) + q\omega\delta^6\ sin(3\theta_k)\right]^{\frac{1}{2}} \tag{3.40}$$

$$\approx \frac{2\sqrt{\omega_R^4 + \delta^4}}{\omega}\left(1 + \frac{q\delta^6 sin(3\theta_k)}{4(\omega_R^4 + \delta^4)\omega} - \frac{\omega_R^2}{\omega^2} + ..\right). \tag{3.41}$$

These illuminating results clearly show the effect of anisotropic band structure on both the conventional and anomalous Rabi oscillations. Now we reinforce these observations by studying another case where anisotropy is important, namely with Rashba interaction.

3.6 Bloch-Siegert Shift in Graphene - Rashba Interaction

In case of Rashba spin-orbit (SO) interaction, Hamiltonian of the single layer graphene has form [197]

$$H = \begin{pmatrix} 0 & v_F\pi^\dagger & 0 & -v_\lambda\pi \\ v_F\pi & 0 & 3i\lambda_R & 0 \\ 0 & -3i\lambda_R & 0 & v_F\pi^\dagger \\ -v_\lambda\pi^\dagger & 0 & v_F\pi & 0 \end{pmatrix}, \tag{3.42}$$

where $v_\lambda = \frac{3\lambda_R d}{2\hbar}$, $v_F = \frac{3\gamma_0 d}{2\hbar}$ with $v_\lambda << v_F$ as expressed in Ref.[197], $\pi = p_x + ip_y$ and $\pi^\dagger = p_x - ip_y$ with d being the nearest neighbor distance. The strength of spin-orbit coupling is represented by λ_R, which may be due to a perpendicularly applied electric field or due to a graphene-substrate interaction. At low energy, there is a change in the topology of the bands close to the Dirac points due to trigonal warping. The band dispersion - single layer graphene with Rashba spin-orbit interaction and bilayer graphene with trigonal warping effect - are quite similar (we refer to fig.1(a) and 1(c) in Ref.[197] and fig.7(b) and 7(c) in Ref.[201]).

Using the above Hamiltonian, we derive the Bloch equations, which are then solved in both the resonance and far from resonance regions [178] and expressions for the corresponding Rabi frequencies are obtained. With Rashba interaction, the SO coupling leads to harmonic resonances in the RWA regime $\Big($here $\delta_n = n\omega - 2E_k$ and $E_k = \pm\left|\frac{p_+^2}{2m} - v_3 p_-\right|\Big)$, $\pm$ corresponds to conduction and valance band respectively, where $p_\pm = p_x \pm ip_y$

$$\Omega_{RWA,\omega} = \sqrt{\delta_1^2 + \frac{2|\mathbf{p}|^2}{m}\omega_{R2} + \omega_{R1}^2};\ \Omega_{RWA,2\omega} = \sqrt{\delta_2^2 + \omega_{R2}^2}. \tag{3.43}$$

Here $n = 1, 2$ is the index that labels the harmonic resonance. In first harmonic resonance $|\delta_1| << \omega$ and in the second harmonic resonance $|\delta_2| << \omega$. The anomalous Rabi frequency is given by

$$\Omega_{ARWA} = 2\sqrt{E_k^2 + \frac{\omega_{R12}^2}{4}}, \tag{3.44}$$

where $\omega_{R12} = \frac{\omega_{R2}^2}{\omega} + \frac{4|\mathbf{p}|^2\omega_{R2}}{m\omega} - \frac{2\omega_{R1}^2}{\omega}$, $\omega_{R1} = v_3|A(0)|$, $\omega_{R2} = \frac{|A(0)|^2}{2m}$, $\delta_1 = \omega - 2E_k$, $m \approx \frac{3\lambda_R}{2v_F^2}$, $A(0) = \frac{e}{c}(A_x(0) + i\ A_y(0))$ and $A_x(0)$ and $A_y(0)$ are complex. We note that the origin of anisotropy is in the expression for the energy eigenvalue E_k. Now we proceed to a graphical discussion of the consequences of these effects.

3.7 Results and Discussion

In the earlier sections, we saw how the successive inclusion of frequency doubling, next-nearest neighbor hopping and Rashba interaction affect both conventional and anomalous Rabi frequencies. In this section, we wish to study these effects pictorially. Specifically, we focus on anomalous Rabi oscillations where we see large shifts in the resonance condition brought about by a combination of frequency doubling (counter rotating terms), next nearest neighbor hopping or Rashba effect.

Compared to these shifts, some of which in percentage terms are infinite, the shifts in conventional Rabi oscillations are rather tiny. This section, therefore, reconfirms our suspicion that anomalous Rabi oscillations are a useful indicator of the nature of low energy band structure of graphene. To obtain these plots, we have to choose numerical values for the various constants that enter into the formalism. We have made the following choices that are consistent with the requirements of the various limits under consideration.

Quantity	Numerical value
$\nu = \frac{\omega}{2\pi}$	500 THz
v_F	1×10^6 m/s
$q = \frac{a_{cc}}{v_F}$	1.42×10^{-16} sec
E_{max}	250×10^5 V/m
ω_R	$1.21 \times 10^{13} rad/sec$
v_3^*	$9.7 \times 10^4 m/s$
$m = 0.054 m_e^*$	$0.49 \times 10^{-31}\ kg$
$\frac{\omega_R}{\omega}$	3.85×10^{-3}
$q\omega$	0.477
$\frac{mv_3^{2}{}^*}{\hbar\omega}$	1.40×10^{-3}
$\frac{\omega_{R1}{}^*}{\omega}$	3.75×10^{-4}
$\frac{\omega_{R2}{}^*}{\omega}$	5.031×10^{-5}

TABLE 3.1: *The asterisk is for the Rashba case

Sr. No.	NL	FD	Ras	BSS	% Shift
1.	No	Yes	No	$\frac{\omega_R^2}{8\lvert z_k\rvert}$	0.00037%
2.	Yes	No	No	$\frac{1}{4} q\omega_R^2\ sin(3\theta_k)$	0.00052%
3.	Yes	Yes	No	$\frac{1}{4}\omega_R^2(\tau + \frac{(4qsin(3\theta_k))}{(4-\tau^2\omega_R^2)})$	0.00089%
4.	No	No	Yes	$\frac{\omega}{2}\frac{(2\omega_{R2}-\omega cos(3\theta_k))}{2(2mv_3^2+\omega_{R2}-2\omega cos(3\theta_k))}$	0.9%[a]

TABLE 3.2: This table shows the RWA case of Bloch-Siegert shift. The abbreviations are, NL - nonlinearity, FD - frequency doubling, Ras - Rashba spin orbit interaction and BSS stands for Bloch-Siegert shift in the resonant frequency relative to the case with "No" for all the entries. [a]In the Rashba case, we see a strong anisotropy and large shifts in the direction $|cos(3\theta_k)| = 1$. The percentage shift in Sr. No. 4 is for the case when $cos(3\theta_k) = 0$ which is when the formula for the shift is consistent with the other assumptions.

In table 3.4, the expression for RWA Rabi frequency in Case 4 is strictly speaking valid only when $\omega_{R1}^2 >> \frac{\omega^2\,\omega_{R2}}{2mv_3^2}$, $u(\theta_k) = -1 + 36cos(6\theta_k) - 27cos(12\theta_k)$ and [b]$\chi(\theta_k) = \sqrt{u(\theta_k) + \sqrt{2}\sqrt{-7 + 9cos(6\theta_k)}(5cos(3\theta_k) - 9cos(9\theta_k))}$. Due to the presence of the factor $sin(3\theta_k)$ in many formulas, we see a pronounced anisotropy in these plots. The most interesting directions are when $|sin(3\theta_k)| = 0, 1$. The fig.(3.1) depicts conventional Bloch-Siegert shift due to frequency doubling that is common to

Sr. No.	NL	FD	Ras	BSS	% Shift
1.	No	Yes	No	0	0%
2.	Yes	No	No	0	0%
3.	Yes	Yes	No	$\frac{4\lvert cosec(3\theta_k)\rvert}{q}$; $sin(3\theta_k) < 0$	∞
4.	No	No	Yes	$\rho(\theta_k)$	∞

TABLE 3.3: This table shows the ARWA case of Bloch-Siegert shift. Here $\rho(\theta_k) = \frac{mv_3^2}{4}(6cos(3\theta_k) + \sqrt{2}\sqrt{(-7+9cos(6\theta_k))})$. The Bloch-Siegert shift (BSS) is a shift in resonance condition for anomalous Rabi oscillations from the trivial value $v_3k = 0$ to the nontrivial value shown in this column. The bands are isotropic in cases 1 and 2 and show no BSS. In cases 3 and 4 the bands are anisotropic and the minimum is shifted to a nontrivial location and the shift in percentage terms is infinite.

both two-level systems as well as graphene. The fig.(3.2) shows that both the next nearest neighbor interaction (nonlinearity in the dispersion) and frequency doubling can lead to Bloch-Sigert shifts in the conventional Rabi frequency. However, both these shifts are quite tiny, the former being even smaller. The figures (3.3) and (3.4) are central to the present work. fig.(3.3) shows the landscape of anomalous Rabi frequencies as a function of the wave vector. In one case the anisotropy seen is attributable to nnn hopping and the other to Rashba interaction.

Sr. No.	SRF (RWA)	SRF (ARWA)
1.	$\sim \omega_R$	$\frac{2\omega_R^2}{\omega}(1 - \frac{\omega_R^2}{\omega^2})$
2.	$\frac{1}{2}\omega_R^2(2 + q\omega\ sin(3\theta_k))$	$\frac{2\omega_R^2}{\omega}$
3.	$\sim \frac{1}{2}\omega_R^2(2 + q\omega\ sin(3\theta_k))$	0
4.	$\sqrt{\omega_{R1}^2 + \frac{\omega^2\ \omega_{R2}}{2mv_3^2}}\ ^a$	$2mv_3^2\chi(\theta_k)^b$

TABLE 3.4: This table shows the shifted Rabi frequencies (SRF) in both RWA and ARWA case. The ARWA Rabi frequency with both nonlinearity and frequency doubling included effectively becomes zero at a Bloch-Siegert shifted value of the wave number for appropriate directions. The meaning of cases 1-4 is as in the other tables.

In both cases, we see a Bloch-Siegert shift from the trivial zero momentum anomalous Rabi frequency to a different anomalous Rabi frequency at a shifted wavenumber in some specific directions. Since the shift is from a zero momentum value to a nonzero value, the percentage Bloch-Siegert shift is actually infinite in these two cases. This shows that the anomalous Rabi frequency is sensitive to qualitative changes in the low-energy band structure of graphene and as such may serve as an indirect alternative to determining the low energy electronic structure of chiral massless Dirac fermion systems. In fig.(3.4) we see more clearly the Bloch-Siegert shifts in anomalous Rabi frequency. It must be stressed that it is the anomalous Rabi frequency that undergoes such significant shifts whereas the

conventional Rabi frequency follows the trends of the two-level systems where the shifts are known to be negligible.

We have looked for experimental work that may have already seen these anomalous Rabi oscillations. One possible experimental tool for detecting Rabi oscillations is the pump-probe experiment. Typically, incoherent optical properties such as optical dephasing and relaxation of band electrons in semiconductors are studied using the pump-probe experiment [49, 157] in which two successive laser pulses are used, one to prepare the system in certain way, called pump pulse and one to test it after a variable time delay, called probe pulse. Coherent optical effects such excitonic optical Stark effect of a semiconductor [193–195] may also be studied by the pump-probe technique in which the pump pulse excites the material energetically below the exciton resonance and probe pulse monitors the transmission change at exciton resonance.

In a recently published paper [202], we have conducted theoretical analysis of the pump-probe experiment and computed the differential transmission coefficient (DTC) versus the time delay between pump and probe, taking into account incoherent effects such as dephasing. There we showed that the DTC is a decaying function of the time delay, due to dephasing. However, more interestingly, we find, superimposed on the overall decay, oscillations whose frequency is precisely the anomalous Rabi frequency we have been discussing. An examination of the experimental work of Breusing *et al* [63], specifically fig.1(c) of this work appears to confirm our predictions, including the numerical values of the anomalous Rabi frequency. To verify the predictions of the present work, these experiments will have to be repeated for a range of intensities and the dependence of the anomalous Rabi frequency on the field strength has to be ascertained. A quantitative comparison of the present work with already published experimental works such as Breusing *et al* [63] is not possible since such data are presently unavailable in the public domain.

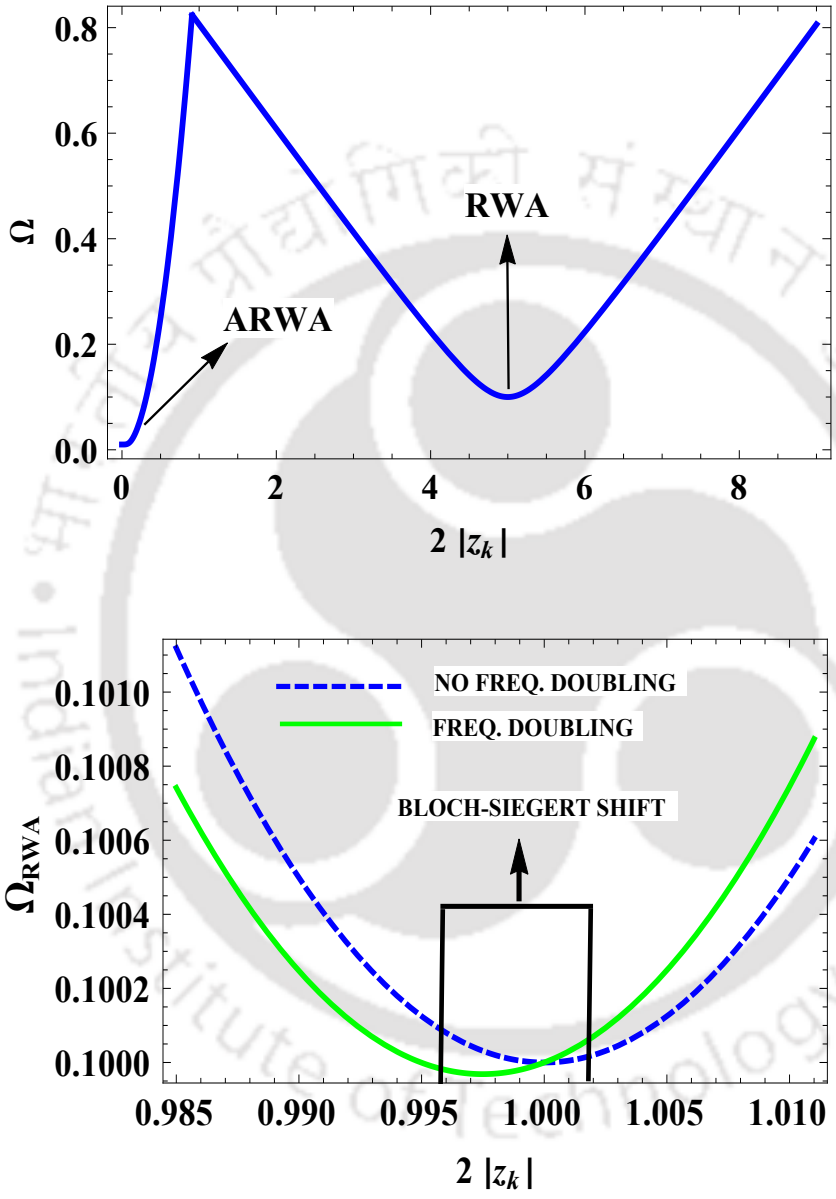

FIGURE 3.1: The first figure demonstrates the cross-over phenomenon spanning both the conventional and anomalous resonance regions ($\Omega = \Omega_{RWA}$ Or Ω_{ARWA}). The second figure shows the conventional Rabi frequency with and without frequency doubling. The lateral shift in this plot is the conventional Bloch-Siegert shift. The BS shift in this plot is exaggerated for clarity by choosing $\frac{\omega_R}{\omega} = 0.1$, parameters are plotted in unit of ω and $z_k = v_F(p_x - ip_y)$.

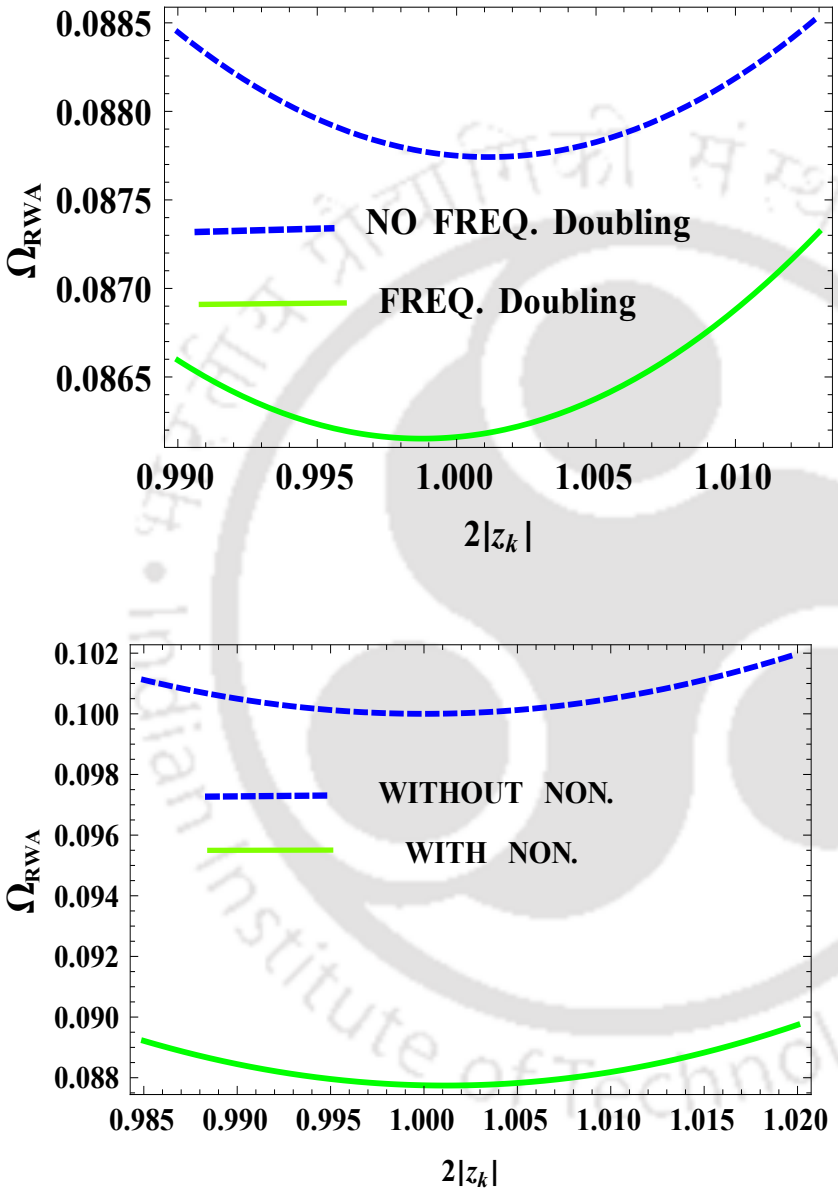

FIGURE 3.2: In the first figure the conventional Rabi frequency including nonlinearity with and without frequency doubling is plotted, depicting the conventional Bloch-Siegert shift as in fig.(3.1). The second figure shows a much smaller Bloch-Siegert like shift even without frequency doubling, due to nonlinearity(on considering $sin(3\theta_k) = -1$, $z_k = v_F(p_x - ip_y)$).

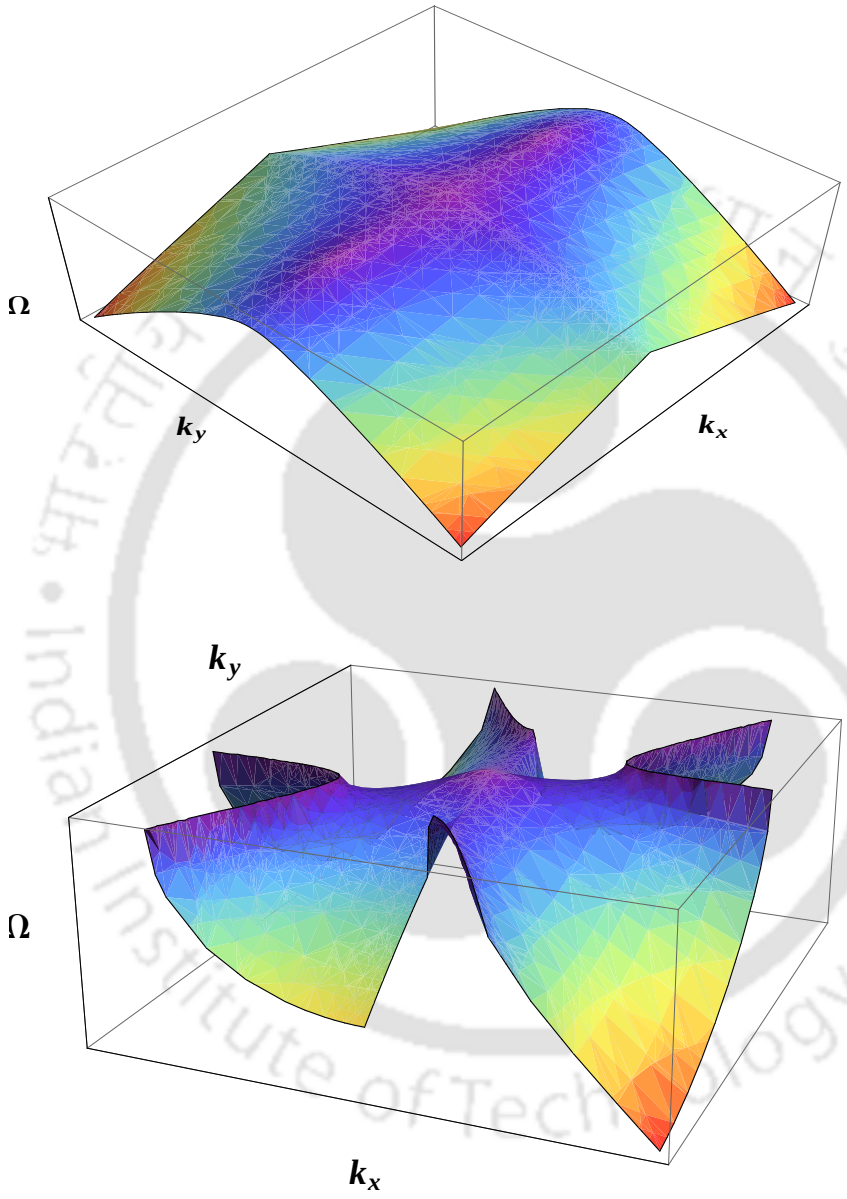

FIGURE 3.3: The first figure is the plot of the anomalous Rabi frequency versus the two cartesian components of the wave vector including the Rashba effect. The second figure is a plot of the anomalous Rabi frequency including frequency doubling and nnn hopping but no Rashba effect. In both cases we see strong anisotropy. In particular, there are new minima in appropriate directions away from the trivial minimum corresponding to Bloch-Siegert shifted anomalous Rabi oscillations.

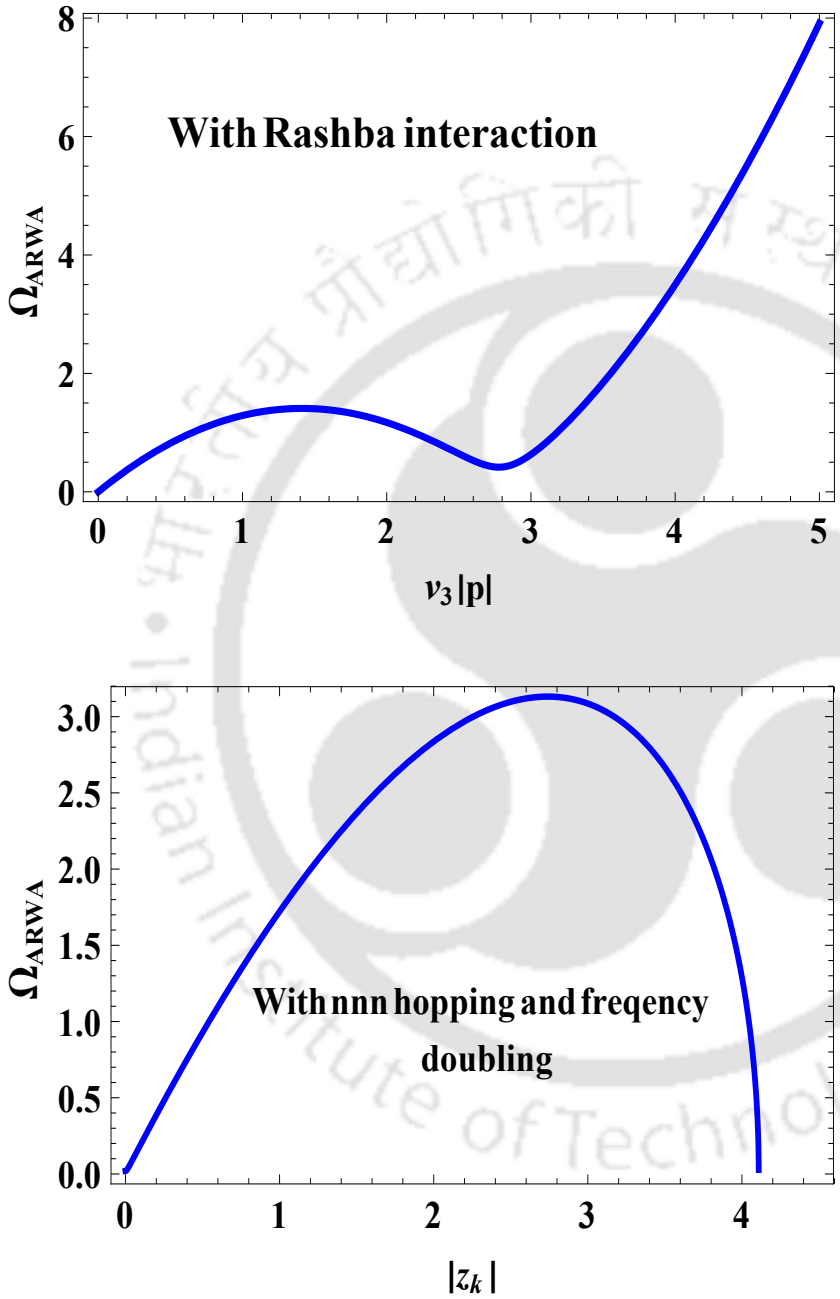

FIGURE 3.4: The first plot shows the anomalous Rabi frequency versus wave number in the Rashba case, indicating a new Bloch-Siegert shifted minimum. The parameters are plotted in unit of $10^{-3}\omega$ (here $\cos 3\theta = 1$). The second plot shows the nnn hopping and frequency doubling case (parameters are plotted in unit of ω, here we have chosen $sin(3\theta_k) = -1$, $z_k = v_F(p_x - ip_y)$).

3.8 Conclusions

In this work, we have highlighted the nature of changes in the resonance condition of Rabi oscillations (known as a Bloch-Siegert shift) in graphene due to band anisotropy. This is in contrast to the conventional Bloch-Siegert shift that is due to strong fields alone and is associated with Rabi oscillations near conventional resonance. However, graphene exhibits anomalous Rabi oscillations far from conventional resonance. The anomalous resonance condition itself undergoes a Bloch-Siegert shift in the presence of band anisotropy, which in percentage terms is infinite, unlike the tiny shifts are seen in conventional Rabi oscillations. This observation reinforces the assertion we have been making namely that anomalous Rabi oscillations are a useful probe of the low-energy band structure of graphene, in particular and chiral massless Dirac fermion systems, in general.

3.9 Appendix

3.9.1 Derviation of Bloch Equation in Graphene

Hamiltonian of graphene has the form

$$H = v_F(p_x\sigma_x + p_y\sigma_y). \tag{3.45}$$

Writing equation (1) in matrix form

$$H = v_F \begin{bmatrix} 0 & p_x + ip_y \\ p_x - ip_y & 0 \end{bmatrix}.$$

The state vector of above equation

$$\psi = \begin{bmatrix} c_A \\ c_B \end{bmatrix}.$$

So the Hamiltonian in second quantized form

$$H = \begin{bmatrix} c_A^\dagger & c_B^\dagger \end{bmatrix} v_F \begin{bmatrix} 0 & p_x - ip_y \\ p_x + ip_y & 0 \end{bmatrix} \begin{bmatrix} c_A \\ c_B \end{bmatrix},$$

$$H = v_F\ [(p_x - ip_y)c_A^\dagger c_B + (p_x + ip_y)c_B^\dagger c_A].$$

The commutation relation for fermionic operator

$$[AB, CD] = A[B, CD] + [A, CD]B,$$

$$= A[\{B, C\}D - C\{B, D\}] + [\{A, C\}D - C\{A, D\}]B,$$

$$= A\{B, C\}D - AC\{B, D\} + \{A, C\}DB - C\{A, D\}B.$$

So Bloch equation $\langle c_A^\dagger c_A\rangle, < c_B^\dagger c_B >, < c_A^\dagger c_B >, < c_B^\dagger c_A >$

$$i\frac{d < c_A^\dagger c_A >}{dt} = v_F\ [(p_x - ip_y)c_A^\dagger c_B - (p_x + ip_y)c_B^\dagger c_A],$$

$$i\frac{d < c_B^\dagger c_B >}{dt} = v_F\ [-(p_x - ip_y)c_A^\dagger c_B + (p_x + ip_y)c_B^\dagger c_A].$$

We define $n_{diff}(\mathbf{p}, t) =< c_A^\dagger c_A > - < c_B^\dagger c_B >$ and $P(\mathbf{p}, t) =< c_A^\dagger c_B >$. So

$$i\frac{dn_{diff}(\mathbf{p}, t)}{dt} = 2v_F\ [(p_x - ip_y)c_A^\dagger c_B - (p_x + ip_y)c_B^\dagger c_A],$$

$$i\frac{dn_{diff}(\mathbf{p}, t)}{dt} = 2v_F\ \left[(p_x + ip_y)P(\mathbf{p}, t) - (p_x - ip_y)P^*(\mathbf{p}, t)\right]. \tag{3.46}$$

Now first equation for polarization

$$i\frac{d < c_A^\dagger c_B >}{dt} = v_F\ (p_x + ip_y)[c_A^\dagger c_A - c_B^\dagger c_B].$$

So finally equation will be

$$i\frac{dP(\mathbf{p}, t)}{dt} = v_F\ (p_x + ip_y)n_{diff}(\mathbf{p}, t). \tag{3.47}$$

Now Second equation for polarization

$$i\frac{d < c_B^\dagger c_A >}{dt} = v_F\ (p_x - ip_y)[c_B^\dagger c_B - c_A^\dagger c_A]$$

So finally equation will be

$$i\frac{dP^*(\mathbf{p}, t)}{dt} = -v_F\ (p_x - ip_y)n_{diff}(\mathbf{p}, t). \tag{3.48}$$

On including vector potential i.e. $p \to p - \frac{eA(0)}{c}e^{-i\omega t}$. Here $A(0) = A_x(0) + iA_y(0)$.

$$p_x + ip_y = \left(p_x + ip_y - \frac{eA(0)}{c}e^{-i\omega t}\right),$$

$$p_x - ip_y = \left(p_x - ip_y - \frac{eA^*(0)}{c}e^{i\omega t}\right).$$

If we consider

$$z_k^* = p_x + ip_y,$$

$$z_k = p_x - ip_y,$$

$$z_R = \frac{e}{c}[A_x(0) + iA_y(0)],$$

$$z_R^* = \frac{e}{c}[A_x^*(0) - iA_y^*(0)].$$

So Bloch equation will be

$$i\frac{dn_{diff}(\mathbf{p},t)}{dt} = 2v_F \left[\left(p_x - ip_y - \frac{eA^*(0)}{c}e^{i\omega t}\right)P(\mathbf{p},t) - \left(p_x + ip_y - \frac{eA(0)}{c}e^{-i\omega t}\right)P^*(\mathbf{p},t)\right], \tag{3.49}$$

$$i\frac{dP(\mathbf{p},t)}{dt} = v_F \left(p_x + ip_y - \frac{eA(0)}{c}e^{-i\omega t}\right)n_{diff}(\mathbf{p},t), \tag{3.50}$$

$$i\frac{dP^*(\mathbf{p},t)}{dt} = -v_F \left(p_x - ip_y - \frac{eA^*(0)}{c}e^{i\omega t}\right)n_{diff}(\mathbf{p},t). \tag{3.51}$$

Above equation in terms of z_k^*, z_k, z_R, z_R^* and we define $z_A = z_R e^{-i\omega t}$

$$i\frac{dn_{diff}(\mathbf{p},t)}{dt} = 2v_F \left[\left(z_k - z_R^* e^{i\omega t}\right)P(\mathbf{p},t) - \left(z_k^* - z_R e^{-i\omega t}\right)P^*(\mathbf{p},t)\right], \tag{3.52}$$

$$i\frac{dP(\mathbf{p},t)}{dt} = v_F \left(z_k^* - z_R e^{-i\omega t}\right)n_{diff}(\mathbf{p},t), \tag{3.53}$$

$$i\frac{dP^*(\mathbf{p},t)}{dt} = -v_F \left(z_k - z_R^* e^{i\omega t}\right)n_{diff}(\mathbf{p},t). \tag{3.54}$$

3.9.2 Derviation of Band Curvature Effects in Graphene

$$H = -t\sum_{<ij>\sigma}\left(a_{i\sigma}^\dagger b_{j\sigma} + h.c.\right) - t'\sum_{<<ij>>\sigma}\left(a_{i\sigma}^\dagger a_{j\sigma} + b_{i\sigma}^\dagger b_{j\sigma} + h.c.\right), \tag{3.55}$$

$$b_{j\sigma} = \frac{1}{\sqrt{N}}\sum_{\mathbf{k}} e^{i\mathbf{k}\cdot\mathbf{r}_{B,j}} b_{\mathbf{k}\sigma}, \tag{3.56}$$

$$a_{i\sigma} = \frac{1}{\sqrt{N}} \sum_{\mathbf{k}} e^{i\mathbf{k}\cdot\mathbf{r}_{A,i}} a_{\mathbf{k}\sigma}. \tag{3.57}$$

Lattice A contains carbon atoms at locations

$$\vec{r}^{\,A}(n_1, n_2) = n_1\mathbf{A}_1 + n_2\mathbf{A}_2. \tag{3.58}$$

$\mathbf{A}_1 = \sqrt{3}a_{cc}\,(\frac{\sqrt{3}}{2}\hat{i} + \frac{1}{2}\hat{j})$ and $\mathbf{A}_2 = \sqrt{3}a_{cc}\,\hat{j}$ and lattice B also contains carbon atoms at locations

$$\vec{r}^{\,B}(n_1, n_2) = a_{cc}\hat{i} + n_1\mathbf{A}_1 + n_2\mathbf{A}_2, \tag{3.59}$$

where a_{cc} is the nearest carbon-carbon distance.

$$\vec{r}^{\,A}(n_1, n_2) - \vec{r}^{\,B}(n_1^{'}, n_2^{'}) = (n_1 - n_1^{'})\sqrt{3}a_{cc}\,\left(\frac{\sqrt{3}}{2}\hat{i} + \frac{1}{2}\hat{j}\right) + (n_2 - n_2^{'})\sqrt{3}a_{cc}\,\hat{j} - a_{cc}\hat{i}. \tag{3.60}$$

$\mathbf{A}_1 = \sqrt{3}a_{cc}\,\left(\frac{\sqrt{3}}{2}\hat{i} + \frac{1}{2}\hat{j}\right)$ and $\mathbf{A}_2 = \sqrt{3}a_{cc}\,\hat{j}$ and lattice B also contains carbon atoms at locations

$$\vec{r}^{\,B}(n_1, n_2) = a_{cc}\hat{i} + n_1\mathbf{A}_1 + n_2\mathbf{A}_2, \tag{3.61}$$

$$(\vec{r}_{A,j} - \vec{r}_{A,i}) = (n_1^{'} - n_1)\vec{a}_1 + (n_2^{'} - n_2)\vec{a}_2, \tag{3.62}$$

$$(\vec{r}_{A,j} - \vec{r}_{A,i}) = (n_1^{'} - n_1)a_{cc}\,\frac{3}{2}\hat{i} + \left[(n_1^{'} - n_1)\,\frac{1}{2} + (n_2^{'} - n_2)\right]\sqrt{3}a_{cc}\,\hat{j}. \tag{3.63}$$

From above equation, nearest neighbors choice will be $\left(0, \pm\sqrt{3}\right)a_{cc}$ and $\left(\pm\frac{3}{2}, \pm\frac{\sqrt{3}}{2}\right)a_{cc}$.

$$\vec{r}^{\,A,i} - \vec{r}^{\,B,j} = \left((n_1 - n_1^{'})\frac{3}{2} - 1\right)a_{cc}\hat{i} + \left((n_1 - n_1^{'})\frac{1}{2} + (n_2 - n_2^{'})\right)\sqrt{3}a_{cc}\hat{j}. \tag{3.64}$$

From above equation, nearest neighbors choice will be $(-1,0)a_{cc}$, $\left(\frac{1}{2},\frac{\sqrt{3}}{2}\right)a_{cc}$ and $\left(\frac{1}{2},-\frac{\sqrt{3}}{2}\right)a_{cc}$.

$$H = -t^{'}\sum_{\sigma}\sum_{<<i,j>>}\frac{1}{N}\sum_{\mathbf{k}}\left(e^{i\mathbf{k}\cdot(\mathbf{r}_{A,j}-\mathbf{r}_{A,i})}(a^{\dagger}_{\mathbf{k}\sigma}a_{\mathbf{k}\sigma}+b^{\dagger}_{\mathbf{k}\sigma}b_{\mathbf{k}\sigma})+h.c.\right) - t\sum_{<ij>\sigma}\frac{1}{N}\sum_{\mathbf{k}}\left(e^{-i\mathbf{k}\cdot(\mathbf{r}_{A,i}-\mathbf{r}_{B,j})}\ a^{\dagger}_{\mathbf{k}\sigma}b_{\mathbf{k}\sigma}+h.c.\right). \quad (3.65)$$

The Hamiltonian becomes

$$H = -t^{'}\sum_{\sigma}\sum_{\mathbf{k}}\left(g(\mathbf{k})(a^{\dagger}_{\mathbf{k}\sigma}a_{\mathbf{k}\sigma}+b^{\dagger}_{\mathbf{k}\sigma}b_{\mathbf{k}\sigma})+h.c.\right) - t\sum_{\sigma}\sum_{\mathbf{k}}\left(f(\mathbf{k})\ a^{\dagger}_{\mathbf{k}\sigma}b_{\mathbf{k}\sigma}+h.c.\right). \quad (3.66)$$

Here

$$g(\mathbf{k}) = e^{i\mathbf{k}\cdot(0,\sqrt{3})a_{cc}}+e^{i\mathbf{k}\cdot\left(0,-\sqrt{3}\right)a_{cc}}+e^{i\mathbf{k}\cdot(\frac{3}{2},\frac{\sqrt{3}}{2})a_{cc}}+e^{i\mathbf{k}\cdot\left(-\frac{3}{2},\frac{\sqrt{3}}{2}\right)a_{cc}} +e^{i\mathbf{k}\cdot\left(\frac{3}{2},-\frac{\sqrt{3}}{2}\right)a_{cc}}+e^{i\mathbf{k}\cdot\left(-\frac{3}{2},-\frac{\sqrt{3}}{2}\right)a_{cc}}, \quad (3.67)$$

$$f(\mathbf{k}) = e^{-i\mathbf{k}\cdot(-1,0)a_{cc}}+e^{-i\mathbf{k}\cdot\left(\frac{1}{2},\frac{\sqrt{3}}{2}\right)a_{cc}}+e^{-i\mathbf{k}\cdot\left(\frac{1}{2},-\frac{\sqrt{3}}{2}\right)a_{cc}}. \quad (3.68)$$

We can write above equation in form

$$g(\mathbf{k}) = e^{ip_y\sqrt{3}a_{cc}}+e^{-ip_y\sqrt{3}a_{cc}}+e^{i(p_x\frac{3}{2}+p_y\frac{\sqrt{3}}{2})a_{cc}}+e^{i(-\frac{3}{2}p_x+\frac{\sqrt{3}}{2}p_y)a_{cc}} +e^{i(\frac{3}{2}p_x-\frac{\sqrt{3}}{2}p_y)a_{cc}}+e^{i(-\frac{3}{2}p_x-\frac{\sqrt{3}}{2}p_y)a_{cc}}, \quad (3.69)$$

$$f(\mathbf{k}) = e^{ip_xa_{cc}}+e^{-i(\frac{1}{2}p_x+\frac{\sqrt{3}}{2}p_y)a_{cc}}+e^{-i(\frac{1}{2}p_x-\frac{\sqrt{3}}{2}p_y)a_{cc}}. \quad (3.70)$$

We expand around $K=(\frac{2\pi}{3a_{cc}},\frac{2\pi}{3\sqrt{3}a_{cc}})$, $\mathbf{k}=\mathbf{K}+\mathbf{p}$.

$$g(\mathbf{k}) = -3+\frac{9}{4}(p_x^2+p_y^2)+..., \quad (3.71)$$

$$f(\mathbf{k}) = \frac{3}{4}(-i-\sqrt{3})(p_x-ip_y)+\frac{3}{8}(i+\sqrt{3})p_xp_y+\frac{3}{16}(1-i\sqrt{3})p_x^2 +\frac{3}{16}i(i+\sqrt{3})p_y^2+..., \quad (3.72)$$

$$f(\mathbf{k}) = \frac{3}{4}(-i-\sqrt{3}) \ \ [(p_x - ip_y) + \frac{i}{4}(p_x + ip_y)^2] + ..., \tag{3.73}$$

$$f(\mathbf{k}) = -\frac{3}{2}e^{i\frac{\pi}{6}} \ \ [(p_x - ip_y) + \frac{i}{4}(p_x + ip_y)^2] + ... \tag{3.74}$$

The Hamiltonian is (the phase factor $e^{i\frac{\pi}{6}}$ may be absorbed into the definitions of a and b)

$$H = \begin{pmatrix} -2t^{'}\left(-3+\frac{9}{4}(pa_{cc})^2\right) & \frac{3ta_{cc}}{2} \ \ [(p_x - ip_y) + \frac{ia_{cc}}{4}(p_x + ip_y)^2] \\ \frac{3ta_{cc}}{2} \ \ [(p_x + ip_y) - \frac{ia_{cc}}{4}(p_x - ip_y)^2] & -2t^{'}\left[-3+\frac{9}{4}(pa_{cc})^2\right] \end{pmatrix}. \tag{3.75}$$

Here, $v_F = \frac{3ta_{cc}}{2}$ is the Fermi velocity.

3.9.3 Conventional Way (Old Approach) of Bloch-Siegert Shift in Graphene - Linear Dispersion

The graphene Hamiltonian has from

$$H = v_F \begin{bmatrix} 0 & p_x - ip_y \\ p_x + ip_y & 0 \end{bmatrix}. \tag{3.76}$$

On applying vector potential

$$H = v_F \begin{bmatrix} 0 & (p_x - ip_y) - \frac{e}{c}A_0^* e^{i\omega t} \\ (p_x + ip_y) - \frac{e}{c}A_0 e^{-i\omega t} & 0 \end{bmatrix}, \tag{3.77}$$

$$H = v_F \begin{bmatrix} 0 & (p_x - ip_y) \\ (p_x + ip_y) & 0 \end{bmatrix} + e^{-i\omega t} v_F \begin{bmatrix} 0 & 0 \\ -\frac{e}{c}A_0 & 0 \end{bmatrix} + e^{i\omega t} v_F \begin{bmatrix} 0 & -\frac{e}{c}A_0^* \\ 0 & 0 \end{bmatrix}. \tag{3.78}$$

We know $A_0 = A_0^* = \frac{c\omega_R}{ev_F}$ and ω_R is Rabi frequency.

$$H = v_F \begin{bmatrix} 0 & (p_x - ip_y) \\ (p_x + ip_y) & 0 \end{bmatrix} - e^{-i\omega t} \begin{bmatrix} 0 & 0 \\ \omega_R & 0 \end{bmatrix} - e^{i\omega t} \begin{bmatrix} 0 & \omega_R \\ 0 & 0 \end{bmatrix}. \tag{3.79}$$

From evolution equation

$$i\frac{\partial}{\partial t}\psi(t) = H\psi(t). \tag{3.80}$$

Let we write eigenvector

$$\psi(t) = \begin{bmatrix} u(t) \\ v(t) \end{bmatrix}. \tag{3.81}$$

For solving above evolution equation in case of graphene, first we do diagonalization by matrix

$$\begin{bmatrix} u(t) \\ v(t) \end{bmatrix} = \begin{pmatrix} \frac{ip_y - p_x}{\sqrt{p_x^2+p_y^2}} & \frac{p_x - ip_y}{\sqrt{p_x^2+p_y^2}} \\ 1 & 1 \end{pmatrix} \begin{bmatrix} u_1(t) \\ v_1(t) \end{bmatrix}. \tag{3.82}$$

Applying transformation $u_1(t) = e^{it\sqrt{p_x^2+p_y^2}} u_2(t)$ and $v_1(t) = e^{-it\sqrt{p_x^2+p_y^2}} v_2(t)$ (consider $\hbar = 1$, $v_F = 1$), we will get equations

$$i\frac{\partial}{\partial t}u_2(t) = \frac{e^{-it\omega}\sqrt{p_x^2+p_y^2}\omega_R}{2p_x+2ip_y}u_2(t) - \frac{e^{-it\left(\omega+2\sqrt{p_x^2+p_y^2}\right)}\left(p_x-ip_y\right)\omega_R}{2\sqrt{p_x^2+p_y^2}}v_2(t)$$

$$+\frac{e^{it\omega}\left(p_x+ip_y\right)\omega_R}{2\sqrt{p_x^2+p_y^2}}u_2(t) + \frac{e^{it\left(\omega-2\sqrt{p_x^2+p_y^2}\right)}\left(p_x+ip_y\right)\omega_R}{2\sqrt{p_x^2+p_y^2}}v_2(t), \tag{3.83}$$

$$i\frac{\partial}{\partial t}v_2(t) = \frac{e^{-it\left(\omega-2\sqrt{p_x^2+p_y^2}\right)}\sqrt{p_x^2+p_y^2}\omega_R}{2p_x+2ip_y}u_2(t) - \frac{e^{-it\omega}\left(p_x-ip_y\right)\omega_R}{2\sqrt{p_x^2+p_y^2}}v_2(t)$$

$$-\frac{e^{it\left(\omega+2\sqrt{p_x^2+p_y^2}\right)}\left(p_x+ip_y\right)\omega_R}{2\sqrt{p_x^2+p_y^2}}u_2(t) - \frac{e^{it\omega}\left(p_x+ip_y\right)\omega_R}{2\sqrt{p_x^2+p_y^2}}v_2(t). \tag{3.84}$$

For seeing effect of off resonance term, we are only considering them and leaving other term from above equation

$$i\frac{\partial}{\partial t}u_2(t) = -\frac{e^{-it\left(\omega+2\sqrt{p_x^2+p_y^2}\right)}\left(p_x-ip_y\right)\omega_R}{2\sqrt{p_x^2+p_y^2}}v_2(t), \tag{3.85}$$

$$i\frac{\partial}{\partial t}v_2(t) = -\frac{e^{it\left(\omega+2\sqrt{p_x^2+p_y^2}\right)}\left(p_x+ip_y\right)\omega_R}{2\sqrt{p_x^2+p_y^2}}u_2(t). \tag{3.86}$$

After substitution in eq. (3.86) in eq. (3.85), we get the equation

$$\left[\frac{\partial^2}{\partial t^2}u_2(t) + i\left(\omega + 2\sqrt{p_x^2+p_y^2}\right)\frac{\partial}{\partial t}u_2(t) + \frac{\omega_R^2}{4}u_2(t)\right] = 0. \tag{3.87}$$

The solution of above equation has form like $u_2(t) \propto e^{-i\alpha t}$, so we can write

$$-\alpha^2 + \left(\omega + 2\sqrt{p_x^2+p_y^2}\right)\alpha + \frac{\omega_R^2}{4} = 0, \tag{3.88}$$

$$\alpha = \frac{\left(\omega + 2\sqrt{p_x^2+p_y^2}\right)}{2} \pm \frac{\sqrt{\left(\omega + 2\sqrt{p_x^2+p_y^2}\right)^2 + \omega_R^2}}{2} = \alpha_{\pm}. \tag{3.89}$$

By Taylor's expansion, if $\omega, \omega_0 >> \kappa\varepsilon$

$$\alpha_+ \simeq \left(\omega + 2\sqrt{p_x^2+p_y^2}\right) + \frac{\omega_R^2}{4\left(\omega + 2\sqrt{p_x^2+p_y^2}\right)}, \tag{3.90}$$

$$\alpha_- \simeq -\frac{\omega_R^2}{4\left(\omega + 2\sqrt{p_x^2+p_y^2}\right)}. \tag{3.91}$$

The solution of equations (3.85,3.86) have form

$$u_2(t) = Ae^{-i\alpha_+ t} - \frac{(p_x - ip_y)\,\omega_R}{2\sqrt{p_x^2+p_y^2}}\frac{1}{\alpha_-}Be^{-i\alpha_- t}, \tag{3.92}$$

$$v_2(t) = -2\frac{\sqrt{p_x^2+p_y^2}}{(p_x - ip_y)\,\omega_R}Ae^{i(\omega+\omega_0-\alpha_+)t} + Be^{i(\omega+\omega_0-\alpha_-)t} \tag{3.93}$$

$$u_1(t) = e^{it\sqrt{p_x^2+p_y^2}}u_2(t), \tag{3.94}$$

$$v_1(t) = e^{-it\sqrt{p_x^2+p_y^2}}v_2(t). \tag{3.95}$$

So

$$\begin{bmatrix} u_1(t) \\ v_1(t) \end{bmatrix} = \begin{bmatrix} e^{it\sqrt{p_x^2+p_y^2}}u_2(t) \\ e^{-it\sqrt{p_x^2+p_y^2}}v_2(t) \end{bmatrix}, \tag{3.96}$$

$$\begin{bmatrix} u_1(t) \\ v_1(t) \end{bmatrix} = \begin{bmatrix} e^{it\sqrt{p_x^2+p_y^2}} \left(Ae^{-i\alpha_+ t} - \frac{(p_x-ip_y)\omega_R}{2\sqrt{p_x^2+p_y^2}} \frac{1}{\alpha_-} Be^{-i\alpha_- t} \right) \\ e^{-it\sqrt{p_x^2+p_y^2}} \left(-2\frac{\sqrt{p_x^2+p_y^2}}{(p_x-ip_y)\omega_R} Ae^{i(\omega+\omega_0-\alpha_+)t} + Be^{i(\omega+\omega_0-\alpha_-)t} \right) \end{bmatrix}, \tag{3.97}$$

$$\begin{bmatrix} u_1(t) \\ v_1(t) \end{bmatrix} = \begin{bmatrix} Ae^{-i\left(\alpha_+ - \sqrt{p_x^2+p_y^2}\right)t} - \frac{(p_x-ip_y)\omega_R}{2\sqrt{p_x^2+p_y^2}} \frac{1}{\alpha_-} Be^{-i\left(\alpha_- - \sqrt{p_x^2+p_y^2}\right)t} \\ -2\frac{\sqrt{p_x^2+p_y^2}}{(p_x-ip_y)\omega_R} Ae^{i(\omega+\frac{\omega_0}{2}-\alpha_+)t} + Be^{i(\omega+\frac{\omega_0}{2}-\alpha_-)t} \end{bmatrix}, \tag{3.98}$$

$$\begin{bmatrix} u(t) \\ v(t) \end{bmatrix} = \begin{pmatrix} \frac{ip_y-p_x}{\sqrt{p_x^2+p_y^2}} & \frac{p_x-ip_y}{\sqrt{p_x^2+p_y^2}} \\ 1 & 1 \end{pmatrix} \begin{bmatrix} u_1(t) \\ v_1(t) \end{bmatrix}, \tag{3.99}$$

$$\begin{bmatrix} u_1(t) \\ v_1(t) \end{bmatrix} = \begin{bmatrix} Ae^{-i\left(\alpha_+ - \frac{\omega_0}{2}\right)t} \\ Be^{i(\omega+\frac{\omega_0}{2}-\alpha_-)t} \end{bmatrix}, \tag{3.100}$$

$$\alpha_+ \simeq \left(\omega + 2\sqrt{p_x^2+p_y^2}\right) + \frac{\omega_R^2}{4\left(\omega + 2\sqrt{p_x^2+p_y^2}\right)}, \tag{3.101}$$

$$\alpha_- \simeq -\frac{\omega_R^2}{4\left(\omega + 2\sqrt{p_x^2+p_y^2}\right)}, \tag{3.102}$$

$$\begin{bmatrix} u_1(t) \\ v_1(t) \end{bmatrix} = \begin{bmatrix} Ae^{-i\left[\left(\omega+2\sqrt{p_x^2+p_y^2}\right)+\frac{\omega_R^2}{4\left(\omega+2\sqrt{p_x^2+p_y^2}\right)}-\frac{\omega_0}{2}\right]t} \\ Be^{i\left[\omega+\frac{\omega_0}{2}+\frac{\omega_R^2}{4\left(\omega+2\sqrt{p_x^2+p_y^2}\right)}\right]t} \end{bmatrix}, \tag{3.103}$$

$$\begin{bmatrix} u_1(t) \\ v_1(t) \end{bmatrix} = \begin{bmatrix} Ae^{-i\left(\omega+\frac{\omega_0}{2}+\alpha_-\right)t} \\ Be^{i(\omega+\frac{\omega_0}{2}+\alpha_-)t} \end{bmatrix}. \tag{3.104}$$

This implies that energy of upper level is shifted upward by $\hbar\alpha_-$ and lower level is shifted downward by $\hbar\alpha_-$.

$$2\hbar\alpha_- \simeq \frac{\hbar\omega_R^2}{2\left(\omega + 2\sqrt{p_x^2+p_y^2}\right)}. \tag{3.105}$$

If we want BS shift at resonance condition i.e.

$$\left(\omega - 2\sqrt{p_x^2 + p_y^2}\right) = 0 \Rightarrow \omega = 2\sqrt{p_x^2 + p_y^2}. \tag{3.106}$$

So

$$2\hbar\alpha_- \simeq \frac{\hbar\omega_R^2}{2\left(2\sqrt{p_x^2 + p_y^2} + 2\sqrt{p_x^2 + p_y^2}\right)} = \frac{\hbar\omega_R^2}{8\sqrt{p_x^2 + p_y^2}}. \tag{3.107}$$

This is Bloch-Siegert shift, which is exactly matching with eq.(3.30).

Chapter 4

A Theoretical Analysis of the Pump-Probe Experiment in Dirac-Weyl Systems

4.1 Introduction

In science, verification of a theory is usually accomplished by performing a suitable experiment. As theorists, our resources are limited and we are unable to perform the experiments ourselves. The next best alternative is to suggest an experiment and provide a detailed analysis of the outcome of this experiment. So that interested experimental groups with the requisite resources and expertise may then carry out the suggested experiments.

In this chapter, we have described pump-probe spectroscopy [62–64, 202, 214], which is used to justify the phenomenon of anomalous Rabi oscillations [155] - a central idea in this thesis. By using the pump-probe experiment, incoherent optical properties such as optical dephasing and relaxation of band electrons in semiconductors have been studied [48, 49]. In this experiment two successive laser pulses are used, one for exciting the system in a certain way, called pump pulse and other to test it after a variable time delay, called probe pulse. Femtosecond laser pulses are required for studying these incoherent optical properties because time scales for these phenomena are short (sub picosecond). The pump-probe technique can also be used for studying the coherent optical responses e.g. the excitonic optical Stark effect (EOSE) in a semiconductor [193–195]. In the thesis,

we have described an interesting, coherent optical phenomenon viz. anomalous Rabi oscillations using pump probe spectroscopy.

4.2 Problem Formulation

The pump-probe method is a well-known technique used to investigate nonlinear optical phenomena experimentally [63, 215, 216]. It involves exciting the sample with a high-intensity ultra-short duration laser light and then after a delay probing the sample with a much weaker version of the same pulse. This method has been used successfully to establish the presence of Rabi oscillations in semiconductors [215, 216]. Ultrafast carrier relaxation phenomenon has been studied experimentally by Breusing *et al.* [63] using the pump probe method in graphene. Conventionally, the differential transmission coefficient (DTC) is plotted as a function of time delay and the dephasing times are extracted from it. We wish to use this approach to establish the presence of anomalous Rabi oscillations. We do this by plotting the DTC not versus time delay but versus the duration of the pump pulse (alternatively, versus "area of the pump pulse") [215, 216]. When everything else remains fixed, this plot shows periodic oscillations with the characteristic anomalous Rabi frequency. Dephasing is introduced in a phenomenological manner to make the analysis more realistic, but is not the central theme of this analysis.

In this chapter, we describe the expected outcomes of an experiment for detection of anomalous Rabi oscillations (ARO) in Dirac-Weyl fermionic systems by performing a theoretical analysis of the proposed experiment. The experimental method, which we suggest for detecting anomalous Rabi frequency is known as the ultrafast pump probe technique. First, we derive rate equations for the amplitude of matter waves in a Dirac-Weyl fermionic system in the presence of a pump field considered as a pulse. Then we linearize evolution equation for a weak probe pulse and compute the differential transmission coefficient (the probe transmission with and without the pump) and see how this differential transmission coefficient behaves in various Dirac-Weyl fermionic systems. The differential transmission coefficient is seen to be an oscillatory function of the pump-probe delay. The slowest frequency that may be discerned from these oscillations is precisely the anomalous Rabi frequency. Hence this is an explicit experimental method to study these anomalous oscillations. Dephasing merely diminishes the amplitude of these oscillations but not the frequency.

In this chapter, we describe the pump-probe experiment. Typically this method is used to investigate incoherent phenomena such as dephasing. However, the aim of the present work is just the opposite viz. to study coherent phenomena using pump probe spectra. It is certainly true that by measuring the dependence of the differential transmission coefficient on the time delay between pump and probe pulses, it is possible to extract dephasing and other relaxation rates. However, it is interesting to note that from this plot (differential transmission coefficient vs. time delay) it is possible to infer the existence of anomalous Rabi oscillation which is a coherent phenomenon.

4.2.1 Pump-Probe Spectra in Graphene

Many studies have been conducted on dephasing of transient excitations in graphene placed on different substrates [62–67, 217, 218]. When graphene layers are epitaxially grown on SiC substrate [64], ultrafast relaxation of photogenerated carriers depend upon carrier-phonon and carrier-carrier scatterings. An examination of the plot between the differential transmission coefficient $\frac{T-T_0}{T_0}$ where, $T(T_0)$ is the probe transmission coefficient with (without) pump field, vs time delay between pump and probe pulse shows two types of relaxations τ_1 and τ_2 with a concomitant dependence on the pump pulse energy and temperature. The short relaxation time τ_1 has a range of $70-120fs$ and the long relaxation time τ_2 has a range $0.4-1.2ps$ [62]. Short relaxation τ_1 is due to the intraband carrier-carrier scattering, which produces quasiequilibrium states with a Fermi-Dirac distribution. The slower time delays τ_2 is typically due to intraband carrier-phonon scattering and is responsible for energy relaxation.

Considering the case of graphene on the mica substrate, the experimental plot between the differential transmission coefficient $\frac{T-T_0}{T_0}$ vs. delay time between pump and probe pulses of carrier relaxation by using femtosecond laser [63], is almost the same as earlier experiments [64] possess, some intermittent discrepancies in sign. First, there is some increase (almost linear) in differential transmission coefficient comes in the plot due to the presence of Pauli blocking [1] or due to the repulsion by the initially generated electron-hole density on further generated photoelectrons. Then there is a decrease in transmission coefficient; it comes in the plot due to intra-band carrier-carrier and intra-band carrier-phonon scattering. From this, we can conclude that carrier relaxation in graphene is almost same as that of graphite.

[1] Pauli blocking occurs when the final transition states are filled, so an incoming electron can no longer do that transition.

This shows that coupling between different graphite layers plays a minor role in ultrafast carrier relaxation. Time resolved terahertz spectroscopy is one of the powerful tool for investigation of carrier dynamics in semiconductors [218]. The study of multi-layer graphene nanostructures is very important for applications to optoelectronics [219, 220].

4.2.2 Pump-Probe Spectra in Topological Insulator

Many pump-probe studies have been carried out in TI, as described below. Optical pump-THz probe spectroscopy at low temperatures and the behavior of hot carrier response in thin Bi_2Se_3 films of several thicknesses are able to distinguish the bulk from surface transient response and can be utilized in future optoelectronic applications [221]. TI exhibits spin-dependent signals only during laser excitation. They reveal themselves while studying real and imaginary parts of the complex Kerr angle upon disentangling spin and lattice contributions. This signal is seen only when the pump-pulse is present and may be expressed in terms of Raman coherence time. So there is a coherent femtosecond control of spin-polarization for electronic states at near the Dirac cone [222]. Pump-probe spectroscopy can also be used to study carrier and phonon dynamics in Bi_2Se_3 crystals. There are oscillations in differential reflection, which have two distinct frequencies and are attributed to coherent optical and acoustic phonons, respectively [223]. Pump-probe photoemission spectroscopy has been used to study optically excited Dirac surface states in the bulk-insulating topological insulator Bi_2Te_2Se. The observed optical properties are in sharp contrast to those found in bulk-metallic topological insulators. There is a gigantic lifetime for excited surface states in the bulk of a TI, giving strong evidence for a power-law charge relaxation. This is evidence for two-dimensional electrodynamics and provides a direct optical signature of low bulk conductivity in a TI. From this observation, there is opportunity of development of optical devices, like optical p-n junction and a solar cell using optically excited Dirac surface states [224].

4.2.3 Pump-Probe Spectra in Weyl Semimetals

In future study, pump-probe ARPES (angle-resolved photoelectron spectroscopy) is able to see the Fermi arc in $Mo_xW_{1-x}Te_2$, which is a Weyl semimetal [225, 226]. By using first principles calculations it can be shown that femtosecond laser pulses with circularly polarized light can be used to switch between Weyl semimetal,

Dirac semimetal and topological insulator states in a generic three-dimensional (3D) Dirac material [227].

In the present work, theoretical modeling of the pump-probe experiment is done in order to observe the anomalous Rabi oscillations in these Dirac-Weyl fermionic systems. This is similar to experiments performed by the above authors especially Kumar et.al. [62], Breusing *et.al.* [63] and Dawalty *et.al.* [64]. While these authors focus on the incoherent aspects, the main focus of the present work is anomalous Rabi oscillations - a coherent phenomenon. If a quantum system interacts with a (classical) environment it is known as an open quantum system. This causes dissipation in the quantum system which manifests itself as a non-unitary time evolution of the wavefunction of the quantum system. It is imperative however, to ensure that probability is conserved even though the time evolution is non-unitary. This is typically done by the Lindblad super-operator method [228] which modifies the evolution equation of the density matrix of the quantum system. For the present purposes, a simpler alternative has been found which involves modifying the evolution equation for the wave function directly to include dissipation which leads to a nonunitary time evolution but is nevertheless probability conserving.

4.3 Dephasing in Open Quantum Systems: The Lindblad Superoperator

If a quantum system interacts with a (classical) environment, it is known as an open quantum system. This causes dissipation in the quantum system which manifests itself as a nonunitary time evolution of the wavefunction of the quantum system. It is imperative however, to ensure that probability is conserved even though the time evolution is non-unitary. This is typically done by the Lindblad super-operator method [228] which modifies the evolution equation of the density matrix of the quantum system. For our purposes, we have found a simpler alternative which involves modifying evolution equation for the wave function directly to include dissipation which leads to a nonunitary time evolution but is nevertheless probability conserving.

We know Liouville's equation in term of density matrix in a closed system is

$$i\dot{\rho} = [H, \rho]. \tag{4.1}$$

So its solution $\rho(t) = e^{iHt}\rho(0)e^{-iHt}$ will take form according to the (strongly continuous) unitary group related with Hamiltonian and density matrix is just a unitary conjugation of the density matrix from which we started. There is no change in the spectrum and the initial pure state (rank-one projection) always stays in a pure state.

However, if the external environment (bath) affects the system under study, the spectrum of ρ changes continuously. We can also choose a model (bath + system) with Hamiltonians and then solve the whole system. However, there is a way for trace out the bath directly and getting evolution equation for the remaining system for which we are interested. So we design a master equation for open quantum system known as Lindblad equation [228] has following form

$$\dot{\rho} = -i[H, \rho] + \sum \gamma \left(A\rho A^{\dagger} - \frac{1}{2}A^{\dagger}A\rho - \frac{1}{2}\rho A^{\dagger}A \right), \tag{4.2}$$

where second part of RHS of above equation known as the Lindblad superoperator and equation can be rewritten as:

$$\dot{\rho} = -i[H, \rho] + L(\rho). \tag{4.3}$$

The Lindblad superoperator $L(\rho)$ is used for environmental conditions that make up the open quantum system such as dephasing and relaxation. The operator A inside Lindblad superoperator is collapse operator and crucial for defining what the Lindblad superoperator describes. For different environments, different collapse operators are used. γ is an important constant which belongs from dephasing rate, rephasing rate, relaxation rate, etc. Actually, it is a corresponding rate for the coupling of the environment to the system.

4.4 The Pump-Probe Experiment

A quantum system typically interacts with the environment whose characteristics are known imprecisely. Such a system is known as an open quantum system. We have proposed an alternative to the Lindblad technique which involves introducing dephasing directly into the evolution equation of the amplitude of matter waves without compromising probability conservation. We now go on to discuss the various time scales and the phenomena that occur in those time scales. This

broadly consists of two parts - the times where the pump fields are present and the times when the system is being probed by a weak probe field.

4.4.1 Pump Equation

4.4.1.1 Case I: For Time $t < 0$:

In this case, the system is in equilibrium i.e. in the ground state, and no external field is applied. Evolution equation has the form

$$i\partial_t \psi(\mathbf{p}, t) = H_0(\mathbf{p})\psi(\mathbf{p}, t). \tag{4.4}$$

This means, $\psi(\mathbf{p}, t) = e^{-iH_0(\mathbf{p})t}\ \psi(\mathbf{p}, 0) \equiv \psi_{eq}(\mathbf{p}, t)$, where $\psi_{eq}(\mathbf{p}, t)$ is the reference equilibrium wavefunction of the bulk.

4.4.1.2 Case II: For Time $0 < t < t_{pu}$:

During this time the pump field is on and the wavefunction evolves in the following manner

$$i\partial_t \psi(\mathbf{p}, t) = H_0\left(\mathbf{p} - \frac{e}{c}\mathbf{A}(t)\right)\psi(\mathbf{p}, t). \tag{4.5}$$

Thus equation has a formal solution as follows

$$\psi(\mathbf{p}, t_{pu}) = T\left(e^{-i\int_0^{t_{pu}} H_0(\mathbf{p}-\frac{e}{c}\mathbf{A}(t'))dt'}\right)\ \psi(\mathbf{p}, 0), \tag{4.6}$$

where T is the time ordering symbol. We assume that for the duration of the pump pulse dephasing effects have not set in - largely due to the short time scales involved.

4.4.1.3 Case III: For Time $t > t_{pu}$:

Once the pump fields are turned off, dephasing sets in. Evolution equation is modified in the following manner to capture the phenomenon of dephasing

$$i\partial_t \psi(\mathbf{p}, t) = H_0(\mathbf{p})\psi(\mathbf{p}, t) - \frac{i}{T_2}\Big(\psi(\mathbf{p}, t) - \Lambda(t)\psi_{eq}(\mathbf{p}, t)\Big). \tag{4.7}$$

Here T_2 is a quantity which fixes the dephasing time scale and $\Lambda(t)$ is a real function of time which is called the dephasing scaling function which has to be chosen to ensure norm conservation. Furthermore it is such that $\Lambda(t \to \infty) = 1$ which ensures that long after the pump pulse is turned off, the wavefunction returns to the equilibrium form. This means

$$\psi(\mathbf{p},t) = e^{-i(t-t_{pu})H_0(\mathbf{p})} \left(e^{-\frac{(t-t_{pu})}{T_2}} \psi(\mathbf{p},t_{pu}) + \int_{t_{pu}}^{t} \frac{dt'}{T_2} e^{\frac{(t'-t)}{T_2}} \psi_{eq}(\mathbf{p},t_{pu}) \Lambda(t') \right). \tag{4.8}$$

On taking complex conjugate of eq.(4.8)

$$\psi^\dagger(\mathbf{p},t) = \left(e^{-\frac{(t-t_{pu})}{T_2}} \psi^\dagger(\mathbf{p},t_{pu}) + \int_{t_{pu}}^{t} \frac{dt'}{T_2} e^{\frac{(t'-t)}{T_2}} \psi^\dagger_{eq}(\mathbf{p},t_{pu}) \Lambda^*(t') \right) e^{i(t-t_{pu})H_0(\mathbf{p})}. \tag{4.9}$$

Now we are verifying probability conservation. So first we calculate $\psi^\dagger(\mathbf{p},t)\psi(\mathbf{p},t)$. However, as it stands there is no guarantee that this time evolution is norm-preserving. Probability (norm) conservation means, $1 = \sum_{\mathbf{p}} \psi^\dagger(\mathbf{p},t)\psi(\mathbf{p},t)$. Define $W = \sum_{\mathbf{p}} \psi^\dagger_{eq}(\mathbf{p},t_{pu})\psi(\mathbf{p},t_{pu})$ and

$$z(t) = \left(\int_{t_{pu}}^{t} \frac{dt'}{T_2} e^{\frac{(t'-t)}{T_2}} \Lambda(t') \right). \tag{4.10}$$

Hence imposing norm conservation implies

$$1 = e^{-\frac{(t-t_{pu})}{T_2}} \left(e^{-\frac{(t-t_{pu})}{T_2}} + W\ z^*(t) \right) + \left(e^{-\frac{(t-t_{pu})}{T_2}} W^* + z^*(t) \right) z(t), \tag{4.11}$$

$$1 = \left[e^{-\frac{2(t-t_{pu})}{T_2}} + \left(W\ z^*(t) + W^* z(t) \right) e^{-\frac{(t-t_{pu})}{T_2}} + z^*(t)z(t) \right]. \tag{4.12}$$

This in turn means the $\Lambda(t)$ - the dephasing scaling function, has to be chosen in such a way that eq.(4.12)

$$z(t) = \frac{1}{2} \left(\sqrt{(W+W^*-2)(W+W^*+2)e^{-\frac{2(t-t_{pu})}{T_2}} + 4} - (W+W^*)e^{\frac{t_{pu}-t}{T_2}} \right). \tag{4.13}$$

These choices ensure that not only is the evolution non-unitary and hence is able to capture dissipation effects but is also norm preserving which is mandatory in

quantum mechanics. The present approach is more direct than the usual approach based on the Lindblad superoperator method applied to the density matrix [228].

4.4.2 Probe Equations: $t > t_{pu} + \tau_d$

The effect produced by the pump pulse can be studied by a probe field which by virtue of being weak, obeys a equation that is linear in the probe strength. For linearizing evolution equation, we make the substitution $\psi(\mathbf{p},t) \rightarrow \psi(\mathbf{p},t) + \delta\psi(\mathbf{p},t)$. $\delta\psi(\mathbf{p},t)$ is the linear response function due to the probe pulse $\delta A(t)$. It is assumed that the probe pulse is switched on after a time delay τ_d after the pump pulse is tuned off. So

$$i\partial_t\Big(\psi(\mathbf{p},t)+\delta\psi(\mathbf{p},t)\Big) = \Big[H_0\Big(\mathbf{p}-\frac{e}{c}\big(\mathbf{A}(t)+\delta\mathbf{A}(t)\big)\Big)\Big]\Big(\psi(\mathbf{p},t)+\delta\psi(\mathbf{p},t)\Big). \tag{4.14}$$

Assume that derivatives of $H_0(\mathbf{p})$ higher than second in $\mathbf{p}$ vanish identically. We expand Taylor series expansion in following expression:

$$i\partial_t\Big(\psi(\mathbf{p},t)+\delta\psi(\mathbf{p},t)\Big) = \Big[H_0(p)-\frac{e}{c}\big(\mathbf{A}(t)+\delta\mathbf{A}(t)\big)\nabla_p H_0(p)\Big]\Big(\psi(\mathbf{p},t)+\delta\psi(\mathbf{p},t)\Big), \tag{4.15}$$

$$i\partial_t\Big(\psi(\mathbf{p},t)+\delta\psi(\mathbf{p},t)\Big) = H_0(p)\Big(\psi(\mathbf{p},t)+\delta\psi(\mathbf{p},t)\Big) - \frac{e}{c}\Big(\mathbf{A}(t)+\delta\mathbf{A}(t)\Big)\nabla_p H_0(p)\Big(\psi(\mathbf{p},t)+\delta\psi(\mathbf{p},t)\Big), \tag{4.16}$$

$$i\partial_t\Big(\psi(\mathbf{p},t)+\delta\psi(\mathbf{p},t)\Big) = H_0(p)\Big(\psi(\mathbf{p},t)+\delta\psi(\mathbf{p},t)\Big) - \frac{e}{c}\mathbf{A}(t)\Big(\psi(\mathbf{p},t) + \delta\psi(\mathbf{p},t)\Big) - \frac{e}{c}\delta\mathbf{A}(t)\nabla_p H_0(p)\Big(\psi(\mathbf{p},t)+\delta\psi(\mathbf{p},t)\Big). \tag{4.17}$$

Since we are discussing the case of non-overlapping pump and probe pulses. So the above equation becomes

$$i\partial_t\delta\psi(\mathbf{p},t) = H_0(\mathbf{p})\delta\psi(\mathbf{p},t) - \frac{e}{c}\Big(\delta\mathbf{A}(t)\cdot\nabla_{\mathbf{p}}H_0(\mathbf{p})\Big)\psi(\mathbf{p},t). \tag{4.18}$$

Define

$$\mathbf{V}(\mathbf{p},t') = e^{it'H_0(\mathbf{p})}\Big(\nabla_{\mathbf{p}}H_0(\mathbf{p})\Big)\ e^{-it'H_0(\mathbf{p})}. \tag{4.19}$$

Such that

$$\delta\psi(\mathbf{p},t) = \frac{ie}{c}\int_{t_{pu}+\tau_d}^{t} dt'\ e^{i(t'-t)H_0(\mathbf{p})}\Big(\delta\mathbf{A}(t')\cdot\mathbf{V}(\mathbf{p},t')\Big)\psi(\mathbf{p},t'), \tag{4.20}$$

where τ_d is the time delay between pump and probe. Hence the solution of above equation has the form

$$\delta\psi(\mathbf{p},t) = \frac{ie}{c}\int_{t_{pu}+\tau_d}^{t} dt'\ e^{i(t'-t)H_0(\mathbf{p})}\Big(\delta\mathbf{A}(t')\cdot\nabla_{\mathbf{p}}H_0(\mathbf{p})\Big)\psi(\mathbf{p},t'). \tag{4.21}$$

Here τ_d is time delay between probe and pump pulse.

4.4.2.1 Probe Without Pump

The probe response without pump is first studied and forms the reference against which deviations caused in the probe response had a pump pulse preceded it, could then be computed. The probe wavefunction in absence the the pump is denoted by $\delta\psi$. When the pump pulse preceded it the probe wavefunction is denoted by $\delta\psi_*$. In absence of the pump pulse

$$\delta\psi(\mathbf{p},t) = e^{-itH_0(\mathbf{p})}\ \frac{ie}{c}\int_{t_{pu}+\tau_d}^{t} dt'\ \Big(\delta\mathbf{A}(t')\cdot\mathbf{V}(\mathbf{p},t')\Big)\psi_{eq}(\mathbf{p},0). \tag{4.22}$$

4.4.2.2 Probe With Pump: $t > t_{pu}+\tau_d$

From the earlier section, we know

$$\psi(\mathbf{p},t) = e^{-i(t-t_{pu})H_0(\mathbf{p})}\ \left(e^{-\frac{(t-t_{pu})}{T_2}}\ \psi(\mathbf{p},t_{pu}) + z(t)\ \psi_{eq}(\mathbf{p},t_{pu})\right), \tag{4.23}$$

$$z(t) = \frac{1}{2}\left(\sqrt{(W+W^*-2)(W+W^*+2)e^{-\frac{2(t-t_{pu})}{T_2}}+4} - (W+W^*)e^{\frac{t_{pu}-t}{T_2}}\right). \tag{4.24}$$

In case of probe with pump $t - t_{pu} >> T_2$. So

$$z(t) \approx \frac{1}{2}\left(2 - (W + W^*)e^{\frac{t_{pu}-t}{T_2}}\right) \approx \left(1 - \frac{(W + W^*)}{2}\ e^{\frac{t_{pu}-t}{T_2}}\right). \tag{4.25}$$

Inserting the value of $z(t)$ in eq.(4.23)

$$\psi(\mathbf{p}, t) \approx \quad e^{-i(t-t_{pu})H_0(\mathbf{p})}\ \left[e^{-\frac{(t-t_{pu})}{T_2}}\ \psi(\mathbf{p}, t_{pu}) + \left(1 - \frac{(W + W^*)}{2}\ e^{\frac{t_{pu}-t}{T_2}}\right) \psi_{eq}(\mathbf{p}, t_{pu})\right], \tag{4.26}$$

$$\psi(\mathbf{p}, t) \approx \quad e^{-i(t-t_{pu})H_0(\mathbf{p})}\ \left[e^{-\frac{(t-t_{pu})}{T_2}}\ \psi(\mathbf{p}, t_{pu}) - \frac{(W + W^*)}{2}\ e^{-\frac{(t-t_{pu})}{T_2}}\psi_{eq}(\mathbf{p}, t_{pu})\right] + e^{-i(t-t_{pu})H_0(\mathbf{p})}\psi_{eq}(\mathbf{p}, t_{pu}), \tag{4.27}$$

$$\psi(\mathbf{p}, t) \approx \quad e^{-i(t-t_{pu})H_0(\mathbf{p})}e^{-\frac{(t-t_{pu})}{T_2}}\ \left[\ \psi(\mathbf{p}, t_{pu}) - \frac{(W + W^*)}{2}\ \psi_{eq}(\mathbf{p}, t_{pu})\right] + e^{-i(t-t_{pu})H_0(\mathbf{p})}\psi_{eq}(\mathbf{p}, t_{pu}). \tag{4.28}$$

Hence for $t - t_{pu} >> T_2$

$$\psi(\mathbf{p}, t) \approx \quad \psi_{eq}(\mathbf{p}, t) + e^{-\frac{(t-t_{pu})}{T_2}}\ e^{-i(t-t_{pu})H_0(\mathbf{p})}\ \left(\psi(\mathbf{p}, t_{pu}) - \frac{(W + W^*)}{2}\ \psi_{eq}(\mathbf{p}, t_{pu})\right), \tag{4.29}$$

where $e^{-i(t-t_{pu})H_0(\mathbf{p})}\psi_{eq}(\mathbf{p}, t_{pu}) = \psi_{eq}(\mathbf{p}, t)$. If we define

$$\phi(\mathbf{p}, t_{pu}) = e^{it_{pu}H_0(\mathbf{p})}\ \left(\psi(\mathbf{p}, t_{pu}) - \frac{(W + W^*)}{2}\ \psi_{eq}(\mathbf{p}, t_{pu})\right). \tag{4.30}$$

So

$$\psi(\mathbf{p}, t) \approx \psi_{eq}(\mathbf{p}, t) + e^{-\frac{(t-t_{pu})}{T_2}}\ e^{-itH_0(\mathbf{p})}\ \phi(\mathbf{p}, t_{pu}), \tag{4.31}$$

It is defined $t - t_{pu} = \tau_d$, then

$$\psi(\mathbf{p}, t) \approx \psi_{eq}(\mathbf{p}, t) + e^{-\frac{\tau_d}{T_2}}\ e^{-itH_0(\mathbf{p})}\ \phi(\mathbf{p}, t_{pu}). \tag{4.32}$$

So probe with pump have form

$$\delta\psi_*(\mathbf{p},t) = \frac{ie}{c}\int_{t_{pu}+\tau_d}^{t} dt'\ e^{i(t'-t)H_0(\mathbf{p})}\Big(\delta\mathbf{A}(t')\cdot\nabla_{\mathbf{p}}H_0(\mathbf{p})\Big) \Big(\psi_{eq}(\mathbf{p},t') + e^{-\frac{\tau_d}{T_2}}\ e^{-it'H_0(\mathbf{p})}\ \phi(\mathbf{p},t_{pu})\Big), \tag{4.33}$$

$$\delta\psi_*(\mathbf{p},t) = \Bigg[\frac{ie}{c}\int_{t_{pu}+\tau_d}^{t} dt'\ e^{i(t'-t)H_0(\mathbf{p})}\Big(\delta\mathbf{A}(t')\cdot\nabla_{\mathbf{p}}H_0(\mathbf{p})\Big)\psi_{eq}(\mathbf{p},t') + e^{-itH_0(\mathbf{p})}e^{-\frac{\tau_d}{T_2}}\frac{ie}{c}\int_{t_{pu}+\tau_d}^{t} dt'\ (\delta\mathbf{A}(t')\cdot e^{it'H_0(\mathbf{p})}\nabla_{\mathbf{p}}H_0(\mathbf{p})e^{-it'H_0(\mathbf{p})})\ \ \phi(\mathbf{p},t_{pu})\Bigg]. \tag{4.34}$$

Define

$$\delta\psi_{\text{NoPump}} = \frac{ie}{c}\int_{t_{pu}+\tau_d}^{t} dt'\ e^{i(t'-t)H_0(\mathbf{p})}(\delta\mathbf{A}(t')\cdot\nabla_{\mathbf{p}}H_0(\mathbf{p}))\psi_{eq}(\mathbf{p},t'). \tag{4.35}$$

So the above equation will be

$$\delta\psi_*(\mathbf{p},t) = \Big[\delta\psi_{\text{NoPump}} + e^{-itH_0(\mathbf{p})}e^{-\frac{\tau_d}{T_2}}\frac{ie}{c}\int_{t_{pu}+\tau_d}^{t} dt'\ (\delta\mathbf{A}(t')\cdot\mathbf{V}(\mathbf{p},t'))\ \phi(\mathbf{p},t_{pu})\Big], \tag{4.36}$$

where,

$$\mathbf{V}(\mathbf{p},t') = e^{it'H_0(\mathbf{p})}(\nabla_{\mathbf{p}}H_0(\mathbf{p}))\ e^{-it'H_0(\mathbf{p})}. \tag{4.37}$$

The differential transmission coefficient is defined as

$$\frac{\Delta T}{T} = \frac{\text{Integrated probe strength with pump} - \text{Integrated probe strength without pump}}{\text{Integrated probe strength without pump}}. \tag{4.38}$$

Hence

$$\frac{\Delta T}{T} = \frac{\sum_{\mathbf{p}} < (\delta\psi_*(\mathbf{p},t))^*\delta\psi_*(\mathbf{p},t) > - \sum_{\mathbf{p}} < (\delta\psi(\mathbf{p},t))^*\delta\psi(\mathbf{p},t) >}{\sum_{\mathbf{p}} < (\delta\psi(\mathbf{p},t))^*\delta\psi(\mathbf{p},t) >}. \tag{4.39}$$

Assuming $\tau_d >> T_2$. So

$$\frac{\Delta T}{T} = \frac{e^{-\frac{\tau_d}{T_2}} \sum_{\mathbf{p}} \left\langle \int_{t_{pu}+\tau_d}^{t} dt' \ \psi^{\dagger}_{eq}(\mathbf{p},0)(\delta\mathbf{A}^{*}(t')\cdot\mathbf{V}(\mathbf{p},t')) \ \int_{t_{pu}+\tau_d}^{t} dt' \ \delta\mathbf{A}(t')\cdot\mathbf{V}(\mathbf{p},t') \ \phi(\mathbf{p},t_{pu})\right\rangle + c.c.}{\sum_{\mathbf{p}} \left\langle \left| \int_{t_{pu}+\tau_d}^{t} dt' \ (\delta\mathbf{A}(t')\cdot\mathbf{V}(\mathbf{p},t'))\psi_{eq}(\mathbf{p},0)\right|^2 \right\rangle}. \tag{4.40}$$

4.5 Differential Transmission Coefficient of Dirac-Weyl Fermionic System

The computation of the differential transmission coefficient (DTC) involves summing over momenta in the Brillouin zone. In this work, we consider only low energy physics close to the Dirac/Weyl nodes. Therefore, it is imperative to look for physical quantities that are insensitive to short distance physics and are independent of large momentum cutoffs that are always needed to render integrals over momenta, finite. The DTC itself depends strongly of these cutoffs. Hence, we recommend studying the following ratio $\chi(t_{pu})$ (versus t_{pu}), which may be shown to be independent of large momentum cutoffs.

$$\chi(t_{pu}) = \frac{\frac{\partial}{\partial t_{pu}}\frac{\Delta T}{T}}{\frac{\partial}{\partial t_{pu}}\Big|_{t_{pu}=t_0}\frac{\Delta T}{T}}, \tag{4.41}$$

where t_{pu} is the pump duration and t_0 is some fixed pump duration which is in some fixed ratio relative to the intrinsic time scales in the problem.

4.5.1 Graphene and Weyl Semimetal

For graphene, the low energy Hamiltonian has form $H_0 = vp_x\sigma_x + vp_y\sigma_y$ so $\nabla_{\mathbf{p}}H_0 = v\sigma_x\hat{i} + v\sigma_y\hat{j}$. In case of Weyl semimetal, the low energy Hamiltonian has the form, $H_0 = vp_x\sigma_x + vp_y\sigma_y + +vp_z\sigma_z$ so $\nabla_{\mathbf{p}}H_0 = v\sigma_x\hat{i} + v\sigma_y\hat{j} + v\sigma_z\hat{k}$. We have defined

$$\mathbf{V}(\mathbf{p},t') = e^{it'H_0(\mathbf{p})}\Big(\nabla_{\mathbf{p}}H_0(\mathbf{p})\Big) \ e^{-it'H_0(\mathbf{p})}. \tag{4.42}$$

Vector potential $\mathbf{A}(t)$ has form

$$\mathbf{A}(t) = A_x(t)\hat{i} + A_y(t)\hat{j} + A_z(t)\hat{k}, \tag{4.43}$$

$$\mathbf{A}(t) = \frac{A_{x0}e^{i\omega t} + A^*_{x0}e^{-i\omega t}}{2}\hat{i} + \frac{A_{y0}e^{i\omega t} + A^*_{y0}e^{-i\omega t}}{2}\hat{j} + \frac{A_{z0}e^{i\omega t} + A^*_{z0}e^{-i\omega t}}{2}\hat{k}. \quad (4.44)$$

Applying condition $A_{x0} = A$, $A_{y0} = Ae^{i\frac{\pi}{2}} = iA$ and $A_{z0} = 0$

$$\mathbf{A}(t) = A\cos(\omega t)\hat{i} + A\sin(\omega t)\hat{j}. \quad (4.45)$$

So vector potential in probe has form

$$\delta\mathbf{A}(t) = \delta A\big(\cos(\omega t)\hat{i} + \sin(\omega t)\hat{j}\big). \quad (4.46)$$

So

$$\Big(\delta\mathbf{A}(t')\cdot\mathbf{V}(\mathbf{p},t')\Big) = \delta A\Big[\cos(\omega t^{'})e^{it'H_0(\mathbf{p})}v\sigma_x e^{-it'H_0(\mathbf{p})} + \sin(\omega t^{'})e^{it'H_0(\mathbf{p})}v\sigma_y e^{-it'H_0(\mathbf{p})}\Big]. \quad (4.47)$$

Let's take first part of numerator of eq. (4.40)

$$= \int_{t_{pu}+\tau_d}^{t} dt'\ \psi^{\dagger}_{eq}(\mathbf{p},0)(\delta\mathbf{A}^*(t')\cdot\mathbf{V}(\mathbf{p},t')), \quad (4.48)$$

$$= \int_{t_{pu}+\tau_d}^{t} dt'\ \psi^{\dagger}_{eq}(\mathbf{p},0)\delta A\Big[\cos(\omega t^{'})e^{it'H_0(\mathbf{p})}v\sigma_x e^{-it'H_0(\mathbf{p})} + \sin(\omega t^{'})e^{it'H_0(\mathbf{p})}v\sigma_y e^{-it'H_0(\mathbf{p})}\Big], \quad (4.49)$$

$$= \int_{t_{pu}+\tau_d}^{t} dt'\ \psi^{\dagger}_{eq}(\mathbf{p},0)\delta A\cos(\omega t^{'})e^{it'H_0(\mathbf{p})}v\sigma_x e^{-it'H_0(\mathbf{p})} + \int_{t_{pu}+\tau_d}^{t} dt'\ \psi^{\dagger}_{eq}(\mathbf{p},0)\delta A\sin(\omega t^{'})e^{it'H_0(\mathbf{p})}v\sigma_y e^{-it'H_0(\mathbf{p})}. \quad (4.50)$$

If ω is very large

$$= \psi^{\dagger}_{eq}(\mathbf{p},0)e^{itH_0(\mathbf{p})}v\sigma_x e^{-itH_0(\mathbf{p})}\delta A\int_{t_{pu}+\tau_d}^{t} dt'\cos(\omega t^{'}) + \psi^{\dagger}_{eq}(\mathbf{p},0)e^{itH_0(\mathbf{p})}v\sigma_y e^{-itH_0(\mathbf{p})}\delta A\int_{t_{pu}+\tau_d}^{t} dt'\ \sin(\omega t^{'}), \quad (4.51)$$

$$= \psi^{\dagger}_{eq}(\mathbf{p},0)e^{itH_0(\mathbf{p})}v\sigma_x e^{-itH_0(\mathbf{p})}\frac{\delta A}{\omega}\left[\sin(\omega t)-\sin(\omega(t_{pu}+\tau_d))\right]$$
$$-\psi^{\dagger}_{eq}(\mathbf{p},0)e^{itH_0(\mathbf{p})}v\sigma_y e^{-itH_0(\mathbf{p})}\frac{\delta A}{\omega}\left[\cos(\omega t)-\cos(\omega(t_{pu}+\tau_d))\right], \quad (4.52)$$

$$= \frac{\delta A}{\omega}\psi^{\dagger}_{eq}(\mathbf{p},0)\Big[e^{itH_0(\mathbf{p})}v\sigma_x e^{-itH_0(\mathbf{p})}\left[\sin(\omega t)-\sin(\omega(t_{pu}+\tau_d))\right]$$
$$-e^{itH_0(\mathbf{p})}v\sigma_y e^{-itH_0(\mathbf{p})}\left[\cos(\omega t)-\cos(\omega(t_{pu}+\tau_d))\right]\Big], \quad (4.53)$$

Other term of of numerator of eq. (4.40)

$$= \int_{t_{pu}+\tau_d}^{t} dt'\ \delta\mathbf{A}(t')\cdot\mathbf{V}(\mathbf{p},t')\ \phi(\mathbf{p},t_{pu}). \quad (4.54)$$

If ω is very large

$$= \frac{\delta A}{\omega}\left[e^{itH_0(\mathbf{p})}v\sigma_x e^{-itH_0(\mathbf{p})}\left[\sin(\omega t)-\sin(\omega(t_{pu}+\tau_d))\right]\right.$$
$$\left.-e^{itH_0(\mathbf{p})}v\sigma_y e^{-itH_0(\mathbf{p})}\left[\cos(\omega t)-\cos(\omega(t_{pu}+\tau_d))\right]\right]\phi(\mathbf{p},t_{pu}). \quad (4.55)$$

So

$$\int_{t_{pu}+\tau_d}^{t} dt'\ \psi^{\dagger}_{eq}(\mathbf{p},0)(\delta\mathbf{A}^*(t')\cdot\mathbf{V}(\mathbf{p},t'))\ \int_{t_{pu}+\tau_d}^{t} dt'\ \delta\mathbf{A}(t')\cdot\mathbf{V}(\mathbf{p},t')\ \phi(\mathbf{p},t_{pu})$$

$$= \frac{\delta A}{\omega}\psi^{\dagger}_{eq}(\mathbf{p},0)\left[e^{itH_0(\mathbf{p})}v\sigma_x e^{-itH_0(\mathbf{p})}\left[\sin(\omega t)-\sin(\omega(t_{pu}+\tau_d))\right]\right.$$
$$\left.-e^{itH_0(\mathbf{p})}v\sigma_y e^{-itH_0(\mathbf{p})}\left[\cos(\omega t)-\cos(\omega(t_{pu}+\tau_d))\right]\right]$$
$$\times\frac{\delta A}{\omega}\psi^{\dagger}_{eq}(\mathbf{p},0)\left[e^{itH_0(\mathbf{p})}v\sigma_x e^{-itH_0(\mathbf{p})}\left[\sin(\omega t)-\sin(\omega(t_{pu}+\tau_d))\right]\right.$$
$$\left.-e^{itH_0(\mathbf{p})}v\sigma_y e^{-itH_0(\mathbf{p})}\left[\cos(\omega t)-\cos(\omega(t_{pu}+\tau_d))\right]\right]\phi(\mathbf{p},t_{pu}), \quad (4.56)$$

$$= \left(\frac{\delta A}{\omega}\right)^2\psi^{\dagger}_{eq}(\mathbf{p},0)\Big(\left[\sin^2(\omega t)+\sin^2(\omega(t_{pu}+\tau_d))-2\sin(\omega t)\sin(\omega(t_{pu}+\tau_d))\right]$$
$$e^{itH_0(\mathbf{p})}v^2\sigma_x^2 e^{-itH_0(\mathbf{p})}-\left[\cos(\omega t)-\cos(\omega(t_{pu}+\tau_d))\right]\left[\sin(\omega t)-\sin(\omega(t_{pu}+\tau_d))\right]$$
$$e^{itH_0(\mathbf{p})}v^2\sigma_y\sigma_x e^{-itH_0(\mathbf{p})}-\left[\sin(\omega t)-\sin(\omega(t_{pu}+\tau_d))\right]\left[\cos(\omega t)-\cos(\omega(t_{pu}+\tau_d))\right]$$
$$e^{itH_0(\mathbf{p})}v^2\sigma_x\sigma_y e^{-itH_0(\mathbf{p})}+\left[\cos^2(\omega t)+\cos^2(\omega(t_{pu}+\tau_d))-2\cos(\omega t)\cos(\omega(t_{pu}+\tau_d))\right]$$
$$e^{itH_0(\mathbf{p})}v^2\sigma_y^2 e^{-itH_0(\mathbf{p})}\Big)\phi(\mathbf{p},t_{pu}), \quad (4.57)$$

After taking time average, $\cos(\omega t)\sin(\omega t)$ type terms will cancel, $\cos^2(\omega t)$ and $\sin^2(\omega t)$ become $\frac{1}{2}$

$$= \left(\frac{\delta A}{\omega}\right)^2 \psi^\dagger_{eq}(\mathbf{p},0)\left(\left[\frac{1}{2}+\frac{1}{2}\right]e^{itH_0(\mathbf{p})}v^2\sigma_x^2e^{-itH_0(\mathbf{p})}+\left[\frac{1}{2}+\frac{1}{2}\right]e^{itH_0(\mathbf{p})}v^2\sigma_y^2e^{-itH_0(\mathbf{p})}\right)\phi(\mathbf{p},t_{pu}), \tag{4.58}$$

$$= \left(\frac{\delta A}{\omega}\right)^2 \psi^\dagger_{eq}(\mathbf{p},0)\left(e^{itH_0(\mathbf{p})}v^2\sigma_x^2e^{-itH_0(\mathbf{p})}+e^{itH_0(\mathbf{p})}v^2\sigma_y^2e^{-itH_0(\mathbf{p})}\right)\phi(\mathbf{p},t_{pu}). \tag{4.59}$$

For graphene, term in numerator

$$\left\langle \int_{t_{pu}+\tau_d}^{t} dt'\ \psi^\dagger_{eq}(\mathbf{p},0)(\delta\mathbf{A}^*(t')\cdot\mathbf{V}(\mathbf{p},t'))\ \int_{t_{pu}+\tau_d}^{t} dt'\ \delta\mathbf{A}(t')\cdot\mathbf{V}(\mathbf{p},t')\ \phi(\mathbf{p},t_{pu})\right\rangle$$

$$= \left(\frac{\delta A}{\omega}\right)^2 v^2\psi^\dagger_{eq}(\mathbf{p},0)\left[\begin{pmatrix}1&0\\0&1\end{pmatrix}+\begin{pmatrix}1&0\\0&1\end{pmatrix}\right]\phi(\mathbf{p},t_{pu}), \tag{4.60}$$

$$= 2\left(\frac{\delta A}{\omega}\right)^2 v^2\psi^\dagger_{eq}(\mathbf{p},0)\phi(\mathbf{p},t_{pu}). \tag{4.61}$$

Applying same procedure in the denominator of eq. (4.40) for graphene, given that ω is very large

$$\left\langle \left| \int_{t_{pu}+\tau_d}^{t} dt'\ (\delta\mathbf{A}(t')\cdot\mathbf{V}(\mathbf{p},t'))\psi_{eq}(\mathbf{p},0)\right|^2\right\rangle$$

$$= \left(\frac{\delta A}{\omega}\right)^2 \psi^\dagger_{eq}(\mathbf{p},0)\left(e^{itH_0(\mathbf{p})}v^2\sigma_x^2e^{-itH_0(\mathbf{p})}+e^{itH_0(\mathbf{p})}v^2\sigma_y^2e^{-itH_0(\mathbf{p})}\right)\psi_{eq}(\mathbf{p},0), \tag{4.62}$$

$$= 2\left(\frac{\delta A}{\omega}\right)^2 v^2\psi^\dagger_{eq}(\mathbf{p},0)\begin{pmatrix}1&0\\0&1\end{pmatrix}\psi_{eq}(\mathbf{p},0) = 2\left(\frac{\delta A}{\omega}\right)^2 v^2. \tag{4.63}$$

Hence the DTC for graphene and Weyl semimetal from eq. (4.40)

$$\frac{\Delta T}{T} = \frac{e^{-\frac{\tau_d}{T_2}} \sum_{\mathbf{p}} \left(\frac{\delta A}{\omega}\right)^2 \psi^{\dagger}_{eq}(\mathbf{p},0) \left(e^{itH_0(\mathbf{p})} v^2 \sigma_x^2 e^{-itH_0(\mathbf{p})} + e^{itH_0(\mathbf{p})} v^2 \sigma_y^2 e^{-itH_0(\mathbf{p})}\right) \phi(\mathbf{p}, t_{pu}) + c.c.}{\sum_{\mathbf{p}} \left(\frac{\delta A}{\omega}\right)^2 \psi^{\dagger}_{eq}(\mathbf{p},0) \left(e^{itH_0(\mathbf{p})} v^2 \sigma_x^2 e^{-itH_0(\mathbf{p})} + e^{itH_0(\mathbf{p})} v^2 \sigma_y^2 e^{-itH_0(\mathbf{p})}\right) \psi_{eq}(\mathbf{p},0)}, \tag{4.64}$$

$$\frac{\Delta T}{T} = e^{-\frac{\tau_d}{T_2}} \frac{\sum_{\mathbf{p}} 2 \left(\frac{\delta A}{\omega}\right)^2 v^2 \psi^{\dagger}_{eq}(\mathbf{p},0) \phi(\mathbf{p}, t_{pu}) + c.c.}{\sum_{\mathbf{p}} 2 \left(\frac{\delta A}{\omega}\right)^2 v^2 \psi^{\dagger}_{eq}(\mathbf{p},0) \psi_{eq}(\mathbf{p},0)}, \tag{4.65}$$

$$\frac{\Delta T}{T} = e^{-\frac{\tau_d}{T_2}} \frac{\sum_{\mathbf{p}} \psi^{\dagger}_{eq}(\mathbf{p},0) \phi(\mathbf{p}, t_{pu}) + c.c.}{\sum_{\mathbf{p}} \psi^{\dagger}_{eq}(\mathbf{p},0) \psi_{eq}(\mathbf{p},0)}. \tag{4.66}$$

We know

$$\psi_{eq}(\mathbf{p},t) = e^{-iH_0(\mathbf{p})t}\ \psi(\mathbf{p},0) \Rightarrow \psi_{eq}(\mathbf{p},0) = \ \psi(\mathbf{p},0), \tag{4.67}$$

$$\phi(\mathbf{p}, t_{pu}) = e^{it_{pu}H_0(\mathbf{p})} \left(\psi(\mathbf{p}, t_{pu}) - \frac{(W + W^*)}{2}\ \psi_{eq}(\mathbf{p}, t_{pu})\right), \tag{4.68}$$

$$W = \sum_{\mathbf{p}} \psi^{\dagger}_{eq}(\mathbf{p}, t_{pu}) \psi(\mathbf{p}, t_{pu}). \tag{4.69}$$

We defined

$$\psi(\mathbf{p},t) = \frac{\psi^{'}(\mathbf{p},0) \sin\left(t\Omega_{\mathrm{ARWA}}(p)\right)}{\Omega_{ARWA}(p)} + \psi(\mathbf{p},0) \cos\left(t\Omega_{\mathrm{ARWA}}(p)\right), \tag{4.70}$$

$$\psi^{'}(\mathbf{p},0) = -iH_{eff}(p)\psi(\mathbf{p},0) \quad \text{(From evolution equation)}. \tag{4.71}$$

So

$$\psi(\mathbf{p},t) = -i\frac{H_{eff}(p)\sin(t\ \Omega_{\mathrm{ARWA}}(p))}{\Omega_{\mathrm{ARWA}}(p)}\psi(\mathbf{p},0) + \psi(\mathbf{p},0)\cos(t\ \Omega_{\mathrm{ARWA}}(p)). \tag{4.72}$$

If we take

$$\psi_{eq}(p,t) = \frac{\mathrm{N}^{eq}_{\psi}(p,t)}{\sqrt{\alpha^{eq}_{\psi}}}, \tag{4.73}$$

$$\psi(p,t) = \frac{\mathrm{N}_\psi(p,t)}{\sqrt{\alpha_\psi}}. \tag{4.74}$$

We know

$$\int \psi^\dagger(p,t)\psi(p,t)d^3p = 1. \tag{4.75}$$

So

$$\alpha_\psi = \int_0^\infty |\mathrm{N}_\psi(p,t)|^2 dp \to \infty. \tag{4.76}$$

Similarly

$$\alpha_\psi^{eq} = \int_0^\infty |\mathrm{N}_\psi^{eq}(p,t)|^2 dp \to \infty, \tag{4.77}$$

$$W = \sum_{\mathbf{p}} \psi_{eq}^\dagger(\mathbf{p},t_{pu})\psi(\mathbf{p},t_{pu}) = \int d^3p\ \psi_{eq}^\dagger(\mathbf{p},t_{pu})\psi(\mathbf{p},t_{pu}), \tag{4.78}$$

$$W = \int d^3p\ \psi_{eq}^\dagger(\mathbf{p},t_{pu})\Big(\psi(\mathbf{p},t_{pu}) - \psi_{eq}(\mathbf{p},t_{pu})\Big) + \int d^3p\ \psi_{eq}^\dagger(\mathbf{p},t_{pu})\psi_{eq}(\mathbf{p},t_{pu}), \tag{4.79}$$

$$W = \int d^3p\ \psi_{eq}^\dagger(\mathbf{p},t_{pu})\Big(\psi(\mathbf{p},t_{pu}) - \psi_{eq}(\mathbf{p},t_{pu})\Big) + 1, \tag{4.80}$$

$$W = \frac{\int d^3p\ \mathrm{N}_\psi^{eq^\dagger}(p,t)\Big(\psi(\mathbf{p},t_{pu}) - \psi_{eq}(\mathbf{p},t_{pu})\Big)}{\sqrt{\alpha_\psi^{eq}}} + 1. \tag{4.81}$$

We have observed earlier that $\alpha_\psi^{eq} \to \infty$. However, the term $\int d^3p \mathrm{N}_\psi^{eq^\dagger}(p,t)\Big(\psi(\mathbf{p},t_{pu}) - \psi_{eq}(\mathbf{p},t_{pu})\Big)$ is finite. Hence

$$\frac{\int d^3p\ \mathrm{N}_\psi^{eq^\dagger}(p,t)\Big(\psi(\mathbf{p},t_{pu}) - \psi_{eq}(\mathbf{p},t_{pu})\Big)}{\sqrt{\alpha_\psi^{eq}}} \to 0. \tag{4.82}$$

So we can take value of $W = 1$. Hence

$$\phi(\mathbf{p}, t_{pu}) = e^{it_{pu}H_0(\mathbf{p})} \Big(\psi(\mathbf{p}, t_{pu}) - \ \psi_{eq}(\mathbf{p}, t_{pu})\Big). \tag{4.83}$$

And

$$\frac{\Delta T}{T} = e^{-\frac{\tau_d}{T_2}} \ \frac{\sum_{\mathbf{p}} \psi^{\dagger}_{eq}(\mathbf{p}, 0)\phi(\mathbf{p}, t_{pu}) + c.c.}{\sum_{\mathbf{p}} \psi^{\dagger}_{eq}(\mathbf{p}, 0)\psi_{eq}(\mathbf{p}, 0)}, \tag{4.84}$$

$$\frac{\Delta T}{T} = e^{-\frac{\tau_d}{T_2}} \ \frac{\sum_{\mathbf{p}} \psi^{\dagger}_{eq}(\mathbf{p}, 0)e^{it_{pu}H_0(\mathbf{p})} \Big(\psi(\mathbf{p}, t_{pu}) - \ \psi_{eq}(\mathbf{p}, t_{pu})\Big) + c.c.}{\sum_{\mathbf{p}} \psi^{\dagger}_{eq}(\mathbf{p}, 0)\psi_{eq}(\mathbf{p}, 0)}. \tag{4.85}$$

Here $\psi_{eq}(\mathbf{p}, t) = e^{-iH_0(\mathbf{p})t} \ \psi(\mathbf{p}, 0)$ is stationary state, so we can replace operator H_0 by ground state energy and $\psi(\mathbf{p}, 0)$ by ground state eigenvalue of above Hamiltonian

$$\psi_{eq}(\mathbf{p}, t) = e^{-iEt} \ \psi(\mathbf{p}, 0) \Rightarrow \psi_{eq}(\mathbf{p}, t_{pu}) = e^{-iEt_{pu}} \ \psi(\mathbf{p}, 0). \tag{4.86}$$

$\psi(\mathbf{p}, t_{pu})$ is defined as

$$\psi(\mathbf{p}, t_{pu}) = -i\frac{H_{eff}(p)\sin(t_{pu}\Omega_{\mathrm{ARWA}}(p))}{\Omega_{\mathrm{ARWA}}(p)}\psi(\mathbf{p}, 0) + \psi(\mathbf{p}, 0)\cos\left(t_{pu}\Omega_{\mathrm{ARWA}}(\mathbf{p})\right). \tag{4.87}$$

For graphene

$$H_0(p) = v\begin{bmatrix} 0 & p_x - ip_y \\ p_x + ip_y & 0 \end{bmatrix}. \tag{4.88}$$

Consider the polar form of momentum $p_x = p\cos\theta$ and $p_y = p\sin\theta$, then the ground state eigenvector and eigenvalues of H_0 becomes

$$\psi(\mathbf{p}, 0) = \frac{1}{\sqrt{2}}\begin{pmatrix} -e^{-i\theta} \\ 1 \end{pmatrix} \quad \text{and} \quad E = -v|p|. \tag{4.89}$$

So

$$\psi_{eq}(\mathbf{p}, t_{pu}) = \ \frac{e^{iv|p|\ t_{pu}}}{\sqrt{2}}\begin{pmatrix} -e^{-i\theta} \\ 1 \end{pmatrix}. \tag{4.90}$$

H_{eff} for graphene from eq. (2.53)

$$H_{eff} = \begin{pmatrix} -\frac{\omega \mathrm{R}^2}{\omega} & e^{-i\theta}pv \\ e^{i\theta}pv & \frac{\omega \mathrm{R}^2}{\omega} \end{pmatrix}. \tag{4.91}$$

The value of the anomalous Rabi frequency Ω_{ARWA} for graphene [152]

$$\Omega_{\mathrm{ARWA}} = 2\sqrt{v^2\left(p_x^2 + p_y^2\right) + \left(\frac{\omega_R^2}{\omega}\right)^2}. \tag{4.92}$$

Similarly, for Weyl semimetal

$$H_0(p) = v\begin{bmatrix} p_z & p_x - ip_y \\ p_x + ip_y & -p_z \end{bmatrix}. \tag{4.93}$$

Consider the spherical form of momentum $p_x = p\cos\theta\sin\phi$, $p_y = p\sin\theta\sin\phi$ and $p_z = p\cos\phi$, then the ground state eigenvector and eigenvalues of H_0 becomes

$$\psi(\mathbf{p}, 0) = \begin{pmatrix} -\frac{e^{-i\theta}\tan\left(\frac{\phi}{2}\right)}{\sqrt{\sec^2\left(\frac{\phi}{2}\right)}} \\ \frac{1}{\sqrt{\sec^2\left(\frac{\phi}{2}\right)}} \end{pmatrix} \quad \text{and} \quad E = -v|p|. \tag{4.94}$$

$$H_{eff} = \begin{pmatrix} pv\cos(\phi) - \frac{\omega \mathrm{R}^2}{\omega} & e^{-i\theta}pv\sin(\phi) \\ e^{i\theta}pv\sin(\phi) & \frac{\omega \mathrm{R}^2}{\omega} - pv\cos(\phi) \end{pmatrix} \tag{4.95}$$

The anomalous Rabi frequency for a Weyl semimetal (from chapter (2))

$$\Omega_{\mathrm{ARWA}} = 2\sqrt{v^2\left(p_x^2 + p_y^2\right) + \left(vp_z - \frac{\omega_R'^2}{\omega}\right)^2}, \tag{4.96}$$

where $\omega_R' = \frac{ev_F}{c}A$ is a parameter which is of the order of the conventional Rabi frequency. Collecting everything together in eq. (4.85), we obtain the transmission coefficient of graphene and Weyl semimetals.

4.5.2 Topological Insulator (TI)

In this section, we study anomalous Rabi oscillations in a two dimensional topological insulator in the bulk. In case this material is finite in one of the directions

(ribbon), it possesses one dimensional boundaries (edges). The low energy Hamiltonian of this system in the bulk has form [2]

$$H_0 = vp_x\sigma_x + vp_y\sigma_y + \left(C - B(p_x^2 + p_y^2)\right)\sigma_z, \tag{4.97}$$

where $C = mv^2$ is the band gap and v has dimensions of speed. Also m and B^{-1} have dimensions of mass. It is well-known that if $BC > 0$, the system is topologically nontrivial and possesses gapless edge states and if $BC < 0$ it becomes topologically trivial and there are no such edge states. Thus when B and C have the same sign, the Chern number is not zero (nontrivial) and have opposite signs when the Chern number is zero (trivial). When the Chern number is not zero, there are surface states with zero energy. Here we wish to establish this fact by examining the behaviour of the pump-probe spectra of the bulk without referring to the edge states. We have found that by choosing a special value for the conventional Rabi frequency ω_R (i.e. by tuning the intensity of the pump pulse) viz. $\omega_R = \sqrt{\omega|C|}$, the anomalous Rabi frequency versus the wave vector is gapless when the Chern number is nonzero and gapped when the Chern number is zero. A conventional or anomalous exponent in the power-law decay of the amplitude of the oscillatory dependence of the DTC on the pump-pulse duration (with all else held fixed) is seen, as a result.

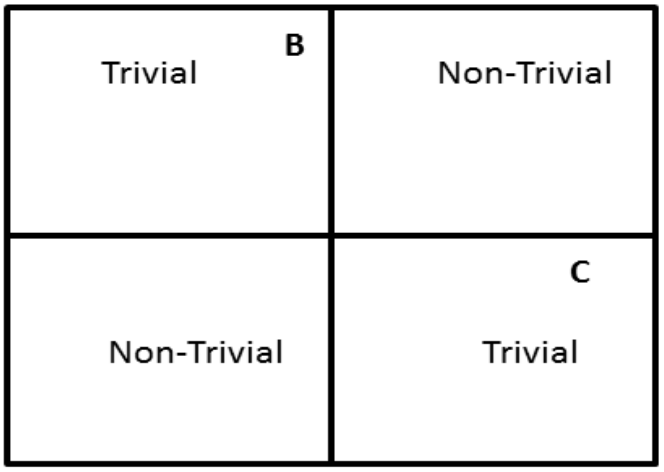

FIGURE 4.1: Phase diagram of topological states.

Expanding eq. (4.97)

$$H_0 = v\underbrace{\begin{bmatrix} 0 & (p_x - ip_y) \\ (p_x + ip_y) & 0 \end{bmatrix}}_{\text{First Part}} + \underbrace{\begin{bmatrix} \left(C - B(p_x^2 + p_y^2)\right) & 0 \\ 0 & -\left(C - B(p_x^2 + p_y^2)\right) \end{bmatrix}}_{\text{Second Part}}. \tag{4.98}$$

On applying potential

$$p^2 = \left(p_x - \frac{e}{c}A_x\right)^2 + \left(p_y - \frac{e}{c}A_y\right)^2, \tag{4.99}$$

$$p^2 = \left[p_x - \frac{e}{2c}\left(A_{x0}e^{i\omega t} + A_{x0}^* e^{-i\omega t}\right)\right]^2 + \left[p_y - \frac{e}{2c}\left(A_{y0}e^{i\omega t} + A_{y0}^* e^{-i\omega t}\right)\right]^2. \tag{4.100}$$

Let's take $A_{x0} = A$ and $A_{y0} = Ae^{i\frac{\pi}{2}} = iA$ (circular polarized condition)

$$p^2 = \left[p_x - \frac{eA}{2c}\left(e^{i\omega t} + e^{-i\omega t}\right)\right]^2 + \left[p_y - i\frac{eA}{2c}\left(e^{i\omega t} - e^{-i\omega t}\right)\right]^2, \tag{4.101}$$

$$p^2 = p_x^2 + p_y^2 + 4\left(\frac{eA}{2c}\right)^2 - 2\frac{eA}{2c}e^{i\omega t}(p_x - ip_y) - 2\frac{eA}{2c}e^{-i\omega t}(p_x + ip_y). \tag{4.102}$$

First part of Hamiltonian after applying vector potential have form

$$H_{\text{First Part}} = v\begin{bmatrix} 0 & (p_x - ip_y) \\ (p_x + ip_y) & 0 \end{bmatrix} + e^{-i\omega t}\omega_R \begin{bmatrix} 0 & -1 \\ 0 & 0 \end{bmatrix} + e^{i\omega t}\omega_R \begin{bmatrix} 0 & 0 \\ -1 & 0 \end{bmatrix}, \tag{4.103}$$

where $\omega_R = \frac{eA}{c}$. Similarly applying vector potential on second part

$$H_{\text{Second Part}} = \begin{bmatrix} \left[C - B\left(p_x^2 + p_y^2 + \frac{\omega_R^2}{v^2}\right)\right] & 0 \\ 0 & -\left[C - B\left(p_x^2 + p_y^2 + \frac{\omega_R^2}{v^2}\right)\right] \end{bmatrix}$$

$$+B\frac{\omega_R}{v}e^{i\omega t}(p_x - ip_y)\begin{bmatrix} 1 & 0 \\ 0 & -1 \end{bmatrix} + B\frac{\omega_R}{v}e^{-i\omega t}(p_x + ip_y)\begin{bmatrix} 1 & 0 \\ 0 & -1 \end{bmatrix}. \tag{4.104}$$

So the total Hamiltonian has form

$$H = \begin{bmatrix} \left[C - B\left(p_x^2 + p_y^2\right)\right] & v(p_x - ip_y) \\ v(p_x + ip_y) & -\left[C - B\left(p_x^2 + p_y^2\right)\right] \end{bmatrix} + \begin{bmatrix} -B\frac{\omega_R^2}{v^2} & 0 \\ 0 & B\frac{\omega_R^2}{v^2} \end{bmatrix} + e^{-i\omega t}\omega_R \left(\begin{bmatrix} 0 & -1 \\ 0 & 0 \end{bmatrix} + \frac{B}{v}(p_x + ip_y) \begin{bmatrix} 1 & 0 \\ 0 & -1 \end{bmatrix} \right) + e^{i\omega t}\omega_R \left(\begin{bmatrix} 0 & 0 \\ -1 & 0 \end{bmatrix} + \frac{B}{v}(p_x - ip_y) \begin{bmatrix} 1 & 0 \\ 0 & -1 \end{bmatrix} \right). \quad (4.105)$$

On comparing above equation with the Hamiltonian

$$H = H_0 + e^{-i\omega t}\, V_+ + e^{i\omega t}\, V_-. \quad (4.106)$$

We will get value of H_0, V_+ and V_-. We have defined

$$H_{eff} = \left(H_0 \; + \frac{1}{\omega}\left[V_-,\; V_+\right] \right) \quad \text{from eq. (2.53).} \quad (4.107)$$

The eigenvalue of H_{eff} is known as anomalous Rabi frequency Ω_{ARWA} of TI

$$\Omega_{ARWA} = \frac{\sqrt{\omega_R^4\left(4B^2p^2 + 1\right) + \omega^2\left(\left(C - Bp^2\right)^2 + p^2\right) - 2\omega\,\omega_R^2\left(Bp^2 + C\right)}}{\omega}. \quad (4.108)$$

If we choose a specific value of $\omega_R = \sqrt{\omega\sqrt{C^2}}$,

$$\Omega_{ARWA} = \frac{\sqrt{\omega^2\left(C^2\left(4B^2p^2 + 1\right) - 2\sqrt{C^2}\left(Bp^2 + C\right) + \left(C - Bp^2\right)^2 + p^2\right)}}{\omega}. \quad (4.109)$$

Case-1

When B is positive and $C < 0$ i.e. $BC < 0$, topologically trivial state with zero Chern number

$$\Omega_{ARWA} = \sqrt{\left(B^2p^2 + 1\right)\left(4C^2 + p^2\right)}. \quad (4.110)$$

Case-2

When B is positive and $C > 0$ i.e. $BC > 0$, topologically nontrivial state and the Chern number has non-zero possibility

$$\Omega_{ARWA} = p\sqrt{B^2p^2 + (1 - 2BC)^2}. \tag{4.111}$$

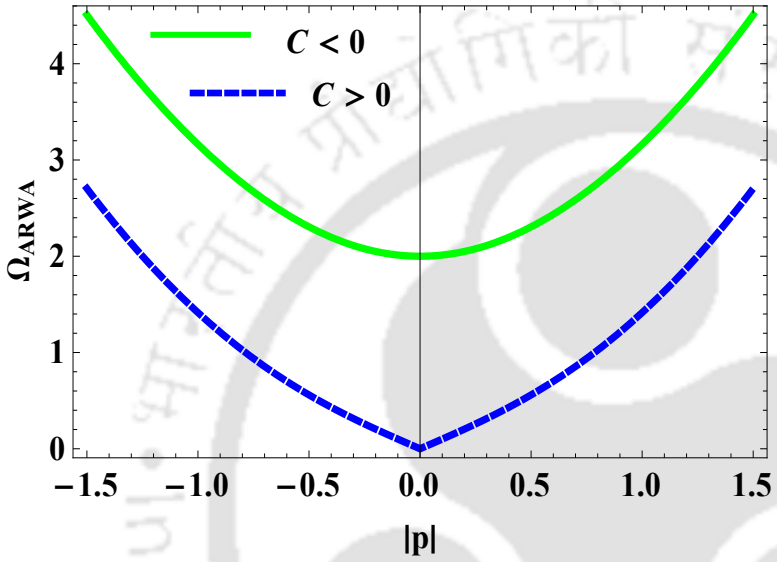

FIGURE 4.2: Anomalous Rabi frequency vs p in TI with $B > 0$.

From fig.(4.2), we see that the minimum value of anomalous Rabi frequency is zero when $B > 0$ and $C > 0$ i.e. for topologically nontrivial state of TI, indicating the presence of gapless modes. While in case $B > 0$ and $C < 0$ i.e. for the trivial state of TI, the Rabi frequency versus wave vector is gapped. Differentiating eq. (4.97)

$$\begin{aligned}\nabla_{\mathbf{p}} H_0 = &\frac{\partial}{\partial p_x}\left[vp_x\sigma_x + vp_y\sigma_y + \left(C - B(p_x^2 + p_y^2)\right)\sigma_z\right]\hat{i} \\ &+\frac{\partial}{\partial p_y}\left[vp_x\sigma_x + vp_y\sigma_y + \left(C - B(p_x^2 + p_y^2)\right)\sigma_z\right]\hat{j},\end{aligned} \tag{4.112}$$

$$\nabla_{\mathbf{p}} H_0 = \left[v\sigma_x - 2Bp_x\sigma_z\right]\hat{i} + \left[v\sigma_y - 2Bp_y\sigma_z\right]\hat{j}, \tag{4.113}$$

So

$$\begin{aligned}\left(\delta\mathbf{A}(t')\cdot\mathbf{V}(\mathbf{p},t')\right) = \quad &\delta A\left[\cos(\omega t')e^{it'H_0(\mathbf{p})}\left[v\sigma_x - 2Bp_x\sigma_z\right]e^{-it'H_0(\mathbf{p})}\right. \\ &\left.+\sin(\omega t')e^{it'H_0(\mathbf{p})}\left[v\sigma_y - 2Bp_y\sigma_z\right]e^{-it'H_0(\mathbf{p})}\right].\end{aligned} \tag{4.114}$$

For TI, term in numerator of eq. (4.40)

$$\left\langle \int_{t_{pu}+\tau_d}^{t} dt'\ \psi^{\dagger}_{eq}(\mathbf{p},0)(\delta\mathbf{A}^{*}(t')\cdot\mathbf{V}(\mathbf{p},t'))\ \int_{t_{pu}+\tau_d}^{t} dt'\ \delta\mathbf{A}(t')\cdot\mathbf{V}(\mathbf{p},t')\ \phi(\mathbf{p},t_{pu})\right\rangle$$

$$= \left(\frac{\delta A}{\omega}\right)^2 \psi^{\dagger}_{eq}(\mathbf{p},0)\left[e^{itH_0(\mathbf{p})}(v\sigma_x - 2Bp_x\sigma_z)^2 e^{-itH_0(\mathbf{p})} + e^{itH_0(\mathbf{p})}(v\sigma_y - 2Bp_y\sigma_z)^2 e^{-itH_0(\mathbf{p})}\right]\phi(\mathbf{p},t_{pu}), \tag{4.115}$$

$$= \left(\frac{\delta A}{\omega}\right)^2 \psi^{\dagger}_{eq}(\mathbf{p},0)\left[\begin{pmatrix} v^2+4B^2p^2\cos^2(\theta) & 0 \\ 0 & v^2+4B^2p^2\cos^2(\theta)\end{pmatrix} + \begin{pmatrix} v^2+4B^2p^2\sin^2(\theta) & 0 \\ 0 & v^2+4B^2p^2\sin^2(\theta)\end{pmatrix}\right]\phi(\mathbf{p},t_{pu}), \tag{4.116}$$

$$= \left(\frac{\delta A}{\omega}\right)^2 \psi^{\dagger}_{eq}(\mathbf{p},0)\begin{pmatrix} 2v^2+4B^2p^2 & 0 \\ 0 & 2v^2+4B^2p^2\end{pmatrix}\phi(\mathbf{p},t_{pu}), \tag{4.117}$$

$$= (2v^2+4B^2p^2)\left(\frac{\delta A}{\omega}\right)^2 \psi^{\dagger}_{eq}(\mathbf{p},0)\phi(\mathbf{p},t_{pu}). \tag{4.118}$$

Similarly denominator for TI of eq. (4.40)

$$= (2v^2+4B^2p^2)\left(\frac{\delta A}{\omega}\right)^2. \tag{4.119}$$

For TI

$$\frac{\Delta T}{T} = e^{-\frac{\tau_d}{T_2}}\ \frac{\sum_{\mathbf{p}}\left(\frac{\delta A}{\omega}\right)^2 \psi^{\dagger}_{eq}(\mathbf{p},0)\left(e^{itH_0(\mathbf{p})}(v\sigma_x - 2Bp_x\sigma_z)^2 e^{-itH_0(\mathbf{p})} + e^{itH_0(\mathbf{p})}(v\sigma_y - 2Bp_y\sigma_z)^2 e^{-itH_0(\mathbf{p})}\right)\phi(\mathbf{p},t_{pu}) + c.c.}{\sum_{\mathbf{p}}\left(\frac{\delta A}{\omega}\right)^2 \psi^{\dagger}_{eq}(\mathbf{p},0)\left(e^{itH_0(\mathbf{p})}(v\sigma_x - 2Bp_x\sigma_z)^2 e^{-itH_0(\mathbf{p})} + e^{itH_0(\mathbf{p})}(v\sigma_y - 2Bp_y\sigma_z)^2 e^{-itH_0(\mathbf{p})}\right)\psi_{eq}(\mathbf{p},0)}, \tag{4.120}$$

$$\frac{\Delta T}{T} = e^{-\frac{\tau_d}{T_2}}\ \frac{\sum_{\mathbf{p}}(2v^2+4B^2p^2)\left(\frac{\delta A}{\omega}\right)^2 \psi^{\dagger}_{eq}(\mathbf{p},0)\phi(\mathbf{p},t_{pu}) + c.c.}{\sum_{\mathbf{p}}(2v^2+4B^2p^2)\left(\frac{\delta A}{\omega}\right)^2 \psi^{\dagger}_{eq}(\mathbf{p},0)\psi_{eq}(\mathbf{p},0)}, \tag{4.121}$$

$$\frac{\Delta T}{T} = e^{-\frac{\tau_d}{T_2}}\ \frac{\sum_{\mathbf{p}}\psi^{\dagger}_{eq}(\mathbf{p},0)\phi(\mathbf{p},t_{pu}) + c.c.}{\sum_{\mathbf{p}}\psi^{\dagger}_{eq}(\mathbf{p},0)\psi_{eq}(\mathbf{p},0)}. \tag{4.122}$$

From eq.(4.81), $W \to 1$. So

$$\phi(\mathbf{p}, t_{pu}) = e^{it_{pu}H_0(\mathbf{p})} \Big(\psi(\mathbf{p}, t_{pu}) - \ \psi_{eq}(\mathbf{p}, t_{pu})\Big), \tag{4.123}$$

$$\frac{\Delta T}{T} = e^{-\frac{\tau_d}{T_2}} \ \frac{\sum_{\mathbf{p}} \psi^{\dagger}_{eq}(\mathbf{p},0) e^{it_{pu}H_0(\mathbf{p})} \Big(\psi(\mathbf{p}, t_{pu}) - \ \psi_{eq}(\mathbf{p}, t_{pu})\Big) + c.c.}{\sum_{\mathbf{p}} \psi^{\dagger}_{eq}(\mathbf{p},0)\psi_{eq}(\mathbf{p},0)}. \tag{4.124}$$

We consider a polar form of momentum $p_x = p\cos\theta$ and $p_y = p\sin\theta$. We know $\psi_{eq}(\mathbf{p}, t) = e^{-iH_0(\mathbf{p})t}\ \psi(\mathbf{p}, 0)$, this is stationary state, so we can replace operator H_0 by ground state energy E and $\psi(\mathbf{p}, 0)$ by ground state eigenvalue of Hamiltonian of eq. (4.97),

$$\psi(\mathbf{p},0) = \begin{pmatrix} -\dfrac{e^{-i\theta}\left(Bp^2 + \frac{\left(v^2-2BC\right)p^2}{2\sqrt{C^2}} - C + \sqrt{C^2}\right)}{pv\sqrt{\frac{\left(Bp^2 + \frac{(v^2-2BC)p^2}{2\sqrt{C^2}} - C + \sqrt{C^2}\right)^2}{p^2v^2} + 1}} \\ \dfrac{1}{\sqrt{\frac{\left(Bp^2 + \frac{(v^2-2BC)p^2}{2\sqrt{C^2}} - C + \sqrt{C^2}\right)^2}{p^2v^2} + 1}} \end{pmatrix} \quad \text{and} \quad E = \frac{p^2\left(2BC - v^2\right)}{2\sqrt{C^2}} - \sqrt{C^2}. \tag{4.125}$$

These values has taken in lower order of p expansion, because our Hamiltonian (eq. (4.97)) posses low energy limit.

Case-1

In this case we assume B is positive and $C < 0$ i.e. $BC < 0$, which is the topologically trivial situation where the Chern number is zero. This means

$$\psi(\mathbf{p},0) = \begin{pmatrix} -\dfrac{e^{-i\theta}\left(p^2v^2 + 4C\left(C - Bp^2\right)\right)}{\sqrt{p^4v^4 + 4Cp^2(3C - 2Bp^2)v^2 + 16C^2(C - Bp^2)^2}} \\ \dfrac{1}{\sqrt{\frac{\left(p^2v^2 + 4C(C - Bp^2)\right)^2}{4C^2p^2v^2} + 1}} \end{pmatrix} \quad \text{and} \quad E = -\left(Bp^2 - \frac{p^2v^2}{2C} - C\right). \tag{4.126}$$

Case-2

When B is positive and $C > 0$ i.e. $BC > 0$, this corresponds to a topologically nontrivial state where and the Chern number has non-zero possibility. This means

$$\psi(\mathbf{p},0) = \begin{pmatrix} -\dfrac{e^{-i\theta}pv}{\sqrt{4C^2 + p^2v^2}} \\ \dfrac{2}{\sqrt{\frac{p^2v^2}{C^2} + 4}} \end{pmatrix} \qquad \text{and} \qquad E = \left(Bp^2 - \frac{p^2v^2}{2C} - C\right). \tag{4.127}$$

Now we calculate $\psi_{eq}(\mathbf{p}, t_{pu}) = e^{-iEt_{pu}}\ \psi(\mathbf{p}, 0)$ and $\psi(\mathbf{p}, t_{pu})$ for both above cases,

$$\psi(\mathbf{p}, t_{pu}) = -i\frac{H_{eff}(p)\sin(t_{pu}\Omega_{\text{ARWA}}(p))}{\Omega_{\text{ARWA}}(p)}\psi(\mathbf{p}, 0) + \psi(\mathbf{p}, 0)\cos(t_{pu}\Omega_{\text{ARWA}}(p)). \tag{4.128}$$

Inserting everything into eq. (4.124), we obtain a formula for the differential transmission coefficient for TI.

4.6 Results and Discussion

The short-distance cutoff independent ratio χ from eq.(4.41) alluded to earlier has the following (asymptotic $t_{pu} \to \infty$) forms for graphene, TI and Weyl semimetal.

Graphene:

$$\chi(t_{pu}) = \frac{\sin\left(\frac{t_{pu}\omega_R^2}{2\omega}\right)}{\sqrt{\frac{t_{pu}\omega_R^2}{2\omega}}} \tag{4.129}$$

The amplitude of the oscillations has a power law decay with characteristic exponent equal to $-\frac{1}{2}$.

Topological Insulator: Here there are two situations:

(a) Topologically trivial ($B > 0$ and $C < 0$ and Chern number is zero):

$$\chi(t_{pu}) = \frac{\cos(Ct_{pu})}{C\ t_{pu}}. \tag{4.130}$$

The amplitude of the oscillations has a power law decay with characteristic exponent equal to -1.

(b) Topologically nontrivial ($B > 0$ and $C > 0$ and Chern number has non-zero possibility):

$$\chi(t_{pu}) = \frac{\sin(Ct_{pu})}{(Ct_{pu})^2}. \tag{4.131}$$

The amplitude of the oscillations has a power law decay with characteristic exponent equal to -2. Both these cases are shown in fig.(4.3).

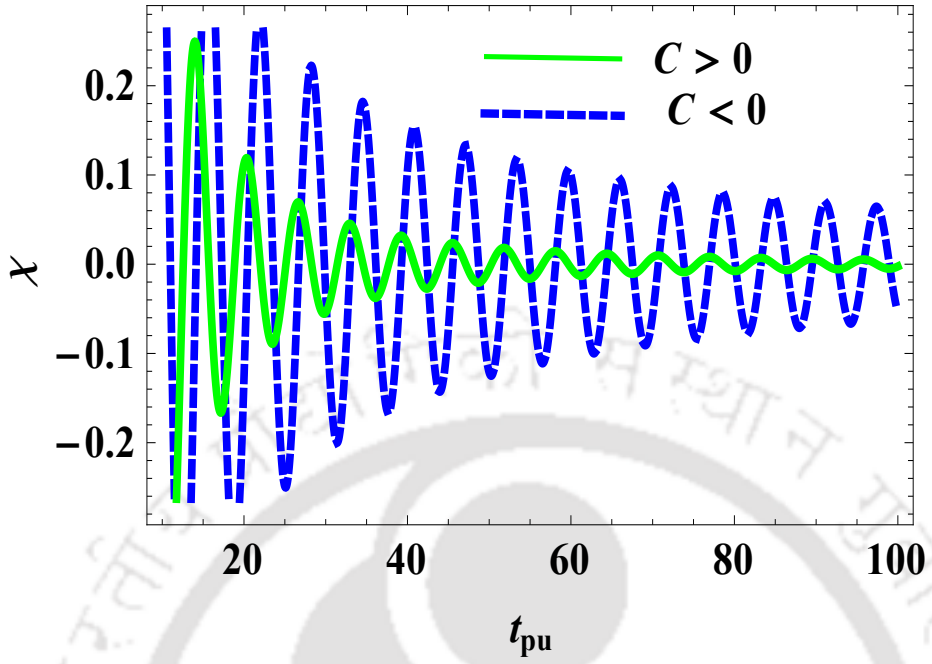

FIGURE 4.3: A plot of the ratio χ versus pump duration t_{pu} in case of TI. It shows how a non-zero Chern number causes a qualitative change in differential transmission coefficient. Time is in units of C^{-1}.

Weyl semimetal:

$$\chi(t_{pu}) = \frac{\sin\left(\frac{t_{pu}\omega_R^2}{\omega}\right)}{\left(\frac{t_{pu}\omega_R^2}{\omega}\right)^{5/2}}, \tag{4.132}$$

The amplitude of the oscillations has a power law decay with characteristic exponent equal to $-\frac{5}{2}$. The nature of $\chi(t_{pu})$ for graphene and Weyl semimetal can be seen in fig.(4.4).

We have proposed, theoretical modeling of the pump-probe experiment to detect anomalous Rabi oscillation. This simply involves looking for periodic oscillations in the differential transmission coefficient versus pump pulse duration (alternatively, the area of the pump pulse). When everything else remains fixed (including pump-probe delay) these plots (fig.(4.3) and fig.(4.4)) exhibit oscillations with a frequency corresponding to the anomalous Rabi frequency. Furthermore, the amplitude of these oscillations decay as a power law in the pump duration with a characteristic exponent that is indicative of the particular system under consideration.

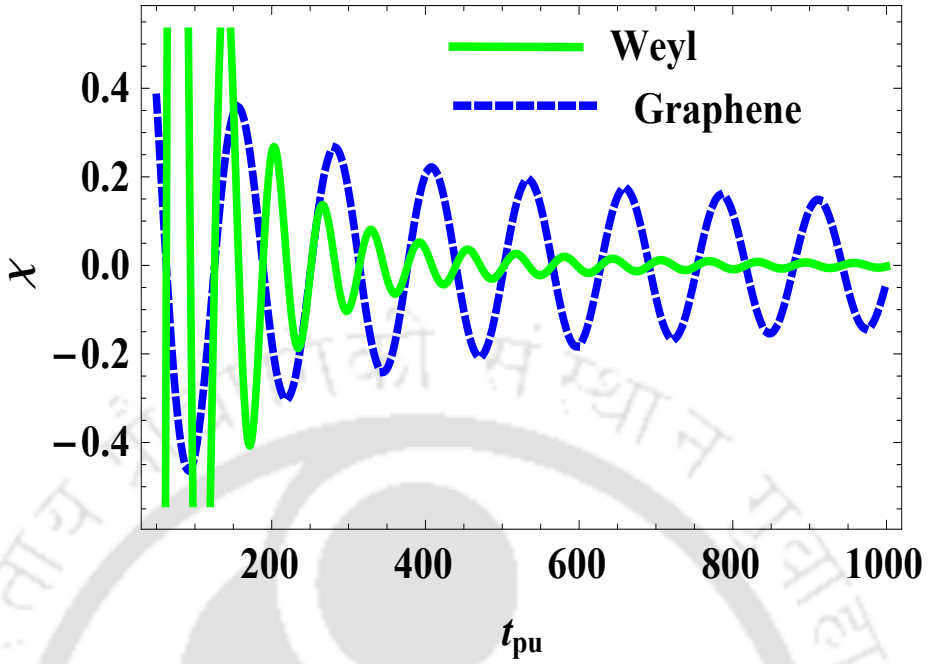

FIGURE 4.4: A plot of the ratio χ versus pump duration t_{pu} in Weyl and graphene. Time is in units of $\frac{\omega}{\omega_R^2}$.

4.7 Conclusions

Floquet theory has been invoked to show that Dirac-Weyl systems (graphene, Weyl semi metals and TIs) exhibit a peculiar form of Rabi oscillation that occurs far from conventional resonance. The associated Rabi frequency and its dispersion relation is sensitive to the low-energy physics of these systems. While the presence of these oscillations is a unifying feature of this family of materials, it is also possible to tell them apart by performing a pump probe experiment and extracting a certain ratio derivable from the differential transmission coefficient. This ratio exhibits sinusoidal oscillations in the pump pulse duration (when all else is held fixed) with a frequency equal to the anomalous Rabi frequency. The amplitudes of these oscillations decay as a power law for large pump durations with an exponent that is characteristic of the specific member of this family of materials. In case of bulk topological insulators, this exponent has a certain value when the Chern number is zero and a different value when the Chern number is non-zero.

Chapter 5

Quantum Rabi Oscillations in Weyl Semimetal

5.1 Introduction

In earlier chapters, the electromagnetic field was treated classically. However, interesting new phenomena are seen in quantum optics when the electromagnetic field is treated quantum mechanically. Traditional examples of such phenomena include the photoelectric effect, Raman effect, stimulated emission and absorption, spontaneous emission, etc. These phenomena can be only explained by the quantum nature of the radiation field. When we treat radiation field quantum mechanically, some new phenomena are found in Rabi oscillations, such as quantum 'collapse' and 'revival' described in various text books [56, 57, 229]. In semiclassical theory, the atom in an excited state cannot make a transition to a lower level without an external field. However, in the quantum case, this transition is possible even in a vacuum because of spontaneous emission (zero point quantum fluctuations of radiation). A solvable model of quantum radiation interacting with a two-level system has been given by Jaynes and Cummings [230, 231]. Rabi oscillations have been well described in semiconductors [49], where energy bands rather than discrete energy levels are involved. The literature of Rabi oscillations and anomalous Rabi oscillations (AROs) in Dirac-Weyl fermionic systems have been well described earlier (chapter 2). In this chapter, it is shown that anomalous Rabi oscillations exist even if the EM field is treated quantum mechanically. This means the AROs are not due to approximations or assumptions we have made.

5.2 Problem Formulation

In earlier chapters, we studied Rabi oscillations using optical Bloch equations in the presence of not only a continuous optical field but also with a pump pulse. In this chapter, we describe the phenomenon of Rabi oscillations in the presence of a purely quantum field. By using probability amplitude equation, we have studied anomalous Rabi oscillations in the presence of a quantum field. Finally, we describe how the classical result of chapter 2 emerge as a limiting case of the quantum results of the present chapter.

5.3 Quantum Rabi Oscillations

For atoms in a cavity, a number of quantum-electrodynamic effects are seen. Vacuum Rabi oscillation is one such phenomenon, induced by vacuum fluctuations of the radiation field. This vacuum-field Rabi oscillations lead to the splitting in the spontaneous-emission spectra of atoms in cavity [232]. On considering the interaction between states $|e\rangle$ and $|g\rangle$ in a two-level system via a plane monochromatic field of frequency ω, having frequency difference between them is ω. The probability $P_{e\to g}$ or $P_{g\to e}$ for making a transition between excited state and ground state and vice versa is given by

$$P_{e\to g}(t) = P_{g\to e}(t) = \sin^2 \frac{\Omega t}{2} \text{ and } \Omega = \frac{2}{\hbar}|\mathbf{p}\cdot\mathbf{E}|. \tag{5.1}$$

Here $\mathbf{p}$ is dipole moment and $\mathbf{E}$ is electric field applied to the system. There are oscillations of the atomic population between the ground and the excited states, with frequency Ω. We have found transition probabilities in eq.(5.1) by regarding the external field as being classical. If the external field is extremely weak i.e., there are only a few photons (eg. in a cavity devoid of matter) we would have to treat the electric field $\mathbf{E}$ quantum mechanically. G. S. Agarwal has studied this phenomenon [233] where he obtains the result

$$P_{e,n\to g,n+1}(t) = \frac{4g^2(n+1)}{\Omega_{n\Delta}^2} \sin^2 \frac{\Omega_{n\Delta} t}{2}. \tag{5.2}$$

Here g is coupling coefficient, states $|e\rangle$ and $|g\rangle$ are separated by the frequency ω_0, $\Delta = \omega_0 - \omega$ and the value of oscillation frequency $\Omega_{n\Delta}$ is

$$\Omega_{n\Delta}^2 = \Delta^2 + 4g^2(n+1). \tag{5.3}$$

Eq.(5.2) becomes similar to eq.(5.1) if $\Delta = 0$. This also holds if the field is initially in the vacuum state. For a field initially in the vacuum, the atomic population oscillates between excited and ground states, called vacuum-field Rabi oscillations or self-induced Rabi oscillations. The exchange of energy between the radiation field and the atom is manifested as these oscillations.

The Jaynes-Cummings model (JCM) [231, 234, 235] is a central model of quantum optics. The interaction between an isolated two-level atom and a single mode quantized electromagnetic field in a lossless cavity is captured in this model. We study this model extensively because it captures the essence of the actual dipole coupling of an atom to an electromagnetic field. This is exactly soluble in the rotating wave approximation. By using this, we can study many non-classical effects of the atom-field interactions, such as collapse-revival phenomena (CRP) [229, 236–238], vacuum Rabi oscillation [233, 239], sub-Poissonian statistics [240] and squeezing of the radiation field [241]. We study Rabi oscillations by using this JCM. We study both cases as in the earlier chapters, i.e. conventional and anomalous Rabi oscillations in quantized form by using this model. Weyl material is a relativistic fermionic system. Our aim is to study nonlinear optics of this system at the Weyl node as all interesting physics at low energy occurs near the Weyl node, particularly the phenomenon of anomalous Rabi oscillation (ARO). The JCM has been used for quantum Rabi oscillation in single layer graphene by our group [155]. Here we study same Rabi oscillation phenomenon, trying to find out the difference between Weyl semimetal and graphene.

5.4 Jaynes Cummings Model (JCM)

JCM is used for a theoretical description of the two-level system (atom) interacting with a quantal mode of an optical cavity in presence or absence of radiation. Many phenomena of atomic physics, quantum optics, and solid-state quantum information circuits are well described by this model. In 1963, Edwin Jaynes and Fred Cummings proposed a model for studying the interrelation between the quantum theory of radiation and the semi-classical theory, for describing the phenomenon of spontaneous emission [231]. In the semi-classical theory of field-atom interaction, the atom is quantized and the field is not an operator but a time-dependent c-number. This theory has been used for describing many phenomena that are seen in modern optics, for example, the existence of Rabi oscillations in atomic excitation probabilities for light fields with a narrow bandwidth. However, JCM

explains, how the quantized radiation field affects the predictions for the evolution of the state of a two-level system in comparison with the semi-classical theory of light-atom interaction. Later, it was discovered that collapse and revival phenomenon [235, 236] is a direct consequence of discreteness of field states (photons). It is a pure quantum effect, which can be explained only by the JCM but not with the semi-classical theory.

Starting from the Rabi Hamiltonian

$$\hat{H} = \hat{H}_0 - \hat{d} \cdot \mathbf{E}(t). \tag{5.4}$$

Where $\hat{H}_0$ is Hamiltonian of two level system, $\hat{d}$ is dipole moment operator and $\mathbf{E}(t)$ is the electric field. We simply replace $\mathbf{E}(t) \rightarrow \hat{E}(t)$. The Hamiltonian in second quantized form is,

$$\hat{H} = \hat{H}_0 - \mathcal{E}_0(\hat{a} + \hat{a}^\dagger)\sin(kz)\hat{d}. \tag{5.5}$$

The Hamiltonian that describes the full system can be written as

$$\hat{H} = \hat{H}_{\text{free field}} + \hat{H}_{\text{atom}} + \hat{H}_{\text{int}}. \tag{5.6}$$

Free Field Hamiltonian

$$\hat{H}_{\text{free field}} = \hbar\omega\left(\hat{a}^\dagger\hat{a} + \frac{1}{2}\right) \approx \hbar\omega\hat{a}^\dagger\hat{a}. \tag{5.7}$$

The Atomic Hamiltonian

If we consider state of two level system

$$|+\rangle = \begin{bmatrix} 1 \\ 0 \end{bmatrix}, \quad |-\rangle = \begin{bmatrix} 0 \\ 1 \end{bmatrix}. \tag{5.8}$$

We may write this Hamiltonian as a sum over all accessible energies

$$\hat{H}_{atom} = E_+|+\rangle\langle+| + E_-|-\rangle\langle-|, \tag{5.9}$$

$$= E_+ \begin{bmatrix}1\\0\end{bmatrix}\begin{bmatrix}1 & 0\end{bmatrix} + E_- \begin{bmatrix}0\\1\end{bmatrix}\begin{bmatrix}0 & 1\end{bmatrix} = E_+ \begin{bmatrix}1 & 0\\0 & 0\end{bmatrix} + E_- \begin{bmatrix}0 & 0\\0 & 1\end{bmatrix} = \begin{bmatrix}E_+ & 0\\0 & E_-\end{bmatrix}. \tag{5.10}$$

The above Hamiltonian may be recast in form

$$\hat{H}_{atom} = \frac{1}{2}\begin{bmatrix}E_+ + E_- & 0\\0 & E_+ + E_-\end{bmatrix} + \frac{1}{2}\begin{bmatrix}E_+ - E_- & 0\\0 & E_- - E_+\end{bmatrix}. \tag{5.11}$$

So atomic excitation Hamiltonian will be

$$\hat{H}_{atom} = \frac{1}{2}\left(E_+ + E_-\right)\hat{I} + \frac{1}{2}(\Delta E)\hat{\sigma}_z. \tag{5.12}$$

Writing Hamiltonian in terms of a Pauli matrix

$$\Delta E = E_+ - E_- \equiv \hbar\omega_0, \tag{5.13}$$

$$\hat{H}_{atom} \approx \frac{1}{2}\hbar\omega_0\hat{\sigma}_z. \tag{5.14}$$

The Interaction Hamiltonian

We know

$$\hat{\sigma}_x = \begin{bmatrix}0 & 1\\1 & 0\end{bmatrix}. \tag{5.15}$$

Raising and lowering operators

$$\hat{\sigma}_+ = \begin{bmatrix}0 & 1\\0 & 0\end{bmatrix}, \quad \hat{\sigma}_- = \begin{bmatrix}0 & 0\\1 & 0\end{bmatrix}. \tag{5.16}$$

So

$$\hat{\sigma}_x = (\hat{\sigma}_+ + \hat{\sigma}_-). \tag{5.17}$$

The electric field in second quantized form can be written as

$$\hat{E}_x(z,t) = \mathcal{E}_0(\hat{a} + \hat{a}^\dagger)\sin(kz). \tag{5.18}$$

So interaction Hamiltonian will be

$$H_{int} = -\mathcal{E}_0(\hat{a} + \hat{a}^\dagger)\sin(kz)\hat{d}. \tag{5.19}$$

Due to parity $\langle e|\hat{d}|e\rangle = \langle g|\hat{d}|g\rangle = 0$ (dipole moment is zero when electron or hole is on the same state), and defining $d = \langle e|\hat{d}|g\rangle$ and we get $d^* = \langle g|\hat{d}|e\rangle$, we find that $\hat{d}$ possess only off-diagonal elements. Without loss off generality we assume a real d and get $\hat{d} = d\sigma_x$. Defining $g = -\mathcal{E}_0 \sin(kz)\hat{d}$, we arrive at

$$H_{int} = g\sigma_x(\hat{a} + \hat{a}^\dagger), \tag{5.20}$$

$$H_{int} = g(\hat{\sigma}_+ + \hat{\sigma}_-)(\hat{a} + \hat{a}^\dagger) = g(\hat{\sigma}_+\hat{a} + \hat{\sigma}_-\hat{a} + \hat{\sigma}_+\hat{a}^\dagger + \hat{\sigma}_-\hat{a}^\dagger). \tag{5.21}$$

In the interaction picture operators are time dependent

$$\hat{a}^\dagger(t) = \hat{a}^\dagger e^{i\omega t}, \quad \hat{a}(t) = \hat{a}e^{-i\omega t}, \quad \hat{\sigma}_+(t) = \hat{\sigma}_+ e^{i\omega_0 t}, \quad \hat{\sigma}_-(t) = \hat{\sigma}_- e^{-i\omega_0 t}. \tag{5.22}$$

So H_{int} in the interaction picture becomes

$$H_{int} = g\left(\hat{\sigma}_+\hat{a}e^{i(\omega_0-\omega)t} + \hat{\sigma}_-\hat{a}e^{-i(\omega_0+\omega)t} + \hat{\sigma}_+\hat{a}^\dagger e^{i(\omega_0+\omega)t} + \hat{\sigma}_-\hat{a}^\dagger e^{-i(\omega_0-\omega)t}\right). \tag{5.23}$$

At zero detuning $\Delta = \omega - \omega_0 = 0$. Neglecting the two terms $\sigma_-\hat{a}$ and $\sigma_+\hat{a}^\dagger$ in above equation, also known as the RWA. Finally, H_{int} has form

$$H_{int} = g\left(\hat{\sigma}_+\hat{a} + \hat{\sigma}_-\hat{a}^\dagger\right). \tag{5.24}$$

So the full Jaynes-Cummings Hamiltonian from eq.(5.6) is

$$H_{JC} = \hbar\omega\hat{a}^\dagger\hat{a} + \frac{1}{2}\hbar\omega_0\hat{\sigma}_z + g\left(\hat{\sigma}_+\hat{a} + \hat{\sigma}_-\hat{a}^\dagger\right). \tag{5.25}$$

5.5 Jaynes Cummings Type Model Hamiltonian for Weyl Semimetal

When the constituent particles are massless, the relativistic fermions are described by a two-component spinor explained by Hermann Weyl in 1929 [183] instead of four-component Dirac spinor. This means the Weyl equation $H\psi = E\psi$ is

governed by the Weyl Hamiltonian

$$H = v_F(p_x\sigma_x + p_y\sigma_y + p_z\sigma_z); \quad E = \pm v_F\sqrt{p_x^2 + p_y^2 + p_z^2}, \tag{5.26}$$

where v_F is hopping velocity between nearest neighbors and p_x, p_y, p_z are momentums in respective x, y, z directions. Using the tight binding approximation, the low-energy Hamiltonian of Weyl metals in momentum space with hopping and interaction with electromagnetic radiation $\mathbf{A}(t)$ is given as

$$H = \sum_{\alpha,\beta} v_F \boldsymbol{\sigma}_{\mathrm{A,B}} \left(\mathbf{p} - \frac{e}{c}\mathbf{A}(t)\right) c^\dagger_{p,\mathrm{A}} c_{p,\mathrm{B}}, \tag{5.27}$$

where the A and B indices stand for either spin up or spin down and $c^\dagger(c)$ is the creation (annihilation) operator. We have taken vector potential $\mathbf{A}(t)$ in form $\mathbf{A}(t) = Re(\mathbf{A_0}e^{-i\omega t})$ i.e. $\mathbf{A}(t) = \frac{1}{2}\mathbf{A_0}e^{-i\omega t} + \frac{1}{2}\mathbf{A_0^*}e^{i\omega t}$. As there are no anomalous Rabi oscillations in case of linear polarization [155], we study the case of circular polarization i.e. no vector potential in z direction $A_z = 0$ and x and y direction potential has nature like $A_{x0} + iA_{y0} = 0$.

We suppress the momentum label in order to bring out the role played by other degrees of freedom, consider $v_F\mathbf{p} = \boldsymbol{\epsilon}$. The Hamiltonian for a Weyl semimetal-like system we suggest is (derived in in appendix (5.10.1))

$$\begin{aligned} H = c_A^\dagger\ \boldsymbol{\sigma}_{AB}\cdot\boldsymbol{\epsilon}\ c_B + c_B^\dagger\ \boldsymbol{\sigma}_{BA}\cdot\boldsymbol{\epsilon}\ c_A + c_A^\dagger\ \boldsymbol{\sigma}_{AA}\cdot\boldsymbol{\epsilon}\ c_A + c_B^\dagger\ \boldsymbol{\sigma}_{BB}\cdot\boldsymbol{\epsilon}\ c_B \\ +\lambda\ c_B^\dagger c_A\ b\ e^{i\omega t} + \lambda^*\ \ c_A^\dagger c_B\ b^\dagger\ e^{-i\omega t}. \end{aligned} \tag{5.28}$$

Here $\boldsymbol{\sigma}_{AB}\cdot\boldsymbol{\epsilon} = \epsilon_x - i\epsilon_y$, $\boldsymbol{\sigma}_{BA}\cdot\boldsymbol{\epsilon} = \epsilon_x + i\epsilon_y$, $\boldsymbol{\sigma}_{AA}\cdot\boldsymbol{\epsilon} = \epsilon_z$, $\boldsymbol{\sigma}_{BB}\cdot\boldsymbol{\epsilon} = -\epsilon_z$, λ is the coupling constant and $[b, b^\dagger] = 1$ are the photon operators. This model may be mapped to the well-known Jaynes-Cummings model through the following identifications, $\sigma_+ = \sigma_x + i\sigma_y = c_B^\dagger c_A$; $\sigma_- = \sigma_x - i\sigma_y = c_A^\dagger c_B$ and $\sigma_z = (c_A^\dagger c_A - c_B^\dagger c_B)$ together with a unitary transformation on the photons which means we replace b with $be^{i\omega t}$ (derived in in appendix (5.10.2)).

5.6 Quantum Rabi Oscillations

In this section, we study the phenomenon of Rabi oscillations of a Weyl semimetal, near conventional resonance i.e. when the external frequency matches the particle-hole frequency (conventional Rabi oscillation) and also when it is much larger than

the particle-hole frequency (anomalous Rabi oscillations). Both these oscillations are seen in the ultra quantum limit of the radiation field. Indeed there are even zero-point anomalous Rabi oscillations in a vacuum. This shows that anomalous Rabi oscillation is a robust phenomenon, not an artifact of any approximations.

To find differences which emerge due to treatment of radiation field classically or quantum mechanically, it is best to keep the matter sector as simple as possible. For this reason, we imagine all processes in the case of Weyl semimetal involve just one electron either on up spin or down spin site of electron, so we choose each state has either **(i)** no electron or hole or **(ii)** one electron and one hole. So only nonzero amplitudes are $\langle 0,1,n|\phi(t)\rangle$ and $\langle 1,0,n|\phi(t)\rangle$. By applying evolution equation $i\hbar\frac{\partial}{\partial_t}|\phi(t)\rangle = \hat{H}|\phi(t)\rangle$, amplitude general can be written down (setting $\hbar = 1$, derived in appendix(5.10.3))

$$i\partial_t\langle 0,1,n|\phi(t)\rangle = \boldsymbol{\sigma}_{BA}\cdot\boldsymbol{\epsilon}\langle 1,0,n|\phi(t)\rangle + \boldsymbol{\sigma}_{BB}\cdot\boldsymbol{\epsilon}\langle 0,1,n|\phi(t)\rangle + \lambda e^{i\omega t}\sqrt{n+1}\langle 1,0,n+1|\phi(t)\rangle, \tag{5.29a}$$

$$i\partial_t\langle 1,0,n+1|\phi(t)\rangle = \boldsymbol{\sigma}_{AB}\cdot\boldsymbol{\epsilon}\langle 0,1,n+1|\phi(t)\rangle + \boldsymbol{\sigma}_{AA}\cdot\boldsymbol{\epsilon}\langle 1,0,n+1|\phi(t)\rangle + \lambda^*\, e^{-i\omega t}\sqrt{n+1}\,\langle 0,1,n|\phi(t)\rangle. \tag{5.29b}$$

5.6.1 Conventional Oscillations: RWA

Using the technique mentioned in many text books such as Haug [49], we solve the above rate equation eq.(5.29a) and eq.(5.29b). The condition for this regime is $\Delta \equiv \omega - 2\epsilon$, where $\epsilon = \sqrt{\epsilon_x^2+\epsilon_y^2+\epsilon_z^2}$. In the semiclassical limit, we set $n+1 \approx n$ and writing eq.(5.29a) and eq.(5.29b) in matrix form

$$i\frac{\partial}{\partial_t}\begin{bmatrix}\langle 1,0,n\ |\phi(t)\rangle\\ \langle 0,1,n\ |\phi(t)\rangle\end{bmatrix} = \begin{bmatrix}\boldsymbol{\sigma}_{AA}\cdot\boldsymbol{\epsilon} & \boldsymbol{\sigma}_{AB}\cdot\boldsymbol{\epsilon}\\ \boldsymbol{\sigma}_{AB}\cdot\boldsymbol{\epsilon} & \boldsymbol{\sigma}_{BB}\cdot\boldsymbol{\epsilon}\end{bmatrix}\begin{bmatrix}\langle 0,1,n\ |\phi(t)\rangle\\ \langle 1,0,n\ |\phi(t)\rangle\end{bmatrix} + \begin{bmatrix}0 & \lambda\, e^{i\omega t}\sqrt{n}\\ \lambda^*\, e^{-i\omega t}\sqrt{n} & 0\end{bmatrix}\begin{bmatrix}\langle 0,1,n\ |\phi(t)\rangle\\ \langle 1,0,n\ |\phi(t)\rangle\end{bmatrix}. \tag{5.30}$$

Setting $\boldsymbol{\sigma}_{AA}\cdot\boldsymbol{\epsilon} = \epsilon_z$, $\boldsymbol{\sigma}_{BB}\cdot\boldsymbol{\epsilon} = -\epsilon_z$, $\boldsymbol{\sigma}_{AB}\cdot\boldsymbol{\epsilon} = \epsilon_x - i\epsilon_y$ and $\boldsymbol{\sigma}_{BA}\cdot\boldsymbol{\epsilon} = \epsilon_x + i\epsilon_y$, to obtain generalized Rabi frequency, we diagonalize above equation via using

following matrix

$$\begin{bmatrix} \langle 0,1,n\ |\phi(t)\rangle \\ \langle 1,0,n\ |\phi(t)\rangle \end{bmatrix} = \begin{bmatrix} -\frac{\epsilon-\epsilon_z}{\epsilon_x+i\epsilon_y} & \frac{\epsilon+\epsilon_z}{\epsilon_x+i\epsilon_y} \\ 1 & 1 \end{bmatrix} \begin{bmatrix} \langle 0,1,\tilde{n}\ |\phi(t)\rangle \\ \langle 1,0,\tilde{n}\ |\phi(t)\rangle \end{bmatrix}. \tag{5.31}$$

The matrix equation obtained after diagonalization, upon substitution

$$\langle 1,0,\tilde{n}\ |\phi(t)\rangle = e^{-i\ |\epsilon|\ t}\langle 1,0,\tilde{\tilde{n}}\ |\phi(t)\rangle, \tag{5.32}$$

$$\langle 0,1,\tilde{n}\ |\phi(t)\rangle = e^{i\ |\epsilon|\ t}\langle 0,1,\tilde{\tilde{n}}\ |\phi(t)\rangle. \tag{5.33}$$

Using RWA approximation we obtain the following equation

$$i\frac{\partial}{\partial_t}\langle 0,1,\tilde{\tilde{n}}\ |\phi(t)\rangle = -\frac{\sqrt{n}\left[e^{it\Delta}\left(\epsilon_x+i\epsilon_y\right)\lambda^*\right]}{2|\epsilon|}\langle 1,0,\tilde{\tilde{n}}\ |\phi(t)\rangle, \tag{5.34}$$

$$i\frac{\partial}{\partial_t}\langle 1,0,\tilde{\tilde{n}}\ |\phi(t)\rangle = -\frac{\sqrt{n}\left[\lambda e^{-it\Delta}\left(\epsilon_z-|\epsilon|\right)^2\right]}{2\left(\epsilon_x+i\epsilon_y\right)|\epsilon|}\langle 0,1,\tilde{\tilde{n}}\ |\phi(t)\rangle, \tag{5.35}$$

Here $\Delta = \omega - 2|\epsilon|$. After solving these coupled equations we will get value of amplitude Rabi frequency $\left(\psi_\pm \sim e^{i\Omega_{R,\pm}t}\right)$

$$\Omega_{R,\pm} = \frac{1}{2}\sqrt{\Delta^2 + |\lambda|^2 n\left(1-\frac{\epsilon_z}{|\epsilon|}\right)^2}. \tag{5.36}$$

Since current density J has form $\psi_+^\dagger\psi_-$, which is a parameter which can be measured in laboratory. So the Rabi frequency associated with the current density will be

$$\Omega_{\text{RWA}} = \sqrt{\Delta^2 + |\lambda|^2 n\left(1-\frac{\epsilon_z}{|\epsilon|}\right)^2}. \tag{5.37}$$

If we consider $\epsilon_x, \epsilon_y = 0$ and $\epsilon_z = \epsilon$

$$\Omega_{\text{RWA}} = \left|\omega - 2|\epsilon_z|\right|. \tag{5.38}$$

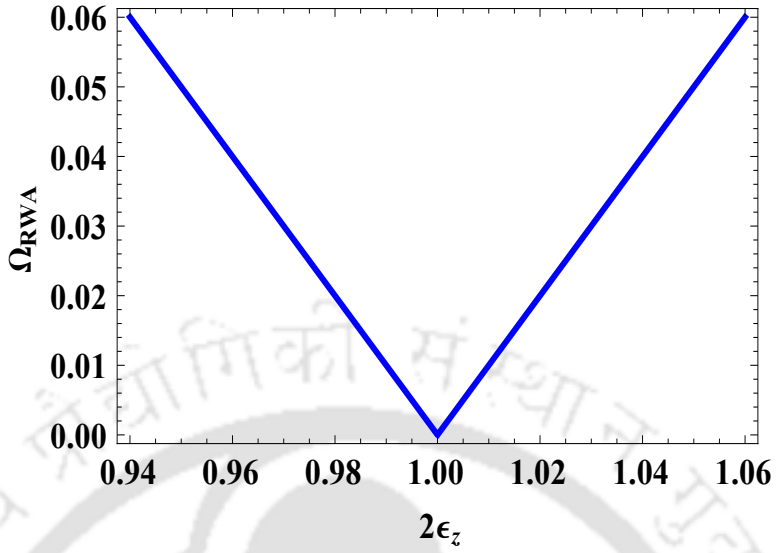

FIGURE 5.1: The plot shows (eq.(5.38)) the Rabi frequency versus energy ϵ_z on considering $\epsilon_x = 0$ and $\epsilon_y = 0$, parameters are plotted in unit of ω and $\lambda = 1$.

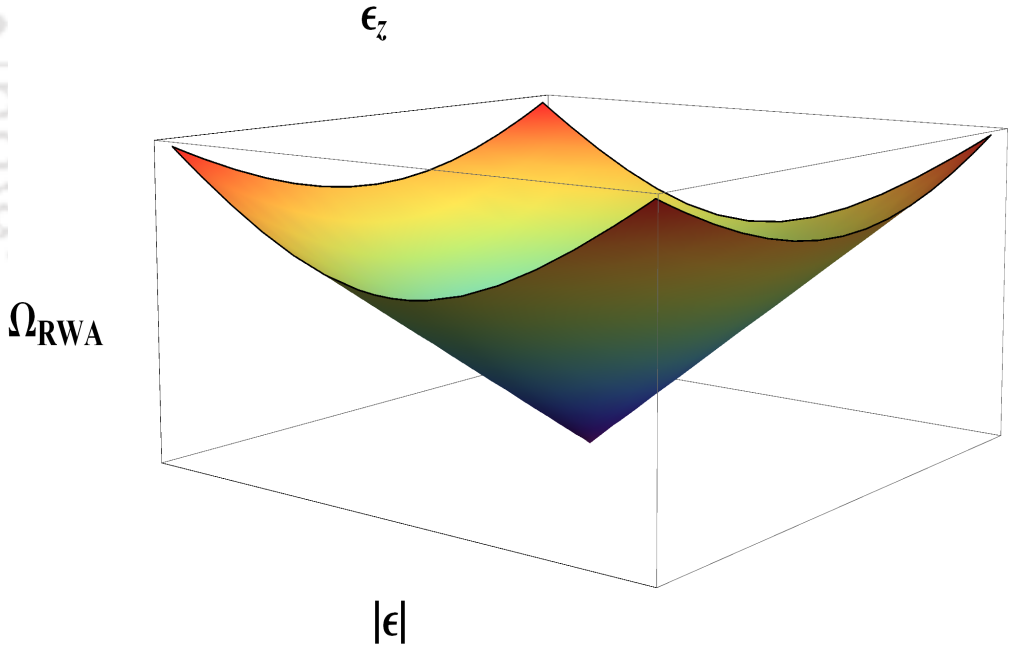

FIGURE 5.2: The plot shows the Rabi frequency versus wave number (eq. (5.37)) on considering $\sqrt{\epsilon_x^2 + \epsilon_y^2 + \epsilon_z^2} = |\epsilon|$, parameters are plotted in unit of ω and $\lambda = 1$.

The above equation eq.(5.38) showing nature of massless quanta of Rabi frequency (shown in fig.(5.1) and fig.(5.2)). Rabi frequency at zero detuning i.e. $\Delta = 0$ is

$$\omega_R = \sqrt{|\lambda|^2 n \left(1 - \frac{\epsilon_z}{|\epsilon|}\right)^2}. \tag{5.39}$$

On taking semi-classical limit, when $n = n^0 >> 1$, we obtain the formula viz.

$$\Omega_{\rm RWA} = \sqrt{\Delta^2 + \omega_R'^2 \left(1 - \frac{\epsilon_z}{|\epsilon|}\right)^2}. \tag{5.40}$$

Here $\omega_R^{'} = \sqrt{n^0}|\lambda|$ and similar to classical field case eq.(2.25).

5.6.2 Anomalous Oscillations: ARWA

In the off-resonance case we consider $\omega >> \epsilon, \sqrt{n|\lambda|^2}$. This is the asymptotic rotating wave approximation (ARWA) regime. In this situation we set

$$<>=<>_s + <>_+ \ e^{-i\omega t} + <>_- \ e^{i\omega t}. \tag{5.41}$$

Inserting this into the full amplitude equations eq.(5.29a) and eq.(5.29b) and making use of the observation $|i\partial_t g_{s,\pm}| << |\omega g_{s,\pm}|$ we obtain

$$\langle 0,1,n|\phi(t)\rangle_+ = 0, \tag{5.42}$$

$$\langle 0,1,n|\phi(t)\rangle_- \ = -\frac{\lambda\sqrt{n+1}\ \langle 1,0,n+1|\phi(t)\rangle_s}{\omega}, \tag{5.43}$$

$$\langle 1,0,n+1|\phi(t)\rangle_+ = \frac{\lambda^*\ \sqrt{n+1}\ \ \langle 0,1,n|\phi(t)\rangle_s}{\omega}, \tag{5.44}$$

$$\langle 1,0,n+1|\phi(t)\rangle_- = 0. \tag{5.45}$$

Inserting these into the equations for the slow part of the amplitude we get

$$\left(i\partial_t - \frac{(n+1)|\lambda|^2}{\omega}\right)\langle 0,1,n|\phi(t)\rangle_s = \boldsymbol{\sigma}_{BA}\cdot\boldsymbol{\epsilon}\ \langle 1,0,n|\phi(t)\rangle_s + \boldsymbol{\sigma}_{BB}\cdot\boldsymbol{\epsilon}\ \langle 0,1,n|\phi(t)\rangle_s, \tag{5.46}$$

$$\left(i\ \partial_t + \ \frac{|\lambda|^2\ n}{\omega}\right)\langle 1,0,n|\phi(t)\rangle_s = \boldsymbol{\sigma}_{AB}\cdot\boldsymbol{\epsilon}\ \langle 0,1,n|\phi(t)\rangle_s + \boldsymbol{\sigma}_{AA}\cdot\boldsymbol{\epsilon}\ \langle 1,0,n|\phi(t)\rangle_s. \tag{5.47}$$

To find the Rabi frequency we set $i\partial_t \equiv \Omega$ and obtain the secular equation for Ω

$$\left(\Omega - \frac{|\lambda|^2\, n}{\omega} - \epsilon_z\right)\left(\Omega + \frac{(n+1)|\lambda|^2}{\omega} + \epsilon_z\right)\langle 1,0,n|\phi(t)\rangle_s = (\epsilon_x^2+\epsilon_y^2)\ \langle 1,0,n|\phi(t)\rangle_s. \tag{5.48}$$

Therefore the Rabi frequency is

$$\Omega_{\rm ARWA} = \frac{-|\lambda|^2 \pm 2\sqrt{\left[|\lambda|^2(n+\frac{1}{2}) - \epsilon_z\,\omega\right]^2 + \omega^2(\epsilon_x^2+\epsilon_y^2)}}{2\omega}. \tag{5.49}$$

So for the current density $J \sim \psi_+^\dagger \psi_-$ value of Rabi frequency in the ARWA regime

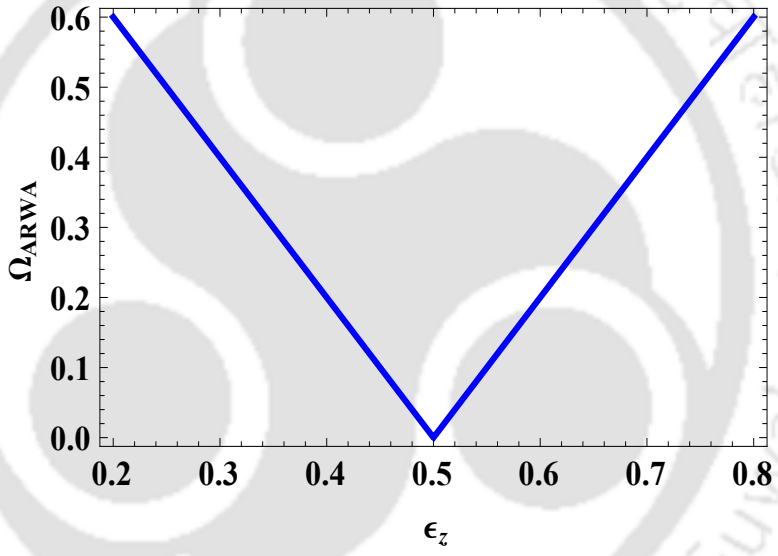

FIGURE 5.3: The plot shows the anomalous Rabi frequency versus energy ϵ_z upon considering $\epsilon_x = 0$, $\epsilon_y = 0$ and $n = 0$ (eq. (5.50)), it depicts the existence of anomalous Rabi oscillation at zero photon limit, the parameters are plotted in the units of ω and $\lambda = 1$.

will be

$$\Omega_{\rm ARWA} = 2\frac{\sqrt{\left[|\lambda|^2(n+\frac{1}{2}) - \epsilon_z\,\omega\right]^2 + \omega^2(\epsilon_x^2+\epsilon_y^2)}}{\omega}. \tag{5.50}$$

The above equation eq.(5.50) showing nature of massless quanta of anomalous Rabi frequency (shown in fig.(5.3) and fig.(5.4)). Upon taking the semi-classical limit, when $n = n^0 >> 1$, we obtain the formula viz.

$$\Omega_{\rm ARWA}(n^0) = 2\frac{\sqrt{(\omega_R'^2 - \epsilon_z\omega)^2 + \omega^2(\epsilon_x^2+\epsilon_y^2)}}{\omega}. \tag{5.51}$$

Here $\omega_R^{'} = \sqrt{n^0}|\lambda|$ and becomes similar to classical field case eq.(2.22). Even in the single (or even zero) photon limit this effect survives. When $n = 0$, the smallest anomalous Rabi frequency will be found and zero-point fluctuations of the photon field leads to anomalous Rabi oscillations in a vacuum.

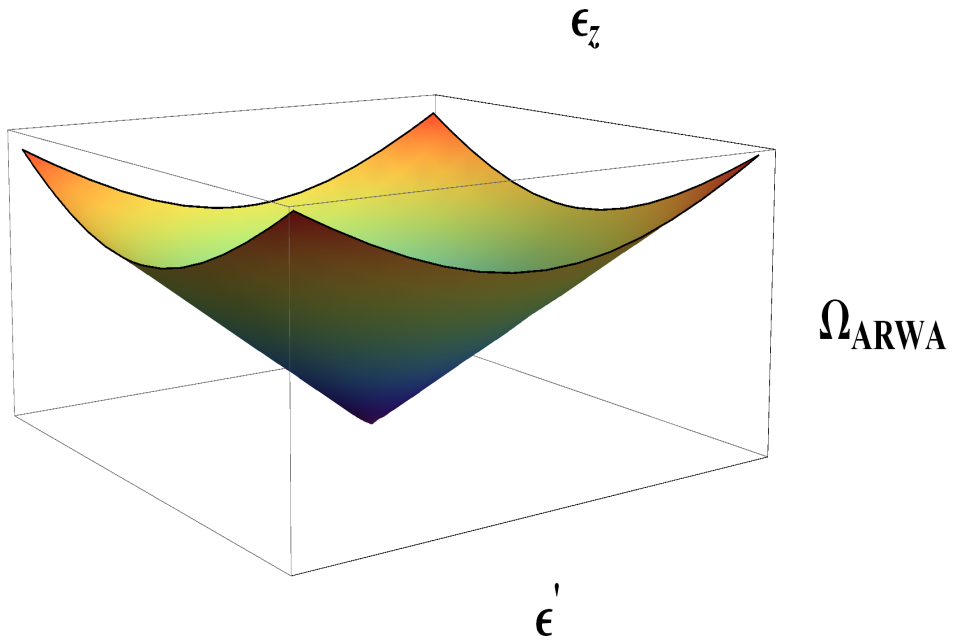

FIGURE 5.4: The plot shows the anomalous Rabi frequency versus energy on considering $\sqrt{\epsilon_x^2 + \epsilon_y^2} = \epsilon^{'}$ (eq. (5.50)), the parameters are plotted in the units of ω and $\lambda = 1$.

5.7 Numerical Solution

In this section, we have shown numerically that the phenomenon of anomalous Rabi oscillation is robust in the sense that is present regardless of whether the EM field is treated classically or quantum mechanically. By examining the plots for slowly oscillating amplitudes and found that their frequency matches the one shown in eq.(5.50). The table 5.1 shows that the approximation scheme we are using viz. ARWA is indeed reliable. For plotting we have taken $n + 1 \approx n$ and $\lambda = 1$. By using the NDSolve routine of Mathematica [184], we solved the Bloch equations (eq.(5.29a) and eq.(5.29b)) fully numerically and found the time period of slow oscillations of these observable have good agreement with the analytical result calculation (table (5.1)). The analytical calculation for the time period is the reciprocal of eq.(5.50). We have defined $\langle 1, 0, n|\phi(t)\rangle = f_{10}(t)$.

$\frac{n}{\omega}$	Time Period (fully analytical)	Time Period (fully numerical)
0.350	20.94	21.15
0.400	31.42	32.05
0.450	62.82	63.46
0.550	62.82	63.46
0.600	31.42	32.05
0.650	20.94	21.15

TABLE 5.1: Time periods are in units of λ^{-1} and $\epsilon^{'} = (0.001)\lambda$, where $\sqrt{\epsilon_x^2 + \epsilon_y^2} = \epsilon^{'}$.

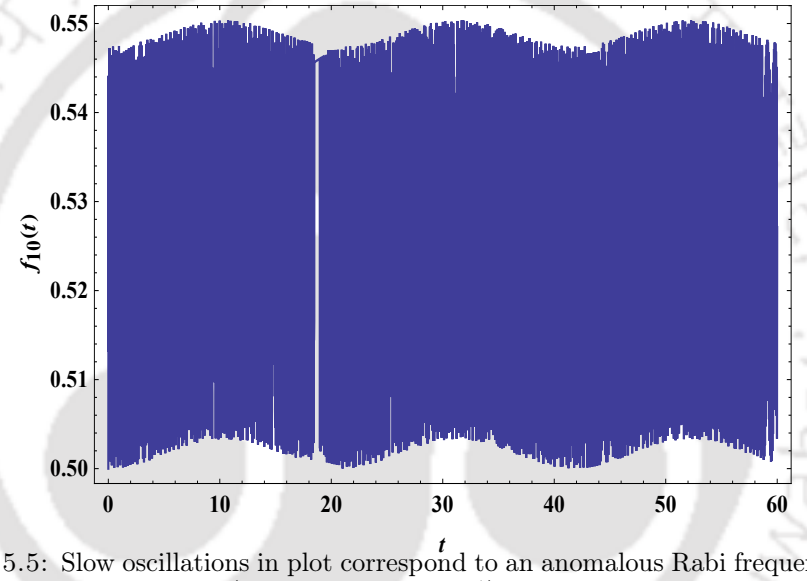

FIGURE 5.5: Slow oscillations in plot correspond to an anomalous Rabi frequency with theoretical periods of 20.94 (time is in unit of λ^{-1}).

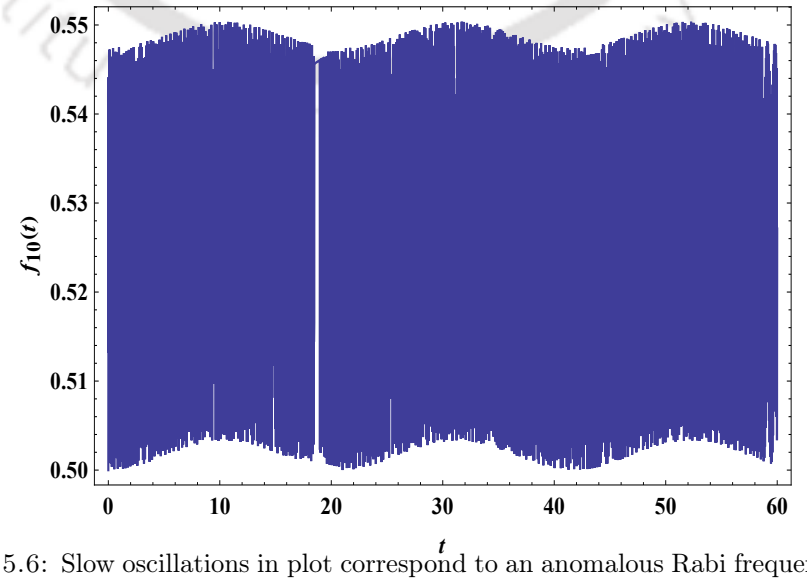

FIGURE 5.6: Slow oscillations in plot correspond to an anomalous Rabi frequency with theoretical periods of 20.94 (time is in unit of λ^{-1}).

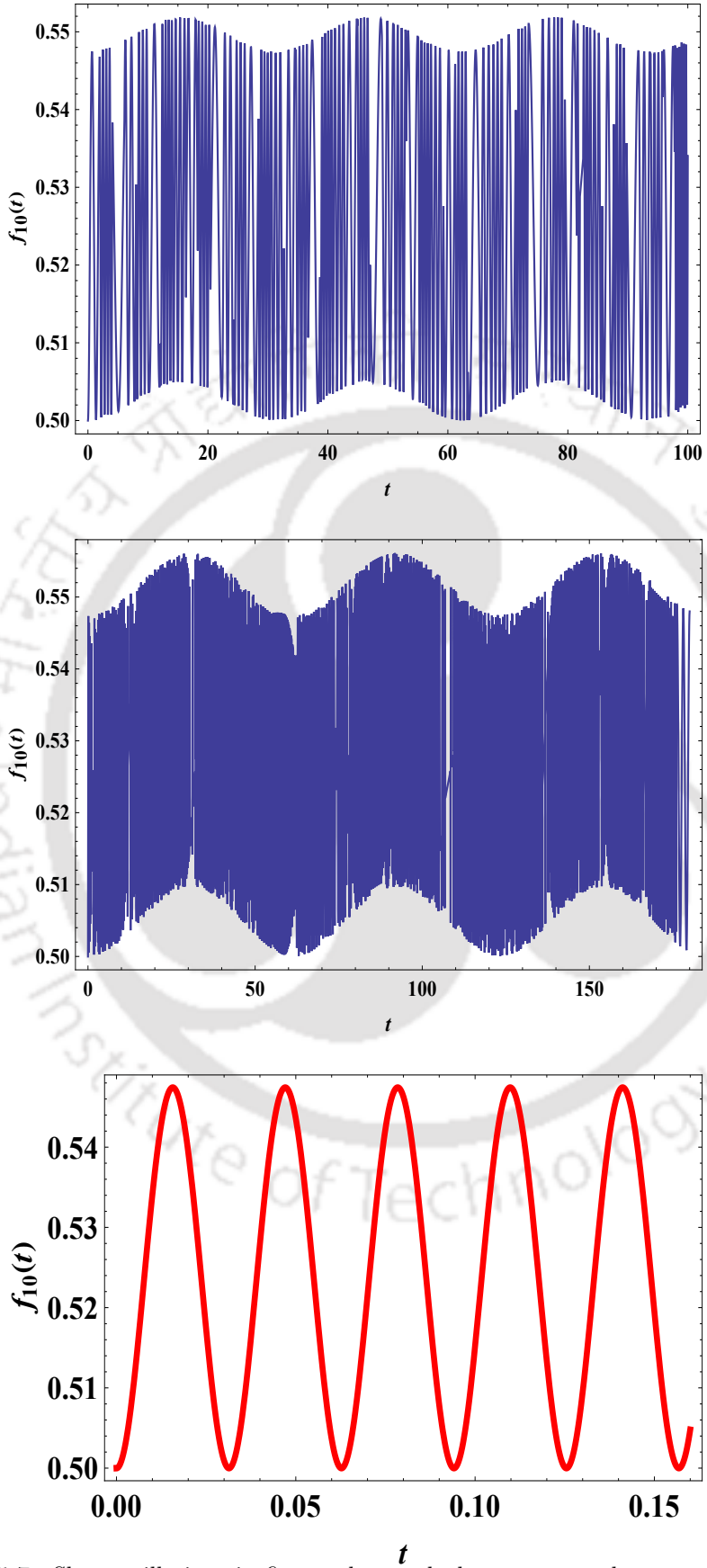

FIGURE 5.7: Slow oscillations in first and second plots correspond to an anomalous Rabi frequency with theoretical periods of 31.42 and 62.82 respectively. Third plot depicts fast oscillations in the above plot that makes the latter appear to have a thick blue line. The fast oscillations have a frequency equal to the frequency of external radiation (time is in unit of λ^{-1}).

5.8 Result and Discussion

In case of graphene, the anomalous Rabi frequency has been found by our group to be [155]

$$\Omega_{\text{ARWA}} = 2\frac{\sqrt{\left[|\lambda|^2(n+\frac{1}{2})\right]^2 + \omega^2(\epsilon_x^2+\epsilon_y^2)}}{\omega}. \tag{5.52}$$

The act of setting $\epsilon_z = 0$ is meant to reduce the dimensionality of the reciprocal space of the Weyl metal to two dimensions which enables an easy comparison with graphene. Having done this we see that eq.(5.50) becomes identical to eq.(5.52). There is a peculiar difference between anomalous Rabi frequency of Weyl semimetal and graphene that, the quanta of anomalous Rabi excitations in graphene always manifest themselves in a form that resembles massive Dirac particles (with mass $\sim \frac{2|\lambda|^2 n}{\omega}$), in Weyl metals, there is a form that resembles massless Dirac particles in certain regions of the momentum space. This result follows from an observation of eq.(5.50). At the point $\epsilon_x = 0$, $\epsilon_y = 0$ and $\epsilon_z \sim \frac{\omega_R'^2}{\omega}$ in reciprocal space, the anomalous Rabi frequency becomes a linear function of ϵ_z, indicating the presence of massless quanta. In case $\epsilon_x, \epsilon_y \neq 0$ these quanta acquire a "mass" equal to ϵ. This is a contrast to graphene where the quanta of anomalous Rabi oscillations are always "massive". Now we turn to a comparison of conventional Rabi frequencies. Setting $\epsilon_z = 0$ in eq.(5.39), the value of conventional Rabi frequency becomes identical to graphene which was found by our group [155] also given below

$$\Omega_{\text{RWA}} = \sqrt{\Delta^2 + n|\lambda|^2}. \tag{5.53}$$

The eq.(5.38) at the point $\omega = 2|\epsilon_z|$ becomes zero which shows that the dispersion relation of the quanta of conventional Rabi oscillations is linear instead of being parabolic, indicating the presence of massless quanta.

5.9 Conclusions

In this chapter, we have investigated the phenomena of anomalous Rabi oscillations in presence of a quantized electromagnetic field in Weyl metals. In Weyl metals, the anomalous Rabi frequency too is peculiar and shows a considerable departure from the form of this quantity seen in graphene. While the quanta of Rabi excitations in graphene always manifest themselves in a form that resembles massive

Dirac particles, in Weyl semimetals, in certain regions of the reciprocal space, we see a form that resembles massless Dirac particles. Thus both the original quasi-particles and the quanta of the collective modes that exist in them in response to time varying fields are relativistic in nature. New phenomena such as zero-point or vacuum anomalous Rabi oscillations are seen. We have found anomalous Rabi oscillation both by treating radiation field quantum mechanically as well as classically. Therefore, it is no hyperbole to say that the anomalous Rabi oscillation is a phenomenon that is unambiguously suited to study relativistic fermionic systems.

5.10 Appendix

5.10.1 Derivation of Jaynes Cummings Type Model Hamiltonian for Weyl Semimetal

We are interested in that result which is analogous to what we obtained in graphene, so we impose the conditions $A_{x0} = A^*_{x0} = A$, $A_{y0} = Ae^{i\gamma}, A^*_{y0} = Ae^{-i\gamma}$ and $A_{z0} = 0, A^*_{z0} = 0$ - the z-component of the vector potential is chosen to be zero thereby eventually enabling a comparison with two dimensional graphene (when the z-component of the momentum is also set to zero) i.e. $A_x = A$ and $A_y = iA$

$$A_y = iA_x \rightarrow iA_y = -A_x \rightarrow A_x + iA_y = 0. \tag{5.54}$$

Consider the Weyl metal described by the Hamiltonian,

$$H = v_F\left(\sigma_x.p_x + \sigma_y.p_y + \sigma_z.p_z\right) = v_F \begin{bmatrix} p_z & p_x - ip_y \\ p_x + ip_y & -p_z \end{bmatrix}. \tag{5.55}$$

Coupling to a vector potential $\mathbf{A}(t) = \mathrm{Re}(\mathbf{A}_0\, e^{-i\omega t})$, the above Hamiltonian becomes

$$\begin{aligned} H = \; v_F \begin{bmatrix} p_z & (p_x - ip_y) \\ (p_x + ip_y) & -p_z \end{bmatrix} + e^{-i\omega t} v_F \begin{bmatrix} -\frac{e}{2c}A_{z0} & -\frac{e}{2c}(A_{x0} - iA_{y0}) \\ -\frac{e}{2c}(A_{x0} + iA_{y0}) & \frac{e}{2c}A_{z0} \end{bmatrix} \\ + e^{i\omega t} v_F \begin{bmatrix} -\frac{e}{2c}A^*_{z0} & -\frac{e}{2c}(A^*_{x0} - iA^*_{y0}) \\ -\frac{e}{2c}(A^*_{x0} + iA^*_{y0}) & \frac{e}{2c}A^*_{z0} \end{bmatrix}. \end{aligned} \tag{5.56}$$

The state vector of above equation is,

$$\psi = \begin{bmatrix} c_A \\ c_B \end{bmatrix}. \tag{5.57}$$

Then Hamiltonian eq.(5.56) in second quantized form

$$\begin{aligned} H = v_F \begin{bmatrix} c_A^\dagger & c_B^\dagger \end{bmatrix} \begin{bmatrix} p_z & (p_x - ip_y) \\ (p_x + ip_y) & -p_z \end{bmatrix} \begin{bmatrix} c_A \\ c_B \end{bmatrix} \\ + e^{-i\omega t} v_F \begin{bmatrix} c_A^\dagger & c_B^\dagger \end{bmatrix} \begin{bmatrix} -\frac{e}{2c}A_{z0} & -\frac{e}{2c}(A_{x0} - iA_{y0}) \\ -\frac{e}{2c}(A_{x0} + iA_{y0}) & \frac{e}{2c}A_{z0} \end{bmatrix} \begin{bmatrix} c_A \\ c_B \end{bmatrix} \\ + e^{i\omega t} v_F \begin{bmatrix} c_A^\dagger & c_B^\dagger \end{bmatrix} \begin{bmatrix} -\frac{e}{2c}A^*_{z0} & -\frac{e}{2c}(A^*_{x0} - iA^*_{y0}) \\ -\frac{e}{2c}(A^*_{x0} + iA^*_{y0}) & \frac{e}{2c}A^*_{z0} \end{bmatrix} \begin{bmatrix} c_A \\ c_B \end{bmatrix}, \end{aligned} \tag{5.58}$$

$$\begin{aligned} H = \left[v_F p_z c_A^\dagger c_A + v_F(p_x - ip_y) c_A^\dagger c_B + v_F(p_x + ip_y) c_B^\dagger c_A - v_F p_z c_B^\dagger c_B \right] \\ + e^{-i\omega t} \left[-\tfrac{e}{2c} v_F A_{z0} c_A^\dagger c_A - \tfrac{e}{2c} v_F (A_{x0} - iA_{y0}) c_A^\dagger c_B - \tfrac{e}{2c} v_F (A_{x0} + iA_{y0}) c_B^\dagger c_A + \tfrac{e}{2c} v_F A_{z0} c_B^\dagger c_B \right] \\ + e^{i\omega t} \left[-\tfrac{e}{2c} v_F A^*_{z0} c_A^\dagger c_A - \tfrac{e}{2c} v_F (A^*_{x0} - iA^*_{y0}) c_A^\dagger c_B - \tfrac{e}{2c} v_F (A^*_{x0} + iA^*_{y0}) c_B^\dagger c_A + \tfrac{e}{2c} v_F A^*_{z0} c_B^\dagger c_B \right]. \end{aligned} \tag{5.59}$$

On applying vector potential conditions $A_z = 0$ and $A_{x0} + iA_{y0} = 0$ the above equation becomes,

$$\begin{aligned} H = & \left[v_F p_z (c_A^\dagger c_A - c_B^\dagger c_B) + v_F(p_x - ip_y) c_A^\dagger c_B + v_F(p_x + ip_y) c_B^\dagger c_A \right] \\ & + e^{-i\omega t} \left(-\frac{e}{2c} v_F (2A_{x0}) c_A^\dagger c_B \right) + e^{i\omega t} \left(-\frac{e}{2c} v_F (2A^*_{x0}) c_B^\dagger c_A \right). \end{aligned} \tag{5.60}$$

The Hamiltonian for a Weyl semimetal-like system, we suggest is

$$\begin{aligned} H = & \; c_A^\dagger \, \boldsymbol{\sigma}_{AB} \cdot \boldsymbol{\epsilon} \, c_B + c_B^\dagger \, \boldsymbol{\sigma}_{BA} \cdot \boldsymbol{\epsilon} \, c_A + c_A^\dagger \, \boldsymbol{\sigma}_{AA} \cdot \boldsymbol{\epsilon} \, c_A + c_B^\dagger \, \boldsymbol{\sigma}_{BB} \cdot \boldsymbol{\epsilon} \, c_B \\ & + \lambda \, c_B^\dagger c_A \, b \, e^{i\omega t} + \lambda^* \;\; c_A^\dagger c_B \, b^\dagger \, e^{-i\omega t}. \end{aligned} \tag{5.61}$$

We have defined $v_F \boldsymbol{p}_\beta = \boldsymbol{\epsilon}_\beta$ where $\beta = x, y, z$, $\boldsymbol{\sigma}_{AB} \cdot \boldsymbol{\epsilon} = \epsilon_x - i\epsilon_y$, $\boldsymbol{\sigma}_{BA} \cdot \boldsymbol{\epsilon} = \epsilon_x + i\epsilon_y$, $\boldsymbol{\sigma}_{AA} \cdot \boldsymbol{\epsilon} = \epsilon_z$, $\boldsymbol{\sigma}_{BB} \cdot \boldsymbol{\epsilon} = -\epsilon_z$, $-\frac{e}{2c} v_F (2A^*_{x0}) = \lambda b$, λ is the coupling constant and $[b, b^\dagger] = 1$ are the photon operators. Here c_A, c_B are the A and B sublattice electrons, $\boldsymbol{\sigma}$ is the pseudo-spin matrices.

5.10.2 Unitary Transformation

Our actual filed interaction Hamiltonian in eq.(5.61) has the form

$$H_1 = \lambda^* c_A^\dagger c_B b_1^\dagger e^{i\omega t} + \lambda c_B^\dagger c_A b_1 e^{-i\omega t}. \tag{5.62}$$

From eq. (5.25), it can be seen, James Cumming model interaction Hamiltonian has form

$$H_2 = \lambda^* c_A^\dagger c_B b_2^\dagger + \lambda c_B^\dagger c_A b_2 + \omega b_2^\dagger b_2. \tag{5.63}$$

H_1 and H_2 can be related by a unitary transformation as shown below

$$i\frac{d}{dt}b_1 = [b_1, H_1] = \lambda^* c_A^\dagger c_B e^{i\omega t}, \tag{5.64}$$

$$i\frac{d}{dt}b_2 = [b_2, H_2] = \lambda^* c_A^\dagger c_B + \omega b_2. \tag{5.65}$$

If we consider $b_2 = b_1 e^{-i\omega t}$ then

$$i\frac{d}{dt}(b_1 e^{-i\omega t}) = \lambda^* c_A^\dagger c_B + \omega b_1 e^{-i\omega t}, \tag{5.66}$$

$$ie^{-i\omega t}\frac{d}{dt}b_1 + \omega b_1 e^{-i\omega t} = \lambda^* c_A^\dagger c_B + \omega b_1 e^{-i\omega t} \Rightarrow i\frac{d}{dt}b_1 = \lambda^* c_A^\dagger c_B e^{i\omega t}. \tag{5.67}$$

So we can relate both eq.(5.62) and eq.(5.63) via unitary transformation.

5.10.3 Bloch Equation

The time evolution equation is

$$i\hbar\frac{\partial}{\partial_t}|\phi\rangle = \sum H\ |n_A, n_B, n_\nu\rangle\langle n_A, n_B, n_\nu|\phi\rangle. \tag{5.68}$$

Where n_A, n_B are number of electron or hole and n_ν is number of photon. On applying both side by $\langle n_{A'}, n_{B'}, n_{\nu'}|$

$$i\hbar\frac{\partial}{\partial_t}\langle n_{A'}, n_{B'}, n_{\nu'}|\phi\rangle = \sum\ \langle n_{A'}, n_{B'}, n_{\nu'}|H|n_A, n_B, n_\nu\rangle\langle n_A, n_B, n_\nu|\phi\rangle. \tag{5.69}$$

On taking Hamiltonian of Weyl Semimetal from eq.(5.28)

$$\begin{aligned} H &= c_A^\dagger\, \boldsymbol{\sigma}_{AB}\cdot\boldsymbol{\epsilon}\, c_B + c_B^\dagger\, \boldsymbol{\sigma}_{BA}\cdot\boldsymbol{\epsilon}\, c_A + c_A^\dagger\, \boldsymbol{\sigma}_{AA}\cdot\boldsymbol{\epsilon}\, c_A + c_B^\dagger\, \boldsymbol{\sigma}_{BB}\cdot\boldsymbol{\epsilon}\, c_B \\ &\quad +\lambda\, c_B^\dagger c_A\, b\, e^{i\omega t} + \lambda^*\ c_A^\dagger c_B\, b^\dagger\, e^{-i\omega t}, \end{aligned} \tag{5.70}$$

$$\begin{aligned} H|n_A,n_B,n_\nu\rangle = \Big[&\boldsymbol{\sigma}_{AB}\cdot\boldsymbol{\epsilon}\, c_A^\dagger c_B|n_A,n_B,n_\nu\rangle + \boldsymbol{\sigma}_{BA}\cdot\boldsymbol{\epsilon}\, c_B^\dagger c_A|n_A,n_B,n_\nu\rangle \\ &+ \boldsymbol{\sigma}_{AA}\cdot\boldsymbol{\epsilon}\, c_A^\dagger c_A|n_A,n_B,n_\nu\rangle + \boldsymbol{\sigma}_{BB}\cdot\boldsymbol{\epsilon}\, c_B^\dagger c_B|n_A,n_B,n_\nu\rangle \\ &+\lambda\, c_B^\dagger c_A|n_A,n_B,n_\nu\rangle\, b\, e^{i\omega t} + \lambda^*\, c_A^\dagger c_B|n_A,n_B,n_\nu\rangle\, b^\dagger\, e^{-i\omega t}\Big]. \end{aligned} \tag{5.71}$$

We know property of rasing and lowering operator $a^\dagger|n\rangle = \sqrt{n+1}\,|n\rangle$ and $a|n\rangle = \sqrt{n}\,|n-1\rangle$

$$\begin{aligned} H|n_A,n_B,n_\nu\rangle = \sum_{n_A,n_B,n_\nu} \Big[&\boldsymbol{\sigma}_{AB}\cdot\boldsymbol{\epsilon}\,\sqrt{n_A+1}\,\sqrt{n_B}\ |n_A+1,n_B-1,n_\nu\rangle + \boldsymbol{\sigma}_{BA}\cdot\boldsymbol{\epsilon}\,\sqrt{n_B+1}\sqrt{n_A}\,|n_A-1,n_B+1,n_\nu\rangle \\ &+ \boldsymbol{\sigma}_{AA}\cdot\boldsymbol{\epsilon}\, n_A|n_A,n_B,n_\nu\rangle + \boldsymbol{\sigma}_{BB}\cdot\boldsymbol{\epsilon}\, n_B|n_A,n_B,n_\nu\rangle + \lambda\,\sqrt{n_B+1}\,\sqrt{n_A}\,\sqrt{n_\nu}\,|n_A-1,n_B+1,n_\nu-1\rangle\ e^{i\omega t} \\ &+\lambda^*\ \sqrt{n_A+1}\sqrt{n_B}\,\sqrt{n_\nu+1}\,|n_A+1,n_B-1,n_\nu+1\rangle\ e^{-i\omega t}\Big]. \end{aligned} \tag{5.72}$$

On applying both sides by $\langle n_{A'},n_{B'},n_{\nu'}|$

$$\begin{aligned} \langle n_{A'},n_{B'},n_{\nu'}|H|n_A,n_B,n_\nu\rangle = \sum_{n_A,n_B,n_\nu} \Big[&\boldsymbol{\sigma}_{AB}\cdot\boldsymbol{\epsilon}\,\sqrt{n_A+1}\,\sqrt{n_B}\ \langle n_{A'},n_{B'},n_{\nu'}|n_A+1,n_B-1,n_\nu\rangle \\ &+\boldsymbol{\sigma}_{BA}\cdot\boldsymbol{\epsilon}\,\sqrt{n_B+1}\sqrt{n_A}\,\langle n_{A'},n_{B'},n_{\nu'}|n_A-1,n_B+1,n_\nu\rangle \\ &+ \boldsymbol{\sigma}_{AA}\cdot\boldsymbol{\epsilon}\, n_A\langle n_{A'},n_{B'},n_{\nu'}|n_A,n_B,n_\nu\rangle + \boldsymbol{\sigma}_{BB}\cdot\boldsymbol{\epsilon}\, n_B\langle n_{A'},n_{B'},n_{\nu'}|n_A,n_B,n_\nu\rangle \\ &+\lambda\,\sqrt{n_B+1}\,\sqrt{n_A}\,\sqrt{n_\nu}\,\langle n_{A'},n_{B'},n_{\nu'}|n_A-1,n_B+1,n_\nu-1\rangle\ e^{i\omega t} \\ &+\lambda^*\ \sqrt{n_A+1}\sqrt{n_B}\,\sqrt{n_\nu+1}\,\langle n_{A'},n_{B'},n_{\nu'}|n_A+1,n_B-1,n_\nu+1\rangle\ e^{-i\omega t}\Big]. \end{aligned} \tag{5.73}$$

Using the Dirac delta property, eq.(5.69) becomes

$$\begin{aligned} i\hbar\frac{\partial}{\partial_t}\langle n_{A'},n_{B'},n_{\nu'}|\phi\rangle = &\boldsymbol{\sigma}_{AB}\cdot\boldsymbol{\epsilon}\,\sqrt{n_A'}\,\sqrt{n_B'+1}\ \langle n_{A'}-1,n_{B'}+1,n_{\nu'}|\phi\rangle \\ &+\boldsymbol{\sigma}_{BA}\cdot\boldsymbol{\epsilon}\,\sqrt{n_A'+1}\,\sqrt{n_B'}\,\langle n_{A'}+1,n_{B'}-1,n_{\nu'}|\phi\rangle \\ &+\boldsymbol{\sigma}_{AA}\cdot\boldsymbol{\epsilon}\, n_A'\,\langle n_{A'},n_{B'},n_{\nu'}|\phi\rangle + \boldsymbol{\sigma}_{BB}\cdot\boldsymbol{\epsilon}\, n_B'\,\langle n_{A'},n_{B'},n_{\nu'}|\phi\rangle \\ &+\lambda\,\sqrt{n_B'}\,\sqrt{n_A'+1}\,\sqrt{n_\nu'+1}\,\langle n_{A'}+1,n_{B'}-1,n_{\nu'}+1|\phi\rangle\ e^{i\omega t} \\ &+\lambda^*\ \sqrt{n_A'}\sqrt{n_B'+1}\,\sqrt{n_\nu'}\,\langle n_{A'}-1,n_{B'}+1,n_{\nu'}-1|\phi\rangle\ e^{-i\omega t}. \end{aligned} \tag{5.74}$$

On putting $n_{A'} = 0$, $n_{B'} = 1$ and $n_{\nu'} = n$

$$i\hbar\frac{\partial}{\partial_t}\langle 0,1,n|\phi\rangle = \Big[\boldsymbol{\sigma}_{BA}\cdot\boldsymbol{\epsilon}\ \langle 1,0,n|\phi\rangle + \boldsymbol{\sigma}_{BB}\cdot\boldsymbol{\epsilon}\ \langle 0,1,n|\phi\rangle + \lambda\ \sqrt{n+1}\, e^{i\omega t}\ \langle 1,0,n+1|\phi\rangle\ \Big]. \tag{5.75}$$

On putting $n_{A'} = 1$, $n_{B'} = 0$ and $n_{\nu'} = n+1$

$$i\hbar\frac{\partial}{\partial_t}\langle 1,0,n+1|\phi\rangle = \Big[\boldsymbol{\sigma}_{AB}\cdot\boldsymbol{\epsilon}\ \langle 0,1,n+1|\phi\rangle + \boldsymbol{\sigma}_{AA}\cdot\boldsymbol{\epsilon}\ \langle 1,0,n+1|\phi\rangle + \lambda^*\, e^{-i\omega t}\ \sqrt{n+1}\ \langle 0,1,n|\phi\rangle\Big]. \tag{5.76}$$

Chapter 6

Summary and Conclusions

In this thesis, we have studied various coherent nonlinear phenomena that arise due to interaction of Dirac-Weyl fermionic system with an electromagnetic field. The motivation behind this thesis work is to study one of the well-known coherent optical effect viz. Rabi oscillations in Dirac-Weyl fermionic system with the matter-field interaction treated both semiclassically as well as quantum mechanically. The phenomenon of Rabi oscillations exists when the frequency of the incident optical field is nearly equal to the transition frequency of the two-level systems, called the resonance condition. Such phenomenon are also seen in two-band systems such as semiconductors (with levels being replaced by bands) though this was observed a long time after its theoretical prediction in the 1980's. Far from resonance, when the frequency of external radiation is large compared to the frequency corresponding to the energy of a particle-hole pair, the Rabi oscillations vanish in two-level systems and also in conventional semiconductors. In case of Dirac-Weyl fermionic system, however, a new type of Rabi oscillation occurs far-from resonance, called anomalous Rabi oscillation, predicated by our group (and also by others where these ideas go under the name of "Floquet theory"). The study anomalous Rabi oscillation is the central theme of this thesis. Finally, we would like to present a brief summary of each of the chapters.

Chapter 1: Introduction

In this chapter, an introduction to the basic theory of Dirac-Weyl fermionic system is presented. These systems work as a bridge between condensed matter and relativistic electrodynamics physics. A survey of the relevant literature of the

importance of Dirac-Weyl fermionic system is presented. It is also explained how these systems may be utilized in applications.

Chapter 2: Rabi Oscillations in Dirac-Weyl Fermionic Systems

In this chapter, we have described one of the important optical properties in relativistic fermionic systems- Rabi oscillations. Rabi oscillations are analyzed using the well-known rotating wave approximation (RWA) and this is applicable only near the conventional resonance condition when the frequency of incident optical field is comparable to the frequency corresponding to particle-hole energy. Far from conventional resonance, only relativistic fermionic systems exhibit a new type of Rabi oscillation, which is absent in conventional semiconductors and two-level systems, known as anomalous Rabi oscillation (ARO). In order to study this, we employ an approximation known as asymptotic rotating wave approximation (ARWA). In this chapter, a new kind of slow oscillation in population and polarization densities that is present only in relativistic fermionic systems is seen far from conventional resonance. We have studied this phenomenon as well as its conventional counterpart close to resonance (ordinary Rabi oscillations) and verified the claims numerically.

Chapter 3: Band-Anisotropy Induced Bloch-Siegert Shift in Graphene

The Bloch-Siegert shift is a phenomenon in quantum optics, typically seen in two-level systems, when the driving field is sufficiently strong (e.g. atoms driven by a strong laser drive or nuclear spins in NMR, driven by a strong oscillating magnetic field). In the conventional RWA, we consider only the slowly varying part of the driving field by neglecting the rapidly part of the oscillating field. Bloch and Siegert studied the effect of the rapidly oscillating term on the resonance frequency and noticed that in the presence of counter-rotating terms, the resonance frequency shows a shift, which is known as the Bloch-Siegert shift (BSS). In case of anomalous Rabi oscillations, however, band anisotropy caused by the inclusion of next-nearest-neighbor hopping together with frequency doubling or the Rashba effect leads to a Bloch-Siegert shift which is quite substantial (in percentage terms, actually infinite), lending credence to the claim that the anomalous Rabi oscillation is sensitive to qualitative changes in the low energy band structure of graphene and as such is a useful indicator of the chiral massless Dirac fermion nature of quasiparticles in graphene.

Chapter 4: A Theoretical Analysis of the Pump-Probe Experiment in Dirac-Weyl Systems

In this chapter, we have theoretically modeled a pump-probe experiment, which is used to justify the phenomenon of anomalous Rabi oscillations - a central idea in this thesis. By using the pump-probe experiment, incoherent optical properties such as optical dephasing and relaxation of band electrons in semiconductors have been studied. In this experiment, two successive laser pulses are used, one for exciting the system in a certain way, called pump pulse and other to test it after a variable time delay, called probe pulse. Femtosecond laser pulses are required for studying these incoherent optical properties because timescales for these phenomena are short (subpicosecond).

Chapter 5: Quantum Rabi Oscillations in Weyl Semimetal

In this chapter, we study anomalous Rabi oscillations in presence of a quantized EM field. New phenomena such as zero-point or vacuum anomalous Rabi oscillations are seen. Anomalous Rabi oscillations are seen even while treating the radiation field quantum mechanically.

Vitae

Mr. Upendra Kumar, born at Raebareli in Uttar Pradesh, India, did his B.Sc. with Physics and Mathematics in 2005 from Bramhanand Degree College, Kanpur, Uttar Pradesh and M.Sc. in Physics in 2007 from C.S.J.M. University Kanpur, Uttar Pradesh, India. He joined IIT Guwahati for Ph.D. in Dec 2010. He was awarded Junior Research Fellowship in 2011, Senior Research Fellowship in 2013 by MHRD, India and got European Union Fellowship (ERASMUS) in 2015-2016 for studying in Vilnius University, Lithuania.

Publications

NATIONAL/INTERNATIONAL:

1. *Signatures of bulk topology in the non-linear optical spectra of Dirac-Weyl materials.*
   Upendra Kumar, Vipin Kumar, Enamullah and Girish S. Setlur, **Eur. Phys. J. B 91, 86 (2018)**.

2. *Band anisotropy induced Bloch-Siegert shift in graphene.*
   Upendra Kumar, Vipin Kumar, Enamullah and Girish S. Setlur, **J. Opt. Soc. Am. B 31, 3042-3049 (2014)**.

3. *Anomalous Bloch-Siegert effect in graphene.*
   Upendra Kumar, Enamullah, Vipin Kumar and Girish S. Setlur, **J. Nanosci. Lett. 4, 30 (2014)**.

4. *Quantum Rabi oscillations in graphene.*
   Enamullah, Vipin Kumar, **Upendra Kumar** and Girish S. Setlur, **J. Opt. Soc. Am. B 31, 484-493 (2014)**.

5. *A theoretical study of pump-probe experiment in single layer, bilayer and multilayer graphene.*
   Enamullah, Vipin Kumar, **Upendra Kumar** and Girish S. Setlur, **Pramana (Indian Academy of sciences) 82(6), 1085-1101 (2014)**.

6. *Coherent nonlinear optical response in SU(2) symmetry broken in single and bilayer graphene.*
   Vipin Kumar, Enamullah, **Upendra Kumar** and Girish S. Setlur, **Physica B 436, 140-148 (2014)**.

7. *Band structure effect on the nonlinear optical response of bilayer graphene.*
   Vipin Kumar, Enamullah, **Upendra Kumar** and Girish S. Setlur, **Eur. Phys. J. B 87, 70 (2014)**.

8. *Coherent nonlinear electromagnetic response in twisted bilayer and few-layer graphene.*
   Vipin Kumar, Enamullah, **Upendra Kumar** and Girish S. Setlur, **Pramana (Indian Academy of sciences), 83(4), 597-617,2014**.

9. *Strain effect on the nonlinear electromagnetic response of 2D carbon based material.*
   Enamullah, Vipin Kumar, **Upendra Kumar**, and Girish S. Setlur, **Adv. Sci. Lett., 20, 1459-1462, 2014**.

Conference Publications:

1. *Bloch-Siegert Shift in Dirac-Weyl fermionic Systems.*
   Upendra Kumar, Vipin Kumar, Enamullah and Girish S Setlur, AIP Conf. Proc. **1942**, 120005 (2018).

2. *Quantum Anomalous Bloch-Siegert Shift in Weyl Semimetal.*
   Upendra Kumar, Vipin Kumar, Enamullah and Girish S Setlur, AIP Conf. Proc. **1953**, 030042 (2018).

3. *Quantized transient non-linear Rabi frequency response in Weyl semimetals.*
   Upendra Kumar, Vipin Kumar, Enamullah and Girish S Setlur, **Accepted** in 'Materials Today: Proceedings'.

4. *Anomalous behavior of Hg Te clean quantum well.*
   Upendra Kumar , Enamullah, Vipin Kumar and Girish S Setlur, **Published** in 'Advances in Nanotechnology and Renewable Energy' Conference Proceedings with ISBN: 978-93-81212-65-3, page no 91.

5. *Rabi oscillations in gapped bilayer graphene.*
   Vipin Kumar, Enamullah, **Upendra Kumar** and Girish S. Setlur, AIP Conf. Proc. **1536**, 266 (2012).

6. *Conventional and anomalous quantum Rabi oscillations in graphene.*
   Enamullah, Vipin Kumar, **Upendra Kumar** and Girish S Setlur, AIP Conf. Proc. **1591**, 318 (2014).

7. *Nonlinear electromagnetic response of strained 2D carbon based material.* Enamullah, Vipin Kumar, **Upendra Kumar** and Girish S Setlur, **Published** in 'Advances in Nanotechnology and Renewable Energy' Conference Proceedings with ISBN: 978-93-81212-65-3, page no 46.

Conferences and Workshop Attended

1. **2012:** National Conference on Carbon Materials held at **Mumbai, India**. Presented a poster.

2. **2013:** 3rd International Conference on Advanced Nanomaterials and Nanotechnology held at **Indian Institute of Technology, Guwahati, India**. Presented a poster.

3. **2013:** International Conference on Nanotechnology held at **Indian Institute of Chemical Engineers, Haldia, West Bengal, India**. Presented a poster.

4. **2013 :** 58th DAE Solid State Physics Symposium held at **Thaper University, Patiala, India**. Presented a poster.

5. **2014:** Non equilibrium Complex Systems held at **Handique Girl's College, Guwahati, India**. Presented a poster.

6. **2014:** International Conference on Optics and Optoelectronics held at **IRDE, Dehradun, India**. Presented a poster.

7. **2014 :** National Conference on Nanotechnology and Renewable Energy (NCNRE 2014) held at **Jamia Millia Islamia Central University, New Delhi, India**, Presented a paper as **Poster**.

8. **2014 :** Attend a workshop on technical wrting held at **IIT Guwahati, Guwahati, India**.

9. **2015:** Second International Conference on Nanotechnology held at **Indian Institute of Chemical Engineers, Haldia, West Bengal, India**. Oral presentation.

10. **2016:** International Conference on Nanoscience and Nanotechnology held at **VIT, Vellore, Tamil Nandu, India**. Poster presentation (*Got best poster award*).

Bibliography

[1] A. Burkov and L. Balents, Physical Review Letters **107**, 127205 (2011).

[2] M. Z. Hasan and C. L. Kane, Reviews of Modern Physics **82**, 3045 (2010).

[3] X.-L. Qi and S.-C. Zhang, Reviews of Modern Physics **83**, 1057 (2011).

[4] S.-Q. Shen, *TOPOLOGICAL INSULATORS: Dirac Equation in Condensed Matter* (SPRINGER, 2017).

[5] M. Neupane, S.-Y. Xu, R. Sankar, N. Alidoust, G. Bian, C. Liu, I. Belopolski, T.-R. Chang, H.-T. Jeng, H. Lin, et al., Nature Communications **5** (2014).

[6] S. Jeon, B. B. Zhou, A. Gyenis, B. E. Feldman, I. Kimchi, A. C. Potter, Q. D. Gibson, R. J. Cava, A. Vishwanath, and A. Yazdani, Nature Materials **13**, 851 (2014).

[7] L. Yang, Z. Liu, Y. Sun, H. Peng, H. Yang, T. Zhang, B. Zhou, Y. Zhang, Y. Guo, M. Rahn, et al., Nature Physics **11**, 728 (2015).

[8] L. Balents, Physics **4**, 36 (2011).

[9] H. Weyl, Zeitschrift für Physik A Hadrons and Nuclei **56**, 330 (1929).

[10] G. E. Volovik, JETP Letters **75**, 55 (2002).

[11] S. M. Young, S. Zaheer, J. C. Teo, C. L. Kane, E. J. Mele, and A. M. Rappe, Physical Review Letters **108**, 140405 (2012).

[12] Z. Wang, Y. Sun, X.-Q. Chen, C. Franchini, G. Xu, H. Weng, X. Dai, and Z. Fang, Physical Review B **85**, 195320 (2012).

[13] Z. Wang, H. Weng, Q. Wu, X. Dai, and Z. Fang, Physical Review B **88**, 125427 (2013).

[14] A. Zyuzin, S. Wu, and A. Burkov, Physical Review B **85**, 165110 (2012).

[15] P. Hosur, Physical Review B **86**, 195102 (2012).

[16] A. C. Potter, I. Kimchi, and A. Vishwanath, Nature Communications **5** (2014).

[17] M. Dadsetani and A. Ebrahimian, Journal of Electronic Materials **45**, 5867 (2016).

[18] M. Katsnelson and K. Novoselov, Solid State Communications **143**, 3 (2007).

[19] I. I. Rabi, Physical Review **51**, 652 (1937).

[20] S. Iijima, Journal of Crystal Growth **50**, 675 (1980).

[21] S. Iijima and T. Ichihashi, Nature **363**, 603 (1993).

[22] K. S. Novoselov, A. K. Geim, S. V. Morozov, D. Jiang, Y. Zhang, S. V. Dubonos, I. V. Grigorieva, and A. A. Firsov, Science **306**, 666 (2004).

[23] A. C. Neto, F. Guinea, N. M. Peres, K. S. Novoselov, and A. K. Geim, Reviews of Modern Physics **81**, 109 (2009).

[24] A. Van Bommel, J. Crombeen, and A. Van Tooren, Surface Science **48**, 463 (1975).

[25] X. Lu, M. Yu, H. Huang, and R. S. Ruoff, Nanotechnology **10**, 269 (1999).

[26] R. B. Little, Journal of Cluster Science **14**, 135 (2003).

[27] C. Berger, Z. Song, T. Li, X. Li, A. Y. Ogbazghi, R. Feng, Z. Dai, A. N. Marchenkov, E. H. Conrad, P. N. First, et al., The Journal of Physical Chemistry B **108**, 19912 (2004).

[28] A. M. Schakel, Physical Review D **43**, 1428 (1991).

[29] J. González, F. Guinea, and M. Vozmediano, Physical Review Letters **77**, 3589 (1996).

[30] E. Gorbar, V. Gusynin, V. Miransky, and I. Shovkovy, Physical Review B **66**, 045108 (2002).

[31] M. Katsnelson, The European Physical Journal B-Condensed Matter and Complex Systems **51**, 157 (2006).

[32] M. Katsnelson, K. Novoselov, and A. Geim, Nature Physics **2**, 620 (2006).

[33] J. Tworzydło, B. Trauzettel, M. Titov, A. Rycerz, and C. W. Beenakker, Physical Review Letters **96**, 246802 (2006).

[34] G. W. Semenoff, Physical Review Letters **53**, 2449 (1984).

[35] E. Fradkin, Physical Review B **33**, 3263 (1986).

[36] F. D. M. Haldane, Physical Review Letters **61**, 2015 (1988).

[37] R. Saito, G. Dresselhaus, and M. S. Dresselhaus, *Physical Properties of Carbon Nanotubes* (World scientific, 1998).

[38] C. Kittel, *Introduction to Solid State Physics* (Wiley, 2005).

[39] N. W. Ashcroft and N. D. Mermin, *Solid State Physics* (Saunders, Philadelphia, 1976).

[40] P. R. Wallace, Physical Review **71**, 622 (1947).

[41] S. Reich, J. Maultzsch, C. Thomsen, and P. Ordejon, Physical Review B **66**, 035412 (2002).

[42] C. Bena and G. Montambaux, New Journal of Physics **11**, 095003 (2009).

[43] Y. Hasegawa, R. Konno, H. Nakano, and M. Kohmoto, Physical Review B **74**, 033413 (2006).

[44] I. E. AbbottŠs, Physics Today **60**, 35 (2007).

[45] A. K. Geim and A. H. MacDonald, Physics Today **60**, 35 (2007).

[46] A. C. Neto, F. Guinea, and N. M. Peres, Physics World **19**, 33 (2006).

[47] J. Baringhaus, M. Ruan, F. Edler, A. Tejeda, M. Sicot, A. Taleb-Ibrahimi, A.-P. Li, Z. Jiang, E. H. Conrad, C. Berger, et al., Nature **506**, 349 (2014).

[48] J. Eberly and L. Allen, *Optical Resonance and Two-level Atoms* (John Wiley & Sons, 1975).

[49] H. Haug and S. W. Koch, *Quantum Theory of the Optical and Electronic Properties of Semiconductors* (World Scientific Publishing Co Inc, 2009).

[50] C. Gerry and P. Knight, *Introductory Quantum Optics* (Cambridge University Press., 2005).

[51] K. S. Novoselov, A. K. Geim, S. Morozov, D. Jiang, M. Katsnelson, I. Grigorieva, S. Dubonos, and A. Firsov, Nature **438**, 197 (2005).

[52] Z. Ni, H. Wang, J. Kasim, H. Fan, T. Yu, Y. Wu, Y. Feng, and Z. Shen, Nano Letters **7**, 2758 (2007).

[53] P. Blake, E. Hill, A. Castro Neto, K. Novoselov, D. Jiang, R. Yang, T. Booth, and A. Geim, Applied Physics Letters **91**, 063124 (2007).

[54] J. Park, A. Reina, R. Saito, J. Kong, G. Dresselhaus, and M. Dresselhaus, Carbon **47**, 1303 (2009).

[55] Z. Ni, W. Chen, X. Fan, J. Kuo, T. Yu, A. Wee, and Z. Shen, Physical Review B **77**, 115416 (2008).

[56] L. Mandel and E. Wolf, *Optical Coherence and Quantum Optics* (Cambridge University Press, 1995).

[57] R. W. Boyd, *Nonlinear Optics* (Academic Press, New York, 2008).

[58] P. A. Lee, Physical Review Letters **71**, 1887 (1993).

[59] A. W. Ludwig, M. P. Fisher, R. Shankar, and G. Grinstein, Physical Review B **50**, 7526 (1994).

[60] K. Ziegler, Physical Review Letters **80**, 3113 (1998).

[61] R. R. Nair, P. Blake, A. N. Grigorenko, K. S. Novoselov, T. J. Booth, T. Stauber, N. M. Peres, and A. K. Geim, Science **320**, 1308 (2008).

[62] S. Kumar, M. Anija, N. Kamaraju, K. Vasu, K. Subrahmanyam, A. Sood, and C. Rao, Applied Physics Letters **95**, 191911 (2009).

[63] M. Breusing, S. Kuehn, T. Winzer, E. Malić, F. Milde, N. Severin, J. Rabe, C. Ropers, A. Knorr, and T. Elsaesser, Physical Review B **83**, 153410 (2011).

[64] J. M. Dawlaty, S. Shivaraman, M. Chandrashekhar, F. Rana, and M. G. Spencer, Applied Physics Letters **92**, 042116 (2008).

[65] J. Shang, Z. Luo, C. Cong, J. Lin, T. Yu, and G. G. Gurzadyan, Applied Physics Letters **97**, 163103 (2010).

[66] P. A. George, J. Strait, J. Dawlaty, S. Shivaraman, M. Chandrashekhar, F. Rana, and M. G. Spencer, Nano Letters **8**, 4248 (2008).

[67] B. A. Ruzicka, L. K. Werake, H. Zhao, S. Wang, and K. P. Loh, Applied Physics Letters **96**, 173106 (2010).

[68] M. Nakahara, *Geometry, Topology and Physics* (CRC Press, 2003).

[69] K. V. Klitzing, G. Dorda, and M. Pepper, Physical Review Letters **45**, 494 (1980).

[70] C. L. Kane and E. J. Mele, Physical Review Letters **95**, 226801 (2005).

[71] J. Yin, H. N. Krishnamoorthy, G. Adamo, A. M. Dubrovkin, Y. D. Chong, N. I. Zheludev, and C. Soci, arXiv preprint arXiv:1702.00302 (2017).

[72] K. L. Wang, M. Lang, and X. Kou, *Handbook of Spintronics* (Springer, 2016).

[73] E. H. Hall, American Journal of Mathematics **2**, 287 (1879).

[74] R. Karplus and J. Luttinger, Physical Review **95**, 1154 (1954).

[75] M. Costato, IL Nuovo Cimento B (1971-1996) **109**, 211 (1994).

[76] D. J. Thouless, *Topological Quantum Numbers in Nonrelativistic Physics* (World Scientific, 1998).

[77] D. Thouless, M. Kohmoto, M. Nightingale, and M. Den Nijs, Physical Review Letters **49**, 405 (1982).

[78] H. Min, J. Hill, N. A. Sinitsyn, B. Sahu, L. Kleinman, and A. H. MacDonald, Physical Review B **74**, 165310 (2006).

[79] J. Boettger and S. Trickey, Physical Review B **75**, 121402 (2007).

[80] B. A. Bernevig, T. L. Hughes, and S.-C. Zhang, Science **314**, 1757 (2006).

[81] B. A. Bernevig and S.-C. Zhang, Physical Review Letters **96**, 106802 (2006).

[82] M. D'yakonov and V. Perel, Soviet Journal of Experimental and Theoretical Physics Letters **13**, 467 (1971).

[83] C. L. Kane and E. J. Mele, Physical Review Letters **95**, 146802 (2005).

[84] Y. Chen, J. Analytis, J.-H. Chu, Z. Liu, S.-K. Mo, X.-L. Qi, H. Zhang, D. Lu, X. Dai, Z. Fang, et al., Science **325**, 178 (2009).

[85] M. König, S. Wiedmann, C. Brüne, A. Roth, H. Buhmann, L. W. Molenkamp, X.-L. Qi, and S.-C. Zhang, Science **318**, 766 (2007).

[86] S. C. Zhang, International Journal of Modern Physics B **6**, 25 (1992).

[87] K. He, Y. Wang, and Q.-K. Xue, National Science Review **1**, 38 (2013).

[88] G. Jotzu, M. Messer, R. Desbuquois, M. Lebrat, T. Uehlinger, D. Greif, and T. Esslinger, Nature **515**, 237 (2014).

[89] L. Fu, C. L. Kane, and E. J. Mele, Physical Review Letters **98**, 106803 (2007).

[90] D. Hsieh, D. Qian, L. Wray, Y. Xia, Y. S. Hor, R. J. Cava, and M. Z. Hasan, Nature **452**, 970 (2008).

[91] P. Di Pietro, F. M. Vitucci, D. Nicoletti, L. Baldassarre, P. Calvani, R. Cava, Y. S. Hor, U. Schade, and S. Lupi, Physical Review B **86**, 045439 (2012).

[92] A. LaForge, A. Frenzel, B. Pursley, T. Lin, X. Liu, J. Shi, and D. Basov, Physical Review B **81**, 125120 (2010).

[93] A. Sushkov, G. Jenkins, D. Schmadel, N. Butch, J. Paglione, and H. Drew, Physical Review B **82**, 125110 (2010).

[94] R. V. Aguilar, A. Stier, W. Liu, L. Bilbro, D. George, N. Bansal, L. Wu, J. Cerne, A. Markelz, S. Oh, et al., Physical Review Letters **108**, 087403 (2012).

[95] L. Wu, M. Brahlek, R. V. Aguilar, A. Stier, C. Morris, Y. Lubashevsky, L. Bilbro, N. Bansal, S. Oh, and N. Armitage, Nature Physics **9**, 410 (2013).

[96] T. Morimoto and N. Nagaosa, Physical Review B **93**, 125125 (2016).

[97] Y. Chen, J. Analytis, J. Chu, Z. Liu, S. Mo, X. Qi, H. Zhang, D. Lu, X. Dai, Z. Fang, et al., arXiv preprint arXiv:0904.1829 (2009).

[98] Y. Xia, D. Qian, D. Hsieh, L. Wray, A. Pal, H. Lin, A. Bansil, D. Grauer, Y. S. Hor, R. J. Cava, et al., Nature Physics **5**, 398 (2009).

[99] P. Hosur and X. Qi, Comptes Rendus Physique **14**, 857 (2013).

[100] P. A. Dirac, in *Proceedings of the Royal Society of London A: Mathematical, Physical and Engineering Sciences* (The Royal Society, 1928), vol. 117, pp. 610–624.

[101] C. Wu, B. A. Bernevig, and S.-C. Zhang, Physical Review Letters **96**, 106401 (2006).

[102] G. Woan, *The Cambridge Handbook of Physics Formulas* (Cambridge University Press, 2000).

[103] G. E. Volovik, *The Universe in a Helium Droplet*, vol. 117 (Oxford University Press on Demand, 2003).

[104] T. Tsuneto, *Superconductivity and Superfluidity* (Cambridge University Press, 2005).

[105] X. Wan, A. M. Turner, A. Vishwanath, and S. Y. Savrasov, Physical Review B **83**, 205101 (2011).

[106] A. Zyuzin and A. Burkov, Physical Review B **86**, 115133 (2012).

[107] J.-H. Jiang, Physical Review A **85**, 033640 (2012).

[108] H. Wei, S.-P. Chao, and V. Aji, Physical Review B **89**, 014506 (2014).

[109] Z. Wang and S.-C. Zhang, Physical Review B **87**, 161107 (2013).

[110] T. Meng and L. Balents, Physical Review B **86**, 054504 (2012).

[111] A. G. Grushin, Physical Review D **86**, 045001 (2012).

[112] V. Aji, Physical Review B **85**, 241101 (2012).

[113] H.-J. Kim, K.-S. Kim, J.-F. Wang, M. Sasaki, N. Satoh, A. Ohnishi, M. Kitaura, M. Yang, and L. Li, Physical Review Letters **111**, 246603 (2013).

[114] C.-X. Liu, P. Ye, and X.-L. Qi, Physical Review B **87**, 235306 (2013).

[115] K. Landsteiner, Physical Review B **89**, 075124 (2014).

[116] E. Gorbar, V. Miransky, and I. Shovkovy, Physical Review B **89**, 085126 (2014).

[117] Z. Jian-Hui, J. Hua, N. Qian, and S. Jun-Ren, Chinese Physics Letters **30**, 027101 (2013).

[118] Y. Chen, S. Wu, and A. Burkov, Physical Review B **88**, 125105 (2013).

[119] P. Hosur, S. Parameswaran, and A. Vishwanath, Physical Review Letters **108**, 046602 (2012).

[120] A. Burkov, M. Hook, and L. Balents, Physical Review B **84**, 235126 (2011).

[121] R. Nandkishore, D. A. Huse, and S. L. Sondhi, Physical Review B **89**, 245110 (2014).

[122] S. Ganichev and W. Prettl, *Intense Terahertz Excitation of Semiconductors*, 14 (Oxford University Press on Demand, 2006).

[123] M. C. Hoffmann, N. C. Brandt, H. Y. Hwang, K.-L. Yeh, and K. A. Nelson, Applied Physics Letters **95**, 231105 (2009).

[124] D. Turchinovich, J. M. Hvam, and M. C. Hoffmann, Physical Review B **85**, 201304 (2012).

[125] M. Cornet, J. Degert, E. Abraham, and E. Freysz, Journal of The Optical Society of America B **31**, 1648 (2014).

[126] C. D. Spataru, S. Ismail-Beigi, L. X. Benedict, and S. G. Louie, Physical Review Letters **92**, 077402 (2004).

[127] J. Deslippe, C. D. Spataru, D. Prendergast, and S. G. Louie, Nano Letters **7**, 1626 (2007).

[128] L. Yang, J. Deslippe, C.-H. Park, M. L. Cohen, and S. G. Louie, Physical Review Letters **103**, 186802 (2009).

[129] M. Dvorak and Z. Wu, Physical Review B **92**, 035422 (2015).

[130] F. Wang, D. J. Cho, B. Kessler, J. Deslippe, P. J. Schuck, S. G. Louie, A. Zettl, T. F. Heinz, and Y. R. Shen, Physical Review Letters **99**, 227401 (2007).

[131] J. Lee, T.-H. Han, M.-H. Park, D. Y. Jung, J. Seo, H.-K. Seo, H. Cho, E. Kim, J. Chung, S.-Y. Choi, et al., Nature communications **7**, 11791 (2016).

[132] D. Cohen-Tanugi and J. C. Grossman, Nano Letters **12**, 3602 (2012).

[133] S.-J. Han, A. V. Garcia, S. Oida, K. A. Jenkins, and W. Haensch, Nature Communications **5** (2014).

[134] M. C. Lemme, T. J. Echtermeyer, M. Baus, and H. Kurz, IEEE Electron Device Letters **28**, 282 (2007).

[135] J. Kedzierski, P.-L. Hsu, P. Healey, P. W. Wyatt, C. L. Keast, M. Sprinkle, C. Berger, and W. A. De Heer, IEEE Transactions on Electron Devices **55**, 2078 (2008).

[136] A. Krishnamurthy, V. Gadhamshetty, R. Mukherjee, B. Natarajan, O. Eksik, S. A. Shojaee, D. A. Lucca, W. Ren, H.-M. Cheng, and N. Koratkar, Scientific Reports **5** (2015).

[137] E. Majorana, Nuovo Cimento **14**, 322 (1937).

[138] R. Jackiw and C. Rebbi, Physical Review D **13**, 3398 (1976).

[139] R. Jackiw and P. Rossi, Nuclear Physics B **190**, 681 (1981).

[140] N. Read and D. Green, Physical Review B **61**, 10267 (2000).

[141] S. D. Sarma, C. Nayak, and S. Tewari, Physical Review B **73**, 220502 (2006).

[142] V. Gurarie, L. Radzihovsky, and A. Andreev, Physical Review Letters **94**, 230403 (2005).

[143] L. Fu and C. L. Kane, Physical Review Letters **102**, 216403 (2009).

[144] R. D. Peccei and H. R. Quinn, Physical Review Letters **38**, 1440 (1977).

[145] F. Wilczek, Physical Review Letters **58**, 1799 (1987).

[146] X.-L. Qi, T. L. Hughes, and S.-C. Zhang, Physical Review B **78**, 195424 (2008).

[147] A. M. Essin, J. E. Moore, and D. Vanderbilt, Physical Review Letters **102**, 146805 (2009).

[148] C. Nayak, S. H. Simon, A. Stern, M. Freedman, and S. D. Sarma, Reviews of Modern Physics **80**, 1083 (2008).

[149] H. Chen, W. Zhu, D. Xiao, and Z. Zhang, Physical Review Letters **107**, 056804 (2011).

[150] X. Zhang, J. Wang, and S.-C. Zhang, Physical Review B **82**, 245107 (2010).

[151] H. Peng, W. Dang, J. Cao, Y. Chen, D. Wu, W. Zheng, H. Li, Z.-X. Shen, and Z. Liu, Nature Chemistry **4**, 281 (2012).

[152] Enamullah, V. Kumar, and G. S. Setlur, Physica B: Condensed Matter **407**, 4600 (2012).

[153] E. Mishchenko, Physical Review Letters **103**, 246802 (2009).

[154] K. L. Ishikawa, Physical Review B **82**, 201402 (2010).

[155] Enamullah, V. Kumar, U. Kumar, and G. S. Setlur, Journal of The Optical Society of America B **31**, 484 (2014).

[156] E. Hecht, *Physics -Optics* (Pearson Addison Wesley, 1998).

[157] L. Allen and J. Eberly, *Optical Resonances and Two-Level Atoms, Inter-Science Monographs and Texts in Physics and Astronomy 28* (Wiley, New York, 1975).

[158] M. Lindberg and S. W. Koch, Physical Review B **38**, 3342 (1988).

[159] M. Welkowsky and R. Braunstein, Physical Review B **5**, 497 (1972).

[160] M. Hirtschulz, F. Milde, E. Malić, S. Butscher, C. Thomsen, S. Reich, and A. Knorr, Physical Review B **77**, 035403 (2008).

[161] R. Binder, S. Koch, M. Lindberg, N. Peyghambarian, and W. Schäfer, Physical Review Letters **65**, 899 (1990).

[162] N. Kosugi, S. Matsuo, K. Konno, and N. Hatakenaka, Physical Review B **72**, 172509 (2005).

[163] E. Hendry, P. J. Hale, J. Moger, A. Savchenko, and S. Mikhailov, Physical Review Letters **105**, 097401 (2010).

[164] S. Mikhailov, Microelectronics Journal **40**, 712 (2009).

[165] P. Romanets and F. Vasko, Physical Review B **81**, 241411 (2010).

[166] B. Dóra, K. Ziegler, P. Thalmeier, and M. Nakamura, Physical Review Letters **102**, 036803 (2009).

[167] S. Mikhailov and K. Ziegler, Journal of Physics: Condensed Matter **20**, 384204 (2008).

[168] H. Avetissian, A. Avetissian, G. Mkrtchian, and K. V. Sedrakian, Physical Review B **85**, 115443 (2012).

[169] D. Hsieh, J. McIver, D. Torchinsky, D. Gardner, Y. Lee, and N. Gedik, Physical Review Letters **106**, 057401 (2011).

[170] S. Chen, C. Zhao, Y. Li, H. Huang, S. Lu, H. Zhang, and S. Wen, Optical Materials Express **4**, 587 (2014).

[171] S. Lu, C. Zhao, Y. Zou, S. Chen, Y. Chen, Y. Li, H. Zhang, S. Wen, and D. Tang, Optics Express **21**, 2072 (2013).

[172] X.-X. Zhang, T. T. Ong, and N. Nagaosa, Physical Review B **94**, 235137 (2016).

[173] L. Wu, S. Patankar, T. Morimoto, N. L. Nair, E. Thewalt, A. Little, J. G. Analytis, J. E. Moore, and J. Orenstein, arXiv preprint arXiv:1609.04894 (2016).

[174] K. Zhang, C. Bao, Q. Gu, X. Ren, H. Zhang, K. Deng, Y. Wu, Y. Li, J. Feng, and S. Zhou, Nature Communications **7** (2016).

[175] U. Kumar, V. Kumar, Enamullah, and G. S. Setlur, Journal of The Optical Society of America B **31**, 3042 (2014).

[176] V. Kumar, Enamullah, U. Kumar, and G. S. Setlur, Physica B: Condensed Matter **436**, 140 (2014).

[177] V. Kumar, Enamullah, U. Kumar, and G. S. Setlur, Pramana **83**, 597 (2014).

[178] V. Kumar, Enamullah, U. Kumar, and G. S. Setlur, European Physics Journal B **87**, 70 (2014).

[179] T. Kitagawa, E. Berg, M. Rudner, and E. Demler, Physical Review B **82**, 235114 (2010).

[180] N. H. Lindner, G. Refael, and V. Galitski, Nature Physics **7**, 490 (2011).

[181] T. Oka and H. Aoki, Physical Review B **79**, 081406 (2009).

[182] H. M. Dong, K. Han, and W. Xu, Journal of Applied Physics **115**, 063503 (2014).

[183] H. Weyl, Proceedings of the National Academy of Sciences **15**, 323 (1929).

[184] W. R. Inc., *Mathematica, Version 11.1*, champaign, IL, 2017.

[185] D. Huertas-Hernando, F. Guinea, and A. Brataas, Physical Review B **74**, 155426 (2006).

[186] Y. Yao, F. Ye, X.-L. Qi, S.-C. Zhang, and Z. Fang, Physical Review B **75**, 041401 (2007).

[187] M. König, H. Buhmann, L. W. Molenkamp, T. Hughes, C.-X. Liu, X.-L. Qi, and S.-C. Zhang, Journal of the Physical Society of Japan **77**, 031007 (2008).

[188] A. A. Zyuzin and A. A. Burkov, Physical Review B **83**, 195413 (2011).

[189] A. A. Zyuzin, M. D. Hook, and A. A. Burkov, Physical Review B **83**, 245428 (2011).

[190] S. F. Islam and T. K. Ghosh, Journal of Physics: Condensed Matter **26**, 165303 (2014).

[191] Y. Zhang, K. He, C.-Z. Chang, C.-L. Song, L. Wang, X. Chen, J. Jia, Z. Fang, X. Dai, W.-Y. Shan, et al., Nature Physics Letters **6**, 584 (2010).

[192] A. Schülzgen, R. Binder, M. Donovan, M. Lindberg, K. Wundke, H. Gibbs, G. Khitrova, and N. Peyghambarian, Physical Review Letters **82**, 2346 (1999).

[193] S. Schmitt-Rink, D. Chemla, and H. Haug, Physical Review B **37**, 941 (1988).

[194] D. Fröhlich, A. Nöthe, and K. Reimann, Physical Review Letters **55**, 1335 (1985).

[195] C. Ell, J. Müller, K. El Sayed, and H. Haug, Physical Review Letters **62**, 304 (1989).

[196] M. Brune, F. Schmidt-Kaler, A. Maali, J. Dreyer, E. Hagley, J. Raimond, and S. Haroche, Physical Review Letters **76**, 1800 (1996).

[197] P. Rakyta, A. Kormanyos, and J. Cserti, Physical Review B **82**, 113405 (2010).

[198] E. I. Rashba, Physical Review B **79**, 161409 (2009).

[199] Y. A. Bychkov and E. Rashba, JETP Letters **39**, 78 (1984).

[200] P. Pfeffer and W. Zawadzki, Physical Review B **59**, R5312 (1999).

[201] E. McCann, D. S. Abergel, and V. I. Fal'ko, The European Physical Journal-Special Topics **148**, 91 (2007).

[202] Enamullah, V. Kumar, U. Kumar, and G. S. Setlur, Pramana **82**, 1085 (2014).

[203] S. Mikhailov, Physica E: Low-dimensional Systems and Nanostructures **40**, 2626 (2008).

[204] F. Bloch and A. Siegert, Physical Review **57**, 522 (1940).

[205] S. A. Vierkötter, Journal of Magnetic Resonance, Series A **118**, 84 (1996).

[206] C. Wei, A. S. Windsor, and N. B. Manson, Journal of Physics B: Atomic, Molecular and Optical Physics **30**, 4877 (1997).

[207] S. Stenholm, Journal of Physics B: Atomic and Molecular Physics **6**, L240 (1973).

[208] A. Saĭko, G. Fedoruk, and S. Markevich, JETP Letters **84**, 130 (2006).

[209] M. Beijersbergen, R. Spreeuw, L. Allen, and J. Woerdman, Physical Review A **45**, 1810 (1992).

[210] V. Ostrovsky and E. Horsdal-Pedersen, Physical Review A **70**, 033413 (2004).

[211] J. H. Shirley, Physical Review **138**, B979 (1965).

[212] S. Swain, Physics Letters A **46**, 435 (1974).

[213] S. Swain, Journal of Physics B: Atomic and Molecular Physics **7**, 2363 (1974).

[214] S. Kumar, N. Kamaraju, K. Vasu, A. Nag, A. Sood, and C. Rao, Chemical Physics Letters **499**, 152 (2010).

[215] A. Schülzgen, R. Binder, M. E. Donovan, M. Lindberg, K. Wundke, H. M. Gibbs, G. Khitrova, and N. Peyghambarian, Physical Review Letters **82**, 2346 (1999).

[216] M. E. Donovan, A. Schuelzgen, K. Wundke, R. H. Binder, J. M. Lindberg, H. M. Gibbs, G. Khitrova, and N. Peyghambarian, in *Optoelectronics' 99-Integrated Optoelectronic Devices* (International Society for Optics and Photonics, 1999), pp. 216–223.

[217] H. Wang, J. H. Strait, P. A. George, S. Shivaraman, V. B. Shields, M. Chandrashekhar, J. Hwang, F. Rana, M. G. Spencer, C. S. Ruiz-Vargas, et al., Applied Physics Letters **96**, 081917 (2010).

[218] R. Ulbricht, E. Hendry, J. Shan, T. F. Heinz, and M. Bonn, Reviews of Modern Physics **83**, 543 (2011).

[219] Q. Chen, C. Zhang, F. Xue, Y. Zhou, W. Li, Y. Wang, W. Tu, Z. Zou, X. Wang, and M. Xiao, arXiv preprint arXiv:1307.0940 (2013).

[220] A. Das, S. Pisana, S. Piscanec, B. Chakraborty, S. Saha, U. Waghmare, R. Yiang, H. Krishnamurhthy, A. Geim, A. Ferrari, et al., arXiv preprint arXiv:0709.1174 (2007).

[221] R. Valdés Aguilar, J. Qi, M. Brahlek, N. Bansal, A. Azad, J. Bowlan, S. Oh, A. Taylor, R. Prasankumar, and D. Yarotski, Applied Physics Letters **106**, 011901 (2015).

[222] F. Boschini, M. Mansurova, G. Mussler, J. Kampmeier, D. Grützmacher, L. Braun, F. Katmis, J. Moodera, C. Dallera, E. Carpene, et al., arXiv preprint arXiv:1506.02692 (2015).

[223] N. Kumar, B. A. Ruzicka, N. Butch, P. Syers, K. Kirshenbaum, J. Paglione, and H. Zhao, Physical Review B **83**, 235306 (2011).

[224] M. Neupane, S.-Y. Xu, Y. Ishida, S. Jia, B. M. Fregoso, C. Liu, I. Belopolski, G. Bian, N. Alidoust, T. Durakiewicz, et al., Physical Review Letters **115**, 116801 (2015).

[225] I. Belopolski, S.-Y. Xu, Y. Ishida, X. Pan, P. Yu, D. S. Sanchez, H. Zheng, M. Neupane, N. Alidoust, G. Chang, et al., Physical Review B **94**, 085127 (2016).

[226] I. Belopolski, D. S. Sanchez, Y. Ishida, X. Pan, P. Yu, S.-Y. Xu, G. Chang, T.-R. Chang, H. Zheng, N. Alidoust, et al., Nature Communications **7** (2016).

[227] H. Hübener, M. A. Sentef, U. De Giovannini, A. F. Kemper, and A. Rubio, Nature Communications **8** (2017).

[228] H. M. Wiseman and G. J. Milburn, *Quantum Measurement and Control* (Cambridge university press, 2009).

[229] P. Knight and G. Gerry, *Introductory Quantum Optics* (Cambridge University Press Cambridge, 2005).

[230] F. Cummings, Physical Review **140**, A1051 (1965).

[231] E. T. Jaynes and F. W. Cummings, Proceedings of the IEEE **51**, 89 (1963).

[232] J. J. Sanchez-Mondragon, N. B. Narozhny, and J. H. Eberly, Physical Review Letters **51**, 550 (1983).

[233] G. S. Agarwal, Journal of The Optical Society of America B **2**, 480 (1985).

[234] H.-I. Yoo and J. H. Eberly, Physics Reports **118**, 239 (1985).

[235] F. W. Cummings, Physical Review **140**, A1051 (1965).

[236] J. H. Eberly, N. B. Narozhny, and J. J. Sanchez-Mondragon, Physical Review Letters **44**, 1323 (1980).

[237] N. B. Narozhny, J. J. Sanchez-Mondragon, and J. H. Eberly, Physical Review A **23**, 236 (1981).

[238] H. Yoo, J. Sanchez-Mondragon, and J. Eberly, Journal of Physics A: Mathematical and General **14**, 1383 (1981).

[239] J. Sanchez-Mondragon, N. Narozhny, and J. Eberly, Physical Review Letters **51**, 550 (1983).

[240] R. Short and L. Mandel, Physical Review Letters **51**, 384 (1983).

[241] P. Meystre and M. Zubairy, Physics Letters A **89**, 390 (1982).